From Theory to Experiment: A Computational Chemistry Perspective on Dative Bond and Non-Covalent Interactions

Ph.D. thesis

Mgr. Maximilián Lamanec

Faculty of Science │ Palacký University

Olomouc
2024

Abstract

This thesis explores advanced computational chemistry methods to investigate chemical bonding and molecular interactions. It uses computational approaches like DFT, MP2, CCSD(T), alongside other methods of computational chemistry, to analyze electronic structures and various properties of molecular systems. The study further examines dative bonds in p-group elements, elucidating their formation, unexpected behavior upon solvation, and significant role in addition reactions of secondary amines with fullerenes. Subsequently, it focuses on the behavior of molecules with hydridic hydrogen, highlighting their unique interactions when hydrogen acts as an electron donor and interacts with electrophiles. Finally, the thesis combines advanced computational chemistry methods with atomic force microscopy and for the first time demonstrates the anisotropic charge distribution on the surface of a covalently bonded halogen (σ-hole) and in the center of an aromatic ring with electronwithdrawing substituents (π-hole), showing excellent correlation between computational models and experimental observations.

Keywords: dative bond, non-covalent interactions, hydridic hydrogen, σ-hole, π-hole, QM calculations

Abstrakt

Táto dizertačná práca používa pokročilé metódy výpočtovej chémie na skúmanie chemických väzieb a molekulových interakcií. Pomocou výpočtových metód ako DFT, MP2, CCSD(T) a ďalších metód výpočtovej chémie, analyzuje elektrónové štruktúry a rôzne vlastnosti molekulových systémov. Dizertačná práca odhaľuje tvorbu datívnej väzby v prvkoch p-skupiny, jej neočakávané správanie pri solvatácii a významnú úlohu v adičných reakciách sekundárnych amínov s fulerénmi. Následne sa zameriava na molekuly obsahujúce hydridický vodík, zdôrazňujúc ich jedinečné interakcie, kde vodík pôsobí ako donor elektrónov a interaguje s elektrofilmi. Nakoniec práca spája pokročilé metódy výpočtovej chémie s mikroskopiou atomárnych síl a po prvýkrát ukazuje nerovnomerné rozloženie náboja na povrchu kovalentne viazaného halogénu (σ-dieru) a v strede aromatického kruhu s elektrofilnými substituentmi (π-dieru), ukazujúc vynikajúcu koreláciu medzi výpočtovými modelmi a experimentálnymi pozorovaniami.

Kľúčové slová: datívna väzba, nekovalentné interakcie, hydridický vodík, σ-diera, π-diera, kvantovomechanické výpočty

I hereby declare that this thesis is the result of my own work and all sources used are named in the list of references, in accordance with the Methodological Instructions on Ethical Principles in the Preparation of University Theses. I furthermore declare that no part of this thesis has been used for obtaining another degree.

Olomouc
March 2024

Maximilián Lamanec
maximilian.lamanec@upol.cz

Acknowledgements

To my beloved wife and our first child

Contents

List of Author's Publications

Articles published in years 2019-2024

1 M. Lamanec[*], R. Lo[*], D. Nachtigallová, A. Bakandritsos, E. Mohammadi, M. Dračínský, R. Zbořil, P. Hobza and W. Wang:
   'The Existence of a N→C Dative Bond in the C_{60}–Piperidine Complex',
   Angewandte Chemie International Edition **60**, 1942–1950 (2021).

2 R. Lo[*], M. Lamanec[*], W. Wang, D. Manna, A. Bakandritsos, M. Dračínský, R. Zbořil, D. Nachtigallová and P. Hobza:
   'Structure-directed formation of the dative/covalent bonds in complexes with C_{70}···piperidine',
   Physical Chemistry Chemical Physics **23**, 4365–4375 (2021).

3 R. Lo[*], D. Manna[*], M. Lamanec[*], W. Wang, A. Bakandritsos, M. Dračínský, R. Zbořil, D. Nachtigallová and P. Hobza:
   'Addition Reaction between Piperidine and C_{60} to Form 1,4-Disubstituted C_{60} Proceeds through van der Waals and Dative Bond Complexes: Theoretical and Experimental Study',
   Journal of the American Chemical Society **143**, 10930–10939 (2021).

4 B. Mallada[*], A. Gallardo[*], M. Lamanec[*], B. de la Torre, V. Špirko, P. Hobza and P. Jelínek:
   'Visualization of σ-hole in molecules by means of Kelvin probe force microscopy',
   Science **374**, 863–867 (2021).

5 R. Lo, D. Manna, M. Lamanec, M. Dračínský, P. Bouř, T. Wu, G. Bastien, J. Kaleta, V. M. Miriyala, V. Špirko, A. Mašínová, D. Nachtigallová and P. Hobza:
   'The stability of covalent dative bond significantly increases with increasing solvent polarity',
   Nature Communications **13**, 2107 (2022).

6 R. Lo, A. Mašínová, M. Lamanec, D. Nachtigallová and P. Hobza:
   'The unusual stability of H-bonded complexes in solvent caused by greater solvation energy of complex compared to those of isolated fragments',
   Journal of Computational Chemistry **44**, 329–333 (2022).

7 S. Civiš[*], M. Lamanec[*], V. Špirko, J. Kubišta, M. Špeťko and P. Hobza:
   'Hydrogen Bonding with Hydridic Hydrogen–Experimental Low-Temperature IR and Computational Study: Is a Revised Definition of Hydrogen Bonding Appropriate?',
   Journal of the American Chemical Society **145**, 8550–8559 (2023).

8   B. MALLADA[*], M. ONDRÁČEK[*], M. LAMANEC[*], A. GALLARDO, A. JIMÉNEZ-MARTÍN, B. DE LA
     TORRE, P. HOBZA and P. JELÍNEK:
     'Visualization of π-hole in molecules by means of Kelvin probe force microscopy',
     Nature Communications **14**, 4954 (2023).

Note: [*]These authors contributed equally.

List of Figures

List of Tables

List of Abbreviations

4BrPhM	tetrakis(4-BromoPhenyl) Methane
4FPhM	tetrakis(4-FluoroPhenyl) Methane
AFM	Atomic Force Micsroscopy
An	Anthracene
aug-cc-pVTZ	augmented-correlation-consistent polarized Valence Triple Zeta basis set
aug-cc-pwCVTZ-PP	augmented-correlation-consistent polarized weighted Core–Valence Triple Zeta basis set with PseudoPotentials
B3LYP	Becke, 3-parameter, Lee-Yang-Parr functional
BJ	Becke-Johnsson damping function
BOA	Born-Oppenheimer Approximation
BSSE	Basis Set Superposition Error
CC	Coupled Cluster
CCSD	Coupled Cluster with variational treatment of Single and Double excitations
CCSDT	Coupled Cluster with variational treatment of Single, Double, and Triple excitations
CCSD(T)	Coupled Cluster with variational treatment of Single and Double excitations and perturbative treatment of Triple excitations
CCSDTQ	Coupled Cluster with variational treatment of Single, Double, Triple, and Quadruple excitations
CCSDTQP	Coupled Cluster with variational treatment of Single, Double, Triple, Quadruple, and Pentuple excitations
CCSD(T)-F12	CCSD(T) with explicit correlation
CIHB	Charge Inverted Hydrogen Bond
CNTs	Carbon NanoTubes
cc-pVnZ	correlation-consistent polarized Valence n Zeta basis set

cc-pwCV*n*Z	correlation-consistent polarized weighted Core–Valence *n* Zeta basis set
cc-pwCV*n*Z-PP	correlation-consistent polarized weighted Core–Valence *n* Zeta basis set with PseudoPotentials
D2	Grimme's D2 dispersion correction
D3	Grimme's D3 dispersion correction
D4	Grimme's D4 dispersion correction
def2-*n*ZVPP	default 2 *n* Zeta Valence basis set with larger set of Polarization functions
def2-QZVP	default 2 Quadruple Zeta Valence basis set with set of Polarization functions
DFT	Density Functional Theory
DNA	DeoxyriboNucleic Acid
ESP	ElectroStatic Potential
F12	refers to r_{12} term in explicitly correlated wavefunction
FCI	Full Configuration Interaction
FCl-An	9,10-dichlorooctafluoroanthracene
GGA	Generalized Gradient Approximation
HF	Hartree-Fock
IR	InfraRed
KPFM	Kelvin Probe Force Microscopy
LDA	Local Density Approximation
LP	Lone Pair
MP2	Second order Møller-Plesset perturbation theory
MP3	Third order Møller-Plesset perturbation theory
MP4	Fourth order Møller-Plesset perturbation theory
MPPT	Møller-Plesset Perturbation Theory
NBO	Natural Bond Orbitals
nc-AFM	noncontact Atomic Force Microscopy
NL	Non-Local
PBE0	Perdew-Burke-Ernzerhof functional with 25% of Hartree-Fock exchange
PES	Potential Energy Surface
QM	Quantum Mechanical
RRHO	Rigid Rotor Harmonic Oscillator
SAPT	Symetry Adapted Perturbation Theory
SCF	Self-Consistent Field
SCS-MP2	Spin-Component-Scaled Second order Møller-Plesset perturbation theory

SE   Schrödinger Equation

VV10   Vydrov and van Voorhis 2010 functional

XC   Exchange-Correlation

ωB97X-D range-separated Becke 97 functional with Hartree-Fock exchange and Grimme's empirical dispersion correction

ωB97X-V range-separated Becke 97 functional with Hartree-Fock exchange and non-local correlation

Chapter 1

Introduction

Significant advances in computer technology have powered the remarkable rise of computational chemistry in recent years. Decades ago, the computational analysis of a simple water dimer using the Hartree-Fock method was a considerable task, whereas today, molecular systems comprising thousands of atoms can be evaluated using advanced Density Functional Theory methods within a similar timeframe. This field has become indispensable across various domains of chemistry, including drug discovery, materials science, and catalysis, providing insights that are often infeasible through experimental methods alone. By allowing the exploration of molecular interactions, reaction mechanisms, and potential energy surfaces *in silico*, computational chemistry not only accelerates the research and development cycle, but also offers a deeper understanding of fundamental chemical principles. Its integration into the standard toolkit of chemists signifies a paradigm shift towards more predictive and cost-effective research.

In recent times, basic research is often overshadowed by the emphasis on applied science, where the former is sometimes seen as "science for the sake of science." This view raises questions about the value and purpose of scientific findings that do not have immediate applications. Yet, it is crucial to recognize that basic research provides the critical foundation, enhancing our understanding of core chemical principles and offering new insights into established chemical knowledge. This thesis mainly aims to clarify the fundamental properties of chemical bonds, a key aspect of basic research. Exploring these basic properties not only expands our scientific knowledge but also inspires new techniques and methods in applied research, highlighting the vital connection between basic and applied sciences.

Chapter 2 establishes the theoretical foundation, crucial for understanding the subsequent discussions on molecular interactions. It offers an in-depth analysis of non-covalent interactions, highlighting their significant impact on molecular structure and properties. This knowledge is vital for explaining the basics of molecular assemblies in various chemical contexts.

In Chapter 3, a comprehensive analysis of computational chemistry methodologies is provided, outlining the theoretical and computational approaches employed in mod-

eling and analyzing chemical entities. This chapter lays a methodological groundwork for the research discussed in later sections, facilitating a detailed investigation of molecular interactions.

Chapter 4 explores dative bonding within p-group elements, introducing a novel type of dative bond wherein carbon atoms in fullerenes act as lone pair acceptors. This chapter bridges the dative bonds and non-covalent interactions, demonstrating comparable stabilities between dative bond complexes and van der Waals complexes involving fullerenes and piperidine. Additionally, it reveals an intriguing observation: dative bonds exhibit enhanced stabilization in solvents with increasing polarity.

Chapter 5 delves into hydridic hydrogen bonds, challenging the traditional view by examining scenarios where hydrogen is more electronegative than its bonding partner. This analysis extends the conventional understanding of hydrogen bonding.

In Chapter 6, Kelvin Probe Force Microscopy is applied to visualize anisotropic charge distributions directly, bringing theoretical predictions to direct observation. Through the visualization of σ-holes and π-holes, this chapter effectively demonstrates the alignment of computational predictions with experimental findings, highlighting the symbiotic relationship between theoretical insights and empirical validation.

Chapter 2

Covalent Bond, Dative Bond and Non-Covalent Interactions in Perspective of Computational Chemistry

The forces that bind atoms within molecules and unite molecules into clusters, crystals, and the complex frameworks of biological structures are collectively known as chemical bonds. First conceptualized in the early 20th century[1], these bonds form through interactions between valence electrons, the outermost participants in an atom's chemical interactions. The landscape of chemical bonding is diverse, featuring covalent, dative, ionic, and various non-covalent bonds. Though varied in nature, these bonds lead to a single outcome: the stabilization of the system through an energy reduction upon bond formation.

In the domain of computational chemistry, a diverse array of tools reveals the complex interplay of atomic and molecular interactions. Strategies for solving the Schrödinger equation (SE) range in accuracy, providing insights into the subtleties of chemical bonding. The spectrum extends from the foundational Hartree-Fock (HF) method to the computationally intensive Full Configuration Interaction (FCI), which encompasses all electron correlations. Positioned between these is the Coupled Cluster (CC) approach, which is often heralded as the 'gold standard' of quantum chemistry in its form with variational treatment of single and double excitations and perturbative treatment of triple excitations (CCSD(T)). Alternatively, to these wavefunction-based methods, Density Functional Theory (DFT) offers a different perspective by treating the Schrödinger equation as a functional of electron density. Through a multitude of functionals, DFT can address a wide array of both general and specific chemical problems.

2.1   Covalent Bond

A covalent bond is established when two atoms approach each other closely enough that their outer electron shells overlap, leading to the sharing of an electron pair. Each electron in the shared pair originates from a different atom.

$$H\cdot + \cdot H \longrightarrow H—H$$
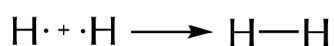
Figure 2.1: Scheme showing the formation of a covalent bond between two hydrogen radicals.

Due to the distinct directional characteristics of atomic orbitals, several types of covalent bonds are recognized. The overlapping of two s-orbitals gives rise to a σ-bond, while the lateral overlapping of two p-orbitals results in a π-bond. In rare cases, the overlapping of two d-orbitals can lead to the formation of a δ-bond[2]. Additionally, there have been reports of a φ-bond, which arises from the overlapping of two f-orbitals[3].

In the case of homonuclear diatomic molecules, the charge distribution is symmetrical. Contrastingly, heteronuclear chemical bonds exhibit an asymmetrical charge distribution, resulting in partial charges. The spatial arrangement of these charges correlates with the atoms' electronegativity; atoms with higher electronegativity attract more electron density, manifesting a partial negative charge[4]. Atoms of lower electronegativity bear a partial positive charge. This disparity in charge distribution culminates in a molecular dipole moment and other multipoles, the magnitude of which is proportional to the electronegativity difference. Consequently, a greater disparity in electronegativity increases the dipole moment.

2.2   Dative Bond

A dative bond, also known as a donor-acceptor, coordinate-covalent, charge-transfer complex bond, or just dative bond, represents a unique bonding interaction in which two atoms share an electron pair, with both electrons originating from the same atom. In this configuration, the electron donor, the atom providing the electron pair, is typically a Lewis base, while the electron acceptor is a Lewis acid[5]. This mode of bonding is distinct from a covalent bond, where each atom contributes one electron to the shared pair. Upon dissociation, a dative bond cleaves heterolytically, allowing the donor atom to retain the electron pair[6,7]. An exemplar of this phenomenon is depicted in Figure 2.2, where the Lewis acid, boron hydride, accepts an electron pair from the Lewis base, ammonia, resulting in a bond strength of 49.9 kcal/mol[8].
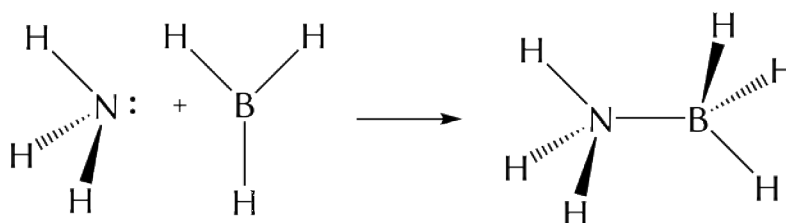
Figure 2.2: Scheme showing the formation of a dative bond between ammonia and boron hydride.

Lewis acids can include transition metals, elements of the s-group in the periodic table, and certain elements of the p-group. In specific cases, fullerenes and other carbon nanostructures can also act as Lewis bases[8–10]. On the other hand, any atom with a lone electron pair can act as a Lewis base.

The corresponding wavefunction for a dative bond can be written as:

$$\Psi_{\text{dative}}(D^+ - A^-) = a\Psi_{\text{covalent}}(D - A) + b\Psi_{\text{ionic}}(D^+, A^-) \tag{2.1}$$

Here, the covalent and ionic structures are distinct for the donor (D)–acceptor (A) complex and the coefficients a and b depend on the ability of D to donate an electron (ionization potential) and A to accept the electron (electron affinity)[11].

2.3 Non-Covalent Interactions

Non-covalent interactions play an essential role in a wide range of chemical processes, supramolecular assembly, and the stability of molecular complexes. These interactions, characterized by their transient nature are responsible for the anomaly of water, the double helix structure of DNA, or the liquifying of noble gases. Contrary to the covalent bond, non-covalent interactions do not involve electron pair sharing between two atoms. Their attractive nature stands on electrostatics, induction, and London dispersion.

Computational chemistry provides a powerful toolset to investigate non-covalent interactions at the atomic level, complementing experimental techniques and offering detailed insights into their underlying mechanisms. Using quantum chemical methods, molecular mechanics, and molecular dynamics simulations, computational chemists can accurately predict and analyze the properties, energetics, and dynamics of non-covalent interactions. This computational approach enables the study of complex systems that are challenging to explore solely through experimental means.

2.3.1 Hydrogen Bond

The hydrogen bond, which is widely recognized as one of the strongest and most prevalent noncovalent interactions, plays a crucial role in numerous chemical processes.

It is characterized by the formation of an X-H⋯Y-Z bond, where X represents a more electronegative atom than hydrogen (H), and Y can be an atom, anion, fragment of a molecule, or a π-electron system. X-H is a proton donor and Y-Z is a proton acceptor[12].

The presence of a hydrogen bond can be easily detected through various spectroscopic techniques. This detection is facilitated by the fact that the atom X is always heavier than hydrogen. When a hydrogen bond is formed, there is a transfer of electron from the electron donor Y to the σ^* antibonding orbital of the X-H bond[13,14]. This charge transfer leads to the elongation of the X-H bond and a red-shift in the corresponding X-H stretching frequency. However, it has been demonstrated by Hobza et al. that under similar conditions, a blue-shift in the stretching frequency is also possible[15,16] as shown in Figure 2.3.
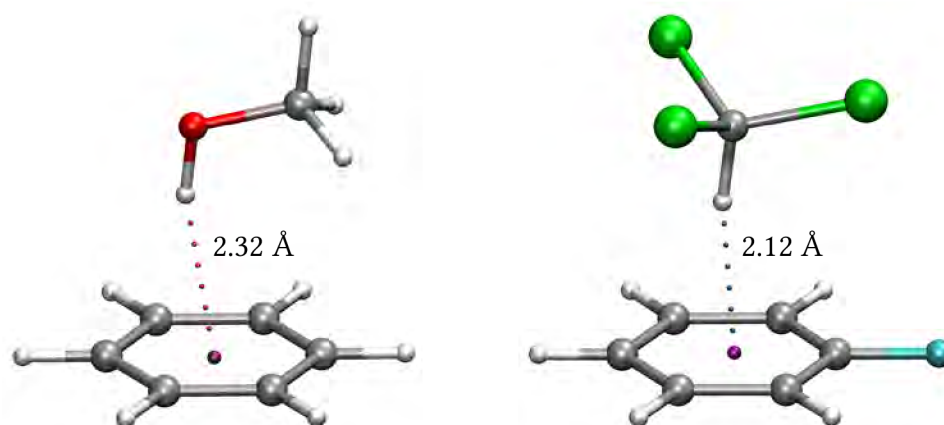
Figure 2.3: Hydrogen bonded complexes showing R-H⋯π interaction. On the left is complex of methanol with benzene. Its measured experimental IR shift of O-H stretching frequency is -14 cm^{-1}[17]. On the right is blueshiftng complex of chloroform and monofluorobenzene with respective shift of C-H stretching frequency by 14 cm^{-1}[15].

The study and understanding of hydrogen bonding have significant implications in va-rious scientific disciplines, including chemistry, biochemistry, and materials science. Hydrogen bonds play a crucial role in molecular recognition, protein folding, solvation phenomena, and the stability of supramolecular structures[18]. The ability to detect and characterize hydrogen bonding through spectroscopic methods provides valuable insights into the nature and behavior of these interactions, aiding in the design and development of functional materials and pharmaceutical compounds.

A unique type of hydrogen bond called a dihydrogen bond can occur when the donor of the hydrogen bond is hydridic hydrogen. Hydridic hydrogen is characterized by its binding to an atom that is less electronegative than hydrogen itself. This leads to charge inverted hydrogen bond also called inverse or hydridic hydrogen bond discussed below.

2.3.2   Charge-Inverted Hydrogen Bond

The charge-inverted hydrogen bond (CIHB) is a distinctive non-covalent interaction wherein a hydrogen atom is linked to a less electronegative atom, conferring upon it a partial negative charge. This peculiar arrangement permits the hydrogen to form bonds with electrophiles, as elucidated by Mirosław Jabłoński in 2006. CIHBs were initially demonstrated in simple dimers such as $H_3XH \cdots YH_3$, where X could be silicon or germanium, and Y could be aluminum or gallium[19]. Subsequent studies expanded the scope to more complex systems with various substituents. Notably, CIHBs exhibit bond elongation and vibrational red-shifting, characteristic of standard hydrogen bonds but arising from a reverse charge transfer direction, specifically $\sigma_{XH} \rightarrow p_y$, as opposed to the conventional $\sigma_{XH} \leftarrow p_y$. Furthermore, dimers such as $H_3X - H \cdots YH_3$ display non-linear structures and interaction energies that are consistent with moderately strong hydrogen bonds, despite their charge-inverted nature[20]. This interaction was experimentally proven by a team led by Professor Hobza[21].
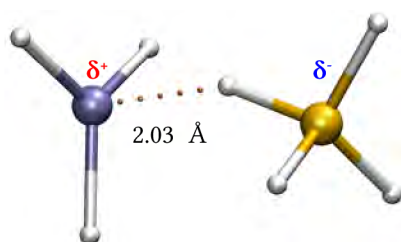
Figure 2.4: CIHB in complex of AlH_3 and SiH_4.

In addition to the traditional hydrogen bond, there are several other types of "hydrogen" bonds that involve hydridic hydrogen, such as the hydride bond, agostic bond, or halogen hydride bond[22]. These various "subspecies" contribute to the confusing complexity of the world of non-covalent interactions. To address this, it has been suggested in ref. 21 to redefine the existing definition of a hydrogen bond to encompass all of these interactions.

2.3.3   Halogen Bond and σ-hole Bonding

The conventional notion of halogens being uniformly negative was challenged in 1986 when Ramasubbu et al. published a groundbreaking study elucidating the proximity of halogen atoms to nucleophiles in various structures found in the Cambridge Structural Database[23]. This finding challenged the established understanding and paved the way for a deeper understanding of halogen bonding. Seven years later, Politzer and his colleagues demonstrated that in the case of chlorine and bromine bonded to carbon, there exists a positively charged region atop the halogen atom, opposed to the covalent bond[24]. This phenomenon was subsequently termed the 'sigma-hole' (σ-hole).
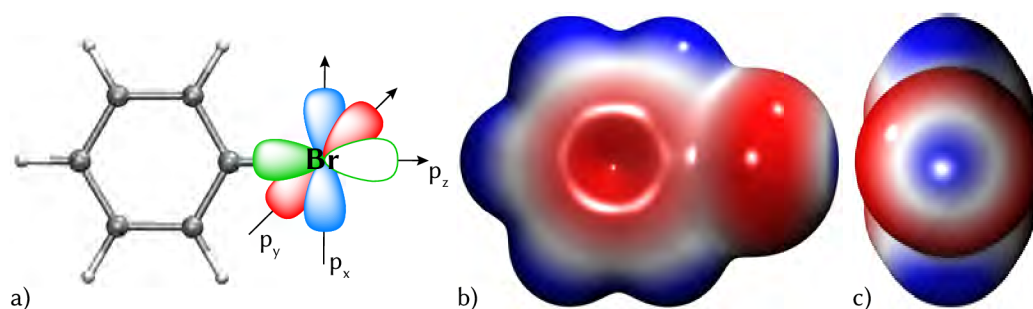
Figure 2.5: a) Representation of valence p-orbitals in bromobenzene: p_x (blue) and p_y (red) orbitals are doubly occupied, whereas p_z contains one electron participating in the C-Br covalent bond. b) ESP figure of bromobenzene showing negative 'belt' around bromine atom. c) ESP figure of bromobenzene σ-hole of bromobenzene. In ESP figures the red color shows negative regions and the blue color symbolizes positive regions.

The presence of a positively charged region on covalently bonded halogens may initially seem paradoxical. However, it can be rationalized through the example of the bromobenzene molecule. Bromine's valence shell electron configuration is $4s^2\ 3d^{10}\ 4p_x^2\ 4p_y^2 4p_z^1$ (illustrated in the Figure 2.5a). Hybridization of the halogen atoms has negligible influence since the s-orbital is energetically much lower than the p-orbitals[25]. The p_x and p_y orbitals are both doubly occupied, forming a negatively charged belt around the bromine atom (cf. Figure 2.5b). On the other hand, one electron from the p_z orbital participates in a covalent bond, resulting in a positive "cap" located opposite to the covalent bond (cf. Figure 2.5c).

This observation underscores the complex electronic structure and spatial distribution of charge in covalently bonded halogens. The existence of the σ-hole reveals a fascinating aspect of halogen bonding and has significant implications for understanding intermolecular interactions and molecular recognition processes in various chemical systems[26–28].

The σ-hole can be visualized via Electrostatic Potential (ESP) mapping, denoted by $V(\mathbf{r})$. It serves as a critical descriptor of the charge distribution within atoms and molecules, encapsulating the balance between nuclear and electronic influences. It quantitatively describes the electric field's potential energy at any point $\mathbf{r}$ in the vicinity of the chemical species, highlighting regions where an electric charge would experience force. This potential is fundamentally defined by the integral over the charge density $\rho(\mathbf{r}')$, mathematically represented by:

$$V(\mathbf{r}) = \int \frac{\rho(\mathbf{r}')}{|\mathbf{r} - \mathbf{r}'|} d\mathbf{r}' \tag{2.2}$$

ESP calculations are fundamental in identifying reactive sites, assessing molecular polarity, and understanding biological recognition and binding interactions[29,30]. Positive ESP regions typically suggest proximity to the nucleus, while negative regions indicate areas shielded by electron density. Such spatial variations in ESP are pivotal in mapping
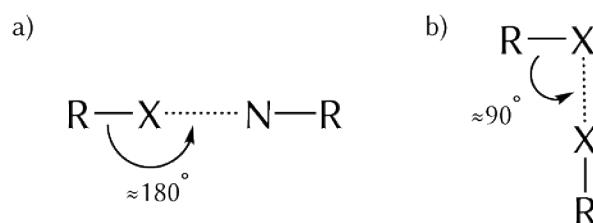
Figure 2.6: Illustration of a halogen bond (a) and a dihalogen bond (b). In (a), 'X' represents a covalently bonded halogen atom, and 'N' is a generic nucleophile. In (b), a covalently bonded halogen interacts with the negative region of another halogen atom.

out reactive sites, assessing molecular polarity, and understanding the complex forces that play in biological recognition and binding processes. One of the mapped reactive sites is the σ-hole.

In 2013, the halogen bond was defined as: *"A halogen bond occurs when there is evidence of a net attractive interaction between an electrophilic region associated with a halogen atom in a molecular entity and a nucleophilic region in another, or the same, molecular entity"*[31]. Its scheme is shown in Figure 2.6. A typical donor of a halogen bond is an atom with a lone pair, anion, or π-electron system. An angle between a covalent bond of halogen and a halogen bond is always close or equal to 180° (Figure 2.6a). There is one special case when halogen with σ-hole interacts with a negative "belt" of another halogen atom. It is called dihalogen bond[32] and the angle between a covalent bond of halogen acceptor and halogen bond is 90° (figure 2.6b). the specific directionality of halogen bonding plays a vital role in molecular recognition, supramolecular chemistry, crystal engineering, and other fields. It contributes to the selective binding of halogen-containing molecules to complementary Lewis bases, leading to the formation of well-defined supramolecular architectures and influencing the properties and reactivity of these systems[33,34].

2.3.4 π-hole Interactions

In 1865, the German chemist Friedrich August Kekulé published a seminal paper[35] describing the structure of benzene as alternating single and double bonds between six carbon atoms. However, this model was revised in 1964 by Bacon and colleagues, who conducted a neutron diffraction experiment revealing that the carbon-carbon bond lengths in benzene are equal, measuring 1.39 Å[36]. The concept of benzene featuring three delocalized π-orbitals was subsequently confirmed by further research[37–39].

Regarding non-covalent interactions, benzene can form dimers in two energetically favorable configurations: parallel-displaced and T-shaped[40]. However, in complexes involving hexafluorobenzene, the most stable configuration is a sandwich-like structure, with the benzene molecule aligning perfectly beneath the hexafluorobenzene[41]. This arrangement is facilitated by the π-hole phenomenon in hexafluorobenzene, a region of electron deficiency perpendicular to its π-bonds[42], allowing favorable interactions

with electron-rich species such as benzene, lone pair-containing molecules, or anions[43].

The π-hole refers to a region of positive electrostatic potential that emerges above and below the plane of a π-system, like an aromatic ring or a conjugated system. This arises from an asymmetric distribution of electronic charge, especially pronounced in molecules with electronegative substituents. The π-hole is characterized by a relative electron deficiency due to electron withdrawal from the π-system, as illustrated in Figure 2.7. In hexafluorobenzene, electrons are also distributed around the fluorine atoms, leading to the formation of a positive 'hole' in the center of the conjugated system.

π-hole bonding plays a pivotal role in anion-π recognition, especially in the selective binding and stabilization of anions. In this process, anions are 'recognized' by a system containing a π-hole. Such insights are crucial in fields like supramolecular chemistry, where designing selective receptors and sensors depends on a deep understanding of non-covalent interactions. Moreover, anion-π interactions are not just of academic interest; they have practical applications in material science and the development of novel therapeutic agents. A nuanced understanding of these interactions can lead to more efficient and targeted molecular designs[44].
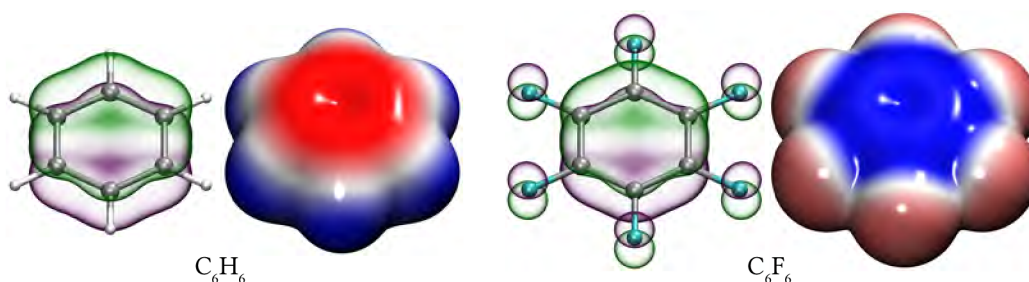
Figure 2.7: Visualization of higher occupied molecular orbitals and ESP of benzene and hexafluorobenzene. In ESP figures the red color shows negative regions and the blue color symbolizes positive regions.

Chapter 3

Methods of Computational Chemistry

Computational chemistry utilizes advanced tools to investigate a wide range of properties of chemical species. Significant progress has been made in recent years, enabling the study of even larger molecules consisting of thousands of atoms, albeit with some compromise in accuracy. As computational power continues to improve, it opens up new possibilities to tackle larger and more complex systems using more accurate and sophisticated methods in the field of computational chemistry. This continuous advancement empowers researchers to explore the behavior and properties of diverse chemical systems, contributing to a deeper understanding of chemical phenomena.

3.1   Schrödinger Equation

At the beginning of the twentieth century, a revolutionary understanding of fundamental physical principles emerged, known as quantum mechanics. This groundbreaking field was initiated by Max Planck's seminal work published in Annalen der Physik, where he introduced the concept that energy is not continuously emitted or absorbed, but rather in discrete units called "quanta". In 1924, Louis de Broglie put forth the hypothesis that all physical systems can be described by a wavefunction, denoted as "Ψ". One year later, Erwin Schrödinger formulated an equation[45] that describes the evolution of the wavefunction over time. For stationary states, he proposed a time-independent equation:

$$\hat{H}|\Psi\rangle = E|\Psi\rangle \tag{3.1}$$

where $\hat{H}$ is Hamiltonian and E is an eigenvalue of energy. The time-independent SE provides a mathematical framework to study the stationary states of quantum systems, where the energy of the system remains constant over time. The equation states that the Hamiltonian operator acting on the wavefunction yields a scalar multiple of the wavefunction itself. This scalar multiple represents the energy of the system associated with the particular wavefunction.

Solving the time-independent SE involves finding the wavefunction $\psi(\mathbf{r})$ and the corresponding energy eigenvalues E for a given Hamiltonian operator. The solutions provide insights into the allowed energy levels and wavefunctions of the system.

The time-independent SE plays a central role in quantum chemistry, solid-state physics, and other branches of quantum mechanics. It allows for the calculation of energy spectra, electron distributions, and other observable properties of quantum systems.

3.1.1 Born-Oppenheimer Approximation

The Schrödinger equation is a partial differential eigenvalue equation that describes quantum systems. As the number of particles increases, the number of variables in the wavefunction and computational complexity also increase. To simplify this problem, the Born and Oppenheimer approximation (BOA) was proposed, which takes advantage of the significant mass difference between nuclei and electrons[46]. According to the BOA, the nuclei can be treated as stationary entities, decoupled from the movement of electrons.

In computational chemistry, the electronic Hamiltonian with the BOA can be written as:

$$\hat{H}_{\text{el}} = -\frac{\hbar^2}{2m} \sum_{i=1}^{N} \nabla_i^2 - \sum_{i=1}^{N} \sum_{j>i}^{N} \frac{Z_i Z_j e^2}{4\pi\epsilon_0 r_{ij}} + \sum_{i=1}^{N} V_{\text{ext}}(\mathbf{r}_i) + \sum_{i=1}^{N} \sum_{j>i}^{N} \frac{e^2}{4\pi\epsilon_0 r_{ij}} \tag{3.2}$$

where $\hat{H}_{\text{el}}$ is the electronic Hamiltonian, $\hbar$ is the reduced Planck's constant, m is the electron mass, N is the number of electrons, ∇_i^2 is the Laplacian operator for the ith electron, Z_i is the nuclear charge of the ith nucleus, e is the elementary charge, ϵ_0 is the vacuum permittivity, r_{ij} is the distance between electrons i and j, and $V_{\text{ext}}(\mathbf{r}_i)$ is the external potential acting on the ith electron. By employing the BOA in computational chemistry the electronic structure of molecules can be efficiently explored by treating the nuclei as fixed while focusing on the electronic behavior. This simplification allows for the study of various molecular properties and phenomena.

3.2 Hartree-Fock Method

The HF method, pivotal in computational quantum chemistry, was formulated through the contributions of Douglas Hartree in 1927[47] and Vladimir Fock in 1930[48]. Hartree initially developed the method using self-consistent field concepts, which Fock later refined by introducing the determinant approach to account for electron exchange and symmetry. This evolution marked a significant milestone, transitioning from qualitative theories to quantitative computational models in chemistry. The HF method significantly advanced the predictive capabilities for electronic structures and properties of atoms and molecules, establishing the foundation for many modern computational techniques in quantum chemistry and physics.

The HF method is a computational approach in quantum chemistry for approximating the wavefunction and energy of a quantum many-body system in a stationary state. It simplifies the complex interactions in a many-electron system to a single electron moving in an average field created by all other electrons. This is done by representing the many-electron wavefunction as a single Slater determinant, an antisymmetrized product of one-electron orbitals, thereby adhering to the Pauli exclusion principle.

The core of the HF method is solving the Fock equations iteratively. These equations, derived from the variational principle, can be expressed as:

$$F\phi_i = \epsilon_i \phi_i \tag{3.3}$$

where F is the Fock operator, ϕ_i are the molecular orbitals, and ϵ_i are the orbital energies. This self-consistent field (SCF) process optimizes orbitals to minimize the total electronic energy. Although HF omits electron correlation, it provides an essential approximation, forming the basis for more advanced methods that include electron correlation, like post-Hartree-Fock techniques.

One of the primary limitations of the HF method is its inability to account for the majority of correlation energy. According to Löwdin's definition[49]:

$$E_{\mathrm{corr}} = E_{\mathrm{exact}} - E_{\mathrm{HF}} \tag{3.4}$$

the correlation energy (E_{corr}) is defined as the difference between the exact energy (E_{exact}) and the HF energy (E_{HF}). This correlation energy, also referred to as Coulomb correlation energy arises from the interaction among electrons, which generally reduces the probability of finding two electrons (of any spin) nearby. The part accounted for the HF method is termed the Fermi correlation. Electrons are indistinguishable particles according to Fermi-Dirac statistics. It means, swapping any two electrons changes the sign of their wavefunction[50]. From this perspective, it is evident that the HF method is insufficient for interactions where electron correlation plays a crucial role.

3.3   Post-Hartree-Fock Methods

Post-Hartree-Fock methods have been developed to correct deficiencies of the HF method like failure to correctly predict dissociation energies, equilibrium bond lengths, and vibrational frequencies. These advanced techniques, including Møller-Plesset perturbation theory (MPPT), Coupled Cluster theory, and Configuration Interaction, aim to incorporate correlation energy more accurately. By going beyond the mean-field approximation of HF, they provide a more complete and precise description of electron interactions in molecules. These methods are pivotal in computational chemistry, offering enhanced predictive capabilities for a wide range of chemical properties and reactions.

3.3.1   Møller-Plesset Perturbation Theory

Møller-Plesset Perturbation Theory, named after Christian Møller and Milton Spinoza Plesset, is a quantum chemistry method used to improve HF calculations. This method falls under the category of post-HF approaches and is widely recognized for its ability to account for electron correlation, a critical aspect that HF theory neglects.

MPPT operates by adding an electron correlation energy term to the HF wavefunction and energy using Rayleigh-Schrödinger perturbation theory. The overall approach is to treat the electron correlation as a perturbation to the mean-field description provided by the HF method[51]. The theory is typically expressed in orders, with the second-order Møller-Plesset perturbation theory (MP2) being the most commonly used. Higher-order terms, such as MP3 and MP4, add further corrections but at the cost of increased computational expense.

$$E = E^{(0)} + E^{(1)} + E^{(2)} + E^{(3)} + \cdots + E^{(n)} \tag{3.5}$$

Here, $E^{(0)}$ is the zeroth-order energy (HF energy), $E^{(1)}$ is the first-order correction , and $E^{(n)}$ represents the nth-order correction to the energy. Since the first-order energy is from definition zero, MP2 is first meaningful correction to HF energy. The second-order energy is then given by the formula:

$$E^{(2)} = \frac{1}{2} \sum_{i,j,a,b} \frac{\langle \varphi_i \varphi_j | \varphi_a \varphi_b \rangle \langle \varphi_a \varphi_b | \varphi_i \varphi_j \rangle}{\epsilon_i + \epsilon_j - \epsilon_a - \epsilon_b} - \frac{1}{2} \sum_{i,j,a,b} \frac{\langle \varphi_i \varphi_j | \varphi_a \varphi_b \rangle \langle \varphi_a \varphi_b | \varphi_j \varphi_i \rangle}{\epsilon_i + \epsilon_j - \epsilon_a - \epsilon_b} \tag{3.6}$$

where φ_i and φ_j are canonical occupied orbitals, φ_a and φ_b are unoccupied orbitals and ϵ_i, ϵ_j, ϵ_a, ϵ_b, are corresponding orbital energies.

However, MP2 has several limitations. It incurs greater computational costs than HF, with the expense scaling as N^5 with respect to the size of the system, rendering it less practical for very large molecules. MP2 is also subject to size consistency errors, implying that the energy may not appropriately scale with the system size. A significant drawback, particularly concerning non-covalent interactions, is MP2's tendency to overestimate dispersion energy, which can lead to inaccuracies in modeling van der Waals complexes[52,53].

3.3.2   Coupled Cluster

Coupled cluster is a widely used numerical technique in computational chemistry, serving as one of the post-Hartree-Fock methods for accurate electronic structure calculations. Its origins can be traced back to its introduction as a method in nuclear physics by Coester and Kümmel in 1960[54]. In subsequent years, Jiří Čížek[55], and later with Josef Paldus[56], adapted and refined the CC method for electron correlation in atoms and molecules.

In CC, the wavefunction is represented as an exponential ansatz of a reference wavefunction:

$$|\Psi\rangle = exp(\hat{T})|\phi_0\rangle \tag{3.7}$$

Typically, the reference wavefunction for equation 3.7, ϕ_0, is obtained from a SCF calculation, often as a Slater determinant. The cluster operator, $\hat{T}$, is expressed as a sum of its many-body excited components. For example, the $\hat{T}_n$ operator corresponds to the n-body excited components and is defined as:

$$\hat{T}_n = \frac{1}{n!} \sum_{\substack{i,j,k,\dots \\ a,b,c,\dots}} t_{ijk\dots}^{abc\dots} \hat{E}_{ijk\dots}^{abc\dots} \tag{3.8}$$

Here, $t_{ijk\dots}^{abc\dots}$ represents the spatial orbital-based cluster amplitudes corresponding to excitations from occupied orbitals $i, j, k\dots$ to unoccupied or virtual orbitals $a, b, c\dots$ and operator $\hat{E}_{ijk\dots}^{abc\dots}$ denotes the spin-summed second-quantization excitation operators[57]. When the method includes only the singles ($\hat{T}_1$) and doubles ($\hat{T}_2$) excitation clusters, it is termed CCSD, with 'S' and 'D' denoting single and double excitations, respectively. However, incorporating triple ($\hat{T}_3$), quadruple ($\hat{T}_4$), and pentuple ($\hat{T}_5$) excitations escalates computational demands significantly. The hierarchy of correlation energy convergence in coupled cluster methods, assuming an appropriate basis set, is confirmed as: CCD < CCSD < CCSDT < CCSDTQ < CCSDTQP < FCI[58]. Extensive research has explored the properties of small isolated molecules, such as ionization potentials, electron affinities, and excitation energies[59]. The CCSDTQ method yields an interaction energy error less than 0.1 kcal/mol compared to the FCI reference, signifying subchemical accuracy. Advancements to the CCSDTQP show negligible improvement relative to the increased computational cost[60]. To expedite calculations, Urban et al. introduced a non-iterative treatment of triples, employing the full cluster operator for single and double excitations and only the $\hat{T}_2$ operator for triple calculations[61]. Nonetheless, the widely recognized 'gold standard' in quantum chemistry is the CCSD(T) method, introduced by Pople and Head-Gordon, which applies a perturbative correction to the CCSD wavefunction to include triple excitation contributions (the 'T' in parentheses indicates perturbative treatment)[62].

3.3.3   Explicitly Correlated Methods

The foundation of explicitly correlated F12 methods can be traced back to the pioneering work of Egil A. Hylleraas in the late 1920s[63]. Hylleraas introduced interelectronic distances into the wavefunction expansion to reduce the basis set incompleteness error, significantly advancing the quantum mechanical treatment of the helium atom. In 1985, Werner Kutzelnigg proposed the idea of factorizing all difficult many-electron integrals into one- and two-electron integrals by inserting the resolution of the identity, and used partial wave analysis to demonstrate how to do this accurately[64]. This led to the development of modern F12 methods, where explicit correlation means adding terms directly to the wavefunction ansatz to treat electronic correlation explicitly.

The first-order Møller-Plesset (MP) wavefunction is obtained by minimizing the Hylleraas functional for the second-order MP energy. The zeroth-order MP Hamiltonian is represented by the Fock operator. The MP1-F12 wavefunction includes explicitly correlated (geminal) functions in addition to the conventional doubly excited determinants found in standard MP2 methods.

The geminal basis functions in MP1-F12, representing quasi-double excitations relative to the reference, are projected by a special operator $\hat{Q}_{12}$, ensuring their strong orthogonality to the standard doubly excited determinants. There are three approaches to treating the projector $\hat{Q}_{12}$[65–68]. The MP2-F12 energy is derived by considering the matrix representation of the first-order interacting space, which includes both the doubly excited determinants and the geminal functions. The approach involves block-diagonalization to address the non-invertibility of the zeroth-order Hamiltonian matrix in MP2-F12 due to the inclusion of geminal functions[69].

The final first-order MP1-F12 wavefunction is expressed as a sum of conventional F12 and "coupling" terms. The coefficients of standard doubles and geminal functions are coupled via the off-diagonal block of the zeroth-order Hamiltonian. The second-order energy in MP2-F12 is a sum of the conventional MP2 energy and an F12 correction term, reflecting the additional considerations brought in by the inclusion of geminal functions in the MP2-F12 method[50].

Nowadays, explicitly correlated *ab initio* methods based on or inspired by the original F12 treatment represent practical alternatives for achieving complete basis set accuracy. Their greatest methodological advantage is that these methods essentially preserve the orbital product expansion, but at the same time effectively describe the electron correlation cusp by introducing orbital pair products multiplied by a correlation factor. In the last decade, it has been revealed that the Slater-type geminal is the most advantageous choice for the explicitly correlated part[70].

3.4   Density Functional Theory

DFT is an influential approach utilized in quantum chemistry and condensed matter physics to tackle the electronic structure problem. At its core lies the Hohenberg-Kohn theorem, which asserts that the ground-state electronic density unequivocally determines the external potential energy of a system. This fundamental theorem establishes a direct correlation between electron density and total energy, forming the basis for the development of practical DFT methodologies. Derived from the Hohenberg-Kohn theorem, the Kohn-Sham equations provide the framework for the widely employed Kohn-Sham DFT method. These equations introduce a set of auxiliary non-interacting electrons governed by an effective potential, enabling the determination of ground-state properties via the solution of a self-consistent field problem. However, the exact form of the DFT functional remains unknown, necessitating the utilization of various approximation methods.

3.4.1 Local Density Approximation

Local Density Approximation (LDA) is the simplest type of DFT functional, which assumes that the exchange-correlation energy depends only on the local electron density at each point in space. LDA originates from a model of homogenous electron gas. Mathematically can be LDA expressed as:

$$E_{XC}^{LDA}[\rho] = \int \rho(\mathbf{r})\epsilon(\rho(\mathbf{r}))\,d\mathbf{r} \tag{3.9}$$

where $\epsilon(\rho(\mathbf{r}))$ is the exchange-correlation (XC) energy of homogenous electron gas at density ρ related to one electron.

LDA provides a good description of bulk properties, typically better than HF-method, but may not accurately capture the details of molecular systems.

3.4.2 Generalized Gradient Approximation

Generalized Gradient Approximation (GGA) improves upon LDA by incorporating information about the density gradient in addition to the local electron density. For this method, XC functional can be expressed as:

$$E_{XC}^{GGA} = \inf \rho(\mathbf{r})f(\rho, \nabla\rho)\,d\mathbf{r} \tag{3.10}$$

Here, in the XC energy besides electron density is also a gradient of electron density $\nabla\rho$. This little improvement leads to higher precision contrary to LDA functionals.

3.4.3 Hybrid Functionals

Hybrid functionals combine the simplicity of LDA or GGA with a fraction of the exact HF exchange. The choice of the exchange mixing parameter in hybrid functionals allows for tuning the balance between computational efficiency and accuracy. Examples of hybrid functionals include B3LYP[71] and PBE0[72], the most commonly used DFT functionals. These functionals provide a good balance between accuracy and computational cost, making the simplicity of LDA widely used in many areas of computational chemistry.

3.4.4 Range-Separated Functionals

Range-separated functionals aim to improve the treatment of long-range interactions, such as van der Waals and dispersion interactions. These interactions typically involve electron-electron correlations that extend over larger distances. For range-separated functionals, Hamiltonian is divided into two parts: short-range and long-range. The short-range part is treated by exchange functional, but the long-range part is treated by HF

exchange. This treatment leads to significant improvement in enthalpies of formation, reaction barriers, or ionization potentials[73,74].

3.4.5 Dispersion Energy in Density Functional Theory

In 2006, Jurečka and co-workers[75] recognized the limitations of current DFT functionals in accurately describing long-range exchange-repulsion and dispersion interactions. To address this issue, they proposed a simple solution by introducing an empirical dispersion correction to the DFT energy. Similarly, Grimme et al. introduced the concept of adding dispersion energy to the DFT energy, known as DFT-D (density functional theory with additional dispersion correction). Over time, they developed different versions, including DFT-D1[76], DFT-D2[77], DFT-D3[78], and more recently, DFT-D4[79]. Among these, DFT-D3 has become widely used. The DFT-D3 energy is given by the equation:

$$E_{DFT-D3} = E_{DFT} + E_{disp} \qquad (3.11)$$

where E_{DFT} represents the energy calculated using any arbitrary DFT functional, and the dispersion part (E_{disp}) is given as a sum of two-body ($E^{(2)}$) and three-body ($E^{(3)}$) term. The two-body term is defined as:

$$E^{(2)} = \sum_{AB} \sum_{n=6,8,10,...} s_n \frac{C_n^{AB}}{r_{AB}^n} f_{d,n}(r_{AB}) \qquad (3.12)$$

Here, the first summation is over all atom pairs in the system, C_n^{AB} means average dispersion coefficient of nth order for atom pair AB and r_{AB} denoted their distance. Global scaling factor s_n is dependent on the type of DFT functional. An important advancement in DFT-D3 was the addition of the three-body term:

$$E^{(3)} = \frac{C_9^{ABC}(3\cos\theta_a\cos\theta_b\cos\theta_c + 1)}{(r_{AB}r_{BC}r_{AC})^3} \qquad (3.13)$$

where θ_a, θ_b and θ_c are angles denoted by distances between atoms ABC (r_{AB}, r_{BC} and r_{BC}) and C_9^{ABC} is triple-dipole constant.

Another way to treat dispersion interaction in van dew Waals DFT functionals was first proposed by Langreth and Lundquist[80]. These methods use only the electron density to include correlation effects. The most promising method is VV10 functional developed by Vydrov and van Voorhis[81]. The non-local (NL) part of VV10 functional is widely used as a correction factor to DFT energy denoted as DFT-NL:

$$E_{NL}^{VV10} = \int \rho(\mathbf{r}) \left[\frac{1}{32} \left[\frac{3}{b^2} \right]^{\frac{3}{4}} + \frac{1}{2} \int \rho(\mathbf{r}')\phi(\mathbf{r},\mathbf{r}',\{b,C\})\,d\mathbf{r}' \right] d\mathbf{r} \qquad (3.14)$$

where $\phi(\mathbf{r},\mathbf{r}',\{b,C\})$ is NL correlation kernel defined in ref. 81.

3.5   Computational Modeling Non-Covalent Interactions

The analysis of non-covalent interactions requires more sophisticated computational methods than those typically necessary for covalent bonds due to their subtler energy scales. Particularly for hydrogen-bonded systems where dispersion forces are significant, a nuanced approach to correlation energy is essential. Advanced quantum mechanical techniques that accurately quantify energy contributions on 1 kcal/mol are thus vital[82]. Interaction Energy (ΔE) is a fundamental metric for assessing the magnitude of these bonds, disassembling a complex (AB) into its individual components (A and B)[83]. There are two principal metrics for evaluating ΔE: Total interaction energy (ΔE^T), which includes deformation energy, defined as follows:

$$\Delta E^T(AB) = E(AB) - E(A_{opt}) - E(B_{opt}) \tag{3.15}$$

In this equation, $E(AB)$ denotes the total energy of the complex, while $E(A_{opt})$ and $E(B_{opt})$ indicate the energies of the independently optimized fragments. The Intrinsic interaction energy, conversely, is determined by:

$$\Delta E^I(AB) = E(AB) - E(A) - E(B) \tag{3.16}$$

where $E(AB)$ represents the total energy of the complex, with $E(A)$ and $E(B)$ reflecting the energies of the separate fragments in complex geometry.

In computational chemistry, the finite basis set introduces an error known as the basis set superposition error (BSSE), which stems from the imbalanced treatment of fragments versus the entire complex. In dimer calculations, each monomer utilizes basis set functions from both monomers, but in monomer calculations, the counterpart's basis set functions are absent. This leads to an artificially stabilized complex compared to its dissociated state. The counterpoise correction (CP) technique, introduced by Boys and Bernardi[84], corrects for this discrepancy:

$$\Delta E^I_{CP}(AB) = E(AB) - E(A^{AB}) - E(B^{AB}) \tag{3.17}$$

In this correction, $E(A^{AB})$ and $E(B^{AB})$ refer to the energies of the fragments calculated within the basis set of the complex, addressing the BSSE to yield more reliable interaction energies.

3.5.1   Vibrational Analysis

In computational chemistry, the Rigid Rotor Harmonic Oscillator (RRHO) model is a QM approximation used to describe the rotational and vibrational motions of molecules. In this model, the 'rigid rotor' component assumes that the molecule rotates without any deformation, akin to a rigid body, while the 'harmonic oscillator' portion posits that

the atoms within the molecule vibrate about their equilibrium positions in a harmonic fashion, where the forces restoring the atoms to their original positions are proportional to their displacements. This harmonic potential leads to quantized energy levels that are equidistant, a characteristic of an ideal harmonic oscillator. The calculation of vibrational frequencies within this model involves determining the force constants from the molecular geometry, which are then used to solve the Schrödinger equation for vibrational motion. This yields energy levels and corresponding vibrational frequencies that are integral to understanding molecular spectroscopy. However, the RRHO model simplifies the potential energy surface to a quadratic form, which only approximates the true behavior of molecular vibrations at low energies or small displacements from equilibrium positions[85].

Specifically, the RRHO model's depiction of X-H vibrations often proves inadequate due to inherent anharmonic behavior. These bonds exhibit pronounced anharmonicity as the energy levels increase, deviating significantly from the idealized equidistant spacing. Such anharmonicity arises because the potential energy well of the X-H bond is not perfectly parabolic, becoming steeper as the atoms move closer and shallower at longer distances. This leads to a breakdown in the RRHO approximation for high-energy vibrational states or when atoms experience large displacements from equilibrium. As a result, more sophisticated models that incorporate anharmonic corrections are required to accurately predict the vibrational spectra of molecules, particularly for the description of high-energy vibrational modes and overtones[86].

3.6 Computational Methods and Software Tools for Quantum Mechanical Analysis

A number of QM programs were used for the quantum mechanical calculations, namely: Gaussian16[87], Molpro 2022[88–90], ORCA 5.0[91], TURBOMOLE versions 7.3[92], 7.5[93], and 7.7[94], and PSI4[95]. For the natural bond orbital (NBO) analysis of the Gaussian16 wavefunction, NBO 3.1[96] and 7.0[97] were employed. Additionally, the Cuby4 framework was utilized to manage some of the calculations[98].

Chapter 4

Dative Bond in p-group Elements

Carbon is capable of forming various allotropes of very diverse shapes, such as nanotubes, graphene, or fullerenes. In 1985, Robert F. Curl et al. discovered fullerenes[99], a groundbreaking discovery that was later honored with the Nobel Prize in Chemistry. Fullerenes are characterized by an even number of carbon atoms forming hexagons and pentagons in varying ratios. A well-known example is "Buckminsterfullerene" made from 60 carbon atoms connected to a football-like structure. A notable example is C_{20}, composed exclusively of five-member rings and first synthesized in 2001[100]. Fullerenes have garnered considerable attention due to their unique cage-like structures, leading to diverse applications in bio-related fields[101,102] and material sciences[103,104]. These spherical molecules exhibit exceptional properties such as high electron affinity and distinct reactivity patterns, particularly with electron-donating compounds like piperidine. Models of used fullerenes are in Figure 4.1.

The findings presented in this Chapter were published in references 8, 9, 10, and 105, all of which are included in the Appendix.

4.1 N→C Dative Bond

C_{60}, widely recognized for forming adducts with primary and secondary amines, including piperidine[106–108], reacts under both light and dark conditions in the presence of oxygen. This process typically spans several days and yields approximately 50%. The reaction initiation involves electron transfer from C_{60}, followed by radical recombination and zwitterion formation. This newly formed structure stabilizes either through a proton transfer to C_{60}, resulting in a C-H bond, or via oxidation leading to deprotonation and further radical recombination.

The solubility behavior of C_{60}, particularly its increased solubility in aromatic solvents compared to polar ones, has been explored in numerous experimental studies. These phenomena have also been the focus of various theoretical and computational investigations, which seek to understand solute-solvent interactions and identify key

C_{20} C_{60} C_{70}
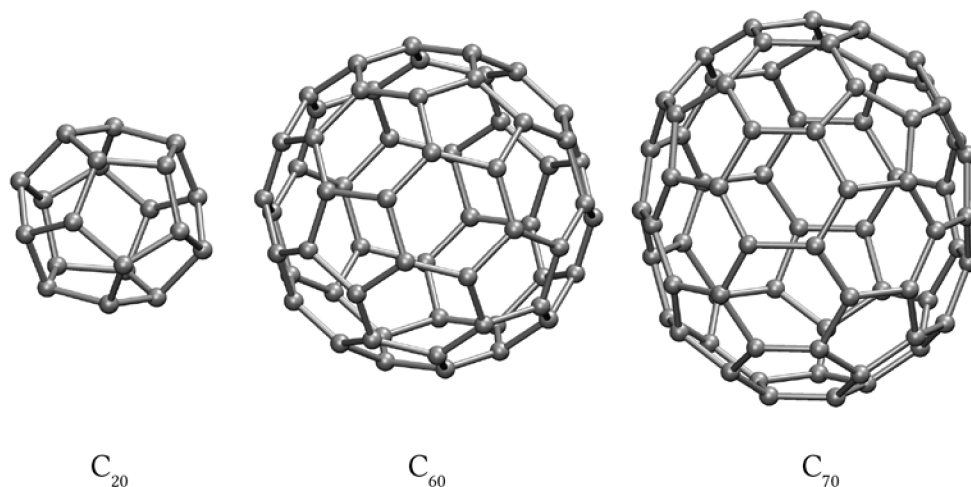
Figure 4.1: Schemes of selected fullerenes.

parameters that influence the solubility of fullerenes in different solvents. The high basicity of piperidine (pKa=11.12), signifying its role as an effective electron donor, casts doubt on the solubility explanation based solely on charge transfer. This skepticism arises especially when considering C_{60}'s limited solubility in oxygen-containing solvents like alcohols, phenols, and ketones.

4.1.1 Complexes of C_{20} and C_{60} with Piperidine

We investigated the interaction dynamics within complexes of piperidine with C_{20} in a 1:1 ratio as a reference point, as well as with C_{60} in a 1:n ratio. The intermolecular interactions were explored using a piperidine dimer, which forms an H-bonded complex. This complex is characterized by an N–H$\cdots$N H-bond length of 2.16 Å, as illustrated in Figure 4.2. The scale of the system allows for the application of the DFT benchmarking method to model the solvation of C_{60}. The interaction energies for the piperidine dimer were computed using PBE0-D3/def2-TZVPP, MP2, and CCSD(T) methods, and the results are summarized in Table 4.1. The minimal differences between ΔE^{T} and ΔE^{I} suggest only slight structural changes upon complexation. The DFT method estimates slightly higher stabilization energies, which necessitates a comparison with benchmark CCSD(T) calculations, further represented by MP2 calculations. When employing triple-zeta basis sets, the DFT calculations tend to overestimate interaction energies by 1.5 and 1.2 kcal/mol, relative to the CCSD(T) and MP2 methods, respectively. The utilization of the more flexible cc-pV5Z basis set narrows this discrepancy to 0.6 kcal/mol, implying that DFT interaction energies are overestimated by about 10%. Since the DFT method exhibits lower basis set dependence than the wavefunction methods under discussion, the errors in DFT-calculated binding energies are unlikely to exceed the observed 10% by a significant margin, in comparison to the CCSD(T) results.

Table 4.1: Intrinsic interaction energies of piperidine dimer (pip_2) and C_{20}-piperidine ($C_{20} \cdots pip$) calculated in cc-pVnZ in kcal/mol

Method	CCSD(T)		MP2				DFT[a]
n	D	T	D	T	Q	5	
pip_2	−3.8	−4.7	−3.8	−5.0	−5.4	−5.6	−6.2(−6.1)
C_{20}-pip	−30.2	−43.2	−29.3	−37.0	−40.1	−41.3	−50.9(−31.7)

[a]in def2-TZVPP. Total interaction energy is given in parentheses.

The optimized geometry and properties of the $C_{20} \cdots$ piperidine complex are showed in Figure 4.2 and Table 4.1. The complex exhibits an N-C bond distance of 1.523 Å, which is longer than the typical covalent C–N bond lengths observed in piperidine, where the optimized C–N bonds are 1.453 Å. The intrinsic interaction energy, ΔE^I, as calculated at the PBE0-D3/def2-TZVPP level, is −50.9 kcal/mol. This is nearly equivalent to the ΔE^I of −49.9 kcal/mol for the N→B dative bond in ammonia borane, which is often considered as the model dative complex. These observations, namely the abbreviated intermolecular distance and the substantial stabilization energy, herald the formation of a novel chemical species characterized by a dative bond between the nitrogen of piperidine and carbon of C_{20}. The literature recognizes various types of dative bonds. The difference of approximately 19 kcal/mol between ΔE^T and ΔE^I reflects a significant structural reconfiguration upon complexation. When accounting for potential shifts in MP2 interaction energies due to an expanded basis set, the PBE0-D3/def2-TZVPP method is projected to yield binding energy computations within an approximate 10% error margin, relative to the CCSD(T) benchmarks. The MP2 method's close alignment with CCSD(T) in terms of stabilization energies confirms its suitability for benchmarking the stabilization energies of C_{60} systems, especially when CCSD(T) calculations are not feasible due to computational demands.

The optimization of $C_{60} \cdots$ piperidine yields to a variety of local minima. This includes non-covalent complexes and the complex involving an N→C dative bond. Their structures, characterized by C$\cdots$N intermolecular distances and ΔE^I as well as ΔE^T computed via the PBE0-D3/def2-TZVPP method, are depicted in Figure 4.3 and Table 4.2. Among these, five non-covalent complexes are observed where piperidine attaches to C_{60} via non-covalent interactions: the C$\cdots$N tetrel bond (C–N structure), NH$\cdots$C and CH$\cdots$C hydrogen bonds (NH-C and CH-C structures, respectively), and the lone-pair N$\cdots\pi$ non-covalent interaction to five- (LP-R5) or six-membered (LP-R6) structures, with bond lengths approximately 3.1 Å. The ΔE^I and ΔE^T values for these complexes are within 1.1 kcal/mol as shown in Table 4.2.

Furthermore, the presence of the N→C dative bond within the C_{60}-piperidine system was corroborated utilizing MP2, as outlined in Table 4.2. The interaction energy in the DB complex, featuring the N→C dative bond, is slightly overestimated in the DFT, aligning with prior findings for the C_{20}-piperidine complex. Nevertheless, the MP2 method predicts an increase in ΔE^I for non-covalent complexes by approximately 2 kcal/mol, consistent with the known tendency of MP2 to overestimate dispersion energy.

Figure 4.2: PBE0-D3/def2-TZVPP optimized geometry of a piperidine dimer and C_{20}-piperidine complex. The figure shows selected bond lengths between fullerene and piperidine in Å(dark blue), hydrogen bond lengths in piperidine (light blue), intrinsic interaction energy (ΔE^{I}, green), and total interaction energy (ΔE^{T}, red) in kcal/mol.

Table 4.2: The intrinsic interaction energies (ΔE^{I}, in kcal/mol) and total interaction energies (ΔE^{T}, in kcal/mol) of $C_{60}\cdots$piperidine complexes showed on the Figure 4.3.

	C-N	DB	LP-R5	LP-R6	CH-C	NH-C
ΔE^{I}_{MP2}	−7.1	−14.0	−7.2	−6.9	−6.8	−6.3
ΔE^{I}_{DFT}	−5.2	−17.2	−5.0	−5.0	−4.1	−4.5
ΔE^{T}_{DFT}	−5.1	0.2	−5.0	−5.0	−4.1	−4.5

The DB complex, characterized by an N→C dative bond, exhibits instability with a ΔE^{T} value of 0.2 kcal/mol. This inference is based on calculations that are limited to gas phase conditions with a solitary piperidine molecule. For a more comprehensive understanding of piperidine's interactions in such complexes, it is essential to consider models that incorporate a broader array of solvent molecules. The analysis, therefore, will proceed in two distinct strands: one focused on exploring the complex with a piperidine dimer, and the other delving into a scenario involving a larger assembly of piperidine molecules in future research.

We examined two complexes of C_{60} with a piperidine dimer: one comprising an N→C dative bond between C_{60} and piperidine (referred to as T1, cf. Figure 4.4) and the other featuring an N$\cdots$C tetrel bond (referred to as T2, cf. Figure 4.4). Contrasting with the DB structure, T1 demonstrates a notably larger ΔE^{T} for the N→C interaction, lower by −13.18 kcal/mol, indicating a more pronounced stabilization effect facilitated by the second piperidine molecule. This augmented stability in T1 can be attributed to a sequential charge transfer: from the outer piperidine to the inner piperidine and then to C_{60}, leading to a more extensive charge separation than in the DB configuration. As a result, the nitrogen atom in the N→C dative bond experiences an increase in electron density,
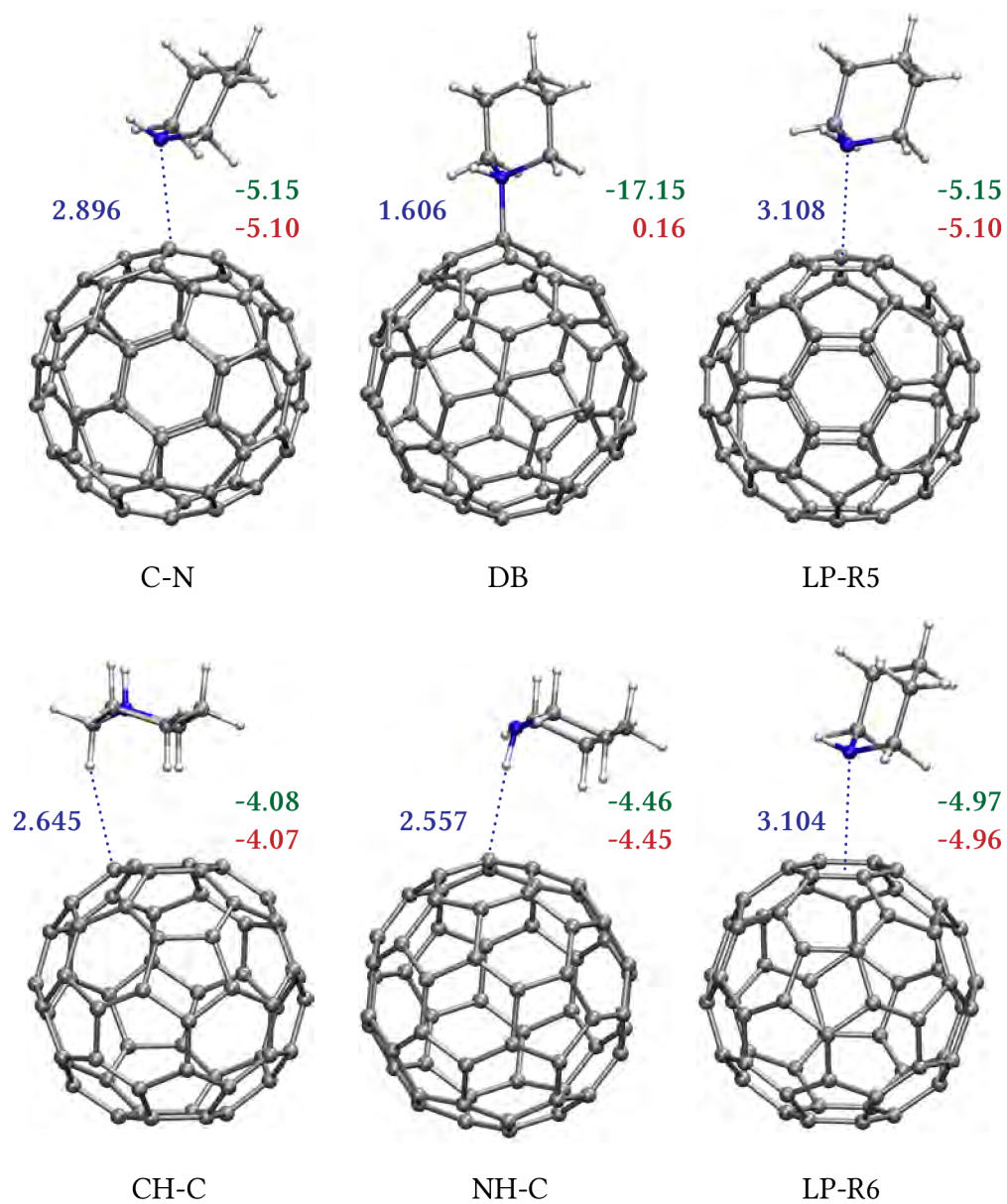
Figure 4.3: PBE0-D3/def2-TZVPP optimized geometry of a C_{60}-piperidine monomer complex. The figure includes selected bond lengths between fullerene and piperidine in Å (dark blue), intrinsic interaction energy (ΔE^{I}, green), and total interaction energy (ΔE^{T}, red) in kcal/mol.
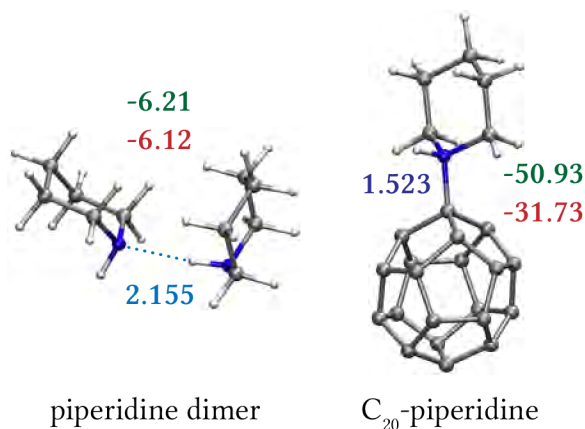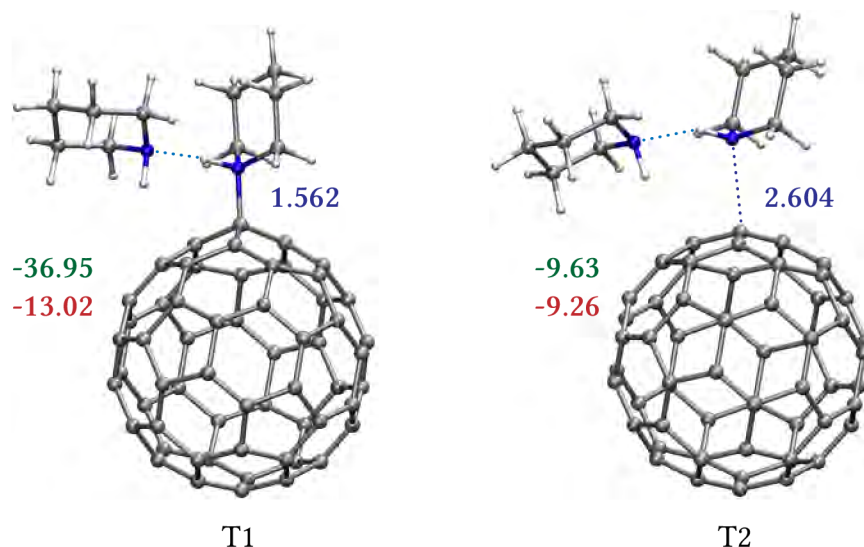
Figure 4.4: PBE0-D3/def2-TZVPP optimized geometry of a C_{60}-piperidine dimer complex. The figure displays selected bond lengths between fullerene and piperidine in Å (dark blue), intrinsic interaction energy (ΔE^{I}, green), and total interaction energy (ΔE^{T}, red) in kcal/mol.

enhancing the bond's strength. This increase in charge transfer is observable in differences in the NBO populations of the σ^*(N-H) antibonding orbital. These populations are computed as 0.017 for an isolated piperidine molecule, 0.030 in a hydrogen-bonded piperidine dimer, 0.026 in the DB structure, and 0.101 in T1. The variance in populations between the initial two structures is indicative of the $N(LP)\cdots\sigma^*$(N-H) hydrogen-bonded piperidine complex formation. The significantly elevated population of σ^*(N-H) in T1 underscores a considerable charge transfer to C_{60}, leading to a strong N→C dative bond.

In the T2 structural arrangement, the inner piperidine molecule establishes interaction with C_{60} through a $C\cdots N$ tetrel bond, mirroring the C-N structure. Concurrently, the outer piperidine molecule forms a $C-H\cdots C$ (C_{60}) hydrogen bond. Within the piperidine dimer subunit of T2, the $N-H\cdots N$ hydrogen bond is shortened by roughly 0.08 Å in comparison to the piperidine dimer. The interaction strength between C_{60} and the inner piperidine in T2 aligns closely with the $C\cdots N$ interaction seen in the C-N complex, as depicted in Figure 4.3, albeit with a bond distance that is significantly reduced by 0.29 Å in the C-N configuration.

4.1.2   Infrared Spectra of C_{60} with Piperidine

Figure 4.5 presents the IR spectra of C_{60} and its mixtures with piperidine, both before (C_{60}-P1) and after (C_{60}-P2) evaporation of excess unbound piperidine molecules. After evaporation, new bands at 872 cm^{-1} and 988 cm^{-1} in the C_{60}-P2 spectrum are attributed
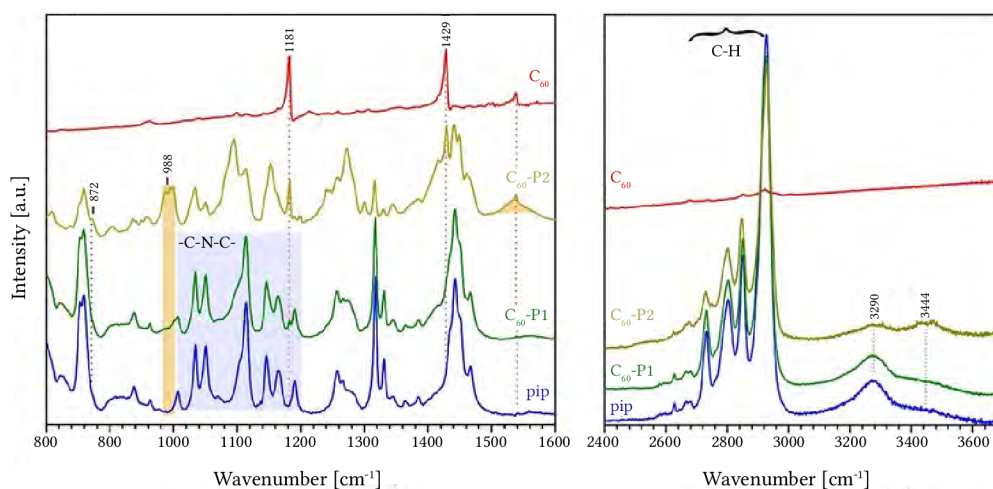
Figure 4.5: Infrared spectra of C_{60} and its complex with piperidine (pip). The spectra are shown before evaporation (C_{60}-P1) and after the evaporation of excess unbound piperidine (C_{60}-P2). Spectral windows focus on the C-N stretching and N-H bending vibrations (left panel), and the N-H stretching vibrations (right panel).

to symmetric and asymmetric stretches of the dative N→C bond in the C_{60}-piperidine dimer complex, as verified by calculations (866 cm^{-1} for symmetric and 994 cm^{-1} for asymmetric N→C stretches in T1 complex).

In the higher frequency region (over 3000 cm^{-1}), shifts in N-H stretching vibrations of piperidine indicate the formation of hydrogen bonds, as evidenced by the appearance of a new band at 3444 cm^{-1} in the C_{60}-P2 spectrum. This band is attributed to the N-H stretch of outer piperidine interacting with C_{60} via van der Waals interactions, contrasting with the retention of C-H vibrations of piperidine in the 2700–3000 cm^{-1} region (Figure 4.5).

Additionally, changes in the spectral region of 1500–1600 cm^{-1}, relevant to N-H bending modes, provide further insights into the nature of the C_{60} interaction with piperidine. The emergence of a band at 1540 cm^{-1} in the C_{60}-P2 spectrum is linked to the bending mode of the NH-bond of inner piperidine, suggesting the formation of a dative bond or non-covalent interactions. This observation excludes the possibility of complexation via the addition of secondary amines to fullerenes through oxidation, as the corresponding hydrogen atom is not released in this process.

4.1.3   Complexes of C_{70} with Piperidine

C_{60} is characterized by its highly symmetrical structure with I_h symmetry, rendering all its carbon atoms equivalent. In contrast, C_{70} features a less symmetrical D_{5h} structure with five distinct types of carbon atoms[109]. Our research focuses on three distinct dative-bonded structures of C_{70} with a piperidine dimer, each engaging with unique A,
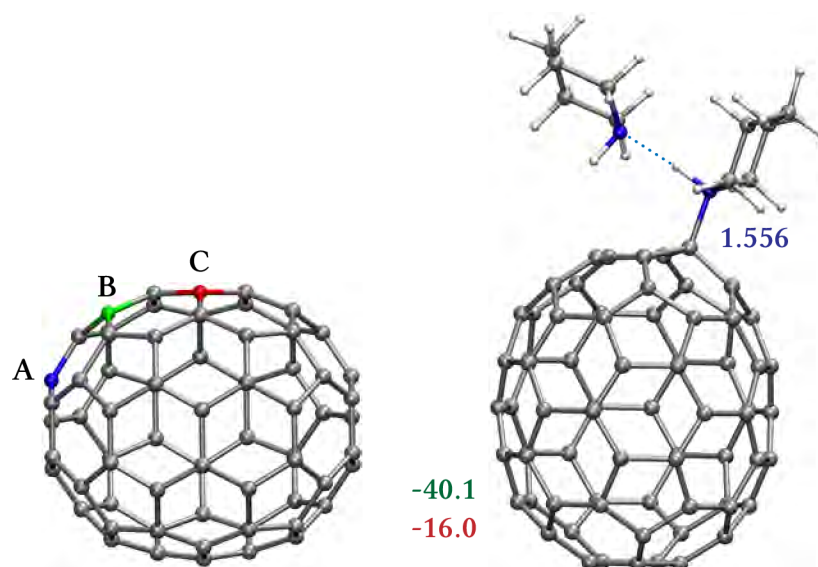
Figure 4.6: Coloured map of sites A, B and C on C_{70} (left). PBE0-D3/def2-TZVPP optimized geometry of a dative bond C_{70}-piperidine dimer complex bounded to site A (right). Illustrated are selected bond lengths between fullerene and piperidine in Å (dark blue), intrinsic interaction energy (ΔE^{I}, green), and total interaction energy (ΔE^{T}, red) in kcal/mol.

B, and C sites on C_{70}, as illustrated in Figure 4.6. the most pronounced ΔE^{T} is observed in the structure where the piperidine dimer bonds to the a site of C_{70} (shown in Figure 4.6). As we examine the central B (Figure 4.7) and C sites (Figure 4.8), there is a weakening of the N→C dative bond, with a decrease in interaction energy by 3.8 kcal/mol at the B site and 11.6 kcal/mol at the C site. Correspondingly, the N→C bond lengthens by 0.013 Å at the B site and by 0.040 Å at the C site. Additionally, complexes featuring N···C tetrel bonds at the B (Figure 4.7) and C (Figure 4.8) sites are also observed, with both exhibiting similar bonding strengths (ΔE^{T} is for both 8.8 kcal/mol).

The computational analysis of interaction energies in complexes of C_{20}, C_{60}, and C_{70} with piperidine, particularly those forming an N→C dative bond, necessitates an indepth discussion on structural prerequisites of carbon allotropes for establishing such dative bonds with electron-donating systems, especially secondary amines. the distinctive symmetry of C_{70}, encompassing carbon binding sites of varied character, specifically five different types based on their location in the C_{70} structure, presents an ideal model for this analysis. Stable dative-bonded complexes of C_{70}···piperidine dimer, characterized by ΔE^{I} values around −36 kcal/mol and ΔE^{T} values close to −13 kcal/mol, are observed. Notably, dative bond minim a in C_{70}···piperidine dimer exist at all three carbon sites (A, B, and C) of C_{70}, with ΔE^{I} and ΔE^{T} spanning from −29 to −40 kcal/mol and −4 to −16 kcal/mol, respectively. These values suggest a stability comparable to the C_{60}···piperidine dimer. Additionally, van der Waals complexes with N···N tetrel bonds are

Figure 4.7: PBE0-D3/def2-TZVPP optimized geometry of a dative bond C_{70}-piperidine dimer complex bounded to site B (left) and van der Waals complex (right). Illustrated are selected bond lengths between fullerene and piperidine in Å (dark blue), intrinsic interaction energy (ΔE^{I}, green), and total interaction energy (ΔE^{T}, red) in kcal/mol.

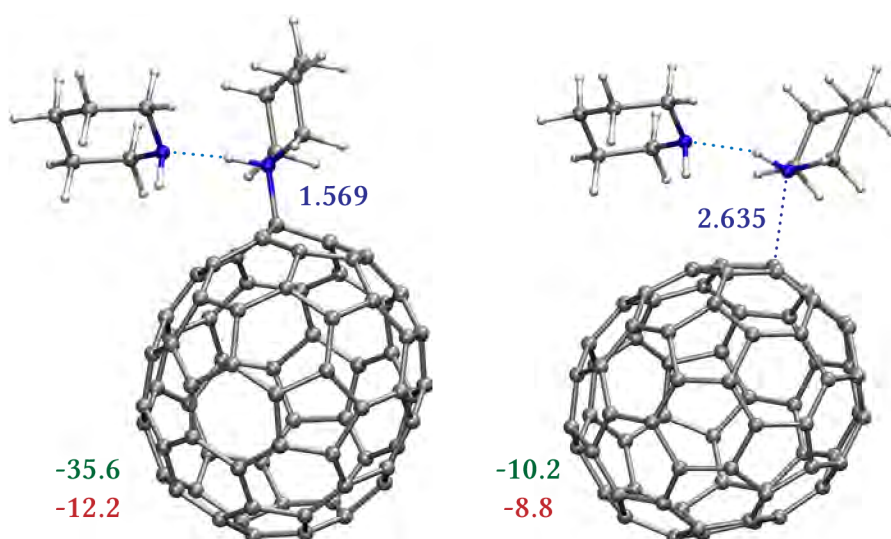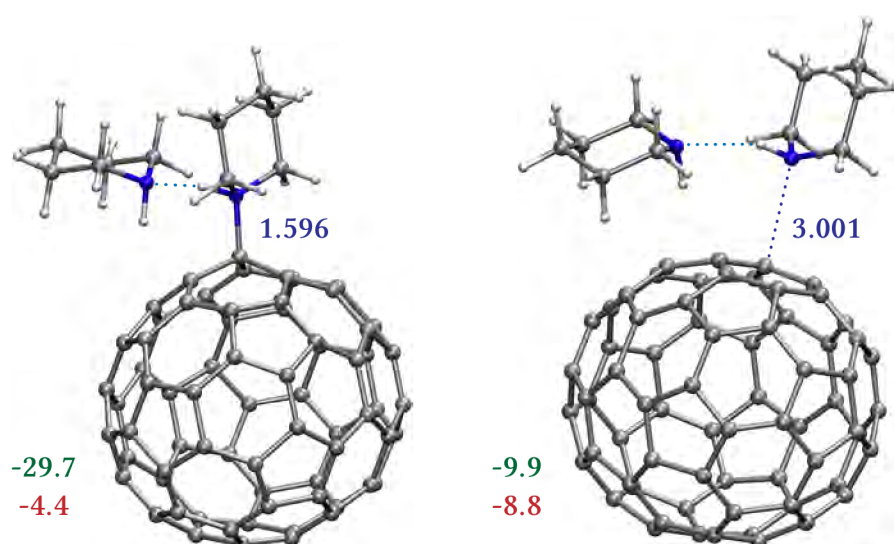**Figure 4.8:** PBE0-D3/def2-TZVPP optimized geometry of a dative bond C_{70}-piperidine dimer complex bounded to site C (left) and van der Waals complex (right). Illustrated are selected bond lengths between fullerene and piperidine in Å (dark blue), intrinsic interaction energy (ΔE^{I}, green), and total interaction energy (ΔE^{T}, red) in kcal/mol.

Table 4.3: The intrinsic interaction energies (ΔE^{I}, in kcal/mol), total interaction energies (ΔE^{T}), and total interaction energies in solvent phase ($\Delta E^{\mathrm{T(S)}}{}_{\mathrm{DFT}}$ for ε=5.9) in kcal/mol of $C_{70}\cdots$piperidine complexes for van der Waals structures (vdW) and dative bond structures (DB).

	vdW		DB		
Site	B	C	A	B	C
$\Delta E^{\mathrm{I}}{}_{\mathrm{MP2}}$	−13.9	−14.3	−40.1	−34.2	−31.0
$\Delta E^{\mathrm{I}}{}_{\mathrm{DFT}}$	−10.2	−9.9	−40.1	−35.6	−29.7
$\Delta E^{\mathrm{T}}{}_{\mathrm{DFT}}$	−8.8	−8.8	−16.0	−12.2	−4.4
$\Delta E^{\mathrm{T(S)}}{}_{\mathrm{DFT}}$	−6.0	−7.1	−19.6	−15.8	−5.7

found at the B and C sites, showing comparable stability, with identical ΔE^{T} values (as detailed in Table 4.3) and similar ΔE^{I} values of −10.2 kcal/mol for the B site and −9.9 kcal/mol for the C site. Interestingly, the ΔE^{T} in a solvent environment, $\Delta E^{\mathrm{T(S)}}$, decreases for the van der Waals complexes but increases for the dative bond complexes, as outlined in Table 4.3. the implications of this observation will be explored in subsequent discussions.

4.1.4   Formation of N→C Dative Bond

The inability of carbon nanotubes (CNTs) to form dative bond complexes[8] suggests that while out-of-plane non-planarity is crucial, it is not the sole determinant for dative bond formation with carbon allotropes. This is partly due to the retained significant aromatic character of six-membered rings. The inclusion of five-membered rings, however, contributes to a more pronounced decrease in aromaticity upon deviation from planarity, facilitating dative bond formation. Our investigations in to $C_{70}\cdots$piperidine dimer complexes underscore the substantial stability of dative bonds at sites containing both five- and six-membered rings (sites a and B). The A-site complex, proximal to the rugby ball's apexes exhibiting greater out-of-plane deviation, demonstrates enhanced stability (as shown in Figure 4.9) compared to the B-site complex, situated near the ball's equator. Surprisingly, the existence of a dative bond at the C-site, comprised solely of six-membered rings, challenges the previously hypothesized prerequisites for dative bond formation[8]. As depicted in Figure 4.9, structural analysis provides insights into the dative bond's presence at the C-site. Examining the geometry variations of the pyrene motif extracted from CNT, C_{70}, and isolated pyrene elucidates the structural distortion patterns in the former two. While the pyrene motif in CNT predominantly deviates unidirectionally from planarity, it exhibits bidirectional deviations in the C_{70} fragment.

Chemical stability and reactivity of non-planar π-conjugated systems are further explored through p-orbital axis vector analysis. Systematic calculations of pyramidalization angles at A, B, and C sites in C_{70} yield angles of 11.91°, 11.51°, and 8.61°, respectively, contrasting with the planar benzene and C_{60} values of 0°and 11.61°. This analysis sug-

five- and six-membered rings   six-membered rings
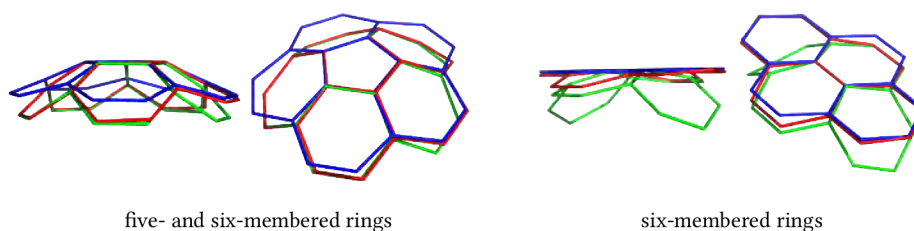
Figure 4.9: Comparison of curvature across various structural motifs. On the left, combined five- and six-membered rings are shown. The solely optimized fragment $C_{30}H_{20}$ is depicted in blue, alongside motifs a (in green) and B (in red) from C_{70}. On the right, structures consisting exclusively of six-membered rings are presented: pyrene in blue, a carbon nano-tube in red, and motif C from C_{70} in green.

$\varepsilon=1.0$	$r=1.632$	$\Delta E^{\mathrm{I}}=-41.8$
$\varepsilon=2.0$	$r=1.623$	$\Delta E^{\mathrm{I}}=-43.7$
$\varepsilon=2.3$	$r=1.622$	$\Delta E^{\mathrm{I}}=-44.0$
$\varepsilon=4.8$	$r=1.616$	$\Delta E^{\mathrm{I}}=-45.6$
$\varepsilon=9.9$	$r=1.612$	$\Delta E^{\mathrm{I}}=-46.6$
$\varepsilon=78.0$	$r=1.608$	$\Delta E^{\mathrm{I}}=-47.5$
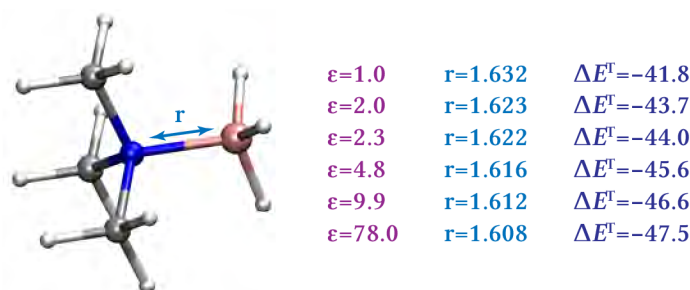
Figure 4.10: The optimized geometry of Me_3N-BH_3. The N→B distances (r in Å) and intrinsic interaction energy (ΔE^{I} in kcal/mol) are given in the gas phase ($\varepsilon= 1$) and various solvents, cyclohexane ($\varepsilon= 2.0$), benzene ($\varepsilon=2.3$), chloroform ($\varepsilon= 4.8$), o-dichlorobenzene ($\varepsilon= 9.9$), and water ($\varepsilon=78.0$).

gests heightened reactivity at the C-site in C_{70} compared to CNTs with various configurations. These findings lend support to the formation of dative bond complexes in these structures.

Consequently, it is concluded that the N→C bond formation between fullerenes and piperidine can occur across various structural motifs, provided there is adequate out-of-plane deviation.

4.2   Stabilization of Dative Bond in Solvent

The combined ionic-covalent character of the dative bond indicates that the solvent might significantly affect the strength and stability of the dative bond complexes. As shown above in Table 4.3, complexes of C_{70} with piperidine dimer show unexpected strengthening of N→C dative bond in implicit conductor-like screening model[110].

Figure 4.10 shows the structural representation of Me_3N-BH_3, focusing on the optimized B−N bond distance as observed in various environments: the gas phase with po-

larity (ε) 1.0 and solvents with differing polarities, including cyclohexane (ε=2.0), benzene (ε=2.3), chloroform (ε=4.8), *o*-dichlorobenzene (ε=9.9), and water (ε=78.0). This figure visualizes the findings similar to those discussed by Bühl et al.[111] and Jonas et al.[112], where the B–N bond length progressively decreases with increasing solvent polarity. Notably, the most substantial bond shortening is observed when the dielectric constant changes from ε=2.0 to ε=9.9, with a reduction of 0.011 Å. As the dielectric constant approaches ε=78 (water), this shortening becomes less pronounced, amounting to only 0.004 Å. A similar trend is noticed in the behavior of ΔE^{T}, the total interaction energy. The stabilization increases by 2.9 kcal/mol as the dielectric constant rises from ε=2.0 to ε=9.9, whereas a further increase in the dielectric constant to ε=78 yields a comparatively smaller stabilization of 0.9 kcal/mol. This observation underscores the significant impact of solvent polarity on molecular interactions and stabilization energies within Me_3BH_3 complexes.
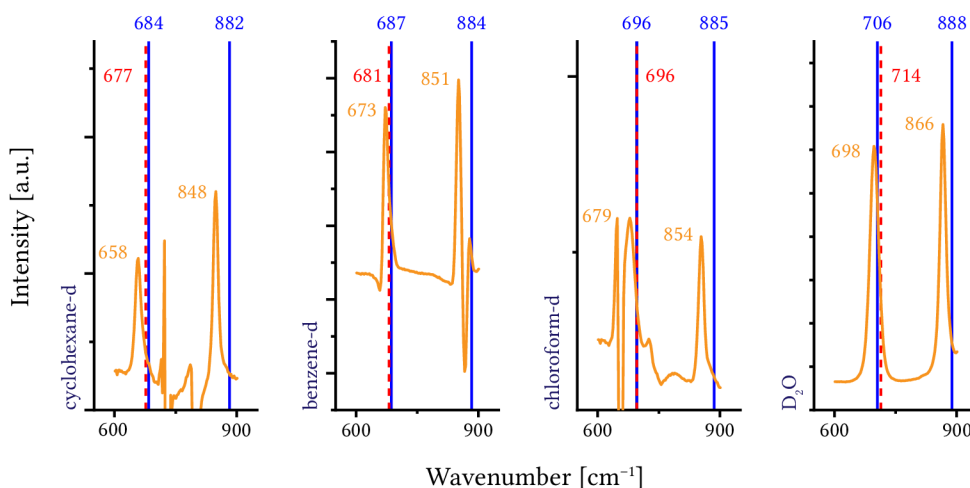
Figure 4.11: The relevant part of the Raman spectra ranging 550–950 cm^{-1} in various solvents (orange color). The PBE0-D3/def2-QZVP calculated harmonic (in blue color) and anharmonic (in red color) frequencies are shown.

The relevant part of the Raman spectra in the range 450–1050 cm^{-1} of Me_3N-BH_3 in cyclohexane, benzene, chloroform, and water and their assignments are given Figure 4.11. The potential energy distribution calculations assign the lower frequency peaks mainly to the N–B stretching (65–69%), while the higher frequency peaks have small contributions (12–18%) and are primarily due to the C–N stretching vibrations (67–75%). The calculations of vibrational spectra within the harmonic approximation overestimate the frequencies more significantly for high-frequency peaks (by 22–34 cm^{-1}); however, they are more consistent than low-frequency peaks, with errors in the range of 8–26 cm^{-1}. Note that the effect of anharmonicity is the largest for H_2O. The dependence of the observed and the calculated harmonic and anharmonic frequencies on the solvent polarity is illustrated in Figure 4.11, showing a gradual blue-shift with increasing solvent polarity with the largest changes in the region up to ε=4.8. Both the anharmonic

and harmonic calculated frequencies thus provide reliable values in terms of the solvation trends and can be used for further discussion.

4.2.1 Other Complexes

Table 4.4 presents the values of ΔE^{T} calculated for various solvents: gas phase (ε=1.0), cyclohexane (ε=2.0), benzene (ε=2.3), chloroform (ε=4.8), o-dichlorobenzene (ε=9.9), dimethylsulfoxide (ε=46.8), and water (ε=78.0). These solvents were chosen to explore the influence of solvent permittivity on different types of dative bonds, including N→B, N→C, P→B, and P→C. The selection of complexes spans a broad range of structures from the prototypical dative bond complex H$_3$B-NH$_3$ to larger systems like C$_{70}$ with a piperidine dimer. In every scenario, solvent effects lead to stabilization of the complex, with the most significant stabilization observed in solvents with ε values from 2.0 to 9.9, achieving up to 5 kcal/mol. Beyond ε=9.9, the rate of stabilization diminishes, with complexes stabilizing by up to 2 kcal/mol in solvents up to ε=78.0.

Table 4.4: ΔE^{T} values for selected dative bond complexes in different implicit solvents, with the solvents' relative permittivity (ε) indicated. The values are in kcal/mol.

Complex	Type	ε						
		1.0	2.0	2.3	4.8	9.9	46.8	78.0
NMe$_3$-BH$_3$	N→B	−42.3	−44.3	−45.0	−46.3	−47.2	−48.1	−48.2
NH$_3$-BH$_3$	N→B	−36.3	−39.5	−40.6	−42.7	−44.3	−45.7	−45.9
PEt$_3$-BH$_3$	P→B	−49.6	−51.2	−51.8	−52.8	−53.6	−54.3	−54.4
pip-C$_{20}$	N→C	−31.7	−35.2	−36.5	−38.9	−40.9	−42.7	−42.7
PEt$_3$-C$_{20}$	P→C	−44.8	−48.2	−49.5	−51.9	−53.8	−55.6	−55.8
pip$_2$-C$_{60}$	N→C	−13.0	−13.9	−14.2	−14.9	−15.4	−15.9	−16.0
PEt$_3$-C$_{60}$	P→C	−12.6	−15.2	−16.1	−17.7	−19.0	−20.1	−20.2
pip$_2$-C$_{70}$ A	N→C	−16.0	−16.9	−17.3	−18.0	−18.6	−19.1	−19.2
pip$_2$-C$_{70}$ B	N→C	−12.1	−13.0	−13.3	−14.1	−14.7	−15.3	−15.4
pip$_2$-C$_{70}$ C	N→C	−4.3	−4.4	−4.5	−4.7	−4.8	−4.9	−5.0

4.3 Addition Reaction between Piperidine and C$_{60}$

The unique properties of fullerene-based materials underscore the importance of investigating the variations in their electronic properties stemming from different bonding characteristics, such as those observed in dative bond and adduct complexes. Consequently, we have expanded our investigation to include comprehensive computational

analyses of the interaction between C$_{60}$ and piperidine. This involves detailed calculations exploring various reaction pathways leading to the formation of C$_{60}$-piperidine complexes and C$_{60}$ with piperidine dimer in an environment devoid of oxygen.

4.3.1   C$_{60}$ with Piperidine

Figure 4.12 presents schematic representations that delineate the formation process of the addition product between C$_{60}$ and piperidine, alongside crucial geometric parameters characterizing the potential energy surface's (PES) critical points. Figure 4.13 depicts the PES associated with the genesis of the addition product from C$_{60}$ and piperidine. In the gas phase reaction sequence, piperidine attaches to C$_{60}$ via a tetrel bond to form the van der Waals (vdW) complex (vdW_a), which is stabilized by 6.7 kcal/mol. The N–H bond in piperidine exhibits negligible alteration. Subsequently, the process transitions through the transition state TS1_a towards the DB_a complex. In TS1_a, while the piperidine's N–H bond remains unaltered, the C–N bond linking C$_{60}$ and piperidine contracts by approximately 0.9 Å. The reaction barrier is minimal, affirming the ease of accessing the DB_a complex, with the transition states being 1.7 kcal/mol more stable than their isolated counterparts. Upon optimization, the DB_a complex manifests minor modifications, notably a 0.2 Å contraction in the C–N bond and slight distortions in the C$_{60}$ structure due to incipient sp^3 hybridization at the carbon atom participating in the dative bond. The comparative stabilization energies for vdW_a and DB_a elucidate the enhanced thermodynamic stability of the former, suggesting the DB_a complex's formation is less favored. However, the scenario transforms upon incorporating solvent effects in the calculations, where despite identifying the vdW_a complex on the PES, it is unlikely to form in solution, steering the reaction directly towards the DB_a complex. Crucially, the stabilization of the DB_a complex in solvent outstrips its gas phase counterpart by approximately 7 kcal/mol, underscoring the pivotal role of N→C dative bond creation facilitated by piperidine solvent presence.

Starting from the DB_a complex, the reaction trajectories exhibit notable similarities across both gas phase and solvent environments, hence are addressed concomitantly. Building on knowledge from previous study[8], we investigated two types of adduct formations: Pdt(5,6)_a and Pdt(6,6)_a, alongside their respective transition states, TS2(5,6)_a and TS2(6,6)_a. In each scenario, piperidine's hydrogen atom engages with the C$_{60}$ framework. Concurrently, the covalent N–H bond in piperidine, initially measuring approximately 1.02 Å, evolves into a non-covalent hydrogen bond with a bond length 2.3–2.4 Å. Assessments of stabilization and activation energies in both media decisively preclude the viability of complexes adopting the (5,6) binding paradigm. Contrastingly, Pdt(6,6)_a emerges as the energetically favored entity within the PES contours. Nonetheless, a formidable transition barrier, approximated at 20 kcal/mol for the DB_a → Pdt(6,6)_a transition, negates the plausible formation of the latter construct.
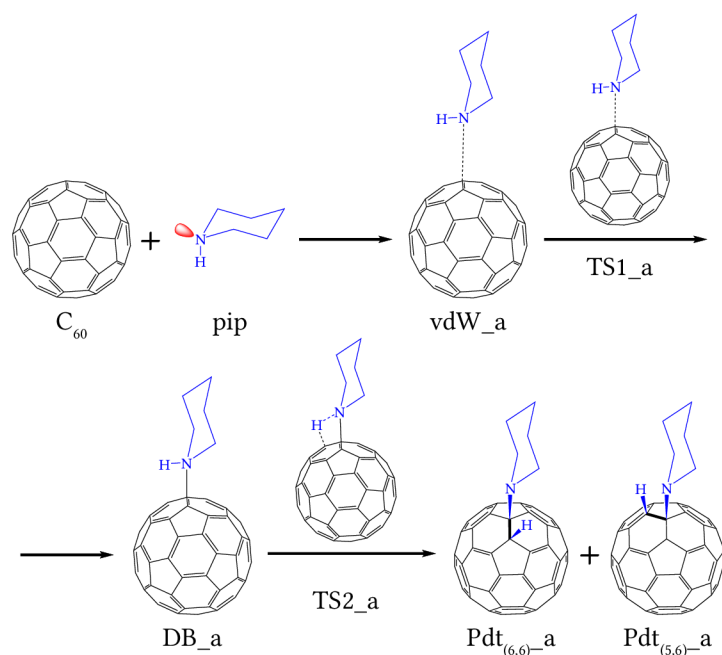
Figure 4.12: Schematic figure illustrating the formation of the addition products from C$_{60}$ with piperidine.

Figure 4.13: Electronic energy diagram for forming the addition product from C$_{60}$ with piperidine in the gas phase (blue color) and piperidine solvent (red color).
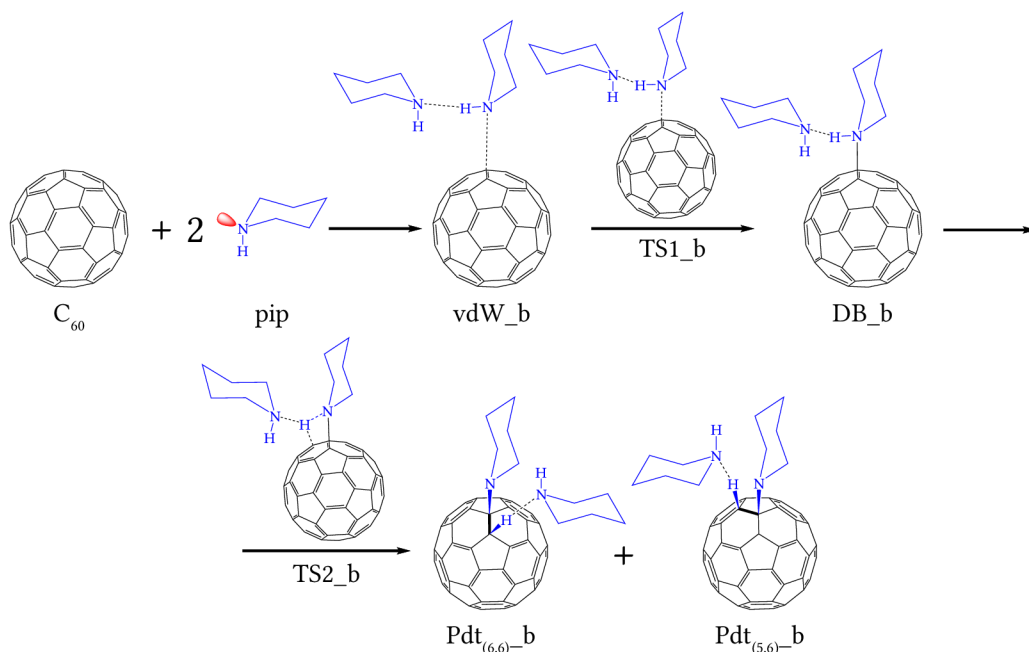
Figure 4.14: Schematic figure illustrating the formation of the addition products from C_{60} with piperidine dimer.

4.3.2 C_{60} with Piperidine Dimer

The extension of the system to C_{60} with a piperidine dimer (Figure 4.14) results in significant modifications in the reaction profile (see Figure 4.13). The van der Waals complex (vdW_b) forms exclusively in the gas phase, exhibiting enhanced stability of approximately 12 kcal/mol, in contrast to the C_{60} complex with a single piperidine, which is stabilized by about 7 kcal/mol. Transitioning from the vdW_b complex to the DB_b complex occurs via the TS1_b transition state, featuring a negligible activation barrier of 0.1 kcal/mol.

    The calculations performed in the solvent environment did not localize either the vdW_b or the TS1_b structures; instead, they directly optimized to the DB_b complex. This complex is characterized by a single dative bond between C_{60} and the piperidine dimer. The DB_b complex benefits from stabilization through (i) an N→C dative bond with an approximate length of 1.57 Å, and (ii) an internal piperidine⋯ outer piperidine hydrogen bond of about 1.75 Å, yielding total stabilization energies of 17.3 and 20.9 kcal/mol in the gas phase and solvent, respectively. The latter stabilization energy closely aligns with 18.0 kcal/mol, as determined via a more precise spin-component-scaled MP2 (SCS-MP2) method.

    Due to energy considerations akin to those for $C_{60}\cdots$piperidine, subsequent analysis solely addresses the reaction pathway leading to the Pdt(6,6)_b product. In this structure, the intramolecular piperidine⋯piperidine hydrogen bond is severed, enabling
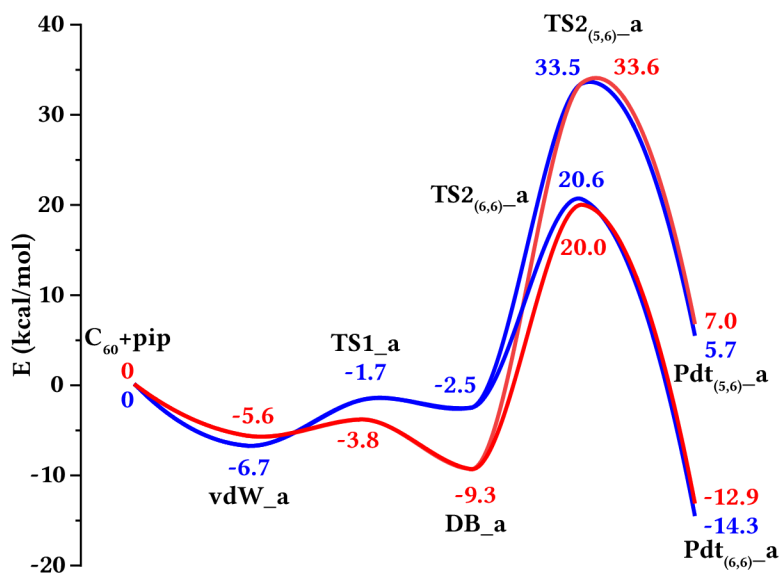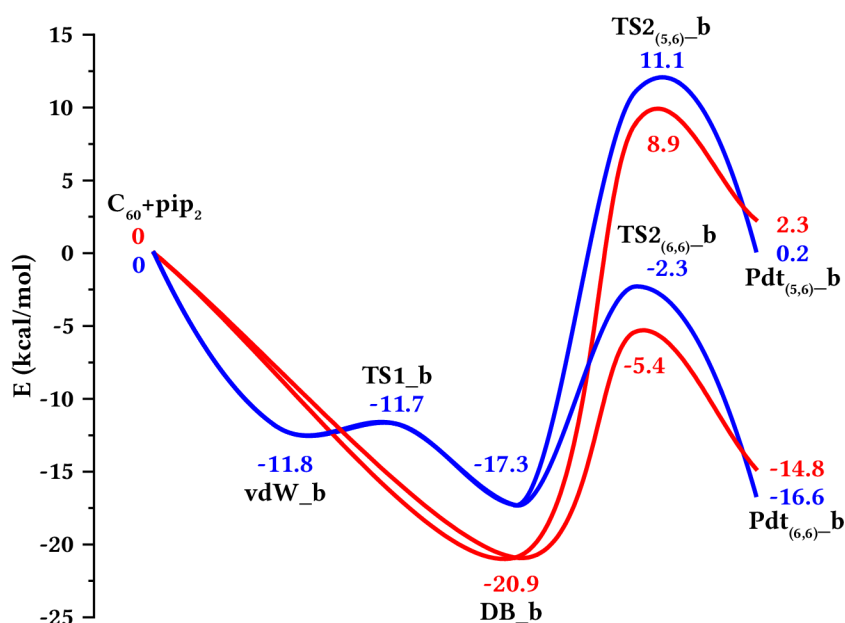
Figure 4.15: Electronic energy diagram for forming the addition product from C_{60} with piperidine dimer in the gas phase (blue color) and piperidine solvent (red color).

the former's hydrogen atom to attach to C_{60}, thereby establishing a new hydrogen bond, approximately 2.2 Å, with the outer pip. The Pdt(6,6)_b complex demonstrates stability of 16.6 and 14.8 kcal/mol in the gas phase and solvent, respectively, with the SCS-MP2 stabilization energy in the solvent reflecting 13.0 kcal/mol, consistent with the corresponding DFT-D valuation. While this complex exhibits a mere 2 kcal/mol greater stability compared to $C_{60} \cdots$ piperidine, its formation is markedly favored as the activation for the DB_b → Pdt(6,6)_b transition is energetically viable; the TS2(6,6)_b transition state presents a stability enhancement of 2.3 kcal/mol (in the gas phase) and 5.4 kcal/mol (in the solvent) relative to the reactants.

4.4   Summary

The outcomes of computational modeling and experimental IR spectroscopy investigations identified a novel type of dative bond between various fullerenes and electron donors possessing lone pairs on nitrogen or phosphorus atoms. Intriguingly, the behavior of these dative bonds in solvents revealed that different types of dative bonds exhibit significant enhancement in bond strength. Moreover, it was demonstrated that the dative bond acts as an intermediate in the addition reaction of secondary amines to fullerenes.

Chapter 5

Hydridic Hydrogen Bond

According to the definition[12], for a hydrogen bond to occur, the involved hydrogen must be bound to an atom X, *"where X is more electronegative than H"*. As of the writing of this thesis, the periodic table lists 118 identified elements, yet only eleven of them possess an electronegativity higher than that of hydrogen. This restriction confines hydrogen bonding to a limited section of the periodic table. Nonetheless, the chemistry of hydrogen is far more diverse. When hydrogen is bound to an element less electronegative than itself, it acquires a negative charge, enabling it to form non-covalent interactions with electrophilic regions, in contrast to the conventional hydrogen bond where hydrogen interacts with nucleophilic regions. Owing to this role reversal in the interaction, where hydrogen becomes partially negative and the acceptor of the "hydrogen bond" is partially positive or contains a positive region, this interaction was termed by Mirosław Jabłoński as a charge-inverted hydrogen bond[19].

The findings presented in this Chapter were published in publication 21, which is included in the Appendix.

5.1   Si-H···X Hydridic Hydrogen Bond

Due to the lower electronegativity of silicon (1.9) compared to hydrogen (2.2), the molecule Me_3SiH exhibits hydridic hydrogen, enabling it to interact with electrophiles. Various electrophiles, including $C_6H_3(CN)_3$, $C_6(CN)_6$, COF_2, NO_2F, BrCN, ICF_3, ICN, $S(CN)_2$, PCl_3, $P(CN)_3$, BF_3, K^+, and HCN, were selected to form CIHB. These electrophiles can be categorized into five groups, encompassing π-, σ-, and p-hole interactions, one cation, and one molecule with a positively charged hydrogen. All considered complexes are illustrated in Figure 5.1. For detailed study were chosen electrophiles ICF_3, BrCN and HCN. To corroborate the theoretical findings, an IR experiment in an Ar matrix was conducted.

The intramolecular Si–H and the intermolecular Si-H···Y distances for the examined complexes are presented in Table 5.1. Relative to the sum of the van der Waals (vdW) radii[113], the intermolecular distances in complexes with ICF_3 and BrCN are significantly
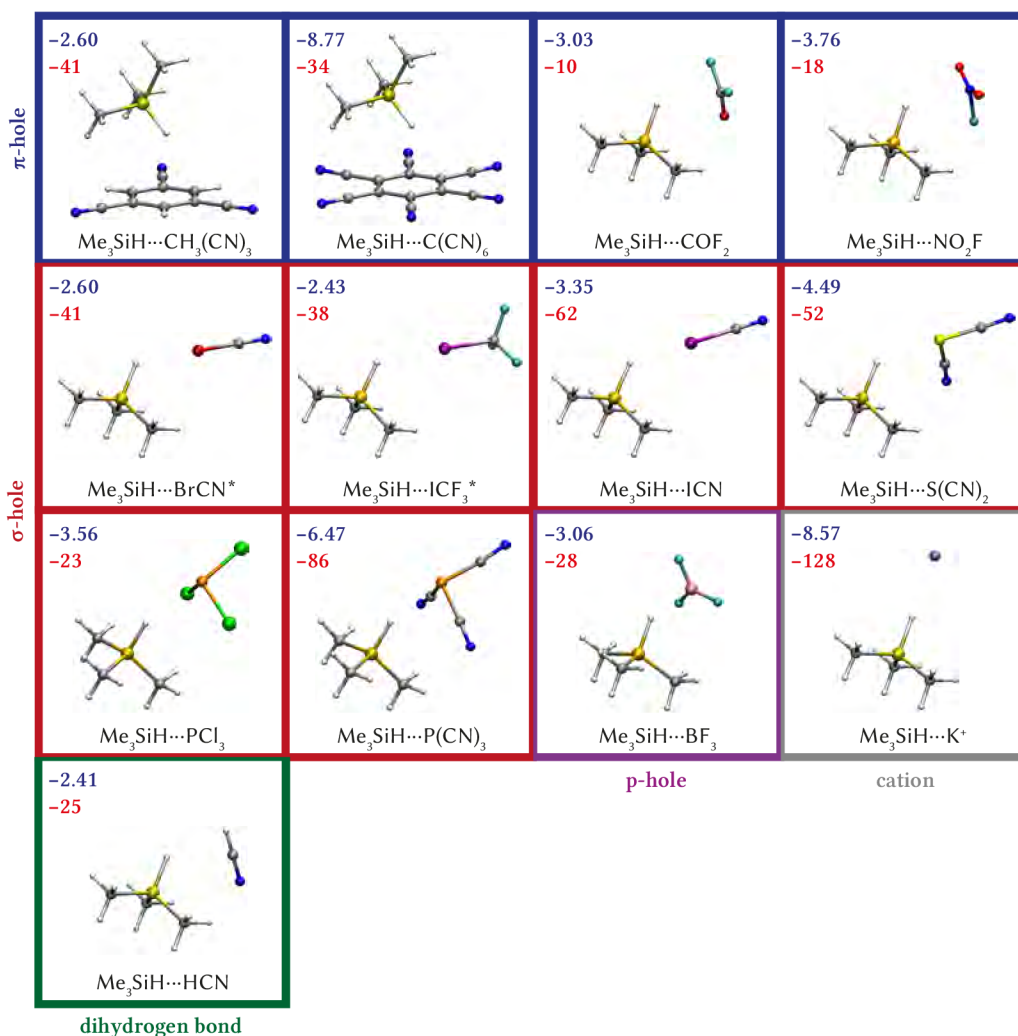
Figure 5.1: Geometries of the complexes investigated optimized at the MP2/cc-pwCVTZ level (cc-pwCVTZ-PP for Br and I). Dark blue is used for the total interaction energy (in kcal/mol) at the MP2/cc-pwCVTZ level for each complex, and red is used for the shift of the Si–H stretching frequency (in cm^{-1}). The complexes with the experiment are marked with asterisks.

Table 5.1: Intermolecular distances and changes in intramolecular bond lengths (in Å) of selected bonds in $Me_3SiH\cdots Y'$ complexes ($Y' = ICF_3$, BrCN, HCN) calculated at the MP2-F12/cc-pVTZ-F12 level.

Y'	Δr(Si-H)	Δr(Si-C)	Δr(I-C)	H⋯I	vdW[a]
ICF_3	0.007	−0.003/−0.001/−0.001	0.002	2.874	−0.573
	Δr(Si-H)	Δr(Si-C)	Δr(Br-C)	H⋯Br	vdW[a]
BrCN	0.008	−0.003/−0.002/−0.002	0.005	2.705	−0.585
	Δr(Si-H)	Δr(Si-C)	Δr(H-C)	H⋯H	vdW[a]
HCN	0.005	−0.003/−0.003/0	0	2.729	+0.320

[a]The difference between the intermolecular distance and the sum of the vdW radii.

reduced (by 0.573 and 0.585 Å, respectively); however, in the complex with HCN, this distance is found to be longer. Additionally, Table 5.1 reveals that all intramolecular Si–H bond lengths consistently increase upon complex formation. It is noteworthy that the Si–H bond elongation is less pronounced than the X–H bond elongation typically observed in X–H⋯Y hydrogen-bonded systems. As anticipated, the Si–C bonds undergo contraction, albeit to a lesser extent. In contrast, the formation of complexes results in an elongation of the I–C and Br–C intramolecular distances, while the H–C distance remains unchanged.

Table 5.2 compiles the calculated energy characteristics of $Me_3SiH\cdots Y'$ complexes, encompassing MP2, MP2–F12, and CCSD(T)-F12 interaction energies along with the binding free energies at 18 K, derived from MP2 and MP2–F12 data. The MP2 stabilization energies across all CIHB complexes show similar stability of all complexes, while the more accurate MP2–F12 and, particularly, CCSD(T)–F12 energies for the first two complexes are analogous and exceed those of the third (dihydrogen-bonded) complex. Moreover, all MP2–F12 and CCSD(T)–F12 stabilization energies range from 2.6 to 3.3 kcal/mol and 2.2 to 2.8 kcal/mol, respectively, aligning the m with the energies characteristic of classical hydrogen-bonded complexes. These results appear to contradict the ESP of the selected subsystems (illustrated in Figure 5.2), where HCN emerges as the strongest electron acceptor, followed by BrCN and ICF_3. Consequently, one would anticipate the strongest complex formation with HCN. Contrary to this expectation, the HCN complex exhibits the weakest binding, a phenomenon attributed to dispersion energy contributions. According to the SAPT(2+3)[114] analysis, the dispersion and total interaction energies for the Me_3SiH complexes with ICF_3, BrCN, and HCN are calculated to be −4.35, −3.79, and −3.05 kcal/mol, and −3.34, −3.20, and −2.50 kcal/mol, respectively. Evidently, the reduced dispersion energy in the HCN complex underlies its lower stabilization energy. Remarkably, the SAPT(2+3) interaction energies for all three complexes show a surprising congruence with the MP2–F12 values. The negative binding free energies at 18 K for all complexes signify the ir spontaneous formation at this temperature.

Table 5.3 presents the variations in orbital occupancies for both the monomers and their complexes, specifically concerning the occupied and unoccupied Si–H σ-orbitals. These occupancy changes are directly correlated with alterations in bond lengths, with
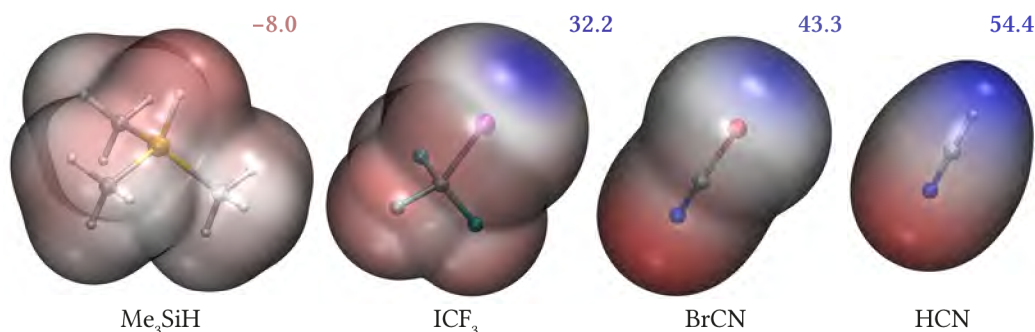
Figure 5.2: Molecular ESP calculated at the ωB97X-D/def2-QZVPP level for the studied monomers. The ESP scale is in kcal/mol. The $V_{s,max}$ on the hydrogen atom from the Me₃SiH molecule is depicted in red. The $V_{s,min}$ in the center of the σ-holes or on top of the hydrogen atom is in blue.

Table 5.2: Energy characteristics of the Me₃SiH···Y′ complexes (Y′ = ICF₃, BrCN, HCN).

Y'	ΔE^{T}_{MP2}	$\Delta E^{T}_{MP2-F12}$	$\Delta E^{T}_{CCSD(T)-F12}$	ΔG^{18K}_{MP2}	$\Delta G^{18K}_{MP2-F12}$
ICF₃	−2.43	−3.27	−2.70	−1.85	−2.43
BrCN	−2.60	−3.02	−2.76	−2.07	−2.77
HCN	−2.41	−2.59	−2.24	−1.79	−1.97

the most significant changes observed in the Si–H bond. A reduction in the occupancy of the Si–H σ-orbitals, coupled with an increase in the σ*-orbitals across all three complexes, results in a weakening of the Si–H bond. This weakening is evidenced by the elongation of the Si–H bond length, as detailed in Table 5.1. Analogous outcomes were noted for the I–C, Br–C, and H–C bonds in the ICF₃, BrCN, and HCN electron acceptors, respectively. In these instances, the bond elongation was less pronounced, and for the HCN complex, it was observed to be negligible. Other changes in orbital occupancy and corresponding bond-length alterations are less significant and are not the focus of further discussion.

Table 5.3: Orbital–occupation difference between monomers and Me₃SiH···Y′ complexes using NBO analysis calculated at the ωB97X-D/aug-cc-pwCVTZ level on MP2-F12/cc-pVTZ-F12 geometries.

Y'	σ(Si-H)	σ*(Si-H)	σ(I-C)	σ*(I-C)	ΣLP I
ICF₃	−0.010	0.004	−0.003	0.005	−0.005
Y'	**σ(Si-H)**	**σ*(Si-H)**	**σ(Br-C)**	**σ*(Br-C)**	**ΣLP Br**
BrCN	−0.010	0.004	−0.001	0.009	−0.002
Y'	**σ(Si-H)**	**σ*(Si-H)**	**σ(H-C)**	**σ*(H-C)**	**LP N**
HCN	−0.001	0.002	−0.001	0	−0.001

Figure 5.3: Ar-matrix spectra of the $Me_3SiH\cdots ICF_3$ complex.
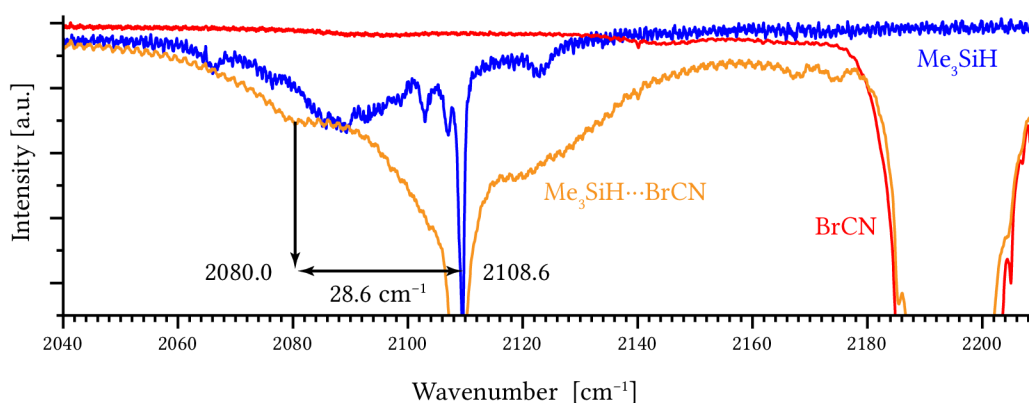
Figure 5.4: Ar-matrix spectra of the $Me_3SiH\cdots BrCN$ complex.

5.1.1   Infrared Spectra and Vibrational Analysis

Figure 5.3 depicts the IR spectrum obtained within an argon (Ar) matrix. This spectrum comprises that of pure trimethylsilyl hydride (Me_3SiH, depicted in blue) and the spectrum of the $Me_3SiH\cdots ICF_3$ complex, captured at the low temperature of 18 K (shown in orange). The observed shift in the Si–H bond within the argon matrix, registering at $27.7\ cm^{-1}$, reflects the specific molecular interactions characterizing this complex.

Similarly, Figure 5.4 illustrates the IR spectrum, again measured within an Ar matrix. It features the spectrum of pure Me_3SiH (in blue) and contrasts it with the spectrum of the $Me_3SiH\cdots BrCN$ complex at 18 K (represented in orange). The Si–H bond in this scenario demonstrates a shift of $28.6\ cm^{-1}$ within the argon matrix, highlighting nuanced differences in the interaction dynamics of the Si–H bond when BrCN is involved, as opposed to ICF_3.

Table 5.4 details the experimental and calculated shifts in Si–H stretching frequencies resulting from complex formation. Notably, the calculated MP2–F12 harmonic shifts consistently exceed those determined via MP2 harmonic calculations and closely align with the unscaled anharmonic results. The commendable correlation between the exper-

imental and calculated frequencies underscores the validity and applicability of all util-ized computational methods. In essence, the concordance between experimental data and computational frequency shifts is robust, with all Si–H frequencies experiencing redshifts post complex formation. As anticipated, the extent of these redshifts is directly proportional to the stability of the respective complexes. Furthermore, an increase in the intensities of the Si–H stretch is observed in all complexes following complex formation. It is important to note, however, that the experimental methodology employed was not capable of discerning changes in intensity.

Table 5.4: Infrared shift ($\Delta \nu$ in cm^{-1}) and change of intensity ($\Delta \nu$ in km/mol) of the Si–H band upon the formation of $Me_3SiH\cdots Y'$ complexes (Y' = ICF_3, BrCN).

Y'	$\Delta \nu_{Ar}$	$\Delta \nu_{anharm.}$	$\Delta \nu_{MP2}$	$\Delta \nu_{MP2\text{-}F12}$	ΔI_{MP2}
ICF_3	−28	−31	−38	−49	+136
BrCN	−29	−36	−41	−50	+138

5.2 Summary

Hydrogen bonded to an element with lower electronegativity exhibits distinct behavior compared to hydrogen in a conventional hydrogen bond. In the context shown in our study, this hydrogen acts as a Lewis base, engaging in interactions with a Lewis acid. These interactions manifest a significant shift in the X-H stretching frequency and an increasing of intensity comparable to conventional hydrogen bonds; however, the nature of these interactions is reversed.

Chapter 6

Visualization of Anisotropic Charge Distribution by Means of Kelvin Probe Force Microscopy

Traditional views on certain chemical entities imply that electrons are evenly distributed around atoms or π-electron systems. For example, halogens are often conceptualized as atoms bearing a uniform negative charge, akin to arenes which are thought to have a consistent π-electron "cloud" enveloping the ring structure. However, this perspective raises questions: How do uniformly negative halogens interact with typical nucleophiles? And how do π-electrons selectively interact with anions? Conventionally, these interactions would be expected to be repulsive. Politzer[42] addressed these paradoxes by introducing the concept of anisotropic charge distribution, σ-holes, and π-holes. In the case of a σ-hole, a covalently bonded halogen contributes its lone z-electron towards the covalent bond, creating a positive "cap" opposite to the bond. On the other hand, π-holes arise when electron-withdrawing groups attached to a π-electron system extract π-electrons, thereby disrupting the π-electron cloud and forming a π-hole.

The development of scanning tunneling microscopy in 1981 represented a groundbreaking advancement in the field of microscopy, enabling for the first time the direct observation of individual atoms. This revolutionary technology laid the foundation for subsequent innovations, notably Atomic Force Microscopy (AFM)[115]. Further progress was achieved with the functionalization of the AFM tip using a single CO molecule, a technique that unlocked the ability to visualize intricate chemical structures, exemplified by the imaging of pentacene[116]. However, the journey towards subatomic resolution continued to pose significant challenges. The functionalization of Kelvin probe force microscopy (KPFM) tip with a CO molecule and a Xe atom marked another leap forward, facilitating the observation of subatomic phenomena. This enhancement in resolution enabled the detailed visualization of σ-holes and π-holes.

The findings presented in this Chapter were published in publications 117 and 118, which are included in the Appendix.

6.1   Visualization of σ-hole

KPFM has emerged as an ideal tool for visualizing the anisotropic charge distribution known as the σ-hole. To effectively observe the σ-hole with a functionalized silver tip, a specific orientation is required: the covalent bond C-X, where X represents a halogen atom, must be perpendicular to the surface. This orientation requirement is fulfilled by the unique tripodal structure of certain compounds, such as tetrakis(4-bromophenyl) methane (4BrPhM) and tetrakis(4-fluorophenyl) methane (4FPhM), which naturally stand on surfaces with the C-X bond in the desired perpendicular alignment, as depicted in Figure 6.1. Its tripodal structure allows to stand on the surface with a C-X bond perpendicular to it. 4BrPhM was chosen for its characteristic σ-hole, while 4FPhM, possessing an isotropic charge distribution, serves as a contrasting system. For the integration of the KPFM tip into QM calculations, a model comprising six silver atoms with a CO molecule (CO-Ag tip) and a Xe atom (Xe-Ag tip) was employed, as visualized in Figure 6.1. This setup is designed to distinctly highlight the differences between the two systems, offering insights into the unique charge distributions of σ-hole and isotropic charge environments.

4FPhM   4BrPhM   CO-Ag tip   Xe-Ag tip
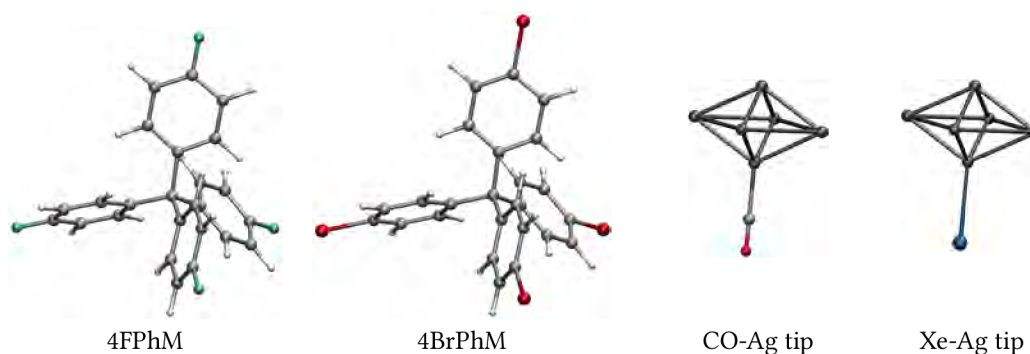
Figure 6.1: PBE0-D3/def2-TZVPP optimized geometries of tetrakis(4-fluorophenyl) methane (4FPhM), tetrakis(4-bromophenyl) methane (4BrPhM) and simplified models of KPFM silver tips functionalized by CO molecule (CO-Ag tip) and Xe atom (Xe-Ag tip).

6.1.1   Calculations of Interaction Energy

The noncontact Atomic Force Miscroscopy (nc-AFM) technique has unlocked unique capabilities for probing interaction energies between individual atoms and molecules at the tip apex and the sample using site-specific force spectroscopies[119,120]. Beyond quantitatively assessing the interaction energies of well-defined entities, nc-AFM has also provided invaluable insights for benchmarking the accuracy of various theoretical methods in describing these weak non-covalent interactions[121,122].
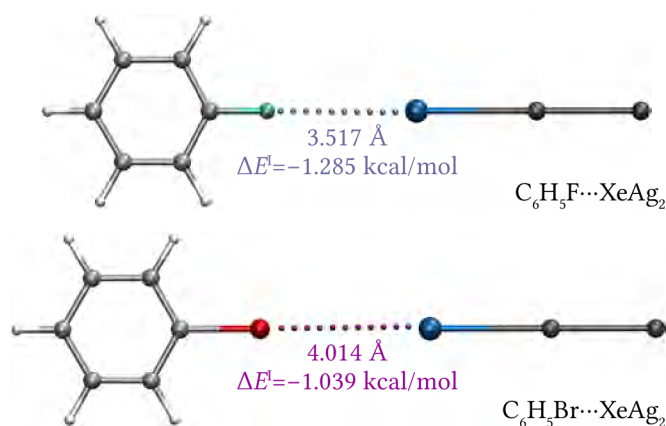
Figure 6.2: MP2/aug-cc-pVTZ (aug-cc-pwCVTZ-PP for Br and Xe) optimized subsystems at CCSD(T)/aug-cc-pVTZ (aug-cc-pwCVTZ-PP for Br and Xe) optimized distance used for benchmark calculation.

To replicate the data obtained from nc-AFM experiments, we selected real molecules, 4FPhM and 4BrPhM, in conjunction with a model silver tip. The tip was approximated by six silver atoms functionalized with either a CO molecule or a Xe atom. Notably, the surface representation was omitted from this model. Given the distinct nature of the Br···Xe interaction, we conducted benchmark calculations of ΔE^{I} at the CCSD(T)/-aug-cc-pVTZ level (aug-cc-pwCVTZ-PP for Br and Xe), a feat nearly impossible in real systems. As proxies for 4FPhM and 4BrPhM, fluorobenzene and bromobenzene were chosen, respectively. In these model systems, the tip was simplified to just two silver atoms. The systems were optimized at the MP2/aug-cc-pVTZ level (aug-cc-pwCVTZ-PP for Br and Xe), followed by scanned calculations of ΔE^{I} at the CCSD(T)/aug-cc-pVTZ level (aug-cc-pwCVTZ-PP for Br and Xe). The resulting minima after extrapolation showed that the model with fluorobenzene and $XeAg_2$ was stabilized by -1.285 kcal/mol at an F···Xe distance of 3.517 Å, while the model with bromobenzene and $XeAg_2$ exhibited a stabilization of -1.039 kcal/mol at a Br···Xe distance of 4.014 Å. Systems are shown on Figure 6.2.

Transitioning from model to real systems necessitates shifting from the computationally demanding CCSD(T) method to more efficient DFT methods. For this purpose, various DFT functionals were benchmarked against CCSD(T) curves. The most promising results were obtained with the functionals ωB97X-V[123], PBE0[72], and the commonly used B3LYP[71] (see Figure 6.3). Both PBE0 and B3LYP were enhanced with Grimme's D3 correction[78] and the Becke-Johnson damping function[124]. Given the separation of ΔE^{I} minima from nc-AFM falls below chemical accuracy (1 kcal/mol), it is crucial to accurately represent the difference between the ΔE^{I} minima of fluorine and bromine model systems, as observed in CCSD(T) calculations. The reference difference in minima is 0.247 kcal/mol. The functional ωB97X-V shows the best fit with a minima difference of 0.316. PBE0 follows closely, exhibiting a difference of 0.141. However, B3LYP demonstrates almost no separation between complexes (-0.006) and, contrary to the reference,
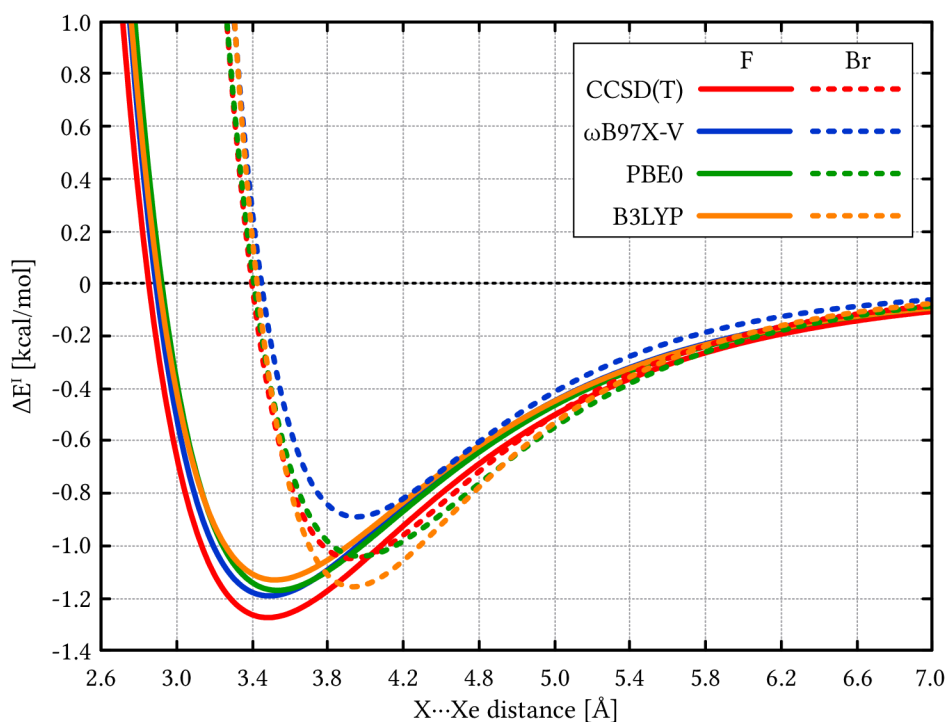
Figure 6.3: The ΔE^{I} curve depicts the interaction energy between fluorobenzene and $XeAg_2$ (above), as well as between bromobenzene and $XeAg_2$ (below), across varying X⋯Xe distances. Here, 'X' represents fluorine and bromine, respectively.

indicates the bromobenzene system as more stable. Therefore, ωB97X-V functional was chosen for real systems analysis. Due to its computational demand, PBE0 was selected for geometry optimization.

The characteristics of non-covalent interactions between real systems and functionalized tips can be elucidated by analyzing the ESP on selected systems in Table 6.1. As anticipated, the fluorine atom in the 4FPhM molecule demonstrates a notably negative ESP, quantified as -12.37 kcal/mol. This contrasts with the bromine atom in the 4BrPhM molecule, which, due to the presence of a positive σ-hole, shows a positive ESP value of V_{s} at the top of the halogen atom, recorded as 15.21 kcal/mol. The functionalized tips employed in the study also exhibit distinct ESPs. The CO-functionalized tip, owing to the covalent bond between silver and carbon atoms, presents a negative ESP on the oxygen atom, calculated at -5.08 kcal/mol. Conversely, the high polarizability of the xenon atom in the xenon-functionalized tip leads to significant polarization by the silver, resulting in a relatively high ESP of 16.04 kcal/mol.

As the functionalized nc-AFM tips, one with a xenon atom and the other with a CO molecule, move across a gold surface coated with 4FPhM or 4BrPhM molecules, they perform scans to measure interaction energies. Each scan reveals unique energy minima, reflecting the specific interactions between the molecules on the surface and the function-

Table 6.1: Analysis of ESP in all studied subsystems on ω-B97X-D/def2-QZVPP level.

Molecule	Studied atom	$V_{s,max}$ [kcal/mol]
$C(C_6H_4F)_4$	F	-12.37
$C(C_6H_4F)_4$	H	20.54
$C(C_6H_4Br)_4$	Br	15.21
$XeAg_6$	Xe	16.04
$COAg_6$	O	-5.08
C_6H_5F	F	-15.74
C_6H_5Br	Br	12.40
$XeAg_2$	Xe	20.01

alized tips. These experimental observations are replicated through scan calculations, wherein PBE0-optimized subsystems are methodically displaced against each other in the z-axis direction by increments of 0.1 Å. For each positional increment, partial geometry optimizations are executed at the PBE0-D3BJ/def2-TZVPP level, with the z-coordinate maintained constant. Concurrently, interaction energy ΔE^I is computed at each step using the ωB97X-V/aug-cc-pVTZ functional (aug-cc-pwCVTZ-PP for Br and Xe atoms).

An intriguing observation was made with the xenon-functionalized nc-AFM tip, which produced two distinct ΔE^I curves with minima values of -0.32 and -0.81 kcal/mol. This dual-minima phenomenon is hypothesized to result from the "tilting" of the 4FPhM molecule on the surface, as illustrated in Figure 6.4. Consequently, the xenon atom in the functionalized tip interacts not with the fluorine atom as expected but with a hydrogen atom from the 4FPhM molecule. In this scenario, the distinct energy minima result from the interactions between the positively charged xenon atom, polarized by the silver tip, and two different atoms: the negatively charged fluorine and the partially positive hydrogen. The interaction with fluorine leads to a deeper minimum, whereas interaction with hydrogen results in less stable complex. These variations in minima reflect the different nature of interactions with each atom. Table 6.1 shows the ESP values of both atoms in the 4FPhM molecule. Moreover, the other experimental minima show excellent correlation with the ωB97X-V calculated values, as depicted in Figure 6.5. In all cases, the calculated values slightly overestimate the experimental results by approximately 0.1-0.2 kcal/mol. This discrepancy could stem from the exclusion of zero-point vibrational energy in the calculations, despite the experiments being conducted at temperatures below 10 K.

6.1.2   Images of σ-hole

Figure 6.6 presents the ESP calculations at the ωB97X-D/aug-cc-pVTZ level on a surface defined by an electron density of 0.001 a.u. alongside the experimental KPFM image using a xenon functionalized tip. For the 4FPhM molecule, the calculated ESP illustrates a uniform negative charge distribution over the F atom, as anticipated from fluorine's

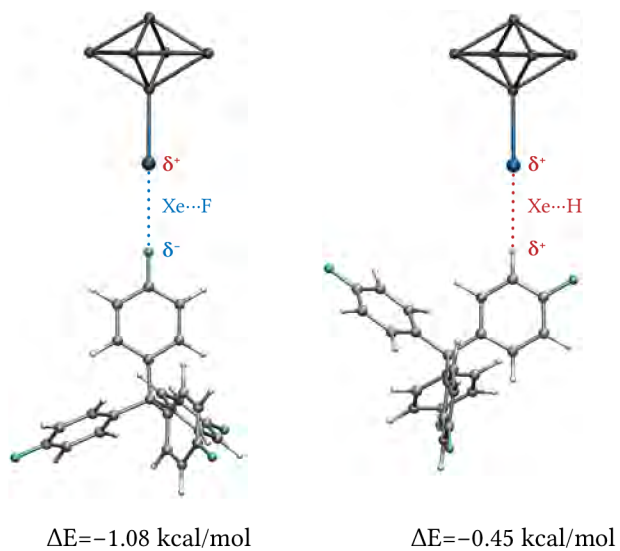ΔE=−1.08 kcal/mol   ΔE=−0.45 kcal/mol

Figure 6.4: Model of calculation two different minima for interaction between 4FPhM molecule and xenon functionalized silver tip.
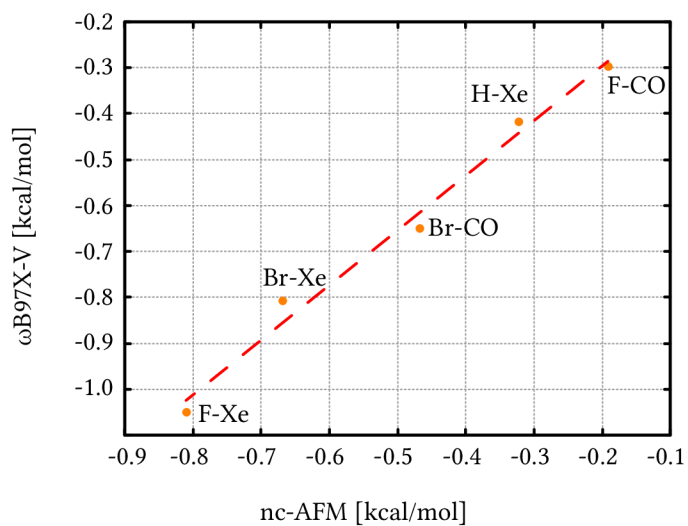
Figure 6.5: Correletion between experimental data from nc-AFM and theoretical data calculated at ωB97X-V/aug-cc-pVTZ (aug-cc-pwCVTZ-PP for Br and Xe) level.
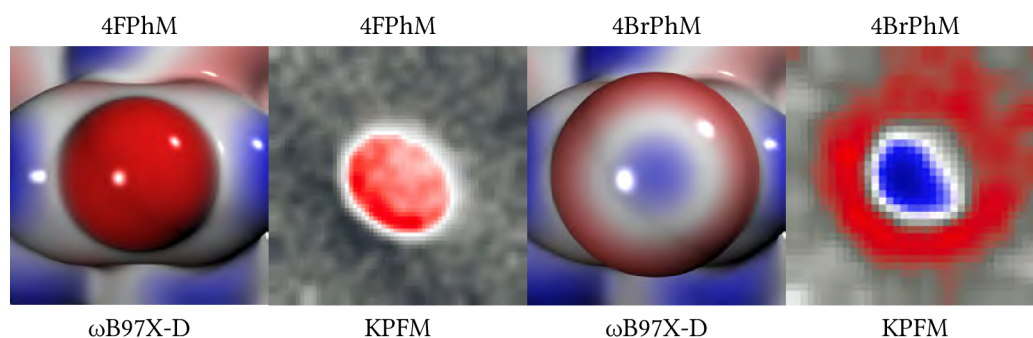
Figure 6.6: Calculated ESP at the ωB97X-D/aug-cc-pVTZ level on the atoms F and Br in molecules 4FPhM and 4BrPhM, compared with KPFM measurements using a functionalized xenon tip on the same atoms. Red color represents negative charge, blue color represents positive charge.

high electronegativity, precluding the formation of a σ-hole. This uniform distribution is corroborated by the KPFM imaging, which reveals a similar negative charge distribution around the F atom. Conversely, the ESP calculated on the Br atom in the 4BrPhM molecule demonstrates an anisotropic charge distribution, a consequence of the participation of the $4p_z$ orbital electron in the covalent bond. This participation results in a deficit of negative charge on the side opposite to the C-Br bond, manifesting as a σ-hole indicated by a blue circle. The electrons from the $4p_x$ and $4p_y$ orbitals create a negative "belt" encircling the Br atom, depicted in red around the σ-hole. The experimental KPFM image validates this theoretical observation, showing a central area of positive charge (the σ-hole) on the Br atom, surrounded by a region of negative charge.

6.2   Visualization of π-hole

For further visualization of anisotropic charge distribution, π-holes were selected for examination using the same experimental setup as for σ-holes. The selection of molecules for this purpose was easier due to the natural tendency of planar π-electron systems to align on surfaces. To ensure clear differentiation of systems on the surface, larger molecular systems were chosen. Two systems were selected for comparative analysis: one featuring a π-hole and the other devoid of it to facilitate contrast observation. Anthracene (An) served as the representative system with π-electrons, whereas 9,10-dichlorooctafluoroanthracene (FCl-An) was selected as the system expected to exhibit a pronounced π-hole due to the electron-withdrawing effects of F and Cl atoms. The structures of both complexes are illustrated in Figure 6.7.

anthracene   9,10-dichlorooctafluoroanthracene
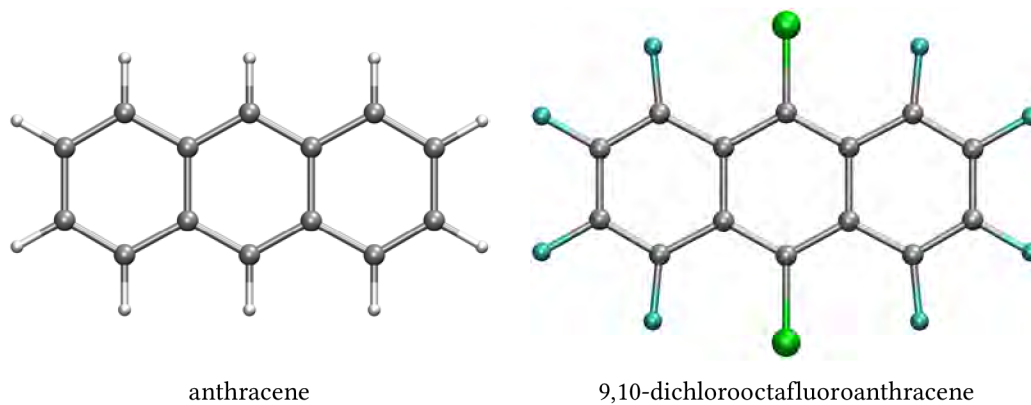
Figure 6.7: MP2/aug-cc-pVTZ optimized geometries of anthracene and 9,10-dichlorooctafluoroanthracene.
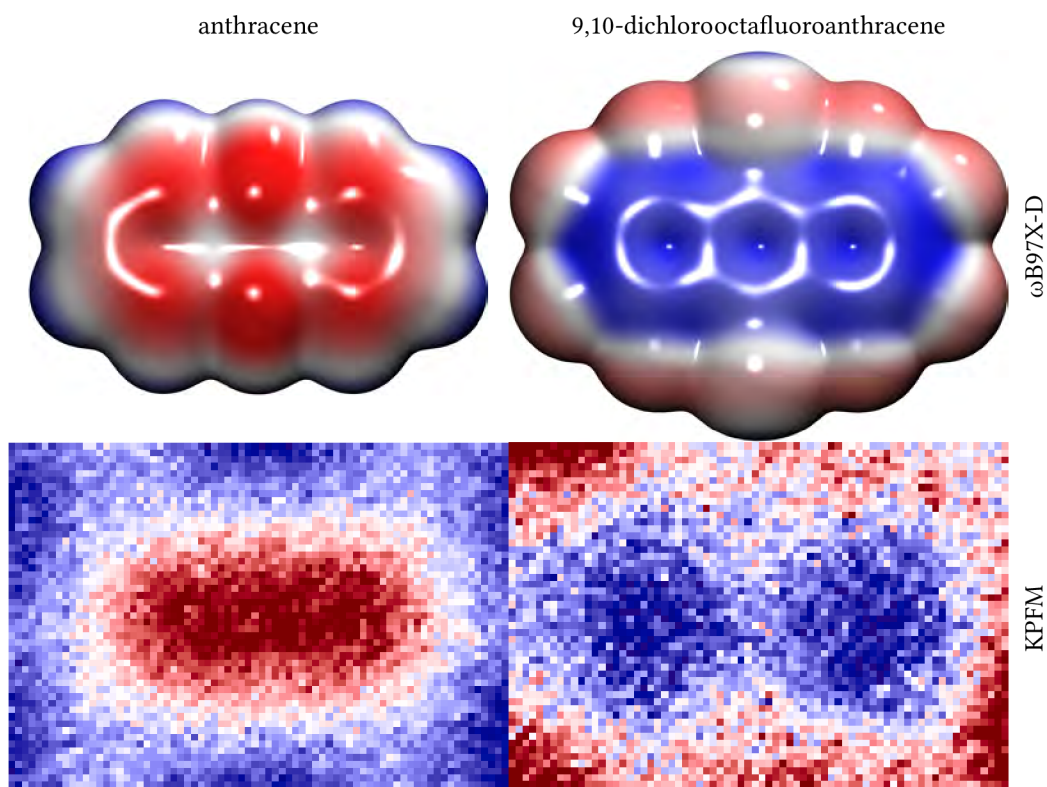
Figure 6.8: Calculated ESP at the ωB97X-D/aug-cc-pVTZ level on molecules An and FCl-An, compared with KPFM measurements using a functionalized CO tip on the same molecules. Red color represents negative charge, blue color represents positive charge.

6.2.1 Images of π-hole

Figure 6.8 illustrates the ESP for An and FCl-An molecules, computed at the ωB97X-D/aug-cc-pVTZ level, alongside experimental images from KPFM with a CO-functionalized tip. The An molecule exhibits a homogeneous negative charge distribution across its surface, attributable to its classical π-electron system. This uniform negative charge is depicted in red across the molecule's ring in Figure 6.8, a finding corroborated by the KPFM image, which reveals a consistent negative charge distribution throughout the molecule. Conversely, the ESP for FCl-An indicates the formation of a π-hole within the molecule, denoted in blue. This phenomenon arises from the electron-withdrawing effect of the F and Cl atoms, which deplete electron density from the molecule's core. The KPFM image validates our theoretical analysis by showcasing a π-hole within the FCl-An molecule.

6.3 Summary

σ-holes and π-holes, long existing as a computational chemistry models, were empirically observed through the application of KPFM, which introduced a subatomic resolution in observations by functionalization of a silver tip with Xe atom and CO molecule. Furthermore, the measurement of interaction energies using the same technique unveiled a perfect correlation between experimental findings and theoretical predictions.

Chapter 7

Conclusion

This thesis presents my research between 2019 and 2024, summarizing findings from publications 8, 9, 10, 21, 105, 117, and 118. It delivers an in-depth examination of dative bonds in p-group elements, highlighting their unique formation and behavior, especially upon solvation. Furthermore, the research scopes into the hydridic hydrogen interactions, illustrating its distinct role in interactions where hydrogen serves as an electron donor. A significant contribution of this work is the visualization and empirical confirmation of anisotropic charge distributions, namely σ-holes and π-holes.

In Chapter 4, we introduced a novel type of dative bond wherein nitrogen acts as the donor and carbon as the acceptor. Due to their distinctive geometry, fullerenes can function as electron pair acceptors, thus forming dative bonds. We demonstrated that piperidine can interact with C_{60} to form various structures stabilized by van der Waals forces, tetrel bond, and dative bond. In a 1:1 ratio, the dative bond product exhibits lesser stability. However, the introduction of a second piperidine molecule significantly stabilizes the dative bond complex due to a cascade of charge transfers from the outer piperidine through the dative bonded piperidine to the C_{60} fullerene. This theoretical prediction was corroborated by IR spectroscopy. While C_{60}, with its I_h symmetry, has equivalent carbon atoms, the transition to the larger C_{70}, which exhibits D_{5h} symmetry, introduces diverse structural motifs. Designated as sites A, B, and C in descending order of curvature, the analysis reveals the most stable dative bond occurs between the piperidine dimer and carbon at site A, with decreasing stability at sites B and C. A comparison of the curvatures of C_{60}, C_{70}, and analogous motifs from other molecules with the respective interaction energies for piperidine dative bonded to these sites indicates that significant curvature is essential for the formation of a dative bond with the carbon framework.

Typically, both covalent and non-covalent interactions exhibit bond weakening upon solvation. However, dative bonds display a distinctive behavior where their strength increases with solvent polarity. Our computational studies predicted stabilization in various complexes featuring N→B, N→C, P→B, and P→C dative bonds. Particularly, the dative bond complex $Me_3N\text{-}BH_3$ was studied in more detail, revealing a decrease in the N-

B distance and an increase of stabilization energy across solvents of varying polarities (ε=1.0, 2.0, 2.3, 4.8, 9.9, and 78.0). These computational predictions were validated experimentally using Raman spectroscopy to analyze the Me_3N-BH_3 complex in cyclohexane, benzene, chloroform, and water. The B-N stretching frequency exhibited a consistent blue shift in line with our theoretical predictions.

Hydrogen bonded to an element less electronegative than itself exhibits behavior distinct from that in a conventional hydrogen bond, acting as a nucleophile. This unique interaction has led to various terminologies such as charge-inverted hydrogen bond or agostic bond. Our research, detailed in Chapter 5, demonstrates that hydridic hydrogen bonds exhibit similarities with conventional hydrogen bonds in terms of interaction energies and shifts in the X-H stretching frequency. Specifically, complexes of Me_3SiH with ICF_3 and BrCN were found to exhibit interaction energies and shifts in the X-H stretching frequency analogous to those observed in conventional hydrogen bonds. IR spectroscopy in an argon matrix confirmed the formation of complexes involving hydridic hydrogen. Given these findings, the term "hydridic hydrogen bond" was suggested, proposing that conventional hydrogen bonds might be better termed as "protonic hydrogen bonds." To resolve this nomenclature ambiguity, we proposed a revised definition of hydrogen bonds in ref. 21 covering both types of interactions.

The concept of the σ-hole was theoretically predicted thirty years ago. Advances in microscopy of atomic forces and the specific functionalization of a silver tip with a xenon atom and a CO molecule have enabled subatomic resolution, crucial for visualizing σ-hole and, subsequently, π-holes. An advantage of the nc-AFM technique is its ability to measure interaction energy directly. For a simplified model, we calculated the potential energy curve and benchmarked various DFT functionals. The ωB97X-V functional demonstrated the best correlation with the CCSD(T) reference, enabling us to accurately reproduce the interaction energy minima for four systems. The separation between these minima was less than 1 kcal/mol, aligning with the threshold for chemical accuracy. Notably, two distinct minima were observed in the nc-AFM analysis for the 4FPhM system using a xenon-functionalized silver tip, identified as contact Xe-F and Xe-H interactions, attributed to tilting of 4FPhM molecule on the surface. This exemplifies how computational chemistry not only corroborates experimental results but also provides insights when experimental data are ambiguous.

This thesis lays the groundwork for future research in the area of dative bonds and non-covalent interactions:

(i) The identification of a new type of dative bond suggests innovative ways to employ fullerenes, creating bonds that are stronger than typical non-covalent interactions yet weaker than standard covalent bonds, thus expanding the applications of fullerenes. Future research should examine dative bond formation in other carbon-based structures and investigate how these bonds can be strengthened in the presence of transition metals and different solvents.

(ii) Extending the concept of hydridic hydrogen bonds to include transition metal hydrides opens up new possibilities. Transition metal hydrides are used in areas

like catalysis and hydrogen storage. Our observations indicate unique properties of hydridic hydrogen compared to the conventional, positively charged hydrogen. The significance of dispersion energy, due to the higher electron density on hydridic hydrogen, and the different interaction strengths and ranges merit further exploration. Future studies could also explore the formation of single-electron dative bonds where hydrogen serves as an electron donor.

(iii) Enhancing the collaboration between computational chemistry and atomic force microscopy promises to yield insights into p-holes and the tunability of σ-holes by various substituents. By varying the molecules or anions used to functionalize the silver tip, it should be possible to develop a comprehensive benchmark for assessing different types of non-covalent interactions.

In conclusion, the research shared in this thesis makes a notable impact on the field of computational chemistry, especially concerning molecular interactions and chemical bonding. The author's work, recognized in esteemed scientific publications, underscores the relevance and caliber of the research undertaken. The proposed future directions offer a clear guide for forthcoming studies, promising continued progress and innovative discoveries in understanding and applying computational chemistry methods to explore molecular systems and interactions.

References

1 L. Pauling:
   'The nature of the chemical bond. application of results obtained from the quantum mechanics and from a theory of paramagnetic susceptibility to the structure of molecules',
   Journal of the American Chemical Society **53**, 1367–1400 (1931).

2 F. A. Cotton and C. B. Harris:
   'The Crystal and Molecular Structure of Dipotassium Octachlorodirhenate(III) Dihydrate, $K_2[Re_2Cl_8]_2H_2O$',
   Inorganic Chemistry **4**, 330–333 (1965).

3 L. Gagliardi and B. O. Roos:
   'Quantum chemical calculations show that the uranium molecule U_2 has a quintuple bond',
   Nature **433**, 848–851 (2005).

4 L. Pauling:
   'The nature of the chemical bond. iv. the energy of single bonds and the relative electronegativity of atoms',
   Journal of the American Chemical Society **54**, 3570–3582 (1932).

5 G. Frenking, K. Wichmann, N. Fröhlich, C. Loschen, M. Lein, J. Frunzke and V. M. Rayón:
   'Towards a rigorously defined quantum chemical analysis of the chemical bond in donor–acceptor complexes',
   Coordination Chemistry Reviews **238-239**, Theoretical and Computational Chemistry, 55–82 (2003).

6 A. Nandi and S. Kozuch:
   'History and Future of Dative Bonds',
   Chemistry – A European Journal **26**, 759–772 (2020).

7 B. A. Smith and K. D. Vogiatzis:
   'σ-Donation and π-Backdonation Effects in Dative Bonds of Main-Group Elements',
   The Journal of Physical Chemistry A **125**, 7956–7966 (2021).

8 M. Lamanec, R. Lo, D. Nachtigallová, A. Bakandritsos, E. Mohammadi, M. Dračínský, R. Zbořil, P. Hobza and W. Wang:
   'The Existence of a N→C Dative Bond in the C_{60}–Piperidine Complex',
   Angewandte Chemie International Edition **60**, 1942–1950 (2021).

9 R. Lo, M. Lamanec, W. Wang, D. Manna, A. Bakandritsos, M. Dračínský, R. Zbořil, D. Nachtigallová and P. Hobza:
   'Structure-directed formation of the dative/covalent bonds in complexes with C_{70}⋯piperidine',
   Physical Chemistry Chemical Physics **23**, 4365–4375 (2021).

10 R. Lo, D. Manna, M. Lamanec, W. Wang, A. Bakandritsos, M. Dračínský, R. Zbořil, D. Nachtigallová and P. Hobza:
   'Addition Reaction between Piperidine and C_{60} to Form 1,4-Disubstituted C_{60} Proceeds through van der Waals and Dative Bond Complexes: Theoretical and Experimental Study',
   Journal of the American Chemical Society **143**, 10930–10939 (2021).

11 J. A. PLUMLEY and J. D. EVANSECK:
'Covalent and Ionic Nature of the Dative Bond and Account of Accurate Ammonia Borane Binding Enthalpies',
The Journal of Physical Chemistry A **111**, 13472–13483 (2007).

12 E. ARUNAN, G. R. DESIRAJU, R. A. KLEIN, J. SADLEJ, S. SCHEINER, I. ALKORTA, D. C. CLARY, R. H. CRABTREE, J. J. DANNENBERG, P. HOBZA, H. G. KJAERGAARD, A. C. LEGON, B. MENNUCCI and D. J. NESBITT:
'Definition of the hydrogen bond (IUPAC Recommendations 2011)',
83, 1637–1641 (2011).

13 G. PIMENTEL and A. MCCLELLAN:
The Hydrogen Bond,
(W. H. Freeman & Co. Ltd., 1960).

14 A. E. REED, F. WEINHOLD, L. A. CURTISS and D. J. POCHATKO:
'Natural bond orbital analysis of molecular interactions: Theoretical studies of binary complexes of HF, H_2O, NH_3, N_2, O_2, F_2, CO, and CO_2 with HF, H_2O, and NH_3',
The Journal of Chemical Physics **84**, 5687–5705 (1986).

15 P. HOBZA, V. ŠPIRKO, Z. HAVLAS, K. BUCHHOLD, B. REIMANN, H. D. BARTH and B. BRUTSCHY:
'Anti-hydrogen bond between chloroform and fluorobenzene',
Chemical Physics Letters **299**, 180–186 (1999).

16 P. HOBZA and Z. HAVLAS:
'Blue-Shifting Hydrogen Bonds',
Chemical Reviews **100**, 4253–4264 (2000).

17 S. DJAFARI, H.-D. BARTH, K. BUCHHOLD and B. BRUTSCHY:
'Infrared-depletion spectroscopy study on hydrogen-bonded fluorobenzene–methanol clusters',
The Journal of Chemical Physics **107**, 10573–10581 (1997).

18 P. HOBZA and K. MÜLLER-DETHFELS:
Non-covalent Interactions: Theory and Experiment,
(RSC Publishing, 2010).

19 M. JABŁOŃSKI:
'Binding of X–H to the lone-pair vacancy: Charge-inverted hydrogen bond',
Chemical Physics Letters **477**, 374–376 (2009).

20 M. JABŁOŃSKI:
'Ten years of charge-inverted hydrogen bonds',
Structural Chemistry **31**, 61–80 (2020).

21 S. CIVIŠ, M. LAMANEC, V. ŠPIRKO, J. KUBIŠTA, M. ŠPEŤKO and P. HOBZA:
'Hydrogen Bonding with Hydridic Hydrogen–Experimental Low-Temperature IR and Computational Study: Is a Revised Definition of Hydrogen Bonding Appropriate?',
Journal of the American Chemical Society **145**, 8550–8559 (2023).

22 S. J. GRABOWSKI:
'What Is the Covalency of Hydrogen Bonding?',
Chemical Reviews **111**, 2597–2625 (2011).

23 N. RAMASUBBU, R. PARTHASARATHY and P. MURRAY-RUST:
'Angular preferences of intermolecular forces around halogen centers: preferred directions of approach of electrophiles and nucleophiles around carbon-halogen bond',
Journal of the American Chemical Society **108**, 4308–4314 (1986).

24   T. Brinck, J. S. Murray and P. Politzer:
      'Surface electrostatic potentials of halogenated methanes as indicators of directional inter-
      molecular interactions',
      International Journal of Quantum Chemistry **44**, 57–64 (1992).

25   M. H. Kolář and P. Hobza:
      'Computer Modeling of Halogen Bonds and Other σ-Hole Interactions',
      Chemical Reviews **116**, 5155–5187 (2016).

26   P. Metrangolo, H. Neukirch, T. Pilati and G. Resnati:
      'Halogen Bonding Based Recognition Processes: A World Parallel to Hydrogen Bonding',
      Accounts of Chemical Research **38**, 386–395 (2005).

27   P. Politzer, P. Lane, M. C. Concha, Y. Ma and J. S. Murray:
      'An overview of halogen bonding',
      Journal of Molecular Modeling **13**, 305–311 (2007).

28   P. Metrangolo, F. Meyer, T. Pilati, G. Resnati and G. Terraneo:
      'Halogen Bonding in Supramolecular Chemistry',
      Angewandte Chemie International Edition **47**, 6114–6127 (2008).

29   P. Politzer and J. S. Murray:
      'The fundamental nature and role of the electrostatic potential in atoms and molecules',
      Theoretical Chemistry Accounts **108**, 134–142 (2002).

30   J. S. Murray and P. Politzer:
      'The electrostatic potential: an overview',
      WIREs Computational Molecular Science **1**, 153–163 (2011).

31   G. R. Desiraju, P. S. Ho, L. Kloo, A. C. Legon, R. Marquardt, P. Metrangolo, P. Politzer,
      G. Resnati and K. Rissanen:
      'Definition of the halogen bond (IUPAC Recommendations 2013)',
      Pure and Applied Chemistry **85**, 1711–1713 (2013).

32   S. J. Grabowski:
      'Halogen Bond and Its Counterparts: Bent's Rule Explains the Formation of Nonbonding
      Interactions',
      The Journal of Physical Chemistry A **115**, 12340–12347 (2011).

33   G. Cavallo, P. Metrangolo, R. Milani, T. Pilati, A. Priimagi, G. Resnati and G. Ter-
      raneo:
      'The Halogen Bond',
      Chemical Reviews **116**, 2478–2601 (2016).

34   P. Metrangolo and G. Resnati:
      Halogen Bonding,
      (Springer Berlin, 2007).

35   A. Kekulé:
      'Untersuchungen über aromatische Verbindungen',
      Justus Liebigs Annalen der Chemie **137**, 129–196 (1866).

36   G. E. Bacon, N. A. Curry, S. A. Wilson and R. Spence:
      'A crystallographic study of solid benzene by neutron diffraction',
      Proceedings of the Royal Society of London. Series A. Mathematical and Physical Sciences
      279, 98–110 (1964).

37 D. L. Cooper, J. Gerratt and M. Raimondi:
'The electronic structure of the benzene molecule',
Nature **323**, 699–701 (1986).

38 L. Pauling:
'Electronic structure of the benzene molecule',
Nature **325**, 396–396 (1987).

39 R. P. Messmer and P. A. Schultz:
'The electronic structure of the benzene molecule',
Nature **329**, 492–492 (1987).

40 P. Hobza, H. L. Selzle and E. W. Schlag:
'Potential Energy Surface of the Benzene Dimer: Ab Initio Theoretical Study',
Journal of the American Chemical Society **116**, 3500–3506 (1994).

41 K. Pluháčková, P. Jurečka and P. Hobza:
'Stabilisation energy of $C_6H_6 \cdots C_6X_6$ (X = F, C, Br, I, CN) complexes: complete basis set limit calculations at MP2 and CCSD(T) levels',
Phys. Chem. Chem. Phys. **9**, 755–760 (2007).

42 J. S. Murray, P. Lane, T. Clark, K. E. Riley and P. Politzer:
'σ-holes, π-holes and electrostatically-driven interactions',
Journal of Molecular Modeling **18**, 541–548 (2012).

43 H. Wang, W. Wang and W. J. Jin:
'σ-Hole Bond vs π-Hole Bond: A Comparison Based on Halogen Bond',
Chemical Reviews **116**, 5072–5104 (2016).

44 M. Giese, M. Albrecht and K. Rissanen:
'Anion–π Interactions with Fluoroarenes',
Chemical Reviews **115**, 8867–8895 (2015).

45 E. Schrödinger:
'Quantisierung als Eigenwertproblem',
Annalen der Physik **385**, 437–490 (1926).

46 M. Born and R. Oppenheimer:
'Zur Quantentheorie der Molekeln',
Annalen der Physik **389**, 457–484 (1927).

47 D. R. Hartree:
'The Wave Mechanics of an Atom with a Non-Coulomb Central Field. Part I. Theory and Methods',
Mathematical Proceedings of the Cambridge Philosophical Society **24**, 89–110 (1928).

48 V. Fock:
'Näherungsmethode zur Lösung des quantenmechanischen Mehrkörperproblems',
Zeitschrift für Physik **61**, 126–148 (1930).

49 P.-O. Löwdin:
'Quantum theory of cohesive properties of solids',
Advances in Physics **5**, 1–171 (1956).

50 L. Kong, F. A. Bischoff and E. F. Valeev:
'Explicitly Correlated R12/F12 Methods for Electronic Structure',
Chemical Reviews **112**, 75–107 (2012).

51   C. Møller and M. S. Plesset:
      'Note on an Approximation Treatment for Many-Electron Systems',
      Phys. Rev. **46**, 618–622 (1934).

52   K. E. Riley, J. Řezáč and P. Hobza:
      'MP2.X: a generalized MP2.5 method that produces improved binding energies with smaller
      basis sets',
      Phys. Chem. Chem. Phys. **13**, 21121–21125 (2011).

53   M. Loipersberger, L. W. Bertels, J. Lee and M. Head-Gordon:
      'Exploring the limits of second- and third-order møller–plesset perturbation theories for
      noncovalent interactions: revisiting mp2.5 and assessing the importance of regularization
      and reference orbitals',
      Journal of Chemical Theory and Computation **17**, 5582–5599 (2021).

54   F. Coester and H. Kümmel:
      'Short-range correlations in nuclear wave functions',
      Nuclear Physics **17**, 477–485 (1960).

55   J. Čížek:
      'On the Correlation Problem in Atomic and Molecular Systems. Calculation of Wavefunc-
      tion Components in Ursell-Type Expansion Using Quantum-Field Theoretical Methods',
      The Journal of Chemical Physics **45**, 4256–4266 (1966).

56   J. Paldus and J. Čížek:
      'Stability Conditions for the Solutions of the Hartree–Fock Equations for Atomic and Mo-
      lecular Systems. II. Simple Open-Shell Case',
      The Journal of Chemical Physics **52**, 2919–2936 (1970).

57   G. E. Scuseria, C. L. Janssen and H. F. Schaefer III:
      'An efficient reformulation of the closed-shell coupled cluster single and double excitation
      (CCSD) equations',
      The Journal of Chemical Physics **89**, 7382–7387 (1988).

58   R. J. Bartlett:
      'Coupled-cluster theory and its equation-of-motion extensions',
      WIREs Computational Molecular Science **2**, 126–138 (2012).

59   R. J. Bartlett and M. Musiał:
      'Coupled-cluster theory in quantum chemistry',
      Rev. Mod. Phys. **79**, 291–352 (2007).

60   L. Šimová, J. Řezáč and P. Hobza:
      'Convergence of the Interaction Energies in Noncovalent Complexes in the Coupled-Cluster
      Methods Up to Full Configuration Interaction',
      Journal of Chemical Theory and Computation **9**, 3420–3428 (2013).

61   M. Urban, J. Noga, S. J. Cole and R. J. Bartlett:
      'Towards a full CCSDT model for electron correlation',
      The Journal of Chemical Physics **83**, 4041–4046 (1985).

62   K. Raghavachari, G. W. Trucks, J. A. Pople and M. Head-Gordon:
      'A fifth-order perturbation comparison of electron correlation theories',
      Chemical Physics Letters **157**, 479–483 (1989).

63 E. A. Hylleraas:
'Neue Berechnung der Energie des Heliums im Grundzustande, sowie des tiefsten Terms von Ortho-Helium',
Zeitschrift für Physik **54**, 347–366 (1929).

64 W. Kutzelnigg:
'r_{12}-Dependent terms in the wave function as closed sums of partial wave amplitudes for large *l*',
Theoretica chimica acta **68**, 445–469 (1985).

65 W. Klopper and W. Kutzelnigg:
'Møller-plesset calculations taking care of the correlation CUSP',
Chemical Physics Letters **134**, 17–22 (1987).

66 W. Klopper and W. Kutzelnigg:
'MP2-R12 calculations on the relative stability of carbocations',
The Journal of Physical Chemistry **94**, 5625–5630 (1990).

67 W. Klopper and C. C. M. Samson:
'Explicitly correlated second-order Møller–Plesset methods with auxiliary basis sets',
The Journal of Chemical Physics **116**, 6397–6410 (2002).

68 E. F. Valeev:
'Improving on the resolution of the identity in linear R12 ab initio theories',
Chemical Physics Letters **395**, 190–195 (2004).

69 H.-J. Werner, T. B. Adler and F. R. Manby:
'General orbital invariant MP2-F12 theory',
The Journal of Chemical Physics **126**, 164102 (2007).

70 S. Ten-no and J. Noga:
'Explicitly correlated electronic structure theory from R12/F12 ansätze',
WIREs Computational Molecular Science **2**, 114–125 (2012).

71 P. J. Stephens, F. J. Devlin, C. F. Chabalowski and M. J. Frisch:
'Ab initio calculation of vibrational absorption and circular dichroism spectra using density functional force fields',
The Journal of Physical Chemistry **98**, 11623–11627 (1994).

72 C. Adamo and V. Barone:
'Toward reliable density functional methods without adjustable parameters: The PBE0 model',
The Journal of Chemical Physics **110**, 6158–6170 (1999).

73 O. A. Vydrov, J. Heyd, A. V. Krukau and G. E. Scuseria:
'Importance of short-range versus long-range Hartree-Fock exchange for the performance of hybrid density functionals',
The Journal of Chemical Physics **125**, 074106 (2006).

74 O. A. Vydrov and G. E. Scuseria:
'Assessment of a long-range corrected hybrid functional',
The Journal of Chemical Physics **125**, 234109 (2006).

75 P. Jurečka, J. Černý, P. Hobza and D. R. Salahub:
'Density functional theory augmented with an empirical dispersion term. Interaction energies and geometries of 80 noncovalent complexes compared with ab initio quantum mechanics calculations',
Journal of Computational Chemistry **28**, 555–569 (2007).

76   S. GRIMME:
      'Accurate description of van der Waals complexes by density functional theory including
      empirical corrections',
      Journal of Computational Chemistry **25**, 1463–1473 (2004).

77   S. GRIMME:
      'Semiempirical GGA-type density functional constructed with a long-range dispersion cor-
      rection',
      Journal of Computational Chemistry **27**, 1787–1799 (2006).

78   S. GRIMME, J. ANTONY, S. EHRLICH and H. KRIEG:
      'A consistent and accurate ab initio parametrization of density functional dispersion cor-
      rection (DFT-D) for the 94 elements H-Pu',
      The Journal of Chemical Physics **132**, 154104 (2010).

79   E. CALDEWEYHER, S. EHLERT, A. HANSEN, H. NEUGEBAUER, S. SPICHER, C. BANNWARTH and
      S. GRIMME:
      'A generally applicable atomic-charge dependent London dispersion correction',
      The Journal of Chemical Physics **150**, 154122 (2019).

80   K. LEE, É. D. MURRAY, L. KONG, B. I. LUNDQVIST and D. C. LANGRETH:
      'Higher-accuracy van der Waals density functional',
      Phys. Rev. B **82**, 081101 (2010).

81   O. A. VYDROV and T. VAN VOORHIS:
      'Nonlocal van der Waals density functional: The simpler the better',
      The Journal of Chemical Physics **133**, 244103 (2010).

82   P. HOBZA:
      'Calculations on noncovalent interactions and databases of benchmark interaction ener-
      gies',
      Accounts of Chemical Research **45**, 663–672 (2012).

83   P. HOBZA and R. ZAHRADNÍK:
      Weak Intermolecular Interactions in Chemistry and Biology,
      (Academia, 1980).

84   S. BOYS and F. BERNARDI:
      'The calculation of small molecular interactions by the differences of separate total energies.
      Some procedures with reduced errors',
      Molecular Physics **19**, 553–566 (1970).

85   C. H. ALLEN and C. P. CROSS:
      Molecular Vib-rotors: The Theory and Interpretation of High Resolution Infra-red Spectra,
      (Wiley, 1963).

86   D. PAPOUŠEK and M. R. ALIEV:
      Molecular vibrational/rotational spectra,
      (Academia, 1982).

87 M. J. Frisch, G. W. Trucks, H. B. Schlegel, G. E. Scuseria, M. A. Robb, J. R. Cheese-man, G. Scalmani, V. Barone, G. A. Petersson, H. Nakatsuji, X. Li, M. Caricato, A. V. Marenich, J. Bloino, B. G. Janesko, R. Gomperts, B. Mennucci, H. P. Hratchian, J. V. Ortiz, A. F. Izmaylov, J. L. Sonnenberg, D. Williams-Young, F. Ding, F. Lipparini, F. Egidi, J. Goings, B. Peng, A. Petrone, T. Henderson, D. Ranasinghe, V. G. Zakrzewski, J. Gao, N. Rega, G. Zheng, W. Liang, M. Hada, M. Ehara, K. Toyota, R. Fukuda, J. Hasegawa, M. Ishida, T. Nakajima, Y. Honda, O. Kitao, H. Nakai, T. Vreven, K. Throssell, J. A. Montgomery Jr., J. E. Peralta, F. Ogliaro, M. J. Bearpark, J. J. Heyd, E. N. Brothers, K. N. Kudin, V. N. Staroverov, T. A. Keith, R. Kobayashi, J. Normand, K. Raghavachari, A. P. Rendell, J. C. Burant, S. S. Iyengar, J. Tomasi, M. Cossi, J. M. Millam, M. Klene, C. Adamo, R. Cammi, J. W. Ochterski, R. L. Martin, K. Morokuma, O. Farkas, J. B. Foresman and D. J. Fox:
Gaussian16 Revision C.01,
Gaussian Inc. Wallingford CT, 2016.

88 H.-J. Werner, P. J. Knowles, P. Celani, W. Györffy, A. Hesselmann, D. Kats, G. Knizia, A. Köhn, T. Korona, D. Kreplin, R. Lindh, Q. Ma, F. R. Manby, A. Mitrushenkov, G. Rauhut, M. Schütz, K. R. Shamasundar, T. B. Adler, R. D. Amos, S. J. Bennie, A. Bernhard-sson, A. Berning, J. A. Black, P. J. Bygrave, R. Cimiraglia, D. L. Cooper, D. Coughtrie, M. J. O. Deegan, A. J. Dobbyn, K. Doll, M. Dornbach, F. Eckert, S. Erfort, E. Goll, C. Hampel, G. Hetzer, J. G. Hill, M. Hodges, T. Hrenar, G. Jansen, C. Köppl, C. Kollmar, S. J. R. Lee, Y. Liu, A. W. Lloyd, R. A. Mata, A. J. May, B. Mussard, S. J. Mc-Nicholas, W. Meyer, T. F. Miller III, M. E. Mura, A. Nicklass, D. P. O'Neill, P. Palmieri, D. Peng, K. A. Peterson, K. Pflüger, R. Pitzer, I. Polyak, M. Reiher, J. O. Richardson, J. B. Robinson, B. Schröder, M. Schwilk, T. Shiozaki, M. Sibaev, H. Stoll, A. J. Stone, R. Tarroni, T. Thorsteinsson, J. Toulouse, M. Wang, M. Welborn and B. Ziegler:
Molpro, 2022 , a package of ab initio programs,
see `https://www.molpro.net/`.

89 H. J. Werner, P. J. Knowles, G. Knizia, F. R. Manby and M. Schütz:
'Molpro: a general-purpose quantum chemistry program package',
Wiley Interdisciplinary Reviews: Computational Molecular Science **2**, 242–253 (2012).

90 H. J. Werner, P. J. Knowles, F. R. Manby, J. A. Black, K. Doll, A. Heßelmann, D. Kats, A. Köhn, T. Korona, D. A. Kreplin, Q. Ma, T. F. Miller, A. Mitrushchenkov, K. A. Peterson, I. Polyak, G. Rauhut and M. Sibaev:
'The Molpro quantum chemistry package',
The Journal of Chemical Physics **152**, 144107 (2020).

91 F. Neese, F. Wennmohs, U. Becker and C. Riplinger:
'The ORCA quantum chemistry program package',
The Journal of Chemical Physics **152**, 224108 (2020).

92 *TURBOMOLE V7.3 2018, a development of University of Karlsruhe and Forschungszentrum Karlsruhe GmbH, 1989-2007, TURBOMOLE GmbH, since 2007; available from*
`http://www.turbomole.com`.

93 *TURBOMOLE V7.5 2020, a development of University of Karlsruhe and Forschungszentrum Karlsruhe GmbH, 1989-2007, TURBOMOLE GmbH, since 2007; available from*
`https://www.turbomole.org`.

94 *TURBOMOLE V7.7 2022, a development of University of Karlsruhe and Forschungszentrum Karlsruhe GmbH, 1989-2007, TURBOMOLE GmbH, since 2007; available from*
`https://www.turbomole.org`.

95 D. G. A. Smith, L. A. Burns, A. C. Simmonett, R. M. Parrish, M. C. Schieber, R. Galvelis, P. Kraus, H. Kruse, R. Di Remigio, A. Alenaizan, A. M. James, S. Lehtola, J. P. Misiewicz, M. Scheurer, R. A. Shaw, J. B. Schriber, Y. Xie, Z. L. Glick, D. A. Sirianni, J. S. O'Brien, J. M. Waldrop, A. Kumar, E. G. Hohenstein, B. P. Pritchard, B. R. Brooks, I. Schaefer Henry F., A. Y. Sokolov, K. Patkowski, I. DePrince A. Eugene, U. Bozkaya, R. A. King, F. A. Evangelista, J. M. Turney, T. D. Crawford and C. D. Sherrill: 'PSI4 1.4: Open-source software for high-throughput quantum chemistry', The Journal of Chemical Physics **152**, 184108 (2020).

96 E. D. Glendening, A. E. Reed, J. Carpenter and F. Weinhold: *NBO 3.1*, Theoretical Chemistry Institute, University of Wisconsin, Madison, 2005.

97 E. D. Glendening, J. K. Badenhoop, A. E. Reed, J. E. Carpenter, J. A. Bohmann, C. M. Morales, P. Karafiloglou, C. R. Landis and F. Weinhold: *NBO 7.0*, Theoretical Chemistry Institute, University of Wisconsin, Madison, 2018.

98 J. Řezáč: 'Cuby: an integrative framework for computational chemistry', Journal of Computational Chemistry **37**, 1230–1237 (2016).

99 H. W. Kroto, J. R. Heath, S. C. O'Brien, R. F. Curl and R. E. Smalley: 'C_{60}: Buckminsterfullerene', Nature **318**, 162–163 (1985).

100 Z. Wang, X. Ke, Z. Zhu, F. Zhu, M. Ruan, H. Chen, R. Huang and L. Zheng: 'A new carbon solid made of the world's smallest caged fullerene C_{20}', Physics Letters A **280**, 351–356 (2001).

101 C. M. Sayes, A. M. Gobin, K. D. Ausman, J. Mendez, J. L. West and V. L. Colvin: 'Nano-C_{60} cytotoxicity is due to lipid peroxidation', Biomaterials **26**, 7587–7595 (2005).

102 N. Gharbi, M. Pressac, M. Hadchouel, H. Szwarc, S. R. Wilson and F. Moussa: '[60]Fullerene is a Powerful Antioxidant in Vivo with No Acute or Subacute Toxicity', Nano Letters **5**, 2578–2585 (2005).

103 S. Günes, H. Neugebauer and N. S. Sariciftci: 'Conjugated Polymer-Based Organic Solar Cells', Chemical Reviews **107**, 1324–1338 (2007).

104 K. A. Mazzio and C. K. Luscombe: 'The future of organic photovoltaics', Chemical Society Reviews **44**, 78–90 (2015).

105 R. Lo, D. Manna, M. Lamanec, M. Dračínský, P. Bouř, T. Wu, G. Bastien, J. Kaleta, V. M. Miriyala, V. Špirko, A. Mašínová, D. Nachtigallová and P. Hobza: 'The stability of covalent dative bond significantly increases with increasing solvent polarity', Nature Communications 2022 13:1 **13**, 1–7 (2022).

106 G. Schick, K.-D. Kampe and A. Hirsch: 'Reaction of [60]fullerene with morpholine and piperidine: preferred 1,4-additions and fullerene dimer formation', Journal of the Chemical Society, Chemical Communications, 2023–2024 (1995).

107 A. Hirsch, Q. Li and F. Wudl:
'Globe-trotting hydrogens on the surface of the fullerene compound c60h6(n(ch2ch2)2o)6',
Angewandte Chemie International Edition in English **30**, 1309–1310 (1991).

108 Y. Li and L. Gan:
'Selective addition of secondary amines to c60: formation of penta- and hexaamino[60]fullerenes',
The Journal of Organic Chemistry **79**, 8912–8916 (2014).

109 K. Hedberg, L. Hedberg, M. Bühl, D. S. Bethune, C. A. Brown and R. D. Johnson:
'Molecular Structure of Free Molecules of the Fullerene C70 from Gas-Phase Electron Diffraction',
Journal of the American Chemical Society **119**, 5314–5320 (1997).

110 A. Klamt and G. Schüürmann:
'COSMO: a new approach to dielectric screening in solvents with explicit expressions for the screening energy and its gradient',
J. Chem. Soc., Perkin Trans. 2, 799–805 (1993).

111 M. Bühl, T. Steinke, P. von Ragué Schleyer and R. Boese:
'Solvation Effects on Geometry and Chemical Shifts. An Ab Initio/IGLO Reconciliation of Apparent Experimental Inconsistencies on H_3B *cdot* NH_3',
Angewandte Chemie International Edition in English **30**, 1160–1161 (1991).

112 V. Jonas, G. Frenking and M. T. Reetz:
'Comparative Theoretical Study of Lewis Acid-Base Complexes of BH_3, BF_3, BCl_3, $AlCl_3$, and SO_2',
Journal of the American Chemical Society **116**, 8741–8753 (1994).

113 S. S. Batsanov:
'Van der Waals Radii of Elements',
Inorganic Materials **37**, 871–885 (2001).

114 B. Jeziorski, R. Moszynski and K. Szalewicz:
'Perturbation Theory Approach to Intermolecular Potential Energy Surfaces of van der Waals Complexes',
Chemical Reviews **94**, 1887–1930 (1994).

115 G. Binnig, C. F. Quate and C. Gerber:
'Atomic Force Microscope',
Phys. Rev. Lett. **56**, 930–933 (1986).

116 L. Gross, F. Mohn, N. Moll, P. Liljeroth and G. Meyer:
'The Chemical Structure of a Molecule Resolved by Atomic Force Microscopy',
Science **325**, 1110–1114 (2009).

117 B. Mallada, A. Gallardo, M. Lamanec, B. de la Torre, V. Špirko, P. Hobza and P. Jelinek:
'Real-space imaging of anisotropic charge of σ-hole by means of Kelvin probe force microscopy',
Science **374**, 863–867 (2021).

118 B. Mallada, M. Ondráček, M. Lamanec, A. Gallardo, A. Jiménez-Martín, B. de la Torre, P. Hobza and P. Jelínek:
'Visualization of π-hole in molecules by means of Kelvin probe force microscopy',
Nature Communications **14**, 4954 (2023).

119   M. A. LANTZ, H. J. HUG, R. HOFFMANN, P. J. A. VAN SCHENDEL, P. KAPPENBERGER, S. MARTIN,
       A. BARATOFF and H.-J. GÜNTHERODT:
       'Quantitative Measurement of Short-Range Chemical Bonding Forces',
       Science **291**, 2580–2583 (2001).

120   Y. SUGIMOTO, P. POU, M. ABE, P. JELINEK, R. PÉREZ, S. MORITA and Ó. CUSTANCE:
       'Chemical identification of individual surface atoms by atomic force microscopy',
       Nature **446**, 64–67 (2007).

121   Z. SUN, M. P. BONESCHANSCHER, I. SWART, D. VANMAEKELBERGH and P. LILJEROTH:
       'Quantitative atomic force microscopy with carbon monoxide terminated tips',
       Phys. Rev. Lett. **106**, 046104 (2011).

122   C. WAGNER, N. FOURNIER, V. G. RUIZ, C. LI, K. MÜLLEN, M. ROHLFING, A. TKATCHENKO, R.
       TEMIROV and F. S. TAUTZ:
       'Non-additivity of molecule-surface van der Waals potentials from force measurements',
       Nature Communications **5**, 5568 (2014).

123   N. MARDIROSSIAN and M. HEAD-GORDON:
       'ωB97X-V: A 10-parameter, range-separated hybrid, generalized gradient approximation
       density functional with nonlocal correlation, designed by a survival-of-the-fittest strategy',
       Phys. Chem. Chem. Phys. **16**, 9904–9924 (2014).

124   A. D. BECKE and E. R. JOHNSON:
       'A density-functional model of the dispersion interaction',
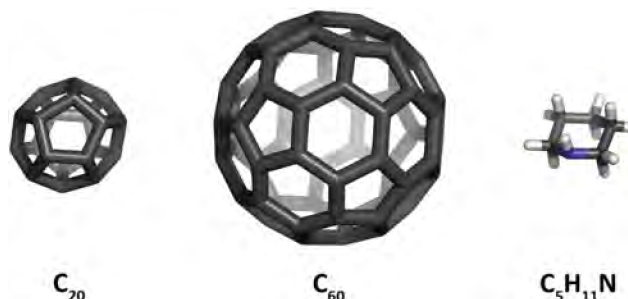   The Journal of Chemical Physics **123**, 154101 (2005).

Appendix

Dative Bonds

The Existence of a N→C Dative Bond in the C$_{60}$–Piperidine Complex

Maximilián Lamanec[+], Rabindranath Lo[+], Dana Nachtigallová,* Aristides Bakandritsos,
Elmira Mohammadi, Martin Dračínský, Radek Zbořil,* Pavel Hobza,* and Weizhou Wang*

Abstract: *The complexes formed between carbon allotropes (C$_{20}$, C$_{60}$ fullerenes, graphene, and single-wall carbon nanotubes) and piperidine have been investigated by means of computational quantum chemical and experimental IR and NMR techniques. Alongside hydrogen bonds, the C···N tetrel bond, and lone-pair···π interactions, the unexpected N→C dative/covalent bond has been detected solely in complexes of fullerenes with piperidine. Non-planarity and five-member rings of carbon allotropes represent the key structural prerequisites for the unique formation of a dative N→C bond. The results of thermodynamics calculations, molecular dynamics simulations, and NMR and FTIR spectroscopy explain the specific interactions between C$_{60}$ and piperidine. The differences in behavior of individual carbon allotropes in terms of dative bonding formation brings a new insight into their controllable organic functionalization.*

Introduction

Buckmisterfullerene C$_{60}$ (further named as fullerene (FL), Scheme 1), a ball-shaped compound, and its derivatives represent the class of carbon allotropes which received considerable attention due to their applications in bio-related[1–3] and material-chemistry fields.[4–6] Their unique

[*] M. Lamanec[+,++], R. Lo[+,++], D. Nachtigallová, M. Dračínský, R. Zbořil, P. Hobza
Institute of Organic Chemistry and Biochemistry
Czech Academy of Sciences
Flemingovo Náměstí 542/2, 16000 Prague (Czech Republic)
E-mail: dana.nachtigallova@uochb.cas.cz
radek.zboril@upol.cz
pavel.hobza@uochb.cas.cz

M. Lamanec[+,++]
Department of Physical Chemistry, Palacký University Olomouc
tr. 17 listopadu 12, 771 46 Olomouc (Czech Republic)

R. Lo[+,++], D. Nachtigallová, A. Bakandritsos, E. Mohammadi
Regional Centre of Advanced Technologies and Materials
Faculty of Science, Palacký University
Šlechtitelů 27, 78371 Olomouc (Czech Republic)

W. Wang
College of Chemistry and Chemical Engineering, and Henan Key Laboratory of Function-Oriented Porous Materials
Luoyang Normal University, Luoyang 471934 (China)
E-mail: wzw@lynu.edu.cn

R. Zbořil, P. Hobza
CATRIN, Šlechtitelů 27, 78371 Olomouc (Czech Republic)

[+] These authors contributed equally to this work.

[++] co-first authors.

Supporting information and the ORCID identification number(s) for the author(s) of this article can be found under:
https://doi.org/10.1002/anie.202012851.

Scheme 1. Fullerenes C$_{20}$ and C$_{60}$ and pip (C$_5$H$_{11}$N).

cage structure, buckyball, greatly affects their aromaticity by distortion of the π-conjugation from planarity leading to a decrease of p-orbitals involved in the π-bonds and an increase of s-orbital contribution in sp^2 carbon atoms, respectively.[7] In particular, the energy of the lowest unoccupied orbitals (LUMO) decreases and, at the same time, the electron affinity of FLs increases. Determination of the electron affinity (EA) of C$_{60}$ has been the subject of several experimental investigations[8] and has been approached by means of computational studies based on the DFT methods.[9] The EA value has been estimated as 2.684 eV.[8]

The unusual electronic properties of FLs open the door to designing new materials via FL's functionalization. However, what goes hand in hand with these excellent opportunities is a well-known problem of their solubility,[10] which shows very unusual behavior.[11] Frequently observed aggregation of FLs,[12] originating from the positive values of their EA, discussed above,[9] is one of the key drawbacks restricting the application potential of FL.

The behavior of C$_{60}$ upon solvation, showing an increased solubility in aromatic compared to polar liquids, has been the subject of several experimental studies.[11, 13–17] To explain these experimental observations, several theoretical and computational studies have been reported,[18–30] aiming to resolve the origin of solute-solvent interactions and to find the most relevant parameters to correlate the solvent properties and their efficiency to dissolve FLs.[18–22] Despite the strong basic character of piperidine (pip, pK_a = 11.12), which makes it an efficient electron donor, the explanation of the solubility based purely on the charge transfer is somewhat questionable, considering the low solubility of C$_{60}$ in oxygen-containing solvents, alcohols, phenols and ketones.[20,22]

C$_{60}$ is well known to form adducts[23–25] with primary and secondary amines, including pip. The reaction proceeds in the presence of oxygen under both, light and dark conditions, on a time-scale of days and with the yields of about 50%. The addition starts with an electron transfer C$_{60}$ followed by

radical recombination and the zwitterion formation, which stabilizes either by proton transfer to C_{60}, forming C−H bond, or by oxidation and consequent deprotonation and radical recombination.

We have examined the character of the interactions in the complexes of pip with C_{20} (1:1), C_{60} (1:n) and its fragment $C_{30}H_{20}$ (1:1), all containing five-member rings, as well as in the graphene, modelled with circumcoronene, and graphene nanotubes, modelled with $C_{54}H_{18}$ and $C_{228}H_{38}$, respectively, although solely containing six-member rings. The calculations were performed by the dispersion-corrected-DFT method, employing the PBE0-D3[26] functional, whose reliability was verified on the basis of the comparison with the results obtained from pip···pip (pip$_2$) and C_{20}···pip complexes by the method of high-accuracy CCSD(T). The interactions are described in terms of both interaction and binding free energies at 298 K. To provide a more realistic picture of the solvation, molecular dynamics simulations were performed on C_{60} in pip droplet containing up to 21 molecules of the solvent at 298 K. The experimental results obtained by means of FTIR and (H,C)-NMR spectroscopies fully support the predicted character of the C_{60}···pip interaction.

Our results demonstrate the formation of the dative bond between the electron donor (secondary amine pip) and the electron acceptor (FL), qualitatively different from the addition of secondary amines to FLs under light and in the presence of oxygen, which occurs through oxidation of the previously formed ion pair between FLs and secondary amines.[25,27,28] A dative bond represents a type of covalent bond, hence the name covalent/dative bond, in which one fragment donates two electrons to the bond, unlike the electron sharing bond formed from the interactions of one unpaired electron of both fragments.[29,30]

We clearly proved that the changes in the aromaticity of non-planar carbon allotropes, previously explained by a smaller overlap of p-orbitals, differ for systems that contain five-member rings with respect to those constructed purely from six-member rings.[31]

Results and Discussion

Interaction Energies

The character of interactions between the solvent molecules is investigated using pip dimer, the H-bonded complex with the N−H···N H-bond length of 2.16 Å (in Figure 1). The size of the system also allows employing the benchmarking DFT method to model the C_{60} solvation. The interaction energies of pip$_2$ dimer calculated using PBE0-D3/def2-TZVPP, MP2 and CCSD(T) methods are given in Table 1. The negligible difference between ΔE and ΔE^{INTR} indicates only marginal structure changes upon complexations. The DFT method provides slightly larger stabilization energies, and its comparison with the benchmark CCSD(T) calculations makes room for discussion, also based on the MP2 calculations. When the triple-zeta basis sets are used, the DFT
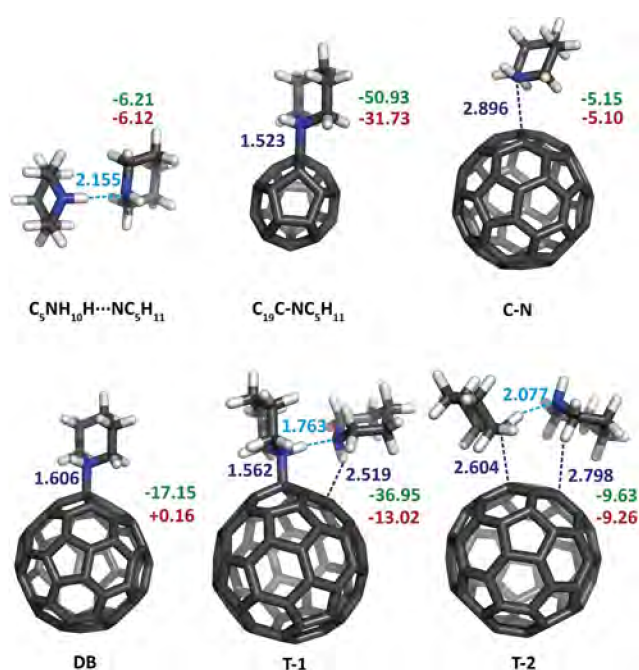

Figure 1. PBE0-D3/def2-TZVPP optimized geometry of pip$_2$, C_{20} with pip, C_{60} with pip, and C_{60} and pip$_2$ with selected bond lengths between fullerene and pip in Å (dark blue), hydrogen bond lengths between pips (light blue) in Å, and ΔE^{INTR} (green), and ΔE (red) in kcal mol^{-1}.

Table 1: Intrinsic interaction energies (ΔE^{INTR}, in kcal mol^{-1}) of pip$_2$ and C_{20}···pip complexes.

Method	CCSD(T)[a]		MP2				DFT[b]
N	D	T	D	T	Q	5	
pip$_2$	−3.8	−4.7	−3.8	−5.0	−5.4	−5.6	−6.2 (−6.1)[c]
C_{20}···pip	−30.2	−43.2	−29.3	−37.0	−40.1	−41.3	−50.9 (−31.7)[c]

[a] cc-pVnZ basis set. [b] def2-TZVPP. [c] Total interaction energy (ΔE) is given in parentheses.

overestimates the interaction energies by 1.5 and 1.2 kcal mol^{-1}, in comparison with CCSD(T) and MP2 methods, respectively. The more flexible cc-pV5Z basis set gives the energy difference of 0.6 kcal mol^{-1}, thus the DFT interaction energies are overestimated by about 10%. As the DFT method is known to be less basis-set-dependent, compared to the discussed wave-function methods, the error in DFT-calculated binding energies is not expected to significantly exceed the observed 10%, with respect to the CCSD(T) results extrapolated to the complete basis set (CBS) limit. The fair agreement between the MP2 and CCSD(T) stabilization energies which makes the former method suitable for benchmarking of C_{60} systems stabilization energies where the CCSD(T) calculations are not computationally feasible.

The optimized structure and properties of C_{20}···pip complex are displayed in Figure 1 and Table 1. The N−C distance in the complex is 1.523 Å, only slightly larger than the typical values of covalent C−N bonds (the optimized C−N bonds in pip are 1.453 Å). Notably, the similar type of interaction as described in the current paper has been already reported for the complex between C_{20} and N_2H_2.[32] Importantly, ΔE^{INTR}

calculated at the PBE0-D3/def2-TZVPP level is 50.9 kcal mol^{-1}, almost identical to ΔE^{INTR} value of 49.9 kcal mol^{-1} obtained for the N→B dative bond in ammonia borane (H$_3$NBH$_3$) addressed as the prototype dative complex. In conclusion, the short intermolecular distance and large stabilization energy indicate the formation of a new chemical entity with the dative bond between N (pip) and C (C$_{20}$). Several types of dative bonds have been reported previously.[29,33–41]

The difference between the ΔE and ΔE^{INTR} values of about 19 kcal mol^{-1} shows a significant structure deformation upon complexation. Assuming changes in the MP2 interaction energies with the increasing basis set, the PBE0-D3/def2-TZVPP approach is expected to provide results of the binding energies with an error of about 10%, compared to extrapolated reference CCSD(T) levels. Our results obtained with PBE0-D3 functional are in good agreement with those calculated for C$_{20}$⋯N$_2$H$_2$, that is, complex with two C−N bonds, employing M06-2X functional and 6-311G(d,p) basis set, which gives the interaction energy of −57.8 kcal mol^{-1} and the bond length of 1.472 Å.[32]

The optimization of C$_{60}$⋯pip provides a more complex picture with a large variety of local minima, including non-covalent complexes and the complex with the N→C dative bond. Their structures, characterized by C⋯N intermolecular distances and intrinsic and total interaction energies obtained by the PBE0-D3/def2-TZVPP approach are given in Figure 1 (Supporting Information, Figure S1) and Table 2. In the former complex type pip is attached to C$_{60}$ via non-covalent NH⋯C and CH⋯C hydrogen bonds (NH-C and CH-C structures, respectively), the C⋯N tetrel bond[42] (C–N structure) with bond lengths of 2.6–2.9 Å and the lone-pair (N)⋯π noncovalent interaction to five-(LP-R5) or six-membered (LP-R6) structures with bond lengths of about 3.1 Å. Their ΔE^{INTR} and ΔE values are within 1.1 kcal mol^{-1} (Table 2).

Figure 1 displays two optimized complexes, labeled C-N and DB, with similar mutual orientations of C$_{60}$ and pip, leading to different orientations of the N (pip) lone pair, with respect to the C$_{60}$ buckyball structure, significant differences in intermolecular C⋯N distances (cf. 2.896 Å and 1.606 Å for C-N and DB, respectively) and ΔE^{INTR} values (see Table 2) of −5.2 and −17.2 kcal mol^{-1}, respectively. By comparison, the interaction energies for the stacked configurations of the complex C$_{60}$⋯benzene are in the range of −5.49 to −4.13 kcal mol^{-1}.[19]

The values of the interaction energies in DB deserve a detailed discussion, based also on the comparison with non-covalent complexes and C$_{20}$⋯pip. In particular, the negative value of the intrinsic interaction energy ($\Delta E^{\mathrm{INTR}} = -17.2$ kcal mol^{-1}) is compensated by an almost identical value of the

deformation energy, leading to slightly repulsive interactions of +0.2 kcal mol^{-1}. The large deformation energy (cf Table S3) is explained by a distortion of C$_{60}$ in DB, compared to the regular buckyball structure of the other non-covalent C$_{60}$⋯pip complexes (see Figure 1), with negligible deformation energies not larger than 0.05 kcal mol^{-1} (Table 2).

The existence of the N→C dative bond in the C$_{60}$-pip system was also verified using MP2 (see Table 2). The interaction energy in DB with the N→C dative bond is slightly larger at the DFT level, in agreement with the previous observation on the C$_{20}$⋯pip. The MP2 method, however, predicts ΔE^{INTR} in non-covalent complexes to increase by about 2 kcal mol^{-1}, which is consistent with the well-known overestimation of the dispersion energy at the MP2 level.

Although the N→C dative bond was predicted in C$_{60}$⋯pip complex, the large deformation energy casts doubt on its existence. However, the above-discussed stability is based on the gas-phase calculations, and only one pip molecule is considered. The description of C$_{60}$⋯pip interactions in pip solvent requires calculations of models with more solvent molecules and will proceed in two directions: analyses of the C$_{60}$ complex with pip$_2$ and with pip droplet containing up to 21 pip molecules.

The complexes of C$_{60}$ with pip$_2$ investigated in this study include binding via a dative bond (T-1, Figure 1) and non-covalent N⋯C bonds (T-2, Figure 1). Both, total and intrinsic interaction energies (see also Table 3) are calculated with respect to pip$_2$, in which pip molecules are labeled as *inner* and *outer* pip.

In the case of the T-1 complex, pip subunits bound to C$_{60}$ via the N→C dative bond (*inner* pip), with the bond length of 1.562 Å (cf. 1.606 Å in DB), and the NH⋯C hydrogen bond (*outer* pip), with the bond length of 2.519 Å Figure 1 (cf. 2.557 Å in NH-C; Supporting Information, Figure S1). It should be noted that the H-bond between the pip subunits in C$_{60}$⋯pip$_2$ significantly shortens (by 0.39 Å), compared to the H-bond in pip$_2$. The intrinsic interaction energy is analyzed in terms of partial energies of the *inner* and *outer* pip subunits in Table 3. Binding of the former is increased by about 3 kcal mol^{-1} and decreased by 1 kcal mol^{-1} in the case of the *outer* pip, respectively. The difference between their sum and the value of the total intrinsic interaction energy (13 kcal mol^{-1}, cf. the ΣE_{part} and ΔE^{INTR} values in Table 3) demonstrates the significant cooperative effect on the binding of the two pip subunits. Despite the large value of the deformation energy of 24 kcal mol^{-1}, the whole complex is stable with the

Table 2: The intrinsic interaction energies (ΔE^{INTR}, in kcal mol^{-1}) and total interaction energies (ΔE, in kcal mol^{-1}) of C$_{60}$⋯pip complexes.

	C-N	LP-R6	LP-R5	NH-C	CH-C	DB
ΔE^{INTR} (MP2)	−7.1	−6.9	−7.2	−6.3	−6.8	−14.0
ΔE^{INTR} (DFT)	−5.2	−5.0	−5.0	−4.5	−4.1	−17.2
ΔE (DFT)	−5.1	−5.0	−5.0	−4.5	−4.1	+0.2

Table 3: Total and partial intrinsic interaction energies (ΔE^{INTR}, kcal mol^{-1}) for C$_{60}$⋯pip$_2$ complex.

System	E_{part}		ΣE_{part}	ΔE^{INTR}
	ΔE^{INTR} (*inner* pip)[a]	ΔE^{INTR} (*outer* pip)[b]		
T-1	−20.36	−3.67	−24.03	−36.95 (−13.02)[c]
T-2	−4.48	−3.89	−8.76	−9.63 (−9.26)[c]

[a] calculated as the difference between ΔE^{INTR} energy of C$_{60}$⋯pip$_2$ and ΔE^{INTR} of C$_{60}$⋯*outer* pip. [b] Calculated as the difference between ΔE^{INTR} energy of C$_{60}$⋯pip$_2$ and ΔE^{INTR} of C$_{60}$⋯*inner* pip. [c] The total interaction energies (ΔE in kcal mol^{-1}) are given in parentheses.

total interaction energy of -13 kcal mol^{-1}, unlike the slightly unstable DB 1:1 complex. The larger stability of the T-1 can be explained by a charge transfer cascade in the sequence *outer* pip → *inner* pip → C_{60}, which results in a larger charge separation, compared to DB. Consequently, the electron density at N involved in the N→C dative bond increases and the bond strengthens. The increased charge transfer is reflected in the changes in the NBO populations (Supporting Information, Table S4) of the σ*(N-H) antibonding orbital, calculated as 0.017 in an isolated pip molecule, 0.030 in H-bonded pip dimer, 0.026 in DB and 0.101 in T-1, respectively. The difference between the populations of the two former corresponds with the formation of the N(lone pair)···σ*(N-H) H-bonded pip$_2$ complex ($\Delta E^{INTR} = -6.20$ kcal mol^{-1}, Table 1). The large population of the corresponding σ*(N-H) in T-1 evidences a significant charge transfer to C_{60} accompanying the formation of the strong the N→C dative bond ($\Delta E^{INTR} = -20.36$ kcal mol^{-1}, Table 3).

In T-2, the *inner* pip interacts with C_{60} via the C···N tetrel bond (relevant to C-N structure) and the *outer* pip bounds via the C-H···C (C_{60}) H-bond. The N-H···N H-bond within the pip$_2$ subunit shortens by about 0.08 Å, compared to the pip$_2$ dimer. The strength of the C_{60}···*inner* pip interactions is comparable (within the range of 0.6 kcal mol^{-1}) to the corresponding C···N interaction in the C-N complex (Figure 1), although the bond distance is significantly, by 0.29 Å, smaller in C-N. Unlike for T-1, comparable values of ΣE_{part} and ΔE^{INTR} indicate almost additive contributions of *inner* and *outer* pip subsystems to the overall stabilities of T-2; the cooperative effects do not account for more than 10% of the total ΔE^{INTR}. Further, the deformation energy is significantly smaller.

The above-discussed results on T-structures show important differences in the potential energy surface (PES) characters of C_{60}···pip$_2$ and C_{60}···pip. In particular, the slightly unstable DB complex stabilizes upon the extension with an additional H-bonded pip in T-1, which, in contrast to DB, becomes more stable than the non-covalent T-2, and corresponds to the global minimum on the C_{60}-pip$_2$ PES. These changes indicate enhanced electron-acceptor properties of C_{60} in the presence of other pip molecules, along with a preferential formation of dative bond when C_{60} dissolves in pip. The hydrogen bond enhanced strength of the dative bond can be thus regarded as a subclass of noncovalent cooperativity.[43,44] The existence of several minima of C_{60} complexes, such as those found in C_{60}···pip on PES along

single-coordinate (C···N), has been reported previously on other complexes of C_{60}.[45]

The calculations on the carbon allotropes with six-membered rings only do not confirm the existence of dative/covalent bond. In this case, only the non-covalent complexes are formed (see discussion on FTIR spectra, Supporting Information).

C_{60}···pip$_{21}$. The solubility of C_{60} in pip (modelled with 21 pip molecules) was investigated using the PBE0-D3/6-31G* approach. The performance of the less flexible basis set was verified by comparing the interaction energies in smaller complexes with C_{20} and C_{60} (Supporting Information, Table S5). Figure 2a displays the optimized structure of C_{60}···pip$_{21}$ and the intrinsic interaction energy showing one pip interacting via the N→C dative bond and the remaining pip molecules via non-covalent interactions. The intrinsic interaction energies of C_{60}···pip$_{20}$ with one molecule of pip$_2$ (cf T-1 complex) being removed, interacting either non-covalently (Figure 2c) or via the dative bond (Figure 2b), are shown to illustrate their mutual effects on the complex stability. The sum of the intrinsic interaction energies of the former complex (Figure 2c) and dative C_{60}···pip complex (Figure 2d) is -116.3 kcal mol^{-1}, which is by 26 kcal mol^{-1} less than the interaction energy calculated for the full C_{60}···pip$_{21}$ complex (-142.4 kcal mol^{-1}), demonstrating a significant synergy effect of the non-covalent interaction and the N→C dative bond. In particular, the formation of the dative bond increases the electron density of C_{60}, leading to stronger N−H···C and C−H···C hydrogen bonds. Similarly, the sum of the intrinsic interaction energy in Figure 2b (-123.4 kcal mol^{-1}) and energies of two missing H-bonds (ca. 12 kcal mol^{-1}) is lower than ΔE^{INTR} of the C_{60}···pip$_{21}$ (Figure 2a) by about 7 kcal mol^{-1}. This difference can be related to the above-discussed enhancement of the interaction strength of the dative bond in the hydrogen bonded pip$_2$.

More details on the dissolution mechanism were obtained with calculations displayed in Figure 3. Different initial structures with one, two and three pip molecules attached with N→C dative bond to C_{60} and the H-bond to the neighboring pip molecule, respectively, were optimized using the PBE/6-31G* approach (for justification of the PBE-D3 approach see the results of thermodynamics terms in the Supporting Information, Table S5). The calculations show that the most stable arrangement is with two N→C dative bonds, followed by the complex with one and three N→C dative bonds, less stable by 11.2 and 22.1 kcal mol^{-1}, respectively. It should be noted that the last structure resulted from

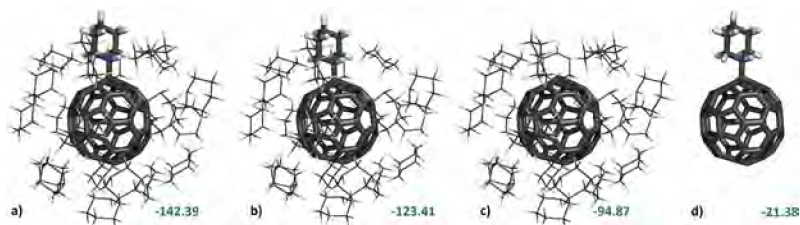**Figure 2.** PBE0-D3/6-31G(d) interaction energies of the complexes C_{60}···$(C_5H_{11}N)_{21}$ (a), C_{60}···$(C_5H_{11}N)_{20}$ (b) with dative bond, C_{60}···$(C_5H_{11}N)_{20}$ (c) without dative bond and C_{60}···$C_5H_{11}N$ (d). The geometries of C_{60}···$(C_5H_{11}N)_{20}$ and C_{60}···$C_5H_{11}N$ are extracted from the PBE0-D3/6-31G(d) optimized geometries of C_{60}···$(C_5H_{11}N)_{21}$.
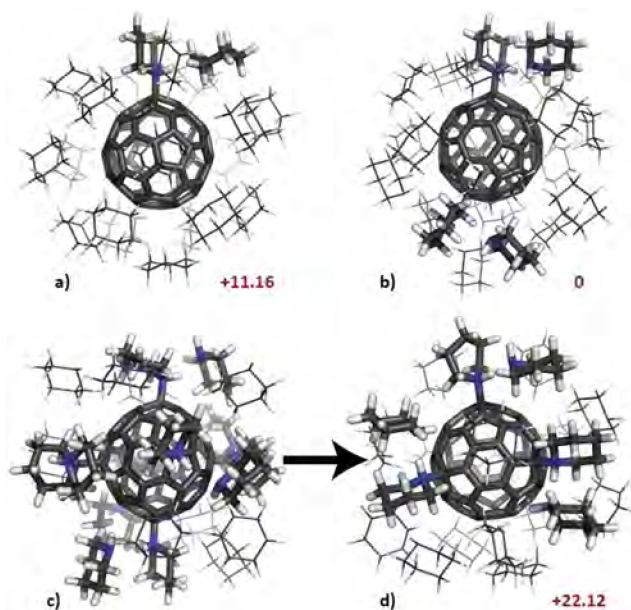
Figure 3. PBE-D3/6-31G* optimized geometry of $C_{60}\cdots pip_{21}$ complex. Structure a) contains one dative bond, structure b) two and structure d) three dative bonds. Optimization of starting structure c) having six dative bonds led to structure d) with three dative bonds. Numbers in red correspond to relative energies in kcal mol^{-1}.

the optimization of the complex with six dative bonds (see Figures 3c,d), which corresponds to the previously stated expectation of the limited ability of C_{60} to form dative bonds with pip.

The free energy calculations (see the Supporting Information for details) support the thermodynamic stability of the of $C_{60}\cdots pip_2$ also at temperature 298 K.

The dative bond was confirmed also using MD simulations of $C_{60}\cdots(pip)_{21}$ performed at 300 K for 0.1 ns. Results are shown in the Supporting Information, section 2.

FTIR Spectra

The FTIR spectra of C_{60} and its mixture with pip before and after the evaporation of some excess amount of unbound pip molecules (labeled C_{60}-P1 and C_{60}-P2, respectively) are shown in Figure 4. The spectrum of the pip alone shows the collective band at 1000–1200 cm^{-1} due to the C−N bond and skeletal -C-N-C stretches[46,47] (Figure 4a), which is in good agreement with the calculated value of 1242 cm^{-1} (intensity 17 km mol^{-1}). The bands of the C-N stretch of pip also dominate the spectrum obtained after the mixing and grinding of pip with C_{60} (Figure 4a, spectrum C_{60}-P1). After evaporation of excess pip, new bands at 872 cm^{-1} and 988 cm^{-1} appear in the spectrum (Figure 4a, spectrum C_{60}-P2), assigned in calculations (Supporting Information, Table S2c and Figure S4) to symmetric (866 cm^{-1}, 383 km mol^{-1}) and asymmetric (994 cm^{-1}, 46 km mol^{-1}) stretches of dative N→C bond in C_{60}-pip$_2$ complex.

The spectra in the frequency region higher than 3000 cm^{-1} reflect the changes of N-H stretching vibrations of pip. The calculated N-H stretching frequency of the pip (Supporting Information, Table S2a) is 3514 cm^{-1} with a negligible intensity of 1 km mol^{-1}. Upon the pip$_2$ and pip$_3$ formation, these bonds are either involved in hydrogen bonding (NH-bond) or remain non-bonded (NH-free). The corresponding band of the former is red-shifted to 3401 cm^{-1}, with intensity of 275 km mol^{-1}, in the case of a single H-bond pip$_2$ and to 3306 and 3340 cm^{-1} (intensities of 434 and 461 km mol^{-1}) owing to a combined more curved later structure bands of the two hydrogen bonds in pip$_3$ (Supporting Information, Table S2). Both, the red-shift and the increased intensity manifest the well-known effect of the hydrogen bond formation. The frequencies and intensities of the NH-free bonds do not change. Based on these calculations, the band at 3280 cm^{-1} visible in the spectra of pip and C_{60}-P1 (Figure 4b) can be assigned to the N-H stretch of the NH-bonds in the pip solvent. In the C_{60}-P2 spectrum, the intensity of the band at 3280 cm^{-1} decreases and, at the same time, a new band at 3444 cm^{-1} appears (Figure 4b). The calculations predict a strongly shifted (by 300 cm^{-1}) and high-intensity peak (2705 cm^{-1}, 1534 km mol^{-1}) in the $C_{60}\cdots pip_2$ complex for the NH-bond, which is, however, hidden within the C−H vibra-
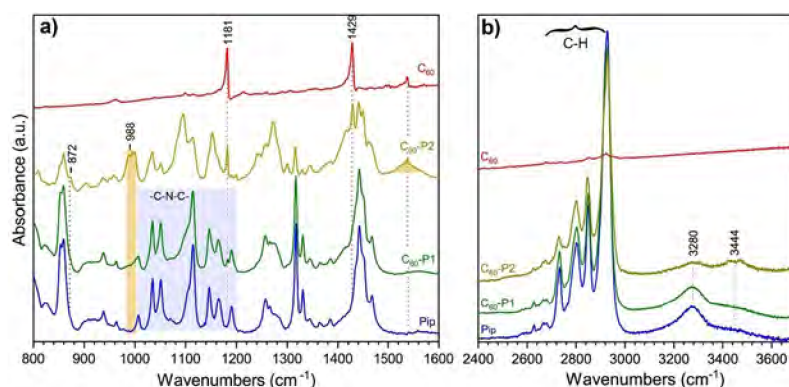

Figure 4. FTIR spectra of C_{60} and its complex with pip (Pip) before evaporation (C_{60}-P1) and after evaporation of some excess amount of unbound pip (C_{60}-P2) at two spectral windows for the observation of (a) the C-N stretching and N-H bending vibrations, and (b) the N-H stretching vibrations.

tional stretching bands (see Figure 4b). Inspection of the calculated vibrational frequencies and intensities of the NH-free bonds in pip, $C_{60}\cdots$pip and $C_{60}\cdots$pip$_2$ reveal both a red-shift and an intensity increase. Based on this and the geometry parameters obtained from the T-1 optimization (the distance between H (*outer pip*) and C(C_{60}) is 2.5 Å, Figure 1), the discussed band at 3444 cm^{-1} in C_{60}-P2 can be linked to the N-H stretch of the outer pip interacting with C_{60} via van der Waals interactions. It should be noted that the C-H vibrations of the pip observed in the frequency region of 2700–3000 cm^{-1} are retained without changes (Figure 4b).

The changes observed in the spectral region of 1500–1600 cm^{-1}, relevant to the N-H bending modes, provide additional information about the character of C_{60} interaction with pip. The characterization of the peaks due to the NH-free bending in pip$_2$ and pip$_3$ is similar to that of pip monomer, that is, the frequency of ≈ 1520 cm^{-1} and a low intensity of about 7 km mol^{-1} (Supporting Information, Table S2b). The formation of hydrogen bonds within the pip cluster (pip$_2$, pip$_3$) results in the blue-shift of the bands by about 70 cm^{-1}, keeping a negligible intensity (Supporting Information, Table S2). In the case of the interaction with C_{60}, the blue-shift is smaller (ca. 40 cm^{-1}) but the intensity is increased to 43 km mol^{-1} (Supporting Information, Table S2). These calculations provide the bases for the interpretations of the band at 1540 cm^{-1}, observed solely in the C_{60}-P2 spectrum, to the bending mode of the NH-bond of the *inner* pip in which the N atom interacts with the electron acceptor (from formation of a dative bond or non-covalent interactions (see below)). Therefore, this new band excludes the possibility of the complexation via the addition of secondary amines to FL, accompanied by oxidation,[25,27,28] since the corresponding hydrogen atom is released upon this reaction.

The FTIR spectra of the mixture of pip with graphene (Gr) and single wall nanotubes (NT) are illustrated in the Supporting Information, Figures S5 and S6, respectively, in the same spectral regions as discussed for the complex with C_{60}. The bands of the starting graphene material at 1272 and 1575 cm^{-1} (Supporting Information, Figure S5a, Gr) are attributed to two different vibrational modes of conjugated aromatic rings in the graphene sheet with defects. Concerning the spectral signs linked to the complex formation between C_{60} and pip: 1) the band at about 3500 cm^{-1} (assigned to 3444 cm^{-1} in C_{60}-P2, see above for its interpretation), and 2) the band at about 1550 cm^{-1} (assigned to 1540 cm^{-1} in C_{60}-P2, see above for its interpretation) become prominent in the spectra of the mixture of pip with Gr or NT. This observation is confirmed by computational modelling of the interactions of pip$_2$ with circumcoronene, representing Gr surface, and a NT fragment (Supporting Information, Figure S6). In both cases, the optimization results in a structural arrangement similar to that of T-2.

Importantly, the bands at 872 and 998 cm^{-1}, due to the stretching modes of the N→C dative bond, are missing in both spectra, demonstrating the inefficiency of these allotropes to form a dative bond with pip.

NMR Spectroscopy

Figure 5 displays the ^{1}H-NMR and ^{13}C-NMR spectra of pure C_{60}, pure pip, and their mixtures in deuterated 1,2-dichlorobenzene. In the aliphatic (pip) region of the proton NMR spectrum of the C_{60}-pip mixture, the broad signal at about 3.4 ppm and narrow signal at about 1.9 ppm correspond to hydrogens in alpha- (H2) and beta-(H3) positions with respect to nitrogen, respectively. The signal due to hydrogens in gamma- position (H4) in the complex is overlapped by the very intense peak of free pip. Its chemical shift can be obtained from two-dimensional proton-carbon correlation experiment (Supporting Information, Figures S8–S14). The lack of the signal due to the NH proton can result either from its overlap with other signals and/or its severe broadening. The chemical shifts of the C−H hydrogens are higher in complexes than in free pip, with the differences 0.53 ppm (H2), 0.29 ppm (H3) and 0.07 ppm (H4), respectively, indicating their smaller shielding in the complex and thus a decrease of electron density upon complexation. The largest
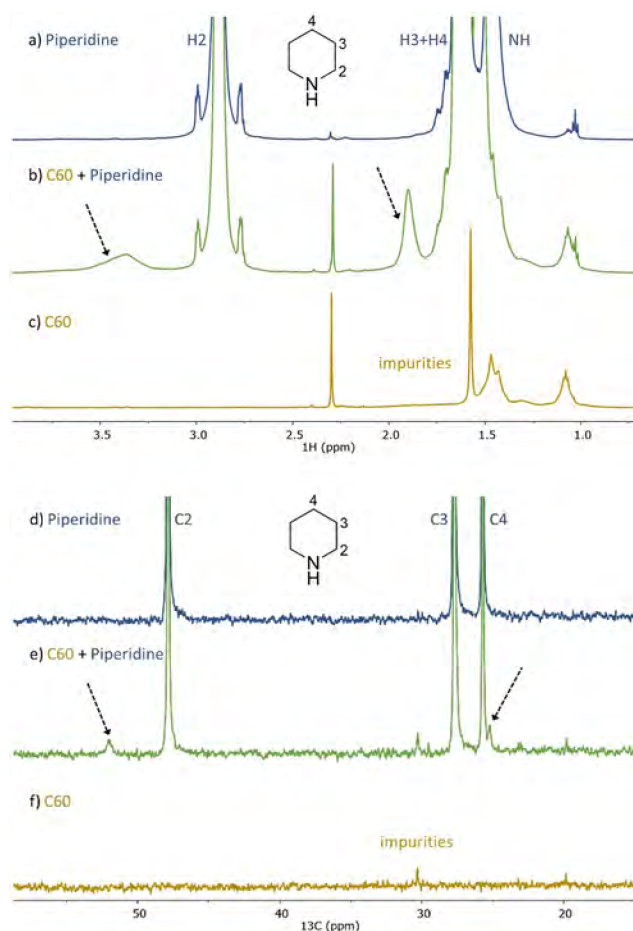

Figure 5. Part of ^{1}H NMR (top) and ^{13}C (bottom) spectra of 1,2-dichlorobenzene-d_4 (550 μL) solutions of a,d) pip (20 μL), b,e) mixture of C_{60} (14.7 mg) and pip (20 μL) and c,f) C_{60} (14.7 mg). The black dashed arrows highlight the signals of the C_{60}-pip complex. Full spectra (including the aromatic region) and spectra with variable amounts of pip are shown in the Supporting Information.

difference in chemical shift observed for H2 indicates a direct involvement of pip N-atom in the complex formation.

Similar to H-NMR spectra, two new signals appear in the aliphatic part of C-NMR spectra of pip and C_{60} mixture, demonstrating the complex formation. Comparison of the differences of chemical shifts of pip C-atoms shows the most pronounced shift for C2 (4.1 ppm), in agreement with corresponding differences observed in H-NMR spectra. The signal corresponding to C3 in the complex is overlapped by that of free pip. Furthermore, new signals appear also in the C_{60} region at 140–150 ppm (Supporting Information, Figure S10). Importantly, no signals are observed in the region of 70–80 ppm, characteristic for addition (that is, covalent bond formation) of secondary amines to C_{60}.[25]

The spectral characterization, that is, the shape and intensity of signals, provides further characterization of the complex behavior. The broader signals due to H2 in the C_{60}-pip complex as compared to free pip can be explained by multiple complex formation (multiple complex structures) and their dynamic behavior, that is, $C_{60}\cdots(pip)_n \leftrightarrow C_{60}\cdots(pip)_{n-1} + pip$ equilibria. The multiple signals observed in the spectra obtained with variable pip concentration (Supporting Information, Figure S10) confirm the presence of multiple complex structures, that is, complexes with one or more pip molecules. The dynamic behavior of the C_{60}-pip complex can be deduced from variable temperature NMR experiments (Supporting Information, Figure S14). Narrowing of the broad signal and intensity decrease observed at elevated temperatures indicate that the signals correspond to metastable species which satisfy the above equilibrium between the complex and its components.

The intensity of the signals of the C_{60}-pip complex are significantly lower than those of the free components. Considering C_{60} and pip concentrations, the integration of the signals in proton NMR spectra can be used to determine the complex concentration and to estimate the complexation free energy. The estimated value of ΔG value at 25 °C is -0.1 kcal mol^{-1}, which is in excellent agreement with the calculated value for $C_{60}\cdots pip_2$ (Supporting Information, Table S5).

Preconditions for the Formation of a N→C Dative Bond: Structural Aspects

Unusual reactivity of carbon allotropes is related to their different structural and electronic properties. Our results concerning the formation of the N→C dative bond between pip and C_{20} or C_{60}, constructed either exclusively from the five-member rings or from both five- and six-membered rings, confirm this explanation. The observed character of the binding of pip to carbon nanotubes, which contain solely six-member rings, raises the question whether the out-of-planarity deviation is the only prerequisite to alter the aromaticity. More detailed analyses of the curvature effect were made by calculations performed on carbon allotropes with six-member rings modelling nanotubes with different diameters, 7 and 15 Å (Supporting Information, Figure S7), which corresponded to those of C_{60} and experimentally used

NT, respectively. The data displayed in the Supporting Information show an absence of dative complexes with pip and confirm our experimental and computational observations of the structural requirement, that is, the presence of five-member rings to form such complexes.

To provide an explanation for the different behavior of allotropes with and without five-member rings, the calculations were performed for the $C_{30}H_{20}\cdots pip_2$ complex, in which the $C_{30}H_{20}$ fragment represents the half of the C_{60} buckyball (Figure 6a). The $C_{30}H_{20}$ is the largest C_{60}-fragment, which can possibly vary the degree of cage curvature in its equilibrium structure. Both, full and partial optimizations of the complex were performed. The full optimization of the complex resulted in a non-covalent complex (Figure 6b, C_{30}(opt)) characterized by a small ΔE^{INTR} value of -7.56 kcal mol^{-1} (Table 4) and relatively large C-N distance of 3.28 Å. During the optimization procedure, the $C_{30}H_{20}$ fragment slightly opens and the curvature of the bowl becomes smaller. In the partial optimization, the $C_{30}H_{20}$ structure was cut from T-1 and kept frozen (Figure 6c). The resulting ΔE^{INTR} of -18.78 kcal mol^{-1} (Table 4) and C−N bond distances of 1.58 Å indicate formation of the complex (labeled as $C_{30}(C_{60})$) with one N→C dative bond. The EA values of isolated C_{30}(opt) and $C_{30}(C_{60})$ fragments (Table 4) significantly differ with the more positive EA value for the more curved later structure. These values correlate well with aromaticity parameters derived from the harmonic oscillator model of aromaticity (HOMA).[48] Using this approximation, the HOMA index fits into the interval HOMA = 0 for the Kekule structure of benzene and HOMA = 1 for aromatic benzene. The values of 0.89 and 0.93 for the 5- and 6-member ring of C_{30}(opt) show its more aromatic character compared to $C_{30}(C_{60})$ with the values of 0.69 and 0.85, respectively. Importantly, the drop of the aromaticity index is significantly larger in the case of the five-member ring (by 0.2) between C_{30}(opt) and $C_{30}(C_{60})$ compared to the lowering by 0.08 for the six-member ring. This result indicates more pronounced structure effects on the aromaticity in the former and provides
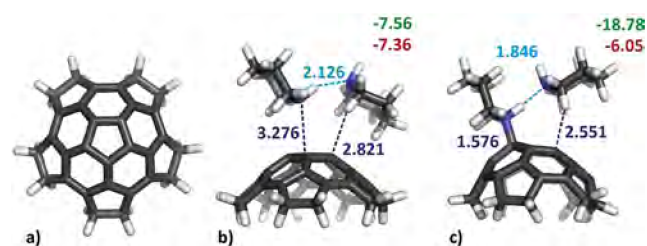

Figure 6. PBE0-D3/def2-TZVPP optimized geometries of $C_{30}H_{20}$ with selected hydrogen bond lengths between pips (light blue) in Å, and ΔE^{INTR} (green) and ΔE (red) in kcal mol^{-1}.

Table 4: The interaction energies (ΔE^{INTR}, kcal mol^{-1}), electron affinity (EA, in eV) and HOMA values of $C_{30}H_{20}\cdots pip_2$ complexes.

Structures	ΔE^{INTR}	EA	HOMA	
			5-membered ring	6-membered ring
C_{30}(opt)	-7.56	$+0.21$	0.887	0.926
$C_{30}(C_{60})$	-18.78	$+0.45$	0.693	0.846

explanation for surprisingly different reactivity of non-planar carbon allotropes, carbon nanotubes, constructed from six-member rings only.

Conclusion

The results of computational modelling and experimental IR and NMR studies of the complexes of a secondary amine, pip, and various carbon allotropes have been performed to provide insight into the unusual behavior of FLs with respect to other carbon allotropes. It has been shown that the positive electron affinity resulting from non-planarity of carbon framework is responsible for the formation of the covalent/dative bond between pip and FL, in particular C_{60}. Analyses of the aromaticity of carbon allotropes revealed that not only their non-planarity but also the structural motives present in the carbon framework determine the character of the electron affinity, along with their ability to form the covalent/dative bond. This observation is demonstrated on a different bonding character of pip to C_{20} and C_{60} FLs, containing five-member rings, compared to that of pip to single wall carbon nanotubes that were constructed solely from six-member rings. The present observations provide information about the reactivity-structure relations of carbon allotropes potentially useful for their simple and selective covalent functionalization applicable to a broad portfolio of nanotechnologies.

Acknowledgements

Conflict of interest

The authors declare no conflict of interest.

Keywords: covalent functionalization · fullerenes · hydrogen bonds · N→C dative bonds · piperidine

[1] E. De Gianni, E. Turrini, A. Milelli, F. Maffei, M. Carini, A. Minarini, V. Tumiatti, T. Da Ros, M. Prato, C. Fimognari, *Toxins* **2015**, *7*, 535–552.

[2] C. M. Sayes, A. M. Gobin, K. D. Ausman, J. Mendez, J. L. West, V. L. Colvin, *Biomaterials* **2005**, *26*, 7587–7595.

[3] N. Gharbi, M. Pressac, M. Hadchouel, H. Szwarc, S. R. Wilson, F. Moussa, *Nano Lett.* **2005**, *5*, 2578–2585.

[4] K. A. Mazzio, C. K. Luscombe, *Chem. Soc. Rev.* **2015**, *44*, 78–90.

[5] W. Cao, J. Xue, *Energy Environ. Sci.* **2014**, *7*, 2123–2144.

[6] S. Günes, H. Neugebauer, N. S. Sariciftci, *Chem. Rev.* **2007**, *107*, 1324–1338.

[7] M. Saito, H. Shinokubo, H. Sakurai, *Mater. Chem. Front.* **2018**, *2*, 635–661.

[8] D. L. Huang, P. D. Dau, H. T. Liu, L. S. Wang, *J. Chem. Phys.* **2014**, *140*, 224315.

[9] J. Luo, L. M. Peng, Z. Q. Xue, J. L. Wu, *J. Chem. Phys.* **2004**, *120*, 7998–8001.

[10] N. O. Mchedlov-Petrossyan, *Theor. Exp. Chem.* **2020**, *55*, 361–391.

[11] R. S. Ruoff, R. Malhotra, D. L. Huestis, D. S. Tse, D. C. Lorents, *Nature* **1993**, *362*, 140–141.

[12] N. O. McHedlov-Petrossyan, *J. Mol. Liq.* **2011**, *161*, 1–12.

[13] N. O. McHedlov-Petrossyan, *Chem. Rev.* **2013**, *113*, 5149–5193.

[14] R. S. Ruoff, D. S. Tse, R. Malhotra, D. C. Lorents, *J. Phys. Chem.* **1993**, *97*, 3379–3383.

[15] M. V. Korobov, A. L. Mirakyan, N. V. Avramenko, G. Olofsson, A. L. Smith, R. S. Ruoff, *J. Phys. Chem. B* **1999**, *103*, 1339–1346.

[16] K. N. Semenov, N. A. Charykov, V. A. Keskinov, A. K. Piartman, A. A. Blokhin, A. A. Kopyrin, *J. Chem. Eng. Data* **2010**, *55*, 13–36.

[17] F. Cataldo, *Fullerenes Nanotubes Carbon Nanostruct.* **2009**, *17*, 79–84.

[18] J. S. Peerless, G. H. Bowers, A. L. Kwansa, Y. G. Yingling, *J. Phys. Chem. B* **2015**, *119*, 15344–15352.

[19] M. M. Li, Y. B. Wang, Y. Zhang, W. Wang, *J. Phys. Chem. A* **2016**, *120*, 5766–5772.

[20] M. T. Beck, G. Mándi, *Fuller. Sci. Technol.* **1997**, *5*, 291–310.

[21] S. Talukdar, P. Pradhan, A. Banerji, *Fuller. Sci. Technol.* **1997**, *5*, 547–557.

[22] D. Mahdaoui, M. Abderrabba, C. Hirata, T. Wakahara, K. Miyazawa, *J. Solution Chem.* **2016**, *45*, 1158–1170.

[23] G. Schick, K. D. Kampe, A. Hirsch, *J. Chem. Soc. Chem. Commun.* **1995**, 2023–2024.

[24] A. Hirsch, Q. Li, F. Wudl, *Angew. Chem. Int. Ed. Engl.* **1991**, *30*, 1309–1310; *Angew. Chem.* **1991**, *103*, 1339–1341.

[25] Y. Li, L. Gan, *J. Org. Chem.* **2014**, *79*, 8912–8916.

[26] C. Adamo, V. Barone, *J. Chem. Phys.* **1999**, *110*, 6158–6170.

[27] K. N. Semenov, N. A. Charykov, I. V. Vorotyntsev, *Russ. J. Phys. Chem. A* **2015**, *89*, 1206–1210.

[28] H. Isobe, N. Tomita, E. Nakamura, *Org. Lett.* **2000**, *2*, 3663–3665.

[29] L. Zhao, M. Hermann, N. Holzmann, G. Frenking, *Coord. Chem. Rev.* **2017**, *344*, 163–204.

[30] T. Clark, J. S. Murray, P. Politzer, *Phys. Chem. Chem. Phys.* **2018**, *20*, 30076–30082.

[31] E. F. Sheka, *J. Struct. Chem.* **2006**, *47*, 593–599.

[32] R. Ghiasi, M. Z. Fashami, A. H. Hakimioun, *J. Theor. Comput. Chem.* **2014**, *13*, 1450023.

[33] A. Haaland, *Angew. Chem. Int. Ed. Engl.* **1989**, *28*, 992–1007; *Angew. Chem.* **1989**, *101*, 1017–1032.

[34] C. J. Cramer, W. L. Gladfelter, *Inorg. Chem.* **1997**, *36*, 5358–5362.

[35] C. Lepetit, C. Maraval, Y. Canac, R. Chauvin, *Coord. Chem. Rev.* **2016**, *308*, 59–75.

[36] H. Braunschweig, R. D. Dewhurst, L. Pentecost, K. Radacki, A. Vargas, Q. Ye, *Angew. Chem. Int. Ed.* **2016**, *55*, 436–440; *Angew. Chem.* **2016**, *128*, 447–451.

[37] U. B. Demirci, *Int. J. Hydrogen Energy* **2017**, *42*, 9978–10013.

[38] M. Fu, S. Pan, L. Zhao, G. Frenking, *J. Phys. Chem. A* **2020**, *124*, 1087–1092.

[39] M. L. Green, P. Jean, M. C. Heaven, *J. Phys. Chem. Lett.* **2018**, *9*, 1999–2002.

[40] C. F. Pupim, A. J. L. Catão, A. López-Castillo, *J. Mol. Model.* **2018**, *24*, 283.

[41] A. Nandi, S. Kozuch, *Chem. Eur. J.* **2020**, *26*, 759–772.

[42] A. Bauzá, T. J. Mooibroek, A. Frontera, *Angew. Chem. Int. Ed.* **2013**, *52*, 12317–12321; *Angew. Chem.* **2013**, *125*, 12543–12547.

[43] A. M. S. Riel, R. K. Rowe, E. N. Ho, A. C. C. Carlsson, A. K. Rappé, O. B. Berryman, P. S. Ho, *Acc. Chem. Res.* **2019**, *52*, 2870–2880.

[44] G. A. Jeffrey, *Crystallogr. Rev.* **2003**, *9*, 135–176.

[45] T. E. Shubina, D. I. Sharapa, C. Schubert, D. Zahn, M. Halik, P. A. Keller, S. G. Pyne, S. Jennepalli, D. M. Guldi, T. Clark, *J. Am. Chem. Soc.* **2014**, *136*, 10890–10893.

[46] P. Larkin, *Infrared and Raman Spectroscopy: Principles and Spectral Interpretation*, **2011**, Elsevier, Waltham, MA, USA.

[47] Y. S. Mary, H. T. Varghese, C. Y. Panicker, M. Girisha, B. K. Sagar, H. S. Yathirajan, A. A. Al-Saadi, C. Van Alsenoy, *Spectrochim. Acta Part A* **2015**, *150*, 543–556.

[48] E. D. Raczyńska, M. Hallman, K. Kolczyńska, T. M. Stepniewski, *Symmetry* **2010**, *2*, 1485–1509.

Check for updates

Structure-directed formation of the dative/covalent bonds in complexes with C70···piperidine†

Rabindranath Lo, [ID]‡[ab] Maximilián Lamanec,‡[ac] Weizhou Wang, [ID][d]
Debashree Manna,[ab] Aristides Bakandritsos, [ID][be] Martin Dračínský, [ID][a]
Radek Zbořil, [ID][abef] Dana Nachtigallová*[ab] and Pavel Hobza [ID]*[ab]

The combined experimental-computational study has been performed to investigate the complexes formed between C70 carbon allotrope and piperidine. The results of FT-IR, H-NMR, and C-NMR measurements, together with the calculations based on the DFT approach and molecular dynamics simulations, prove the existence of dative/covalent bonding in C70···piperidine complexes. The dative bond forms not only at the region of five- and six-membered rings, observed previously with C60, but also at the region formed of six-membered rings. The structure, i.e., nonplanarity, explains the observed dative bond formation. New findings on the character of interaction of secondary amines with C70 bring new aspects for the rational design of modified fullerenes and their applications in electrocatalysis, spintronics, and energy storage.

1. Introduction

Fullerene, ball-shaped compounds composed of five- and six-membered rings, their functionalized derivatives, and supramolecular assemblies are nowadays widely investigated systems for their promising applications in medicine and material chemistry (see the most recent reviews in ref. 1–6). Compared to the most abundant C60, the chemistry of C70 is less known, although its adducts' performance, e.g., in the solar cells, sometimes appears superior to their C60-analogues.[7] Despite their similar physical and chemical properties[8–11] structural differences between C60 and C70 have resulted in frequently observed diverse reactivity (see ref. 12 and discussion below). Unlike the spherically symmetric C60 possessing I_h symmetry

with all carbon atoms equivalent, C70 has a less symmetrical structure of D_{5h} with five different types of carbon atoms[13] (see Scheme 1). A vast number of studies on the addition reactions with C70, including the addition of secondary amines, under various conditions, have been reported,[14–25] showing significant regioselectivity owing to differences in reactivity of the polar and equatorial regions of the C70 structure.

High reactivity towards addition reactions stems from a distortion of the π-conjugation from planarity, decreasing p-orbital contributions involved to the π-bonds and increasing s-orbital contribution to sp2 carbon atoms, respectively; hence, there is a significant decrease of aromaticity character of these spherical carbon allotropes and enhanced capability to accept electrons.[26] Besides the widely studied addition reaction mechanism, as demonstrated for C70 in the above references, electron-accepting properties of fullerenes proved to facilitate also binding of nucleophilic agents, such as the secondary amine, piperidine (pip), by the N→C dative/covalent bond (further abbreviated as N→C bond). As shown in ref. 27, dative bond (DB) complexes can coexist with non-covalent complexes of piperidine and cage-shaped carbon allotropes. Computational studies on pip complexes with C20, formed exclusively by five-member rings, and with C60, with five- and six-member rings, demonstrated the stronger binding character of the former complexes. The failure to form the N→C bond in non-planar carbon allotropes formed exclusively by six-member rings, such as carbon nanotubes with different diameters, led to the conclusion that the presence of five-membered rings is of crucial importance in binding. Such prediction was based on a larger aromaticity decrease in

[a] *Institute of Organic Chemistry and Biochemistry, Czech Academy of Sciences, Flemingovo Náměstí 542/2, 16000 Prague, Czech Republic. E-mail: pavel.hobza@uochb.cas.cz, dana.nachtigallova@uochb.cas.cz*

[b] *CATRIN, Palacký University, Šlechtitelů 27, 78371 Olomouc, Czech Republic*

[c] *Department of Physical Chemistry, Palacký University Olomouc, Tr. 17 listopadu 12, 771 46 Olomouc, Czech Republic*

[d] *College of Chemistry and Chemical Engineering, and Henan Key Laboratory of Function-Oriented Porous Materials, Luoyang Normal University, Luoyang 471934, China*

[e] *Regional Centre of Advanced Technologies and Materials, Palacký University, Olomouc, Šlechtitelů 27, 78371, Czech Republic*

[f] *Nanotechnology Centre, VŠB-Technical University of Ostrava, 17. Listopadu 2172/15, 708 00 Ostrava-Poruba, Czech Republic*

† Electronic supplementary information (ESI) available. See DOI: 10.1039/d0cp06280d

‡ Both authors contributed equally and can be considered as the first author.

This journal is © the Owner Societies 2021

Phys. Chem. Chem. Phys., 2021, **23**, 4365–4375 | **4365**
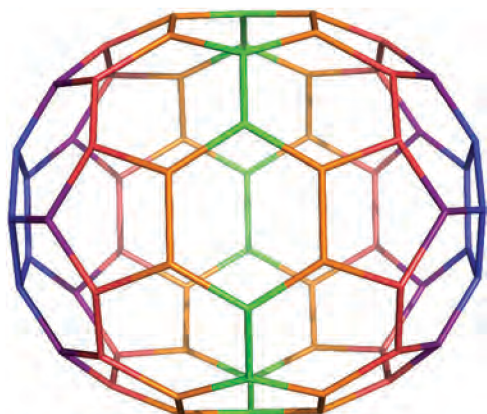
Scheme 1 Illustration of five unequal sites of C_{70} differentiated by colors. The sites considered for piperidine binding are indicated by blue (A-sites), red (B-sites), and green (C-sites), respectively.

five-member rings, which tend to localize double bonds, thus preventing π-electrons from conjugation.[28,29]

To further explore the structural requirements to form the N→C bond in cage-shaped carbon allotropes, the next most abundant C_{70} was considered in the present study employing a combination of IR and NMR spectroscopies and computational modeling, including interaction and binding free energy calculations and molecular dynamics simulations of $C_{70}\cdots(pip)_n$ complexes. The calculations consider three carbon-sites (Scheme 1): (i) sites A and B located at five- and six-member rings and differing by their localization within C_{70} and (ii) site C located within the structure fragments formed solely by six-member rings. The former two sites are similar to the carbon site of C_{60}. To rationalize differences in N→C bond strengths, the local electrophilicity index calculations, using Fukui functions[30,31] were performed. These functions provide atom-specific information on the propensity to undergo electrophilic or nucleophilic attack.[32] Recently, Fukui indices were used extensively, e.g., for a successful rationalization of favorable and competing reactive sites in fullerenes.[33–35]

The present results show different stabilities of $C_{70}\cdots(pip)_{1,2}$ complexes depending on the type of carbon site involved in the reaction. A stronger dative bond is formed at A- and B-sites, i.e., located at five- and six-member rings, while binding to C-site formed solely by six-member rings is weaker. The significant out-of-plane nonplanarity explained the unexpected formation of the dative bond in the latter region. When the entropy is considered, only the former sites' complexes remain stable up to 300 K. Existence of the N→C bond is confirmed by IR and NMR measurements. The presented results confirm the regioselectivity observed for the addition mechanism and provide useful information on structure-specific functionalization.

2. Methods

2.1. Calculations

Calculations were performed using the dispersion-corrected-DFT method, employing the PBE0-D3[36,37] functional with Becke–Johnson damping (BJ)[38] and def2-TZVPP[39] basis set,

whose reliability has been verified in our previous paper.[27] All interactions are described in terms of interaction and binding free energies at 298 K; zero-point energies were included. The free energy calculations, performed at the PBE0-D3/def2-TZVPP level, were calculated using the Gaussian 09[40] program package. The solvent effects were described via the COSMO solvation model,[41] with the dielectric constant value of 5.9. The nucleus-independent chemical shift (NICS) calculations were carried out at wB97XD/def2-TZVP[42,43] level, using the PBE0-D3 optimized geometries with gauge-invariant atomic orbitals (GIAO).[44,45] The reliability of this method for the chemical shifts' calculations in C_{70} was investigated previously.[46]

The systems' stability is defined by two terms, the intrinsic (ΔE^{INTR}) and total (ΔE) interaction energies. ΔE^{INTR} is defined as a difference between energy of the optimized complex and the sum of subsystem energies calculated at the complex geometries. ΔE includes the deformation energies (ΔE^{def}) obtained as a difference of the subsystem energies calculated at the complex's optimized geometry and the equilibrium geometries of isolated subsystems.

The MP2 calculations of ΔE^{INTR} have been performed using the Psi4[47] code.

To obtain a more realistic description of C_{70} solvation, the molecular dynamics (MD) simulations were performed. These simulations use the AM1-D semiempirical approach since the previously used DFT method is prohibitive due to the system's size. We have shown that in terms of stabilization energies and the minimum characterization on $C_{60}\cdots(pip)_n$ complexes, this approach gives the best agreement with respect to the benchmark calculations among other semiempirical methods.[27]

The MD simulations have been performed with the AM1 method implemented in Mopac 2016[48] using the Cuby4 framework[49] with added D3[50] dispersion. The heating of systems was realized from 0 to 300 K by 3000 steps. MD 0.1 ns simulations were carried out at 300 K using the Berendsen thermostat.[51] Domain-based Local Pair Natural Orbital-CCSD(T) (DLPNO-CCSD(T))[52,53] the single-point calculations were performed for the DFT optimized geometries using def2-SVP basis set. An energy decomposition scheme for the total interaction energy within the DLPNO framework, known as local energy decomposition (LED),[54] was used for detailed analyses of the interaction energies.

2.2. IR spectroscopy

A paste of C_{70} (4 mg) and ca. 20 μl of piperidine was mixed in a mortar. It was then ground with a pestle for 5 minutes and placed with a pipette on the ZnSe crystal of the FT-IR instrument. The spectra were collected immediately (C_{60}-P1 sample) and after a few minutes (C_{60}-P2 sample) to let pip molecules evaporate until the IR signal was enriched with the vibrations from the C_{60}–pip complex.

FT-IR spectra were recorded on an iS5 FTIR spectrometer (Thermo Nicolet) using the Smart Orbit ZnSe ATR accessory. The pastes or liquid piperidine were placed on the ZnSe crystal, and the spectra were acquired by summing 32 scans with

nitrogen gas flow through the accessory. Background spectra were collected under identical conditions.

2.3. NMR spectroscopy

Solution-state NMR spectra were recorded on Bruker Avance 600 (^{1}H at 600 MHz, ^{13}C at 151 MHz) spectrometer in deuterated 1,2-dichlorobenzene. The spectra were referenced to the residual solvent signal (the highest-chemical-shift signals at 7.40 ppm for ^{1}H and 132.60 ppm for ^{13}C). All chemicals were purchased from Sigma-Aldrich and were used without further purification. Fullerene C_{70} (11 mg) was dissolved in 1,2-dichlorobenzene-d4 (550 μL) with sonication and vigorous mixing. After the proton and carbon spectra acquisition, piperidine (35 μL) was added, and the proton and carbon spectra of the mixture were measured.

3. Results and discussion

3.1. Interaction energies

$C_{70}\cdots$**pip.** Fig. 1 displays the structures of $C_{70}\cdots$pip complexes formed at A, B, and C sites of C_{70} optimized using the

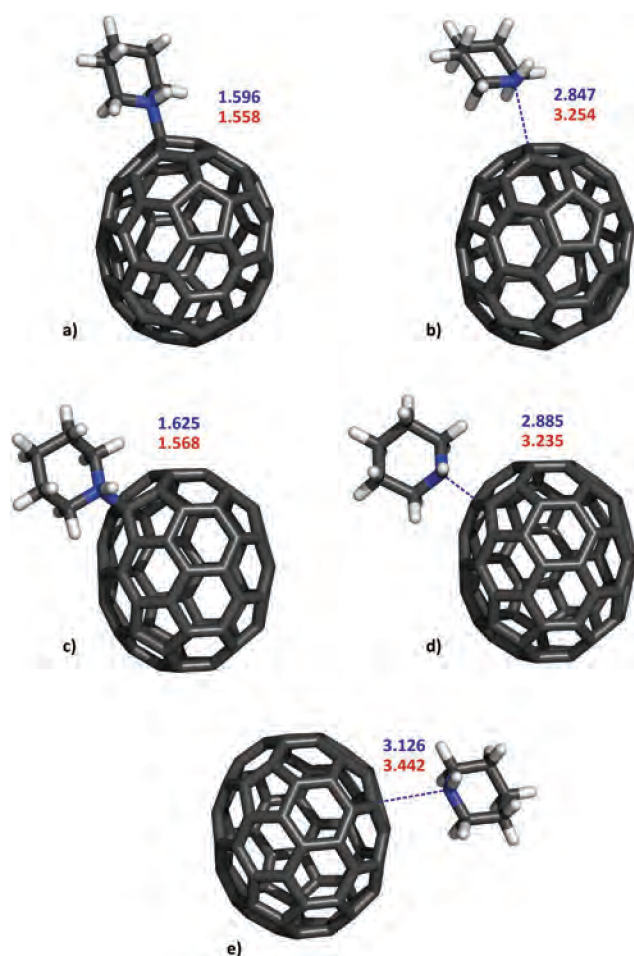**Fig. 1** The minima of $C_{70}\cdots$pip: (a) DB and (b) vdW complexes at site A, (c) DB and (d) vdW complex at site B, and (e) vdW complexes at site C calculated at the PBE0-D3BJ/def2-TZVPP level. The $C_{70}\cdots$pip distances are given in Å (gas phase: dark blue, solvent phase: red).

Table 1 Total DFT interaction energies (ΔE), deformation energies (ΔE^{Def}), and intrinsic interaction energies (ΔE^{INTR}) calculated at the PBE0-D3 and MP2 levels using the def2-TZVPP basis set for DFT and cc-pVQZ for MP2. In brackets are dispersion parts of ΔE^{INTR} calculated from Grimme's DFT-D3 correction. All values are in kcal mol^{-1}

| | Site | PBE0-D3 | | ΔE^{Def} | ΔE^{INTR}(MP2) |
		ΔE	ΔE^{INTR}		
$C_{70}\cdots$pip					
vdW complexes	A	−5.3	−5.3(−4.9)	0.0	−7.4
	B	−5.2	−5.3(−4.9)	0.1	−7.3
	C	−5.5	−5.5(−4.9)	0.0	−7.8
DB complexes	A	−2.6	−20.1(−7.8)	17.5	−18.3
	B	+1.0	−15.3(−7.9)	16.3	−12.1
$C_{70}\cdots$(pip)$_2$					
vdW complexes	B	−8.8	−10.2(−9.7)	1.4	−13.9
	C	−8.8	−9.9(−9.7)	1.1	−14.3
DB complexes	A	−16.0	−40.1(−11.6)	24.0	−40.1
	B	−12.2	−35.6(−12.1)	23.4	−34.2
	C	−4.4	−29.7(−13.0)	25.4	−31.0

PBE0-D3/def2-TZVPP approach. The optimization procedure located two types of minima, formed by the interaction between $C(C_{70})$ and $N(pip)$: the vdW complexes which interact *via* $C\cdots N$ tetrel bond[55] with the bond lengths of 2.9–3.1 Å and the DB complexes interacting *via* $N\rightarrow C$ bond with bond lengths of about 1.6 Å. The calculations show that the vdW complex type can exist on all (A, B, and C) sites with very similar stabilities of 5.2–5.5 kcal mol^{-1}. In all cases, almost identical values of ΔE and ΔE^{INTR} show negligible deformation energies, less than 0.1 kcal mol^{-1} (see also Table 1 for the deformation energies). The results obtained for DB structures provide a less uniform picture. The optimization procedures found the stable minima at A and B sites, located at the intersection of five- and six-member rings. Such a complex does not form at the all-benzoid C site. Both ΔE^{INTR} values and $N\rightarrow C$ bond distances indicate stronger interaction at the A site. Although the ΔE^{INTR} values of localized DB structures are significantly larger than their vdW counterparts, large deformation energies make them only weakly bound (site A, −2.6 kcal mol^{-1}) or unstable (site B, +1.0 kcal mol^{-1}).

$C_{70}\cdots$**(pip)$_2$.** Binding of (pip)$_2$ provides a different picture of both DB and vdW complexes' stabilities. Fig. 2 and Table 1 display their structures and interaction energies. The interaction energies are calculated with respect to (pip)$_2$ in which the inner and outer pips bind *via* $N\rightarrow C$ bond to C_{70} and NH (inner)$\cdots$N (outer) motif, respectively. Contrary to the binding of pip monomer, the vdW complexes formed at B and C sites only; all attempts to localize vdW minimum at the A site resulted in DB structures. For vdW complexes, the calculated ΔE^{INTR} and ΔE values are almost identical, and the values of their deformation energies almost negligible. Interaction energies and C–N distances reveal stronger interaction in C_{70} complexes with pip dimers than their corresponding monomer counterparts. Unlike $C_{70}\cdots$pip, stable DB complexes with (pip)$_2$ formed at all carbon sites of C_{70}. As in monomer, the ΔE^{INTR} values are significantly larger, by 20–25 kcal mol^{-1}, for DB.

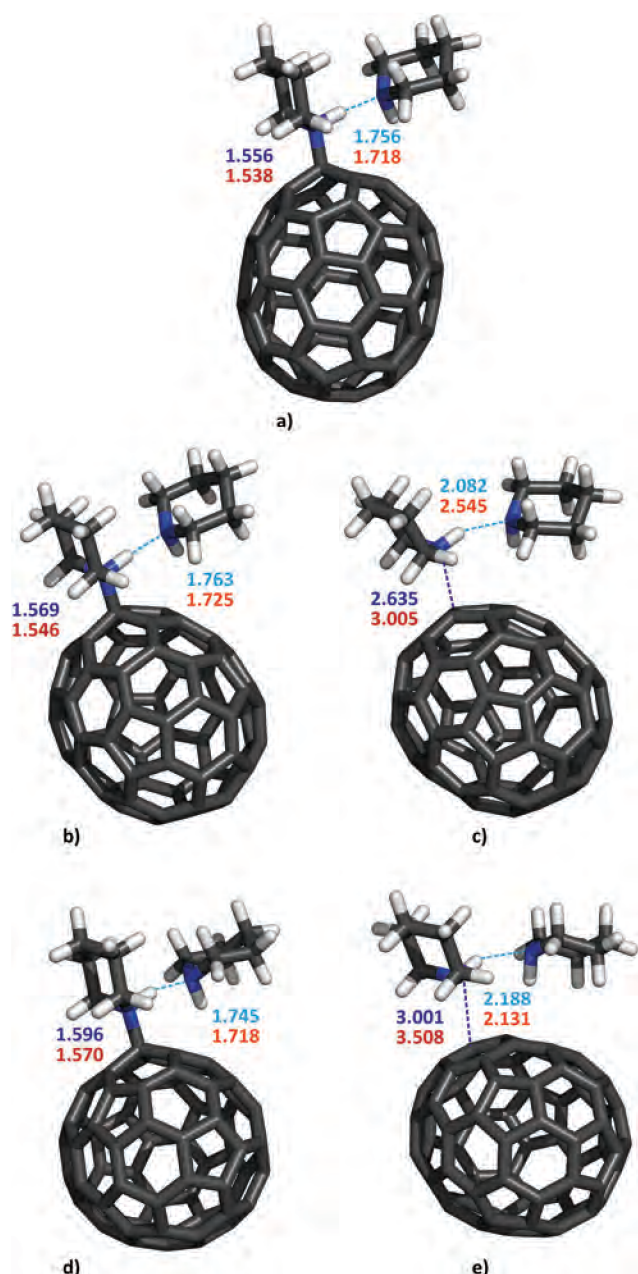**Fig. 2** The minima of $C_{70}\cdots(pip)_2$: the DB complexes at the A-site (a) and B-site (b); the vdW complex at B-site (c), the DB complex at C-site (d), and the vdW complex at the C-site (e). The structures are optimized at the PBE0-D3BJ/def2-TZVPP level. The distances are given in Å (gas phase: blue, solvent phase: red).

Besides, C–N distances in $C_{70}\cdots(pip)_2$ and N–H distances within $(pip)_2$ shorten by 1.0–1.4 Å and by 0.3 Å, respectively, reflecting the strengthening of both interactions in the complexes. Substantially larger stabilities of DB in $C_{70}\cdots(pip)_2$ than that of $C_{70}\cdots pip$, as well as shorter N–C bond lengths (see Fig. 1 and 2 and Table 1) suggest the stabilization due to cascade outer pip → inner pip → C_{70} charge-transfer, which results in strengthening of N → C dative bond. The natural bond orbital (NBO) analysis reveals a substantial charge transfer (0.67 e) from the pip dimer to C_{70}. A similar effect, *i.e.*, the hydrogen

bond strengthening of the dative bond, was observed in our previous studies on the $C_{60}\cdots(pip)_n$ complexes[27] and can be viewed as a subclass of non-covalent cooperativity.[56,57]

The changes in the molecular electrostatic potential of C_{70} and pip complexes (see Fig. S1, ESI†) demonstrate different characters of the interactions. ESP of isolated C_{70} forms small, slightly positively charged islands located on top of the five- and six-membered rings. Upon the complexation with a single pip, the electron density transfers from pip to C_{70} resulting in significantly negative ESP values on the C_{70} region opposite to the pip binding site. These changes are further pronounced in the DB complex with pip dimer.

An electron-dense C_{70} can strengthen the host–guest complex stability when the ellipsoidal guest C_{70} forms a Saturn-shaped complex with a macrocyclic host molecule.[58] As the CH$\cdots\pi$ interactions play an important role in these host–guest complex types, the DB complex of C_{70} should be a better guest molecule than isolated C_{70}.

From an electrochemical perspective, an efficient charge transfer process requires substantial differences in the redox properties, in particular, redox potentials (estimated using adiabatic electron affinities (AEA)),[59] of the isolated C_{70} and DB complex. The calculated AEA of the C_{70} and $C_{70}\cdots pip$ are 2.62 eV and 2.18 eV, respectively, showing decreasing in the electron-accepting ability upon complexation with pip.

The deformation energies of about 25 kcal mol^{-1} for all sites significantly affect DB overall stability, reordering DB and vdW relative stabilities at the C site.

The observed energy balance between the vdW and DB complexes of $C_{70}\cdots pip$ and $C_{70}\cdots(pip)_2$ for different sites reveal different potentials for formation, *i.e.*, the increasing probability of DB complex formation in the C → B → A sequence and the opposite trend for vdW complex formation. This phenomenon is discussed in paragraph 3.6.

Calculated DFT-D3 corrections (Table 1) demonstrate the role of dispersion interactions in complex stabilities, showing their significant contributions in both binding types. In particular, the dispersion energy dominates the interaction energies in the vdW complexes and contributes to the total interaction energies of the DB complexes by 30–50%, respectively. We have performed local energy decomposition (LED) analysis at the DLPNO-CCSD(T)[60,61] level (Table S1, ESI†). Stabilizing electrostatic as well as destabilizing exchange-repulsion energies have a small contribution to the stabilization energy. The DLPNO-CCSD(T) intrinsic energy is in reasonable agreement with that calculated at the DFT level. Table 1 also lists the results of ΔE^{INTR} calculations obtained at the MP2/cc-pVQZ level, showing agreement with PBE0-D3/def2-TZVPP results in the complexes' relative stabilities. The ΔE^{INTR} values do not differ by more than 10% for the majority of structures. Significant overstabilization at the MP2 level for vdW, which accounts for 40–45%, demonstrates the well-known overestimation of the dispersion interactions in the MP2 method. Nevertheless, the present results and benchmarking results with the highly accurate CCSD(T) method performed on smaller fullerenes[27] justify the reliability of the DFT-based

4368 | *Phys. Chem. Chem. Phys.*, 2021, **23**, 4365–4375

This journal is © the Owner Societies 2021

Table 2 Thermodynamic characteristics (in kcal mol^{-1}, T = 298 K) for the formation of $C_{70}\cdots$pip and $C_{70}\cdots$pip$_2$ complexes calculated at PBE0-D3BJ/def2-TZVPP level. The solvent phase results are given in parenthesis

	Site	ΔE	ΔG	ΔH	$-T\Delta S$
$C_{70}\cdots$pip					
vdW complexes	A	−5.3 (−3.9)	4.6 (5.5)	−4.0 (−2.6)	8.6 (8.1)
	B	−5.2 (−4.0)	4.2 (5.5)	−3.9 (−2.7)	8.1 (8.2)
	C	−5.5 (−4.2)	3.5 (5.0)	−4.2 (−2.9)	7.7 (7.8)
DB complexes	A	−2.6 (−9.6)	13.0 (6.3)	−0.3 (−7.0)	13.3 (13.4)
	B	1.0 (−5.7)	16.3 (10.1)	3.2 (−3.2)	13.2 (13.3)
$C_{70}\cdots$(pip)$_2$					
vdW complexes	B	−8.8 (−6.0)	4.2 (5.5)	−8.1 (−5.4)	12.3 (10.8)
	C	−8.8 (−7.1)	0.9 (3.2)	−7.5 (−5.7)	8.4 (8.9)
DB complexes	A	−16.0 (−19.6)	1.8 (−1.8)	−13.7 (−17.3)	15.5 (15.5)
	B	−12.2 (−15.8)	5.6 (1.6)	−10.0 (−13.6)	15.6 (15.2)
	C	−4.4 (−5.7)	12.9 (11.7)	−2.4 (−3.7)	15.3 (15.4)

approach in this case and its use for further studies on $C_{70}\cdots$(pip)$_n$ complexes.

We quantify the local aromaticities of 5- and 6-membered rings of the $C_{70}\cdots$pip and $C_{70}\cdots$(pip)$_2$ DB complexes by NICS(0)$_{zz}$ indexes calculated at the ring centroids[62] and compare them with those of the isolated C_{70} (Fig. S2 and Table S2, ESI†). The aromaticity of the 5-membered rings in the polar region increases upon complex formation with pip. The NICS(0)zz values of the 5-membered rings in the equatorial region in DB complexes significantly change and become antiaromatic.

3.2. Binding free energies

Further insight to the $C_{70}\cdots$pip and $C_{70}\cdots$(pip)$_2$ complex formation is provided by the calculations of the free energy (ΔG) at 298 K, performed at the PBE0-D3/def2-TZVPP level (Table 2). Insertion of entropy effects results in positive ΔG values, which, however, does not rule out the existence of the complex in pip solvent. The solvent pip molecules can stabilize the complex *via* dative and non-covalent bonds. In the continuum solvent model, the $C_{70}\cdots$(pip)$_2$ complex at A-site has a negative ΔG value of −1.8 kcal mol^{-1} (Table 2). Thus, $C_{70}\cdots$(pip)$_2$ complex with (pip)$_2$ attached to the A-site *via* dative bond is the most likely to be formed and detectable in the experiment.

3.3. MD simulations

To provide a more realistic model picture of the complex formation in the piperidine solvent, the MD simulations in the piperidine droplet (26 solvent molecules) were performed. The systems' size prohibits using the DFT approach even with the limited 6-31G* basis set.

Table 3 compares results on the relative stabilities of $C_{70}\cdots$(pip)$_{1,2}$ complexes obtained with the PBE0-D3/def2-TZVPP and MP2/cc-pVQZ and AM1-D methods. The AM1-D approach reproduces the ΔE and ΔE^{INTR} values of vdW complexes with an excellent agreement. Although the interaction energies of $C_{70}\cdots$(pip)$_{1,2}$ are overestimated at this level, AM1-D still predicts larger stabilities of $C_{70}\cdots$(pip)$_2$, with the complexation at C-site being the least probable.

Two minima, with one or two pip molecules interacting *via* N→C bond (S1 and S2, Fig. 3) with A-sites of C_{70}, were found. Note that the dative bond is formed at A-sites even if the optimization procedure started from the structure with N→C bond at C-site. The S1 structure, with one N→C bond, is by 10 kcal mol^{-1} less stable than the S2 system.

The molecular dynamics simulations starting from the S1 and S2 structures and running for 100 000 MD steps (*i.e.*, total simulation time 100 ps) at 298 K confirmed the existence of one and two N→C bonds complex. During the molecular dynamics run, three (S1 structure) and four (S2 structure) pip molecules escape from the surrounding shell.

3.4. FT-IR spectra

Fig. 4 shows the FT-IR spectra of C_{70} and its mixture with piperidine solvent after the evaporation of some excess amount of unbound piperidine molecules (labeled C_{70}-P1 and C_{70}-P2, respectively). For the sake of comparison, the FT-IR spectra of C_{60} with the piperidine solvent (C_{60}-P2 discussed previously (ref. 27)) are also included.[27] In addition to the collective band at 1000–1200 cm^{-1} previously assigned to the C–N bond and skeletal –C–N–C stretchings[63,64] due to unbound piperidine molecules, a new band appears at 983 cm^{-1}. A similar situation was also observed in the C_{60}-P2 spectrum (see also ref. 27).

Table 3 Comparison of the total interaction energies (ΔE, kcal mol^{-1}) and intrinsic interaction energies (ΔE^{INTR}) calculated at the PBE0-D3, MP2, and AM1-D methods

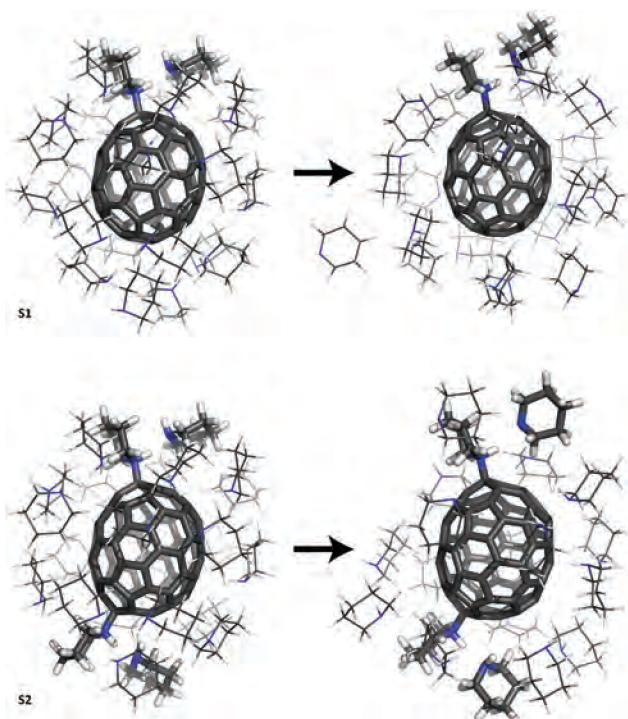|	Site	ΔE (DFT)	ΔE (AM1-D)	ΔE^{INTR} (DFT)	ΔE^{INTR} (MP2)	ΔE^{INTR} (AM1-D)
$C_{70}\cdots$pip						
vdW complexes	A	−5.3	−6.5	−5.3	−7.4	−6.5
	B	−5.2	−6.7	−5.3	−7.3	−6.7
	C	−5.5	−7.1	−5.5	−7.8	−7.1
DB complexes	A	−2.6	−9.8	−20.1	−18.3	−31.1
	B	+1.0	−9.8	−15.3	−12.1	−32.0
$C_{70}\cdots$(pip)$_2$						
vdW complexes	B	−8.8	−11.3	−10.2	−13.9	−12.3
	C	−8.8	−11.2	−9.9	−14.3	−12.4
DB complexes	A	−16.0	−18.7	−40.1	−40.1	−42.3
	B	−12.2	−19.0	−35.6	−34.2	−47.4
	C	−4.4	−6.1	−29.7	−31.0	−34.6

Fig. 3 The mixture of C_{70} with 26 piperidine molecules with one (S1) and two (S2) dative bonds formed in the minima structures (left) obtained in the optimization at the AM1-D level. The structures on the right side are after 0.1 ns MD AM1-D simulation.

The calculations (see Table S3 and Fig. S3, ESI†) interpret this band as a result of the asymmetric stretch (938 cm^{-1}, intensity 73 km mol^{-1}) of the newly formed N→C bond in C_{70}–(pip)$_2$ complex. Calculated symmetric stretch located at 880 cm^{-1} is also present in the C_{70}-P2 spectrum, similar to the C_{60}-P2 spectrum.

The N–H bending vibrations are expected in the spectral region of 1500 and 1650 cm^{-1}. The spectrum of unbound piperidine is consistent with these bands' negligible intensities calculated for (pip)$_{2,3}$ complexes in the previous study.[27] Compared to the C_{60}-P2 spectrum, with one clear band at 1540 cm^{-1} due to the N–H bending mode of the inner piperidine (with the N atom is involved in bond with C_{60}[27]), two bands at 1540 and 1630 cm^{-1} appear in the spectra of C_{70}-P2. Assignment of these bands relies on the (pip)2 bound calculations at three different structural motifs (A, B, and C), giving the N–H bending vibrations frequencies at 1565, 1568, and 1535 cm^{-1} at A-, B-, and C-sites, respectively. Besides, few low-intensity peaks of N–H bending vibrations appeared in the region of 1613–1624 cm^{-1} (Table S3, ESI†).

The spectral region of 2700–3000 cm^{-1} and higher than 3000 cm^{-1} correspond to C–H and N–H stretching vibrations, respectively. (Fig. 4b). The former bands are retained without changes, while an intensity depletion of the later bands upon pip evaporation indicates a decreased number of hydrogen bonds formed within piperidine molecules.

3.5. NMR spectroscopy

Fig. 5 displays the ^{1}H NMR spectrum of the mixture of C_{70} and pip in 1,2-dichlorobenzene. The spectra of pure C_{70} and piperidine, and the mixture of C_{60} with pip in the same solvent are shown for comparison. In agreement with the previously studied $C_{60}\cdots$pip system (Fig. 5 and ref. 27), the character of the spectrum at the chemical shift of about 3.5 ppm also changes in the $C_{70}\cdots$pip mixture, however, in a more complex manner. Based on the previous study on $C_{60}\cdots$pip in 1,2-dichlorobenzene,[27] the observed changes are interpreted by forming the N→C bond. A larger number of the new signals and lower intensities (Fig. 5) most likely result from the lower symmetry of C_{70} compared to C_{60}, hence a presence of multiple complexes. However, the observed experimental results cannot
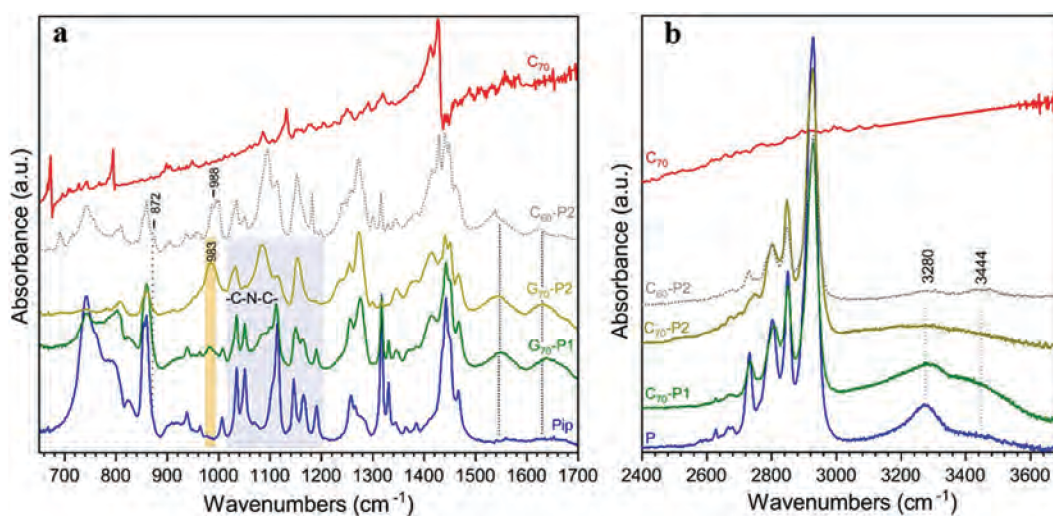

Fig. 4 FT-IR spectra of C_{70} and its complex with piperidine before evaporation (C_{70}-P1) and after evaporation of some excess amount of unbound piperidine molecules (C_{70}-P2) at two spectral windows for the observation of (a) the C-N stretching and N-H bending vibrations, and (b) the N–H stretching vibrations. The spectra of pure piperidine and its complexes with C_{60} (C_{60}-P2) are given for comparison.[27]
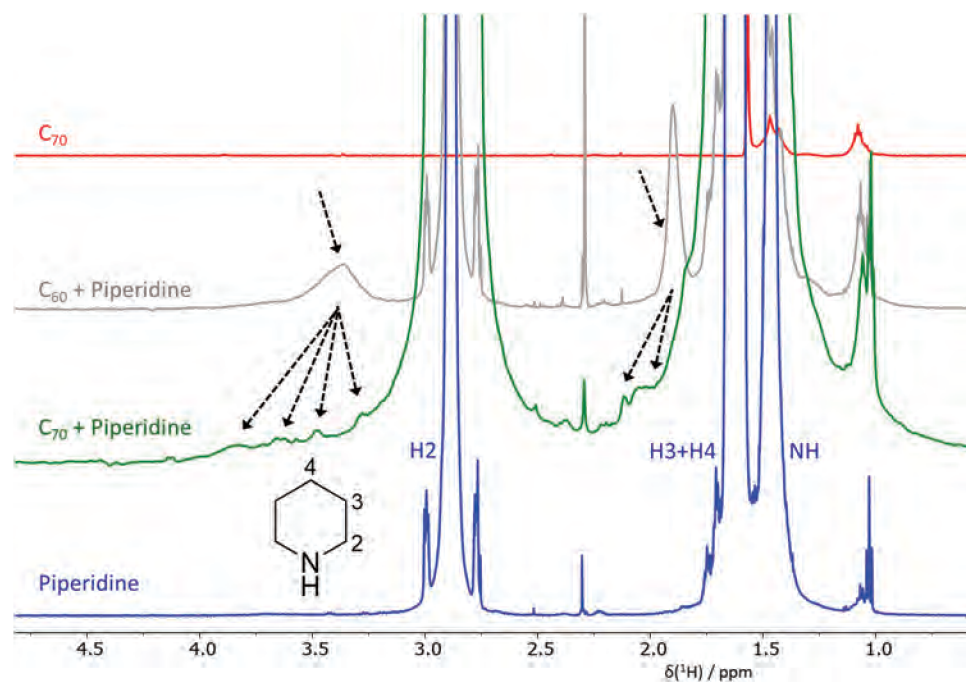
4370 | *Phys. Chem. Chem. Phys.*, 2021, **23**, 4365–4375

This journal is © the Owner Societies 2021

Fig. 5 Part of ^{1}H NMR spectra of 1,2-dichlorobenzene-d4 (550 μL) solutions of piperidine, the mixture of C_{70} and piperidine, the mixture of C_{60} and piperidine, and C_{70}. The black dashed arrows highlight the signals of the C_{60}-piperidine and C_{70}-piperidine complexes.

provide a conclusive answer to whether the different signals result from binding of the inner pip to various sites or from a different orientation of the outer pip to C_{70}. The calculated ^{1}H-NMR spectra show the larger chemical shifts of C-H hydrogens at alpha-(H2) positions compared to those in the isolated pip. This observation correlates well with the experimental ^{1}H-NMR spectra (Fig. 5). In fact, the equatorial hydrogens in the inner pip show the largest chemical shifts indicating a direct involvement of pip N in the complex compared to the outer pip (Table S4, ESI†).

The low concentration of the complexes does not allow for fast measurement of carbon NMR spectra. However, the proton–carbon correlation experiment (HSQC, Fig. S4, ESI†) shows that the new proton signals are attached to piperidine carbon atoms with similar chemical shifts as those in the previously studied C_{60}-piperidine complex.[27]

Unfortunately, during 1–2 days required to obtained a C-NMR spectrum with a good signal-to-noise ratio (Fig. S5, ESI†), new signals overlapping with the original signals, observed immediately after dissolution, appear in proton spectra (see Fig. S6, ESI†). These new signals probably correspond to the structures resulting after the addition of piperidine to C_{70}. ^{13}C spectrum of the sample after standing (Fig. S5, ESI†) exhibits signals in the region 70–80 ppm, which are typical for the products of addition (*i.e.*, covalent bond formation) of secondary amines to C_{60}.[65]

3.6. Explanation of different strengths of the N→C dative bond at various structural motifs of C_{70}

The above calculations on the interaction energies in $C_{70}\cdots$pip complexes forming N→C bond together with previously reported results on the character of pip complexes with C_{20}, C_{60}, and CNT structures[27] call for further discussion on

structural prerequisites of carbon allotropes to form the dative bond with electron-donating systems, and the secondary amines, in particular. The symmetry of C_{70} with binding carbon-sites of different characters, *i.e.*, five different types according to their location within the C_{70} structure, offers a sound system for such analysis. Regardless of the thermodynamic (in)stability of the dative bond complexes, stable $C_{70}\cdots$(pip)$_2$ minima with N→C bond exist at all three carbon-sites (A, B, and C) of C_{70}, characterized by ΔE^{INTR} and ΔE values in the range of -29 to -40 kcal mol^{-1} and -4 to -16 kcal mol^{-1}, respectively, *i.e.*, with a similar stabilities as $C_{60}\cdots$(pip)$_2$ DB complexes with ΔE^{INTR} of -36 kcal mol^{-1} and ΔE of -13 kcal mol^{-1}. The failure of CNT to form these complexes led to the conclusion that the out-of-plane planarity is an essential but insufficient requirement to form dative bonds with carbon allotropes due to the still significant aromatic character of the six-membered ring. The presence of the five-membered ring explained the formation of dative bonds due to their larger aromaticity decrease upon deviation from planarity.[27]

Our results on $C_{70}\cdots$(pip)$_2$ reveal the large stability of DB complexes formed at sites that contain five- and six-member rings (sites A and B). The complex formed on the A-site, located close to apexes of the rugby ball with larger out-of-plane deviation, is more stable (see Fig. 6 and Scheme 1) than that formed on the B-site, located close to the central part of the ball. The existence of the dative bond at the C-site containing only the six-member rings is surprising and contradicts the previously proposed prerequisite to forming the dative bond. Fig. 7 explains the observed DB formation at the C-site based solely on structural arguments. Comparison of the geometries of the pyrene motif cut from CNT, C_{70}, and isolated pyrene
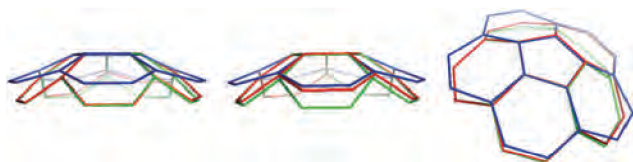
This journal is © the Owner Societies 2021

Phys. Chem. Chem. Phys., 2021, **23**, 4365–4375 | **4371**

Fig. 6 Curvature comparison of Isolated-pentagon-rule motif (blue), A motif from C_{70} (green), and B motif from C_{70} (red) from three different views.
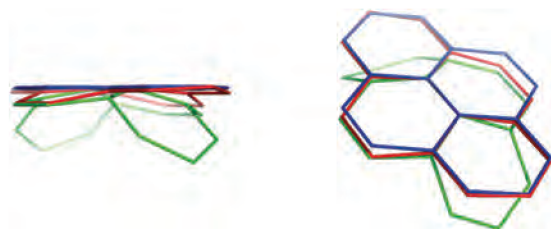

Fig. 7 Comparison of planar pyrene (blue) and pyrene motifs cut from carbon nanotube (red) and C-site of C_{70} (green) viewed from different angles.

shows the trends in structure distortions of the former two systems. While the pyrene motif significantly declines from the plane in one direction in CNT, it deviates from the plane in both directions in the C_{70} fragment.

The stability and chemical reactivity of non-planar π-conjugated systems are described based on the π-orbital axis vector (POAV) analysis.[66–68] For this purpose, the systematic calculations of pyramidalization angles of the carbon atoms at the A, B, and C-sites in C_{70} are performed, giving the values of $11.9°$, $11.5°$, and $8.6°$, respectively. The values for planar benzene and C_{60} are $0°$ and $11.6°$, respectively.[66] This analysis indicates a larger reactivity of the A-site in C_{70} than CNT (m,n), with m = 6–10, n = 0, and CNT (m,m) with m = 5–8. This result further supports the DB complex formation.[68]

Calculations of Fukui indices (f_k^+, see Table S5, ESI†) also reveal different potentials of carbon sites for N→C formation. Larger values of f_k^+ obtained for the A and B sites are in line with their larger interaction energies in DB complexes compared to the smaller stability and small f_k^+ value calculated for the C-site and the inability to form this complex in CNT with the negative value of f_k^+.

Thus, the above analyses conclude that the N→C bond between fullerenes and pip can form at any structural motif providing sufficient out-of-plane deviations.

4. Conclusions

The present studies on the complexes of the secondary amine piperidine and C_{70} performed using computational modeling and experimental IR and NMR spectroscopy prove the dative/covalent complex's existence, previously observed for other ball-shaped carbon allotropes, and provide additional insight into its structural selectivity. Larger out-of-plane

deviations occurred in both directions of the pyrene fragment explain the dative bond formation at the region with six-membered rings, not observed previously with CNT. The calculations reveal stronger bonding on carbon sites which participate in both, five- and six-member rings compared to carbon site located in the region consisting solely of six-member rings. The calculated free energies suggest that only the complexes formed with carbon sites on the poles of the rugby-ball structure are thermodynamically stable. This study provides previously unknown information on the interaction of C_{70} with secondary amines, which may be exploited to design fullerene derivatives with application in spintronics, (electro)catalysis, and energy storage.

Conflicts of interest

The authors declare no competing financial interest.

References

1 D. Jović, V. Jaćević, K. Kuča, I. Borišev, J. Mrdjanovic, D. Petrovic, M. Seke and A. Djordjevic, The Puzzling Potential of Carbon Nanomaterials: General Properties, Application, and Toxicity, *Nanomaterials*, 2020, **10**, 1508.

2 J. Joseph, V. S. Sivasankarapillai, S. Nikazar, M. S. Shanawaz, A. Rahdar, H. Lin and G. Z. Kyzas, Borophene and Boron Fullerene Materials in Hydrogen Storage: Opportunities and Challenges, *ChemSusChem*, 2020, **13**, 3754–3765.

3 E. I. Pochkaeva, N. E. Podolsky, D. N. Zakusilo, A. V. Petrov, N. A. Charykov, T. D. Vlasov, A. V. Penkova, L. V. Vasina, I. V. Murin, V. V. Sharoyko and K. N. Semenov, *Prog. Solid State Chem.*, 2020, **57**, 100255.

4 X. Zhang, H. Cong, B. Yu and Q. Chen, Recent Advances of Water-Soluble Fullerene Derivatives in Biomedical Applications, *Mini-Rev. Org. Chem.*, 2018, **16**, 92–99.

5 L. Jia, M. Chen and S. Yang, Functionalization of fullerene materials toward applications in perovskite solar cells, *Mater. Chem. Front.*, 2020, **4**, 2256–2282.

6 T. Xu, W. Shen, W. Huang and X. Lu, Fullerene micro/nanostructures: controlled synthesis and energy applications, *Mater. Today Nano*, 2020, **11**, 100081.

7 X. Meng, W. Zhang, Z. Tan, Y. Li, Y. Ma, T. Wang, L. Jiang, C. Shu and C. Wang, Highly Efficient and Thermally Stable Polymer Solar Cells with Dihydronaphthyl-Based

4372 | *Phys. Chem. Chem. Phys.*, 2021, **23**, 4365–4375

This journal is © the Owner Societies 2021

[70]Fullerene Bisadduct Derivative as the Acceptor, *Adv. Funct. Mater.*, 2012, **22**, 2187–2193.

8 D. M. Cox, S. Behai, M. Disko, S. M. Gorun, M. Greaney, C. S. Hsu, E. B. Kollin, J. Millar, J. Robbins, W. Robbins, R. D. Sherwood and P. Tindall, Characterization of C_{60} and C_{70} Clusters, *J. Am. Chem. Soc.*, 1991, **113**, 2940–2944.

9 H. Ajie, M. M. Alvarez, S. J. Anz, R. D. Beck, F. Diederich, K. Fosliropoulos, D. R. Huffman, W. Kratschmer, Y. Rubin, K. E. Schriver, D. Sensharma and R. L. Whetten, Characterization of the Soluble All-Carbon Molecules C_{60} and C_{70}, *J. Phys. Chem.*, 1990, **94**, 8630–8633.

10 J. W. Arbogast and C. S. Foote, Photophysical Properties of C_{70}, *J. Am. Chem. Soc.*, 1991, **113**, 8886–8889.

11 J. Baker, P. W. Fowler, P. Lazzeretti, M. Malagoli and R. Zanasi, Structure and properties of C_{70}, *Chem. Phys. Lett.*, 1991, **184**, 182–186.

12 T. Kubo, E. Kanao, T. Matsumoto, T. Naito, T. Sano, M. Yan and K. Otsuka, Specific Intermolecular Interactions by the Localized π-Electrons in C_{70}-fullerene, *ChemistrySelect*, 2016, **1**, 5900–5904.

13 K. Hedberg, L. Hedberg, M. Bühl, D. S. Bethune, C. A. Brown and R. D. Johnson, Molecular Structure of Free Molecules of the Fullerene C_{70} from Gas-Phase Electron Diffraction, *J. Am. Chem. Soc.*, 1997, **119**, 5314–5320.

14 O. A. Troshina, P. A. Troshin, A. S. Peregudov, V. I. Kozlovski and R. N. Lyubovskaya, $C_{70}[NR_2]_2O$: The First C_{70} Intramolecular Ethers Bearing Two Amine Groups, *European*, *J. Org. Chem.*, 2006, 5243–5248.

15 Y. Li, D. Xu and L. Gan, Selective Multiamination of C_{70} Leading to Curved π Systems with 60, 58, 56, and 50 π Electrons, *Angew. Chem., Int. Ed.*, 2016, **55**, 2483–2487.

16 A. Herrmann, M. W. Rüttimann, T. Gibtner, C. Thilgen, F. Diederich, T. Mordasini and W. Thiel, Achiral and chiral higher adducts of C_{70} by Bingel cyclopropanation, *Helv. Chim. Acta*, 1999, **82**, 261–289.

17 W. W. H. Wong and F. Diederich, Regio- and Diastereoselective Synthesis of Bis- and Tetrakisadducts of C_{70} by Directed Remote Functionalization Using Tröger Base Tethers, *Chem. – Eur. J.*, 2006, **12**, 3463–3471.

18 V. S. P. K. Neti, M. R. Cerón, A. Duarte-Ruiz, M. M. Olmstead, A. L. Balch and E. Luis, High-yield, regiospecific bis-functionalization of C_{70} using a Diels–Alder reaction in molten anthracene, *Chem. Commun.*, 2014, **50**, 10584–10587.

19 S. Vidal, M. Izquierdo, W. K. Law, K. Jiang, S. Filippone, J. Perles, H. Yan and N. Martín, Photochemical site-selective synthesis of [70]methanofullerenes, *Chem. Commun.*, 2016, **52**, 12733–12736.

20 M. R. Cerón, M. Izquierdo, A. Aghabali, J. A. Valdez, K. B. Ghiassi, M. M. Olmstead, A. L. Balch, F. Wudl and L. Echegoyen, Tethered Bisadducts of C_{60} and C_{70} with Addends on a Common Hexagonal Face and a 12-Membered Hole in the Fullerene Cage, *J. Am. Chem. Soc.*, 2015, **137**, 7502–7508.

21 A. Aghabali, S. Jun, M. M. Olmstead and A. L. Balch, Piperazine Functionalization of C_{70} for Incorporation into Supramolecular Assemblies, *Chem. – Eur. J.*, 2016, **22**, 18908–18915.

22 C. Thilgen and F. Diederich, The Higher Fullerenes: Covalent Chemistry and Chirality, in *Fullerenes and Related Structures*, ed. A. Hirsch, Topics in Current Chemistry, Springer, Berlin, Heidelberg, 1999, pp. 135–171.

23 H. L. Hou, Z. J. Li, T. Sun and X. Gao, Preparation of a C_{70} Bis-heterocyclic Derivative with High Chemio- and Regioselectivity, *J. Org. Chem.*, 2015, **80**, 5315–5319.

24 P. Jin, L. Yang, C. Liu, M. Chen, Q. Hou, L. Li and Y. Zhao, A comparative study on the N-heterocyclic carbene adducts of I_h-C_{60}, D_{5h}-C_{70} and $Sc_3N@I_h$-C_{80}, *Phys. Chem. Chem. Phys.*, 2017, **19**, 17598–17606.

25 K. Liosi, A. Romero-Rivera, O. Semivrazhskaya, C. D. Caniglia, M. Garcia-Borràs, N. Trapp, S. Osuna and Y. Yamakoshi, Site-Selectivity of Prato Additions to C_{70}: Experimental and Theoretical Studies of a New Thermodynamic Product at the dd-[5,6]-Junction, *Org. Lett.*, 2019, **21**(13), 5162–5166.

26 M. Saito, H. Shinokubo and H. Sakurai, Figuration of bowl-shaped π-conjugated molecules: properties and functions, *Mater. Chem. Front.*, 2018, **2**, 635–661.

27 M. Lamanec, R. Lo, D. Nachtigallová, A. Bakandritsos, E. Mohammadi, M. Dračínský, R. Zbořil, P. Hobza and W. Wang, The Existence of a N→C Dative Bond in the C_{60}–Piperidine Complex, *Angew. Chem., Int. Ed.*, 2021, **60**, 1942–1950.

28 E. Kleinpeter, S. Klod and A. Koch, Endohedral and external through-space shieldings of the fullerenes C_{50}, C_{60}, C_{60}^{6-}, C_{70}, and C_{70}^{6-} – Visualization of (anti)aromaticity and their effects on the chemical shifts of encapsulated nuclei, *J. Org. Chem.*, 2008, **73**, 1498–1507.

29 E. F. Sheka, 'Chemical portrait' of fullerene molecules, *J. Struct. Chem.*, 2006, **47**, 593–599.

30 E. Chamorro, P. Pérez and L. R. Domingo, On the nature of Parr functions to predict the most reactive sites along organic polar reactions, *Chem. Phys. Lett.*, 2013, **582**, 141–143.

31 L. R. Domingo, P. Pérez and J. A. Sáez, Understanding the local reactivity in polar organic reactions through electrophilic and nucleophilic Parr functions, *RSC Adv.*, 2013, **3**, 1486–1494.

32 W. Yang and W. J. Mortier, The Use of Global and Local Molecular Parameters for the Analysis of the Gas-Phase Basicity of Amines, *J. Am. Chem. Soc.*, 1986, **108**, 5708–5711.

33 S. L. Wu, Z. J. Li and X. Gao, Dithiolation of [70]Fullerene with Aliphatic Primary Thiols in the Presence of *n*-Butylamine via Aerobic Oxidation Reaction, *J. Org. Chem.*, 2019, **84**, 3045–3054.

34 S. H. Li, Z. J. Li, W. W. Yang and X. Gao, Controlled Synthesis of C_{70} Equatorial Multiadducts with Mixed Addends from an Equatorial Diadduct: Evidence for an Electrophilic Carbanion, *Org. Lett.*, 2018, **20**, 2328–2332.

35 M. Li, X. He, B. Wang, D. Zhao, C. Rong, P. K. Chattaraj and S. Liu, Changes in Structure and Reactivity of Ng2 Encapsulated in Fullerenes: A Density Functional Theory Study, *Front. Chem.*, 2020, **8**, 566.

36 C. Adamo and V. Barone, Toward reliable density functional methods without adjustable parameters: The PBE0 model, *J. Chem. Phys.*, 1999, **110**, 6158–6170.

37 S. Grimme, J. Antony, S. Ehrlich and H. Krieg, A consistent and accurate ab initio parametrization of density functional dispersion correction (DFT-D) for the 94 elements H-Pu, *J. Chem. Phys.*, 2010, **132**, 154104.

38 S. Grimme, S. Ehrlich and L. Goerigk, Effect of the damping function in dispersion corrected density functional theory, *J. Comput. Chem.*, 2011, **32**, 1456–1465.

39 F. Weigend, Hartree-fock exchange fitting basis sets for H to Rn, *J. Comput. Chem.*, 2008, **29**, 167–175.

40 M. J. Frisch, G. W. Trucks, H. B. Schlegel, G. E. Scuseria, M. A. Robb, J. R. Cheeseman, G. Scalmani, V. Barone, G. A. Petersson, H. Nakatsuji, X. Li, M. Caricato, A. Marenich, J. Bloino, B. G. Janesko, R. Gomperts, B. Mennucci, H. P. Hratchian, J. V. Ortiz, A. F. Izmaylov, J. L. Sonnenberg, D. Williams-Young, F. Ding, F. Lipparini, F. Egidi, J. Goings, B. Peng, A. Petrone, T. Henderson, D. Ranasinghe, V. G. Zakrzewski, J. Gao, N. Rega, G. Zheng, W. Liang, M. Hada, M. Ehara, K. Toyota, R. Fukuda, J. Hasegawa, M. Ishida, T. Nakajima, Y. Honda, O. Kitao, H. Nakai, T. Vreven, K. Throssell, J. A. Montgomery, Jr., J. E. Peralta, F. Ogliaro, M. Bearpark, J. J. Heyd, E. Brothers, K. N. Kudin, V. N. Staroverov, T. Keith, R. Kobayashi, J. Normand, K. Raghavachari, A. Rendell, J. C. Burant, S. S. Iyengar, J. Tomasi, M. Cossi, J. M. Millam, M. Klene, C. Adamo, R. Cammi, J. W. Ochterski, R. L. Martin, K. Morokuma, O. Farkas, J. B. Foresman and D. J. Fox, *Gaussian 09, Revision D.01*, Gaussian, Inc., Wallingford CT, 2016.

41 A. Klamt, G. Schüürmann and COSMO, A New Approach to Dielectric Screening in Solvents with Explicit Expressions for the Screening Energy and Its Gradient, *J. Chem. Soc., Perkin Trans. 2*, 1993, 799–805.

42 J. D. Chai and M. Head-Gordon, Long-Range Corrected Hybrid Density Functionals with Damped Atom-Atom Dispersion Corrections, *Phys. Chem. Chem. Phys.*, 2008, **10**, 6615–6620.

43 F. Weigend and R. Ahlrichs, Balanced Basis Sets of Split Valence, Triple Zeta Valence and Quadruple Zeta Valence Quality for H to Rn: Design and Assessment of Accuracy, *Phys. Chem. Chem. Phys.*, 2005, **7**, 3297–3305.

44 K. Wolinski, J. F. Hinton and P. Pulay, Efficient implementation of the gauge-independent atomic orbital method for NMR chemical shift calculations, *J. Am. Chem. Soc.*, 1990, **112**, 8251–8260.

45 M. Kaupp, M. Behl and V. G. Malkin, *Calculation of NMR and EPR Parameters: Theory and Applications*, Wiley-VCH, Weinheim, 2004.

46 J. Kaminský, M. Buděšínský, S. Taubert, P. Bouř and M. Straka, Fullerene C_{70} characterization by ^{13}C NMR and the importance of the solvent and dynamics in spectral simulations, *Phys. Chem. Chem. Phys.*, 2013, **15**, 9223–9230.

47 R. M. Parrish, L. A. Burns, D. G. A. Smith, A. C. Simmonett, A. E. DePrince, E. G. Hohenstein, U. Bozkaya, A. Y. Sokolov, R. Di Remigio, R. M. Richard, J. F. Gonthier, A. M. James, H. R. McAlexander, A. Kumar, M. Saitow, X. Wang, B. P. Pritchard, P. Verma, H. F. Schaefer, K. Patkowski, R. A. King, E. F. Valeev, F. A. Evangelista, J. M. Turney, T. D. Crawford and C. D. Sherrill, Psi4 1.1: An Open-Source Electronic Structure Program Emphasizing Automation, Advanced Libraries, and Interoperability, *J. Chem. Theory Comput.*, 2017, **13**, 3185–3197.

48 MOPAC2016, James J. P. Stewart, Stewart Computational Chemistry, Colorado Springs, CO, USA, http://OpenMOPAC.net, 2016.

49 J. Řezáč, Cuby: An integrative framework for computational chemistry, *J. Comput. Chem.*, 2016, **37**, 1230–1237.

50 A. Pecina, S. Haldar, J. Fanfrlík, R. Meier, J. Řezáč, M. Lepšík and P. Hobza, SQM/COSMO Scoring Function at the DFTB3-D3H4 Level: Unique Identification of Native Protein-Ligand Poses, *J. Chem. Inf. Model.*, 2017, **57**, 127–132.

51 H. J. C. Berendsen, J. P. M. Postma, W. F. Van Gunsteren, A. Dinola and J. R. Haak, Molecular dynamics with coupling to an external bath, *J. Chem. Phys.*, 1984, **81**, 3684–3690.

52 F. Neese, A. Hansen and D. G. Liakos, Efficient and Accurate Approximations to the Local Coupled Cluster Singles Doubles Method Using a Truncated Pair Natural Orbital Basis, *J. Chem. Phys.*, 2009, **131**, 064103.

53 F. Neese, A. Hansen, F. Wennmohs and S. Grimme, Accurate Theoretical Chemistry with Coupled Pair Models, *Acc. Chem. Res.*, 2009, **42**, 641.

54 W. B. Schneider, G. Bistoni, M. Sparta, M. Saitow, C. Riplinger, A. A. Auer and F. Neese, Decomposition of Intermolecular Interaction Energies within the Local Pair Natural Orbital Coupled Cluster Framework, *J. Chem. Theory Comput.*, 2016, **12**, 4778.

55 A. Bauzá, T. J. Mooibroek and A. Frontera, Tetrel-bonding interaction: Rediscovered supramolecular force?, *Angew. Chem., Int. Ed.*, 2013, **52**, 12317–12321.

56 A. M. S. Riel, R. K. Rowe, E. N. Ho, A. C. C. Carlsson, A. K. Rappé, O. B. Berryman and P. S. Ho, Hydrogen Bond Enhanced Halogen Bonds: A Synergistic Interaction in Chemistry and Biochemistry, *Acc. Chem. Res.*, 2019, **52**, 2870–2880.

57 G. A. Jeffrey, Hydrogen-Bonding: An update, *Crystallogr. Rev.*, 2003, **9**, 135–176.

58 S. Toyota, Y. Yamamoto, K. Wakamatsu, E. Tsurumaki and A. Muñoz-Castro, Nano-Saturn with an Ellipsoidal Body: Anthracene Macrocyclic Ring–C_{70} Complex, *Bull. Chem. Soc. Jpn.*, 2019, **92**, 1721–1728.

59 J. Calbo, R. Viruela, E. Ortí and J. Aragó, Relationship between Electron Affinity and Half-wave Reduction Potential: A Theoretical Study on Cyclic Electron-Acceptor Compounds, *Chem. Phys. Chem.*, 2016, **17**, 3881–3890.

60 J. C. Gonzalez, S. Mondal, F. Ocayo, R. Guajardo-Maturana and A. Muñoz-Castro, Nature of C60 and C70 Fullerene Encapsulation in a Porphyrin-and Metalloporphyrin-Based Cage. Insights from Dispersion Corrected DFT Calculations, *Int. J. Quantum Chem.*, 2020, **120**, e26080.

61 C. O. Ulloa, M. Ponce-Vargas and A. Muñoz-Castro, Formation of Coinage-Metal···Fullerene Adducts. Evaluation of the Interaction Nature between Triangular Coinage Metal

Complexes (M3 = Cu, Ag, and Au) and C60 through Relativistic Density Functional Theory Calculations, *J. Phys. Chem. C*, 2018, **122**, 25110–25117.

62 D. Chen, D. W. Szczepanik, J. Zhu, A. Muñoz-Castro and M. Solà, Aromaticity Survival in Hydrofullerenes: The Case of $C_{66}H_4$ with Its π-Aromatic Circuits, *Chem. – Eur. J.*, 2021, **27**, 802–808.

63 P. Larkin, *Infrared and Raman Spectroscopy: Principles and Spectral Interpretation*, Elsevier, Waltham, MA, USA, 2011.

64 Y. S. Mary, H. T. Varghese, C. Y. Panicker, M. Girisha, B. K. Sagar, H. S. Yathirajan, A. A. Al-Saadi and C. Van Alsenoy, Vibrational spectra, HOMO, LUMO, NBO, MEP analysis and molecular docking study of 2,2-diphenyl-4-(piperidin-1-yl)butanamide, *Spectrochim. Acta, Part A*, 2015, **150**, 543–556.

65 Y. Li and L. Gan, Selective Addition of Secondary Amines to C_{60}: Formation of Penta- and Hexaamino[60]fullerenes, *J. Org. Chem.*, 2014, **79**, 8912–8916.

66 R. C. Haddon, Chemistry of the Fullerenes: The Manifestation of Strain in a Class of Continuous Aromatic Molecules, *Science*, 1993, **261**, 1545–1550.

67 K. H. Lee, C. Lee, J. Kang, S. S. Park, J. Lee, S. K. Lee and D. K. Bohme, Preferential Site of Attack on Fullerene Cations: Frontier Orbitals and Rate Coefficients, *J. Phys. Chem. A*, 2006, **110**, 11730–11733.

68 B. Hong-Cun, Z. Ying, Y. Ni-Ni, J. Yong-Qiang, Q. Wei-Ye and H. Yuan-He, New Solution Method of Pi-Orbital Axis Vector and Its Applications in Fullerenes and Carbon Nanotubes, *Chin. J. Struct. Chem.*, 2013, **32**, 695–703.

Check for updates

The stability of covalent dative bond significantly increases with increasing solvent polarity

Rabindranath Lo [1,2], Debashree Manna[1,3], Maximilián Lamanec[1,4], Martin Dračínský [1], Petr Bouř[1], Tao Wu[1], Guillaume Bastien[1], Jiří Kaleta [1], Vijay Madhav Miriyala[1,2], Vladimír Špirko[1], Anna Mašínová[1], Dana Nachtigallová[1,5 ✉] & Pavel Hobza [1,5 ✉]

It is generally expected that a solvent has only marginal effect on the stability of a covalent bond. In this work, we present a combined computational and experimental study showing a surprising stabilization of the covalent/dative bond in Me_3NBH_3 complex with increasing solvent polarity. The results show that for a given complex, its stability correlates with the strength of the bond. Notably, the trends in calculated changes of binding (free) energies, observed with increasing solvent polarity, match the differences in the solvation energies (ΔE^{solv}) of the complex and isolated fragments. Furthermore, the studies performed on the set of the dative complexes, with different atoms involved in the bond, show a linear correlation between the changes of binding free energies and ΔE^{solv}. The observed data indicate that the ionic part of the combined ionic-covalent character of the bond is responsible for the stabilizing effects of solvents.

[1] Institute of Organic Chemistry and Biochemistry, Czech Academy of Sciences, Flemingovo náměstí 542/2, 16000 Prague, Czech Republic. [2] Regional Centre of Advanced Technologies and Materials, Czech Advanced Technology and Research Institute, Palacký University Olomouc, Křížkovského 511/8, 77900 Olomouc, Czech Republic. [3] Maulana Abul Kalam Azad University of Technology, West Bengal (formerly known as West Bengal University of Technology) Simhat, Haringhata, West Bengal 741249, India. [4] Department of Physical Chemistry, Palacký University Olomouc, 17. listopadu 12, 771 46 Olomouc, Czech Republic. [5] IT4Innovations, VŠB-Technical University of Ostrava, 17. listopadu 2172/15, 70800 Ostrava-Poruba, Czech Republic. ✉email: dana.nachtigallova@uochb.cas.cz; pavel.hobza@uochb.cas.cz

It is well known that the binding character between the two fragments A and D determines the stability of the $(A–D)$ complex: the covalent bond (CB) complexes, realized by electron-sharing mechanisms, are generally more stable than the weaker non-covalent (NC) complexes. The dative bond (DB) complexes, also known as the donor–acceptor, coordinate-covalent, semi-polar, charge-transfer complexes, are bound by the specific type of a CB in which two electrons shared within the bond are provided by one fragment (donor, D) to the other (acceptor, A). A solvent further modifies the complex strength. While the stabilities of the former CB complex usually do not change significantly, the NC complexes are often considerably destabilized in the solvent.

The following equations can rationalize the effect of the solvent:

$$E_{stab} = E(A - D) - [E(A) + E(D)] \quad (1)$$

$$E_{stab}^{solv} = E(A - D)^{solv} - \left[E(A)^{solv} + E(D)^{solv} \right] \quad (2)$$

which describe the binding (stability) energies of the complex in the gas phase and solvent, respectively. The relative values of stabilization energies of isolated fragments A and D with respect to the complex $(A–D)$ decide whether the solvent stabilizes/destabilizes the complex due to the different polarity. These values directly correlate with a particular complex's solvation energy (E^{solv}) in various solvents. For example, the stabilization of the ion-pair complexes gradually decreases with increasing solvent polarity[1], as the solvation of bare ions is larger than that of the neutral complex. Similar destabilization is observed in hydrogen-bonded and other NC complexes[2]. Intuitively, a larger solvation of the complex would require a significant charge redistribution in the complex as opposed to a smaller solvation of the isolated fragments; however, this was not observed in the majority of the NC complexes. A specific character of the DBs (see below) raises the question of the effect of the solvent on the stability of DB complexes.

The discussion on the DB goes back to Lewis's concept of base and acid[3] as species that share two electrons of the base to form a DB. This was followed by the work of Pauling[4], who described the DB as a "double bond" with one ionic and one covalent component. Further work by Haaland[5] proposed a distinction between the dative and CB complex with respect to its dissociation. In the case of the DB complex, the bond breaks heterolytically, yielding neutral, diamagnetic species, while the homolytic bond cleavage prevails in the case of the CB complex. Haaland discussed the nature of the DB for complexes which include main group metals. Further development, primarily done by Frenking, shows that the DB occurs much more frequently than initially thought in the main-group compounds, and it is a common feature of the s/p block atoms[6–14]. Relevant discussions on the nature and concept of the DB continue to appear in the literature[15,16].

The character of the DB, which combines the covalent and ionic character, is described by the wavefunction[17,18],

$$\Psi_{dative}\left(D^+ - A^-\right) = a\Psi_{covalent}(D - A) + b\Psi_{ionic}\left(D^+, A^-\right) \quad (3)$$

Since a charge transfer from the electron donor to the electron acceptor provides a measure of the ionic character, it will be used in further discussion. Electron transfer dynamics in the DB complexes have been observed experimentally employing spectroscopic studies with femtosecond resolution[18]. The character of DB complexes and their stabilities have been addressed in several computational studies[17,19–22].

The unusual behavior of DBs upon the surrounding changes of the environment is reflected by the sensibility of the bond distances when comparing the gas and solid states[23–25]. They

sometimes differ by more than 1 Å, which contradicts the "normal" CB where the corresponding change is insignificant[19]. To our knowledge, the solvent effects on DB complex stability and the strength of the bond have not yet been discussed. However, their understanding, including the DB characterization in various solvents, is of great importance, and has led to growing interest in this type of bond. As discussed in a recent review (see ref. [6] and references therein), the concept of a DB has been addressed in connection to new classes of compounds.

The complex stabilization energy (correlated with the $A–D$ bond dissociation energy (D_e)) and the strength of the $A–D$ bond can characterize the stability of the complex. However, as discussed below, these properties do not always directly correlate[9,13,26].

The bond strength evaluation is not a trivial task, as it is not experimentally observable for polyatomic molecules. Thus, it can be obtained only via the evaluation of other quantities. It has been shown in several cases[9,27] that neither the bond dissociation energy (D_e), the vibrationally corrected zero-point energy (D_0), nor the activation energy of the bond-breaking process to fragments A and D (E^{act}) reflect their bond strength/energy. This is due to possible modifications of the electronic states of the fragments in the $(A–D)$ and separated A and D states. The widely accepted assumption that stronger bonds are shorter than weaker ones is not generally correct.

Moreover, due to the delocalization of the normal coordinates, traditionally used vibrational analyses do not provide direct information on the stretching force constants and fundamental frequency of a particular bond, and consequently, its strength[9,27]. To overcome this problem, Konkoli, Larsson and Cremer[28–31] transformed the delocalized normal modes into new vibrational modes ("adiabatic internal modes"). Alternatively, one can rely on the so-called HBJ approach[32], which is based on introducing a non-rigid reference configuration of the molecular atoms which essentially follows the respected vibrational motion. This approach accounts exactly for anharmonicity of the motion and also allows to account easily for the most important kinematic interaction terms.

The combined ionic-covalent character of the DB indicates that the solvent might significantly affect the strength and stability of the DB complexes. Recently, we investigated the DB complexes between electron acceptors (C_{60}, C_{20}, C_{70}, cyclo[n]carbons, graphene, and single-wall nanotubes) and electron donors (piperidine, piperidine dimer, phosphines) using the tools of computational chemistry and several experimental techniques to characterize the DBs in terms of the charge transfer and stabilization energy[33–38]. The studies are also performed in a solvent, providing surprising findings on the solvent effects that motivated a thorough survey of this phenomenon.

The current paper reports on a combined vibrational Raman and NMR spectroscopic and computational investigation of the solvent effect on the complex stability and bond strength in the Me_3NBH_3 complex, a modification of a prototype covalent dative NH_3–BH_3 complex. The vibrational spectra provide information on the character of DBs in terms of vibration frequencies related to DB force constants. In the NMR experiment, the indirect spin–spin coupling (J-coupling) is mediated by involved electrons. It is thus related to chemical bonding (in contrast to direct coupling, which is a through-space interaction)[39] and is used to discuss the changes in B–N distances. However, the magnitude of the J-coupling cannot be directly correlated to the bond strength. The solvent's effect is further investigated through computational studies for complexes between larger electron acceptors (C_{18}, C_{60} and its derivatives, and C_{70}) and electron donors piperidine (pip) and tris(1-pyrrolidinyl)phosphine (P(pyrr)$_3$).
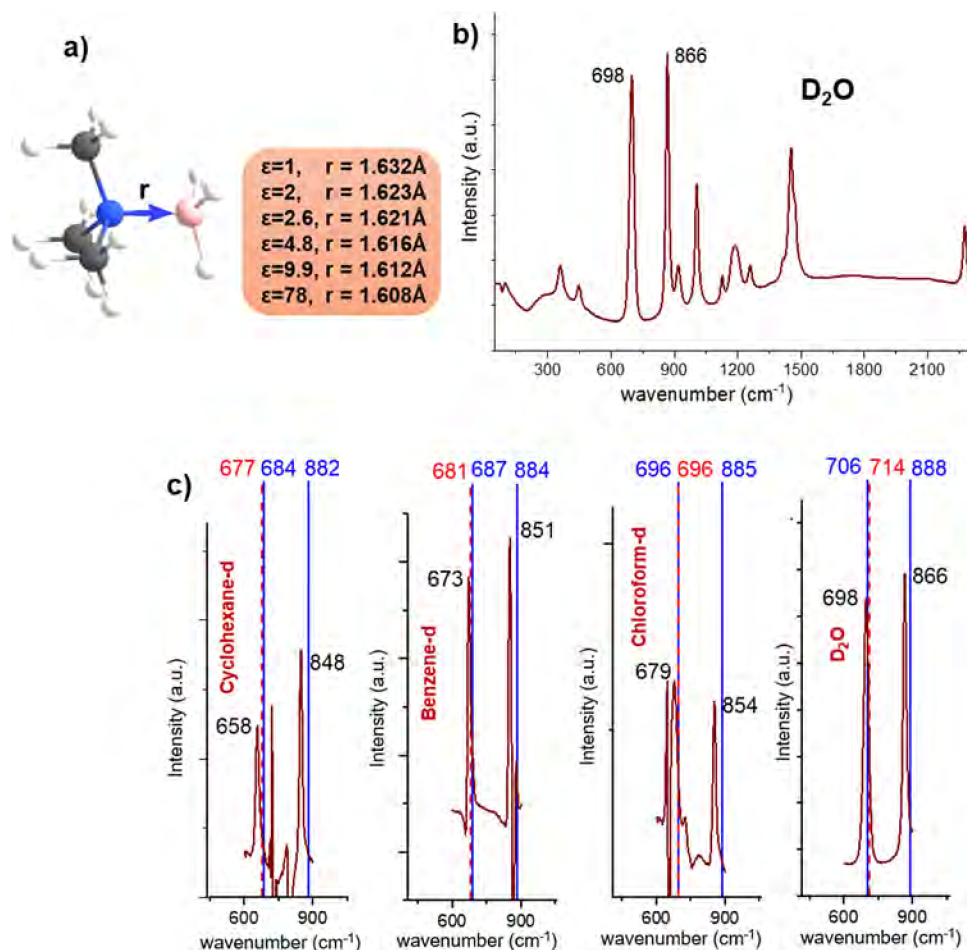
Fig. 1 The calculated and observed structural and spectroscopic data of Me₃NBH₃. **a** The optimized geometry of Me_3NBH_3. The B–N distances (r) are given in the gas phase ($\varepsilon = 1$) and various solvents, cyclohexane ($\varepsilon = 2.0$), carbon disulfide ($\varepsilon = 2.6$), chloroform ($\varepsilon = 4.8$), o-dichlorobenzene ($\varepsilon = 9.9$), and water ($\varepsilon = 78.0$); **b** the Raman spectra of Me_3NBH_3 measured in D_2O; **c** the relevant part of the Raman spectra ranging 450–1050 cm^{-1} in various solvents. The PBE0-D3/def2-QZVP calculated harmonic (in blue color) and anharmonic (in red color) frequencies are shown (C: gray, N: blue, H: white, B: pink).

Results and discussion

Me₃NBH₃. Figure 1a displays the structure of Me_3NBH_3 with the optimized B–N distance obtained in the gas phase ($\varepsilon = 1.0$) and in various solvents, including cyclohexane ($\varepsilon = 2.0$), carbon disulfide ($\varepsilon = 2.6$), chloroform ($\varepsilon = 4.8$), o-dichlorobenzene ($\varepsilon = 9.9$), and water ($\varepsilon = 78.0$). Similar to findings discussed by Bühl et al.[40] and Jonas et al.[19], the distance gradually shortens upon increasing solvent polarity. Notice that MD simulations in explicit solvents $CHCl_3$ and CS_2 (see the SI) fully confirmed this finding.

As stated in ref. [40], the changes in the geometry in the solvent influence the chemical shift observed in the NMR spectra. However, it is difficult to distinguish these geometry-related chemical-shift changes from those caused by the magnetic shielding of the solvent molecules. Therefore, we rely on indirect NMR coupling rather than chemical shift. Supplementary Figure 1 displays the NMR spectrum of Me_3NBH_3 obtained in CD_3CN; the values of indirect one-bond B–N and B–H couplings in various solvents with dielectric constants ranging from 2 to 78 are presented in Supplementary Table 1. The information obtained from the B–H couplings is only indirectly connected to the observed DB. However, the almost linear correlation between the measured J(N–B) and J(B–H) values (Supplementary Fig. 1) justifies using both data for further discussion. Table 1 displays the values of experimental and calculated spin–spin couplings

related to the B–N bond in selected solvents. The calculations underestimate the observed values, with the error in the range of 0.6–0.9 Hz, with the exception of a more significant error of 2.4 Hz in water. Despite these differences, both sets of results show increased spin–spin coupling with increasing solvent polarity. Further calculations show that the Fermi contact couplings are the main contributors to the total spin–spin couplings, with the same dependence on the solvent polarity (Table 1). Both the total spin–spin couplings and Fermi contact parts linearly correlate with the calculated bond distances obtained in the various solvents (Supplementary Fig. 2).

Figure 1b shows the representative Raman spectrum of Me_3NBH_3 measured in D_2O with the two most intensive peaks at 698 and 866 cm^{-1}, mainly due to B–N and C–N stretching vibrations. The relevant part of the Raman spectra in the range 450–1050 cm^{-1} of Me_3NBH_3 in cyclohexane, benzene, chloroform, and water and their assignments are given in Fig. 1c, Table 2 and Supplementary Table 2. The potential energy distribution calculations assign the lower frequency peaks mainly to the N–B stretching (65–69%), while the higher frequency peaks have small contributions (12–18%) and are primarily due to the C–N stretching vibrations (67–75%). The calculations of vibrational spectra within the harmonic approximation overestimate the frequencies more significantly for high-frequency peaks (by 22–34 cm^{-1}); however, they are more consistent than

Table 1 The experimental B–N indirect coupling (^1J(B–N)$_{exp}$), calculated B–N distance (R_{B-N}), B–N indirect coupling (^1J(B–N)$_{calc}$, deviation from the experiment in parenthesis) and Fermi contact coupling ($^1J_{FC}$(B–N)$_{calc}$) of Me$_3$NBH$_3$.

Solvent	ε	^1J(B–N)$_{exp}$ Hz	^1J(B–N)$_{calc}$ Hz	$^1J_{FC}$(B–N)$_{calc}$ Hz	R_{B-N} Å
Cyclohexane	2.0	5.3	4.4 (0.9)	4.13	1.623
Benzene	2.3	6.2	4.6 (0.6)	4.31	1.622
Acetone	20.5	6.8	5.9 (0.9)	5.69	1.610
Acetonitrile	35.7	7.1	6.0 (1.1)	5.77	1.609
Water	78.0	8.5	6.1 (2.4)	5.85	1.608

The values are calculated at the PBE0/def2-QZVP level.

Table 2 Observed fundamental frequencies (ν_{obs}), harmonic frequencies (ν_{harm}), anharmonic (ν_{anharm}), and scaled anharmonic (ν_{anharm}^{scal}) vibrational frequencies calculated using the HBJ approach with rigid-bender reduced masses (μ_{ss}) and scaled masses (μ_{ss}/1.0465), respectively (frequencies given in cm^{-1}, the scaling factor 1.0465 chosen to reproduce the experimental B–N fundamental frequency pertaining to water).

Solvent	ε	ν_{obs}	PED	ν_{harm} ($\Delta\nu$)	ν_{anharm} ($\Delta\nu$)	ν_{anharm}^{scal} ($\Delta\nu$)	μ_{ss}
Gas phase	1.0			670	656	642	0.12854
Cyclohexane	2.0	658	69 (18)	684 (26)	677 (19)	663 (5)	0.12843
Benzene	2.3	673	69 (19)	687 (14)	681 (8)	666 (-7)	0.12840
Chloroform	4.8	679	67 (22)	696 (17)	696 (17)	681 (2)	0.12827
Water	78.0	698	65 (26)	706 (8)	714 (16)	698	0.12817

The deviation from the experiment ($\Delta\nu$) and assignment of B–N stretching with the potential energy distributions, PED% (C–N stretching in parenthesis) of the normal vibrational modes of Me$_3$NBH$_3$ in various solvents. The values are calculated at the PBE0-D3/def2-QZVP level.
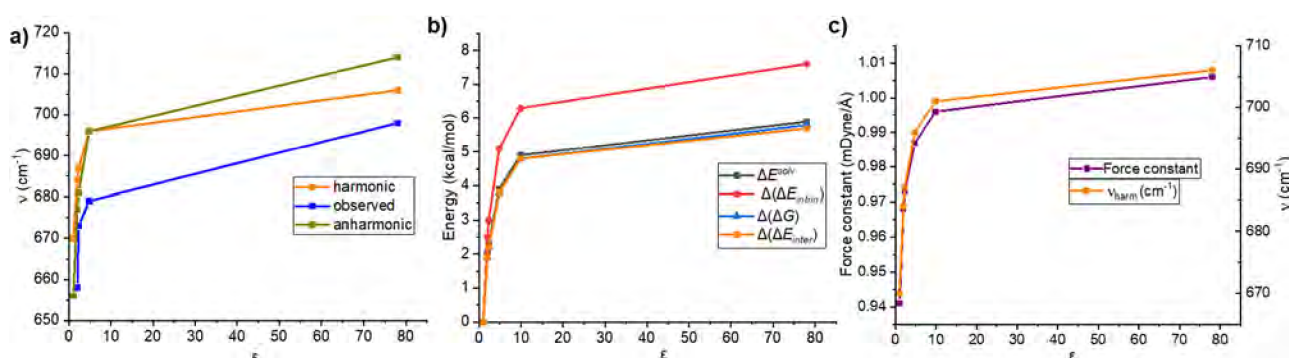
Fig. 2 The correlation between the observed and calculated properties of Me$_3$NBH$_3$ and the solvent polarity expressed by the dielectric constant ε. a The observed and calculated an/harmonic frequencies versus ε; **b** the calculated $\Delta(\Delta G)$, $\Delta(\Delta E_{inter})$, $\Delta(\Delta E_{intrin})$, ΔE^{solv} versus ε; and **c** the force constant and vibration frequency of B–N stretching mode versus ε. The values are calculated at the PBE0-D3/def2-QZVP level.

low-frequency peaks, with errors in the range of 8–26 cm^{-1}. Note that the effect of anharmonicity is the largest for H$_2$O. In addition, we observed a similar decline of calculated harmonic frequencies from the experiment, as found in the case of J(B–N) values. The dependence of the observed and the calculated harmonic and anharmonic frequencies on the solvent polarity is illustrated in Fig. 2, showing a gradual blue-shift with increasing solvent polarity with the largest changes in the region up to $\varepsilon = 4.8$. Both the anharmonic and harmonic calculated frequencies thus provide reliable values in terms of the solvation trends and can be used for further discussion.

Table 3 summarizes the results of the calculated complex stabilities of Me$_3$NBH$_3$ in various solvents. Following the discussion on the characterization of the bond strength (see "Introduction"), we characterized the complex in terms of the interaction energy (ΔE_{inter}), Gibbs free energy (ΔG) calculated at $T = 298$ K, and intrinsic energy (ΔE_{intrin}), which neglects deformation energies of the isolated monomers. The results show considerable stability of the complex even in the gas phase (ΔE_{inter} and ΔG of −41.8 and −24.9 kcal/mol, respectively). The

solvent further stabilizes the complex with respect to its polarity as presented for observed and calculated vibrational frequencies. The differences are most significant for the lower polarity solvents and become smaller once the solvent polarity reaches $\varepsilon \sim 10$. Table 3 also shows the values of ΔE^{solv}, i.e., the differences between the solvation energies of complexes and isolated monomers. Following the discussion in the Introduction, this term is expected to provide specific information on the solvent polarity effect on the complex stability. Figure 2 illustrates that an exact match exists between the changes in the binding free energies ($\Delta(\Delta G)$), intrinsic interaction energies ($\Delta(\Delta E_{intrin})$) and changes in solvation energies, (ΔE^{solv}). Thus, the latter can be used as a reliable indicator of the solvent effects on the dative-bond complex stability. Increasing ΔE^{solv} values can be rationalized by the inspection of the Ψ_{dative} wavefunction, which is a linear combination of $\Psi_{covalent}$ and Ψ_{ionic} (Eq. 3). With the increasing solvent polarity, the corresponding energy term of the covalent contribution changes only negligibly, while that of the ionic contributions significantly stabilizes. The values of the relative charge transfer (Q_{rel}, Table 3) and their almost linear

Table 3 The interaction energies (ΔE_{inter}, kcal/mol), thermodynamics characteristics (ΔG, kcal/mol), differences in the solvation energies (ΔE^{solv}, kcal/mol), intrinsic energies (ΔE_{intrin}, kcal/mol), force constants (k^c, mDyne/Å), and the relative charge transfer (Q_{rel}) of Me$_3$NBH$_3$ in various solvents.

Solvent	ε	ΔE_{inter}	ΔE_{intrin}	ΔG	ΔE^{solv}	k^c	Q_{rel}[a]
Gas phase	1.0	−41.8	−57.6	−24.9	0.0	0.941	0.0
Cyclohexane	2.0	−43.7	−60.1	−26.8	2.0	0.968	0.019
Chloroform	4.8	−45.6	−62.7	−28.7	3.9	0.987	0.032
O-dichlorobenzene	9.9	−46.6	−63.9	−29.7	4.9	0.996	0.038
Water	78.0	−47.5	−65.2	−30.7	5.9	1.006	0.043

The values are calculated at the PBE0-D3/def2-QZVP level.
[a]The values relate to Q in the gas phase (Q = 0.347).

correlation with ΔE^{solv} (Supplementary Fig. 3) nicely illustrate the solvent's effect on the ionic part of the bond.

According to the previous discussion, the stability of the complex in general does not reflect the strength of the bond connecting two fragments. Therefore, it is interesting to investigate whether complex stability and strength of the connecting bond correlate for this specific case. Importantly for this discussion, small changes in the Wiberg bond indexes within the whole range of ε, with the values of 0.58–0.62, indicate that the bond character does not change in investigated solvents. This provides arguments to discuss the correlation of the stability of DB complexes and the relevant bond strengths in terms ($\Delta(\Delta G)$, $\Delta(\Delta E_{inter})$) or ΔE^{solv} with changes in the intrinsic energies ($\Delta(\Delta E_{intrin})$) and force constant of the low-frequency vibrations, also listed in Table 3. Arguments for the validity of the use of ($\Delta(\Delta E_{intrin})$) values are based on the assumption that the low-frequency vibrations are mainly due to the B–N stretching with an almost constant contribution (65–67%, Table 2) to the normal mode motion. Figure 2 illustrates the dependences of all these characteristics and vibration frequency on the solvent polarity, showing almost exact matches in their trends. This observation allows us to conclude that there is a direct correlation between changes in the strength of the DB and the complex stability due to the solvation for a given DB complex. Notably, both values correlate with the ΔE^{solv} value, making it a reliable indicator of changes in complex stabilities with changes in solvent polarities.

Other DB complexes. Table 4 displays the values of ΔG calculated in the gas phase and o-dichlorobenzene ($\varepsilon = 9.9$), $\Delta(\Delta G)$ and ΔE^{solv} values for various DB complexes (see Supplementary Fig. 4). They were selected to include different types of the DB bond, i.e., N → B, N → C, P → B, and P → C bonds. The complexes represent a relatively large variation of their structures, including smaller systems, such as the prototype DB complex H$_3$B-NH$_3$, and large systems, e.g., C$_{60}$(CN)$_{18}$…P(pyrr)$_3$. The investigated complexes represent a large variety in terms of the polarity of their fragments. We thus considered non-polar electron donors C$_{60}$ as well as their highly polar modifications C$_{60}$(CN)$_4$, C$_{60}$(CN)$_{18}$, and C$_{60}$F$_{18}$. Regarding their stabilities based on Gibbs's free energies, the selection covered unstable complexes, e.g., C$_{60}$…pip$_2$, with $\Delta G_{gas} = 4.3$ kcal/mol up to complexes with higher stabilities, e.g., H$_3$B-PMe$_3$ with $\Delta G_{gas} = -31.8$ kcal/mol. In all cases, the solvent stabilized the complex. The values of ΔE^{solv} provided a very similar picture. The functionalization of the electron donor (NH$_3$) with the electron-donating CH$_3$ group leads to a larger complex stabilization in both gas phase and o-DCB. This effect is more pronounced in the gas phase. The functionalization of the electron acceptor (BH$_3$) with electron-withdrawing F atoms destabilizes the complex in both environments. The observed linear relation between $\Delta(\Delta G)$ and ΔE^{solv} of a particular bond type (N → B, N → C, P → C, see

Table 4 The thermodynamic characteristics calculated in the gas phase (ΔG_{gas}, kcal/mol), o-dichlorobenzene (ΔG_{o-DCB}, kcal/mol), their differences $\Delta(\Delta G)$, kcal/mol), and differences in the solvation energies (ΔE^{solv}, kcal/mol) of selected dative bond complexes.

	ΔG_{gas}	ΔG_{o-DCB}	$\Delta(\Delta G)$	ΔE^{solv}
N → B				
H$_3$B-NH$_3$	−19.5	−27.5	8.0	8.4
H$_3$B-NMe$_3$	−24.9	−29.7	4.8	4.9
F$_3$B-NH$_3$	−9.0	−19.1	10.1	11.3
F$_3$B-NMe$_3$	−13.6	−19.0	5.4	6.0
N → C				
C$_{60}$…pip$_2$	4.3	0.9	3.4	4.2
C$_{70}$…pip$_2$	1.8	−2.2	4.0	4.4
C$_{18}$…pip	−1.6	−15.3	13.7	15.5
P → B				
H$_3$B-PMe$_3$	−31.8	−36.1	4.3	4.5
P → C				
C$_{60}$…P(pyrr)$_3$	−0.7	−5.2	4.5	6.1
C$_{60}$F$_{18}$…P(pyrr)$_3$	−6.1	−10.1	4.0	5.5
C$_{60}$(CN)$_4$…P(pyrr)$_3$	−6.0	−9.3	3.3	4.7
C$_{60}$(CN)$_{18}$…P(pyrr)$_3$	−16.3	−16.5	0.2	0.7

The N → B and P → B complexes are calculated at the PBE0-D3/def2-QZVP, whereas C18 complex is computed at the ωB97XD/def2-TZVPP level. The other complexes are calculated at the PBE0-D3BJ/def2-TZVPP level.

Supplementary Fig. 5) indicates that for a given DB, the values of ΔE^{solv} follow almost the same trends as $\Delta(\Delta G)$, and thus can serve as a direct indicator of the solvent effect on the DB complexes.

In summary, it is generally assumed that the complexes decrease their stability in the solvent compared to the gas phase. These changes are small in the complexes bound via "normal" CBs, while that can be significant in NC complexes. The specificity of the DB, which combines covalent and ionic characters, connected with a substantial charge transfer character, opens the question of the solvent polarity of DB complexes. Our calculations in different solvent media show their surprising effects on the DB character:

- All complexes increased their stability in solvent compared to the gas phase. Moreover, for the same bond types (N → C, N → B, P → B, and P → C), increasing stabilities correlate linearly with the differences in solvation energies of the complexes and isolated fragments.
- The combined experimental and computational studies performed for Me$_3$NBH$_3$ show that increasing polarity of the solvent correlates not only with the larger complex stability, evaluated using interaction energies and Gibb's free energies, but also with a stronger DB, evaluated through intrinsic energies, vibrational frequencies, and

force constant. Furthermore, the relative values of the charge transfer correlate with an increasing ionic character of the complex in polar solvents connected to a smaller N–B separation, which stabilizes the energy corresponding to the ionic part of the bond.

Methods

Calculations. The structures of the DB complexes were optimized at the DFT-D level, employing the PBE0-D3 functional[41,42], using the def2-QZVP basis set[43] for H_3NBH_3, Me_3NBH_3, H_3NBF_3, Me_3NBF_3 and Me_3PBH_3 and def2-TZVPP basis set for other systems, respectively. The reliability of the DFT-D approach was justified by a comparison of binding energies calculated at the CCSD(T)/cc-pVTZ level for H_3NBH_3 and Me_3NBH_3. All CCSD(T) results of interaction energies were corrected for the basis set superposition error. Gibbs's free energies were calculated at the temperature $T = 298$ K.

The CCSD(T)/cc-pVTZ and DFT-D binding energies of NH_3BH_3 equal 33.0 and 35.3 kcal/mol, respectively, both in good agreement with the previously reported benchmark value of 31.6 kcal/mol calculated with the CCSD(F12)(T)/CBS approach[16]. The T1 diagnostic value of 0.008 indicates that the complex is predominantly single reference in nature.

The methyl substitution of nitrogen substantially increases its donor ability, increasing binding energy Me_3NBH_3. The binding energy is 41.9 kcal/mol and 41.8 kcal/mol at the CCSD(T)/cc-pVTZ and DFT-D/QZVP, respectively, justifying the use of the latter approach. Note also that the present DFT-D approximation was shown to provide reasonably accurate binding energies and geometries for DAT20 dataset containing 20 DB complexes[16].

The total interaction energies are calculated from the fully optimized structures of complex and fully optimized isolated monomers using the following equation:

$$\Delta E_{inter} = E_{complex} - E^i_{monomer1} - E^i_{monomer2} \qquad (4)$$

The intrinsic interaction energy (ΔE_{intrin}), calculated as a difference between energy of the optimized complex and the sum of the energies of subsystems with geometries taken from the optimized complex geometry.

$$\Delta E_{intrin} = E_{complex} - E_{monomer1} - E_{monomer2} \qquad (5)$$

The solvent effects were included using the continuous model[44], in which the specific solvent is characterized by its dielectric constant ε. The calculations were performed in the gas phase ($\varepsilon = 1.0$) and various solvents, cyclohexane ($\varepsilon = 2.0$), benzene ($\varepsilon = 2.3$), carbon disulfide ($\varepsilon = 2.6$), chloroform ($\varepsilon = 4.8$), 1,2-dichlorobenzene ($\varepsilon = 9.9$), and water ($\varepsilon = 78.0$). The solvation energy (E^{solv}) of the system in a particular solvent is calculated as a difference between the energy of the optimized system in that solvent and the energy of the same geometry in the gas phase. Molecular dynamics studies with the discrete solvent model were performed for selected systems to check for the reliability of the continuous solvent model. In particular, the MD simulations were performed for Me_3NBH_3 in vacuo and embedded in a cluster of 49 molecules of chloroform and 49 molecules of carbon disulfide.

The bond properties (Wiberg bond indices and charge transfer) were evaluated using the NBO analyses[45]. Although the partial charges used for the charge transfer description are not well defined, and their values depend on the method, they can be used to obtain relative values in different solvents.

Vibrational frequencies. The sought vibrational energies associated with the B–N stretching motion are obtained by solving the Schrödinger equation for the following vibrational HBJ Hamiltonian[32],

$$H_{con} = -\frac{1}{2}\mu_{ss}J_s^2 + \frac{1}{2}(J_s\mu_{ss})J_s + \frac{1}{2}\mu^{\frac{1}{4}}\left\{J_s\mu_{ss}\mu^{-\frac{1}{2}}\left[J_s\mu^{\frac{1}{4}}\right]\right\} + V(s), \qquad (6)$$

where $J_s = -i\hbar\left(\frac{d}{ds}\right)$, $\mu_{ss}(s)$ is the B–N stretching component of the tensor that is the inverse of the 4×4 generalized molecular inertia tensor, μ is the determinant of the matrix $[\mu_{\alpha,\beta}]$ ($\alpha, \beta = x, y, z, s; x, y, z$ being the Cartesian atomic coordinates in the molecular-fixed-axis system), and $V(s)$ is the B–N energy minimum path potential. As seen in Supplementary Fig. 6, all the atomic coordinates of Me_3NBH_3 used in this study as a model system exhibit fairly linear dependence on the stretching distortion; for further discussion see SI material.

Nuclear magnetic resonance (NMR) spectroscopy. NMR is a universal analytical method that provides atomic-level insights into molecular structure. Indirect spin–spin coupling (J-coupling) is one of the most important NMR parameters. It is tightly related to chemical bonding because it is mediated by electrons (in contrast to direct coupling due to a through-space interaction)[39]. We prepared a ^{15}N labeled trimethylamine–borane complex and measured indirect one-bond B–N and B–H couplings in various solvents with dielectric constants ranging from 2 to 78 (Supplementary Table 1). Supplementary Figure 1 displays an example spectrum measured in acetonitrile. The B–N coupling values clearly increase with the increasing polarity of the solvent, while the B–H couplings have the opposite trend.

Raman spectroscopy. We used Raman spectra to monitor the DB force constants of the model compound, as reflected in the vibrational frequencies. The same solutions of the trimethylamine–borane complex as for NMR were measured on a spectrometer or a microscope, using the 532 nm laser excitation. Some signals were too weak or masked by fluorescence. However, in most cases, vibrational bands originated to a great extent in the B–N stretching (within ~700–1500 cm^{-1}) could be extracted; the spectra are exemplified in Supplementary Figs. 7–11. The B–N stretching band frequencies exhibited significant solvent dependence; for example, the strongest 866 cm^{-1} vibration in D_2O moved down to 848 cm^{-1} in cyclohexane.

Data availability

All data resulting from the experimental and computational studies of this work are included within this Article and the Supplementary Information.

References

1. Hwang, K.-J. et al. The influence of dielectric constant on ionic and non-polar interactions. *Bull. Korean Chem. Soc.* **24**, 55–59 (2003).
2. Mc Keen, L. W. *Film Properties of Plastics and Elastomers, Introduction to Properties of Plastic and Elastomer Films* 3rd edn (Elsevier, 2012).
3. Lewis, G. N. *Valence and the Structure of Atoms and Molecules* (The Chemical Catalog Company, 1923).
4. Pauling, L. *The Nature of the Chemical Bond and the Structure of Molecules and Crystals* 3rd edn (Cornell University, 1938).
5. Haaland, A. Covalent versus dative bonds to main group metals, a useful distinction. *Angew. Chem. Int. Ed.* **28**, 992–1007 (1989).
6. Zhao, L., Hermann, M., Holzmann, N. & Frenking, G. Dative bonding in main group compounds. *Coord. Chem. Rev.* **344**, 163–204 (2017).
7. Zhao, L., Pan, S., Holzmann, N., Schwerdtfeger, P. & Frenking, G. Chemical bonding and bonding models of main-group compounds. *Chem. Rev.* **119**, 8781–8845 (2019).
8. Frenking, G., Hermann, M., Andrada, D. M. & Holzmann, N. Donor–acceptor bonding in novel low-coordinated compounds of boron and group-14 atoms C–Sn. *Chem. Soc. Rev.* **45**, 1129–1144 (2016).
9. Zhao, L., Zhi, M. & Frenking, G. The strength of a chemical bond. *Int. J. Quantum Chem.* e26773 (2021).
10. Jerabek, P., Schwerdtfeger, P. & Frenking, G. Dative and electron-sharing bonding in transition metal compounds. *J. Comput. Chem.* **40**, 247–264 (2019).
11. Georgiou, D. C., Zhao, L., Wilson, D. J., Frenking, G. & Dutton, J. L. NHC-stabilised acetylene-how far can the analogy be pushed? *Chemistry* **23**, 2926–2934 (2017).
12. Frenking, G. Dative bonds in main-group compounds: a case for more arrows! *Angew. Chem. Int. Ed.* **53**, 6040–6046 (2014).
13. Pan, S. & Frenking, G. A critical look at Linus Pauling's influence on the understanding of chemical bonding. *Molecules* **26**, 4695 (2021).
14. Frenking, G. In *the Chemical Bond. Chemical Bonding Across the Periodic Table* (eds Frenking, G. & Shaik, S.) 175–218 (Wiley VCH, 2014).
15. Nandi, A. & Kozuch, S. History and future of dative bonds. *Chem. Eur. J.* **26**, 759–772 (2020).
16. Smith, B. A. & Vogiatzis, K. D. σ-donation and π-backdonation effects in dative bonds of main-group elements. *J. Phys. Chem. A* **125**, 7956–7966 (2021).
17. Plumley, J. A. & Evanseck, J. D. Covalent and ionic nature of the dative bond and account of accurate ammonia borane binding enthalpies. *J. Phys. Chem. A* **111**, 13472–13483 (2007).
18. Zhong, D. & Zewail, A. H. Femtosecond dynamics of dative bonding: concepts of reversible and dissociative electron transfer reactions. *Proc. Natl Acad. Sci. USA* **96**, 2602–2607 (1999).
19. Jonas, V., Frenking, G. & Reetz, M. T. Comparative theoretical study of Lewis acid-base complexes of BH_3, BF_3, BCl_3, $AlCl_3$, and SO_2. *J. Am. Chem. Soc.* **116**, 8741–8753 (1994).
20. Mo, Y., Song, L., Wu, W. & Zhang, Q. Charge transfer in the electron donor-acceptor complex BH_3NH_3. *J. Am. Chem. Soc.* **126**, 3974–3982 (2004).
21. Fiorillo, A. A. & Galbraith, J. M. A valence bond description of coordinate covalent bonding. *J. Phys. Chem. A* **108**, 5126–5130 (2004).
22. Mo, Y. & Gao, J. Polarization and charge-transfer effects in Lewis acid-base complexes. *J. Phys. Chem. A* **105**, 6530–6536 (2001).
23. Hess, N. J. Spectroscopic studies of the phase transition in ammonia borane: Raman spectroscopy of single crystal NH_3BH_3 as a function of temperature from 88 to 330K. *J. Chem. Phys.* **128**, 034508 (2008).
24. Giesen, D. J. & Phillips, J. A. Structure, bonding, and vibrational frequencies of CH_3CN-BF_3: new insight into medium effects and the discrepancy between the experimental and theoretical geometries. *J. Phys. Chem. A* **107**, 4009–4018 (2003).

25. Dillen, J. & Verhoeven, P. The end of a 30-year-old controversy? A computational study of the B-N stretching frequency of BH_3-NH_3 in the solid state. *J. Phys. Chem. A* **107**, 2570–2577 (2003).

26. Frenking, G. The chemical bond—an entrance door of chemistry to the neighboring sciences and to philosophy. *Isr. J. Chem.* **61**, 1–9 (2021).

27. Cremer, D., Wu, A., Larsson, A. & Kraka, E. Some thoughts about bond energies, bond lengths, and force constants. *J. Mol. Model.* **6**, 396–412 (2000).

28. Konkoli, Z. & Cremer, D. A new way of analyzing vibrational spectra. I. Derivation of adiabatic internal modes. *Int. J. Quant. Chem.* **67**, 1–9 (1998).

29. Konkoli, Z., Larsson, J. A. & Cremer, D. A new way of analyzing vibrational spectra. II. Comparison of internal mode frequencies. *Int. J. Quant. Chem.* **67**, 11–27 (1998).

30. Konkoli, Z. & Cremer, D. A new way of analyzing vibrational spectra. III. Characterization of normal vibrational modes in terms of internal vibrational modes. *Int. J. Quant. Chem.* **67**, 29–40 (1998).

31. Konkoli, Z., Larsson, J. A. & Cremer, D. A new way of analyzing vibrational spectra. IV. Application and testing of adiabatic modes within the concept of the characterization of normal modes. *Int. J. Quant. Chem.* **67**, 41–55 (1998).

32. Hougen, J. T., Bunker, P. R. & Johns, J. W. C. The vibration-rotation problem in triatomic molecules allowing for a large-amplitude bending vibration. *J. Mol. Spectrosc.* **34**, 136–172 (1970).

33. Lo, R. et al. Addition reaction between piperidine and C_{60} to form 1,4-disubstituted C_{60} proceeds through van der Waals and dative bond complexes: theoretical and experimental study. *J. Am. Chem. Soc.* **143**, 10930–10939 (2021).

34. Lamanec, M. et al. The existence of N→C dative bond in C_{60}-piperidine complex. *Angew. Chem. Int. Ed.* **60**, 1942–1950 (2021).

35. Lo, R. et al. Structure-directed formation of the dative/covalent bonds in complexes with $C_{70}\cdots$piperidine. *Phys. Chem. Chem. Phys.* **23**, 4365–4375 (2021).

36. Lo, R., Manna, D. & Hobza, P. Tuning the P–C dative/covalent bond formation in R_3P–C_{60} complexes by changing the R group. *Chem. Commun.* **57**, 3363–3366 (2021).

37. Lo, R., Manna, D. & Hobza, P. Cyclo[n]carbons form a strong N→C dative/covalent bonds with piperidine. *J. Phys. Chem. A.* **125**, 2923–2931 (2021).

38. Lo, R., Manna, D. & Hobza, P. P-doped graphene–C_{60} nanocomposite: a donor–acceptor complex with a P–C dative bond. *Chem. Commun.* **58**, 1045–1048 (2022).

39. Dračínský, M. The chemical bond: the perspective of NMR spectroscopy. *Annu. Rep. NMR Spectrosc.* **90**, 1–40 (2017).

40. Bühl, D.-C. M., Steinke, T., Schleyer, P. V. R. & Boese, R. Solvation effects on geometry and chemical shifts. An ab initio/IGLO reconciliation of apparent experimental inconsistencies on H_3B·NH_3. *Angew. Chem. Int. Ed.* **30**, 1160–1161 (1991).

41. Adamo, C. & Barone, V. Toward reliable density functional methods without adjustable parameters: the PBE0 model. *J. Chem. Phys.* **110**, 6158–6170 (1999).

42. Grimme, S., Antony, J., Ehrlich, S. & Krieg, H. A consistent and accurate ab initio parametrization of density functional dispersion correction (DFT-D) for the 94 elements H-Pu. *J. Chem. Phys.* **132**, 154104 (2010).

43. Weigend, F. & Ahlrichs, R. Balanced basis sets of split valence, triple zeta valence and quadruple zeta valence quality for H to Rn: design and assessment of accuracy. *Phys. Chem. Chem. Phys.* **7**, 3297–3305 (2005).

44. Klamt, A. & Schüürmann, G. COSMO: a new approach to dielectric screening in solvents with explicit expressions for the screening energy and its gradient. *J. Chem. Soc. Perkin Trans. 2.* **2**, 799–805 (1993).

45. Carpenter, J. E. Extension of Lewis structure concepts to open-shell and excited-state molecular species, Ph.D. thesis, University of Wisconsin, Madison, WI, (1987).

Acknowledgements

Author contributions

P.H. and D.N. supervised the project. R.L., D.M., M.L., A.M., and V.M.M. carried out the quantum chemical calculations. V.M.M. carried out molecular dynamics simulations. V.S. performed the anharmonic frequency calculations. M.D., P.B., T.W., G.B., and J.K. performed the experiments. M.D. and P.B. analyzed the experimental data. P.H. and D.N. jointly interpreted all data and wrote the manuscript. All authors discussed the results and commented on the manuscript.

Competing interests

The authors declare no competing interests.

Additional information

Supplementary information The online version contains supplementary material available at https://doi.org/10.1038/s41467-022-29806-3.

Correspondence and requests for materials should be addressed to Dana Nachtigallová or Pavel Hobza.

Peer review information *Nature Communications* thanks the anonymous reviewers for their contribution to the peer review of this work. Peer reviewer reports are available.

Reprints and permission information is available at http://www.nature.com/reprints

Publisher's note Springer Nature remains neutral with regard to jurisdictional claims in published maps and institutional affiliations.

Article

Addition Reaction between Piperidine and C_{60} to Form 1,4-Disubstituted C_{60} Proceeds through van der Waals and Dative Bond Complexes: Theoretical and Experimental Study

Rabindranath Lo,[∥] Debashree Manna,[∥] Maximilián Lamanec,[∥] Weizhou Wang, Aristides Bakandritsos, Martin Dračínský, Radek Zbořil, Dana Nachtigallová,* and Pavel Hobza*

Read Online

ACCESS | 📊 Metrics & More | 📖 Article Recommendations | 🔳 Supporting Information

ABSTRACT: A combined computational and experimental study reveals the character of the C_{60} complexes with piperidine formed under different reaction conditions. The IR and NMR experiments detect the dative bond complex, which according to NMR, is stable in the oxygen-free environment and transforms to the adduct complex in the presence of O_2. Computational studies on the character of reaction channels rationalize the experimental observations. They show that the piperidine dimer rather than a single piperidine molecule is required for the complex formation. The calculations reveal significant differences in the dative bond and adduct complexes' character, suggesting a considerable versatility in their electronic properties modulated by the environment. This capability offers new application potential in several fields, such as in energy storage devices.
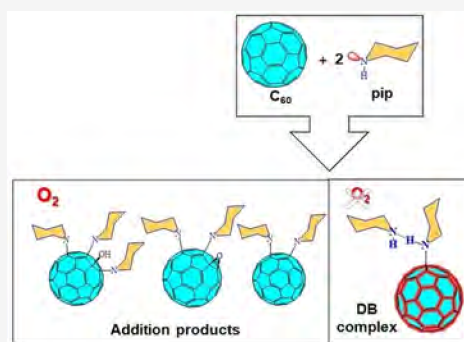
1. INTRODUCTION

The amino-functionalization of carbon nanomaterials undoubtedly represents one of the most popular modifications providing promising systems with applications in several fields.[1] The uses of amino-fullerenes in biorelated disciplines,[2−9] optoelectronics,[10−13] and catalysis[14−16] have already been reported, although there are still many to be uncovered.

The unique structure of fullerenes gives these carbon allotropes the capability to modify their electronic properties widely. This flexibility, among others, makes fullerenes promising candidates for, e.g., battery applications (for review, see ref 17). In this context, the properties of functionalized C_{60}, such as tuning of their redox potentials, directly related to the electron affinity, and others, have been the subjects of several studies[18−20] for their potential use as electrode materials in batteries.[17] As an example, the fullerene's functionalization can change its overall charge, ranging from negative carboxyl-C_{60} to neutral ester-C_{60} and positive piperazine-C_{60}.[21]

The addition of amines to C_{60} fullerene was first reported nearly three decades ago.[22,23] The resulting products were identified as tetraaminofullerene epoxides with a 1,4-addition pattern.[24−26] The observed reaction yield turned out to be very low; however, it increased upon the UV irradiation.[27,28] Lately, penta-amino hydroxyl and hexa-amino adducts have also been synthesized in dark conditions.[29]

It is now generally assumed that the addition starts with the formation of a long-lived contact ion pair (IP; [$C_{60}^{•−}$ $NHR_2^{•+}$]) resulting from the single-electron transfer (SET)

from amine to C_{60}. The SET has been experimentally identified using the near-infrared (NIR) spectroscopy for some tertiary amines-to-fullerene additions[30−32] and secondary amines-to-fullerene additions in polar solvents.[33] The SET process in the amines-to-fullerene addition has also been detected in the reaction of amines and C_{60}/C_{70} fullerenes performed under UV irradiation (photoinduced electron transfer).[34,35]

Detailed studies on the mechanism of the addition reaction of piperidine and other secondary aliphatic amines with C_{60} have shown a substantial increase of the reaction yield of the addition reaction in the polar dimethyl sulfoxide (DMSO)/chlorobenzene solvent mixture,[33] highlighting a crucial role of DMSO to form an IP and subsequent adduct (1,4-tetraaminofullerene epoxide) upon contact with air. Notably, the $C_{60}^{•−}$ characteristic NIR bands (994 and 1077 nm) have not been observed for other mixtures than those containing DMSO.

The above-observed experimental findings, particularly the role of DMSO together with the lack or a lower extent of IP

Scheme 1. Schematic Diagram Illustrating the Formation of the Addition Products from C_{60} with Piperidine
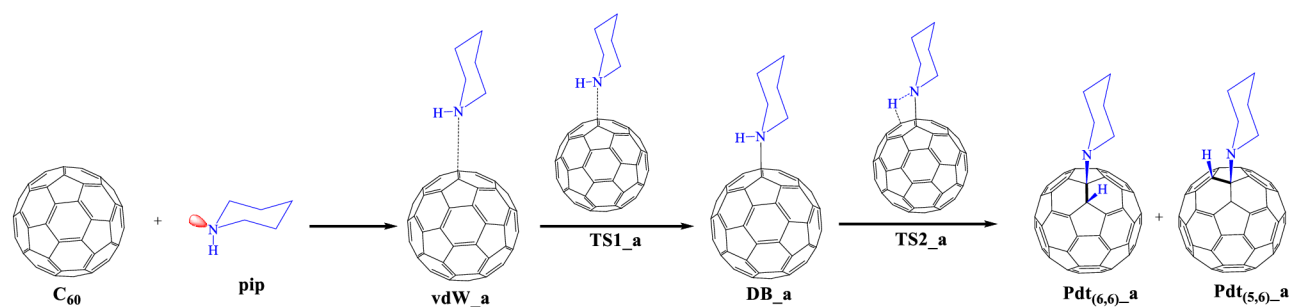
Scheme 2. Schematic Diagram Illustrating the Formation of the Addition Products from C_{60} with Piperidine Dimer
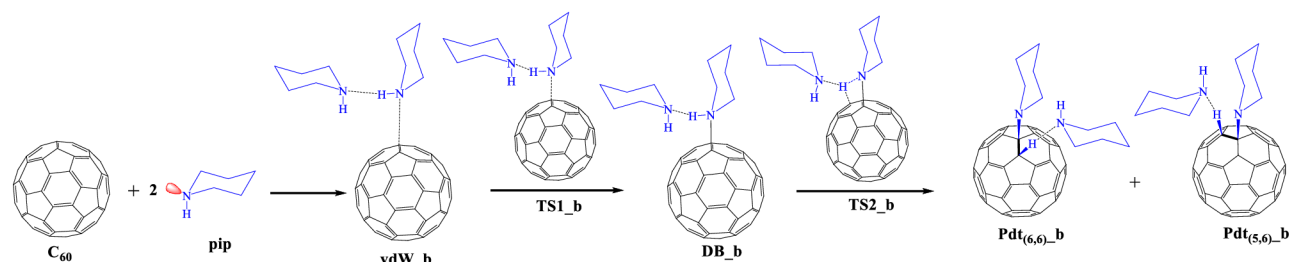
formation,[33] leave the question of the addition mechanism in less polar or nonpolar solvents still open.

We have recently reported on the formation of covalent/dative bonds between C_{60} and piperidine in the less polar solvents, proved by the NMR and IR spectroscopy performed in o-dichlorobenzene and pure piperidine, respectively, in which the nitrogen lone pair of piperidine donates two electrons to electron acceptor C_{60}.[36] Using the computational studies, we have shown that this reaction requires hydrogen-bonded piperidine dimer binding, promoting the charge transfer cascade in the sequence *outer* pip → *inner* pip → C_{60}. The existence of the dative complex has been confirmed by IR and NMR experiments. The dative bond (DB) forms practically immediately after putting the reactants together.

The unique properties of fullerene-based materials make it attractive to search for other possible differences in electronic properties due to differences in their bonding characters, such as in their DB and adduct complexes. For this reason, we extend our studies to more detailed calculations of the reaction of C_{60} with piperidine with calculations of the relevant reaction channels of $C_{60}\cdots$pip and $C_{60}\cdots(pip)_2$ complex formations under an oxygen-free atmosphere (Schemes 1 and 2, respectively) and in the presence of oxygen (Scheme 3 and 4, respectively). The reaction path in Scheme 3 follows that suggested in refs 29 and 33. Contrary to our previous papers dealing exclusively with the DB formation, we also consider the consecutive addition reaction to form 1,4-substituted fullerenes. Previous DFT studies[37−39] show that the addition of amines most likely proceeds across the (6,6) bonds of C_{60} rather than the (5,6) bonds (Figure S1). Our study considers both possible adducts formed from the DB complex. The electronic properties, in particular, charge distribution and electron affinities, for both types of complexes are discussed. The calculations are combined with IR and NMR experiments, run in dark and light and with or without air, allowing the discussion of complex stabilities under different conditions. The experiments are performed in solvents significantly less

polar than DMSO (cf. $D_e(\text{DMSO}) = 46.7$ and $D_e(\text{CS}_2) = 2.6$ used in the IR experiment and $D_e(o\text{-dichloro-benzene}) = 9.9$ used in the NMR experiment).

2. RESULTS AND DISCUSSION

2.1. Calculations. *2.1.1. $C_{60}\cdots$pip and $C_{60}\cdots(pip)_2$.* Figures 1 and S2 show the potential energy surface (PES) of forming the C_{60}−pip complex in the absence of oxygen (Scheme 1) and the most important geometry parameters of the PES's critical points. During the reaction course in the gas phase, piperidine binds to C_{60} via a tetrel bond, leading to the van der Waals (vdW) complex (vdW_a), stabilized by 6.7 kcal/mol. The N−H bond of piperidine changes only negligibly. The reaction then proceeds via transition state TS1_a to the DB_a complex. In the former, the piperidine N−H bond remains unchanged, and the C−N bond between C_{60} and piperidine shortens by about 0.9 Å. The reaction barrier is tiny, and the transition states are stable with respect to their isolated subsystems by 1.7 kcal/mol, which makes the DB_a complex easily accessible. The optimization procedure reveals only small changes in the complex, particularly, shortening of the C−N bond by about 0.2 Å and a slight deformation of the C_{60} buckyball structure due to a partial sp³ hybridization of the carbon atom involved in the dative bond. The stabilization energies of vdW_a and DB_a reveal the former's larger thermodynamic stability, which indicates that the existence of the DB_a complex is unlikely. This picture changes when the solvent is involved in the calculations. Although the calculations localized the vdW_a complex on the PES, this will not form in the solvent, and the reaction will follow directly to the DB_a complex. Most importantly, the DB_a complex's stabilization is significantly larger than in the gas phase (by about 7 kcal/mol), which results during the N → C dative bond formation in the presence of the piperidine solvent.

Starting at the DB_a complex, the reaction profiles are very similar in the gas phase and solvent and are discussed simultaneously. On the basis of the previous experimental and

Scheme 3. Schematic Diagram Illustrating the Formation of the Addition Products from C_{60} with Piperidine in the Presence of O_2
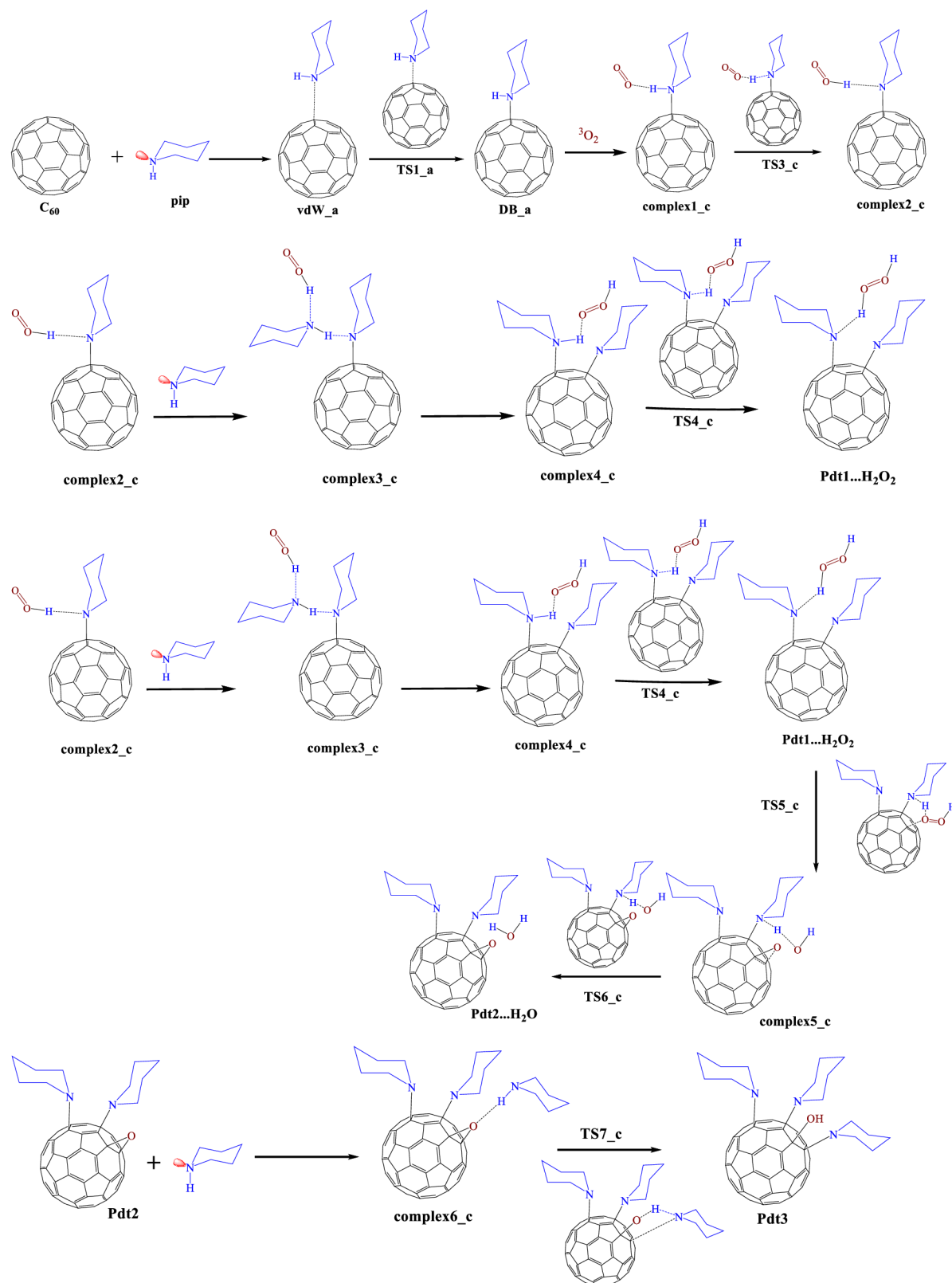
computational findings,[36] two adducts, $Pdt_{(5,6)}$_a and $Pdt_{(6,6)}$_a, and their relevant transitions states, $TS2_{(5,6)}$_a and

$TS2_{(6,6)}$_a, were considered. In both cases, the hydrogen of piperidine binds to the C_{60} skeleton. Simultaneously, the
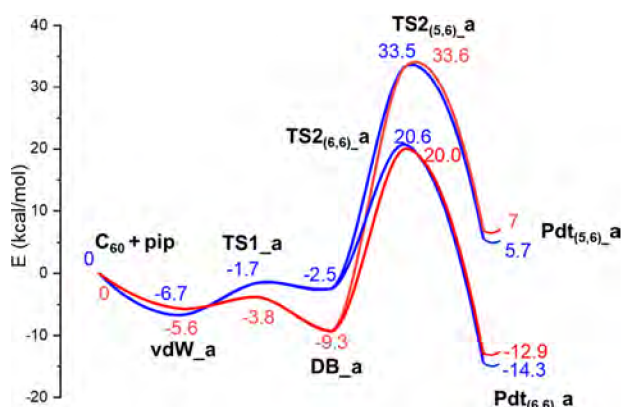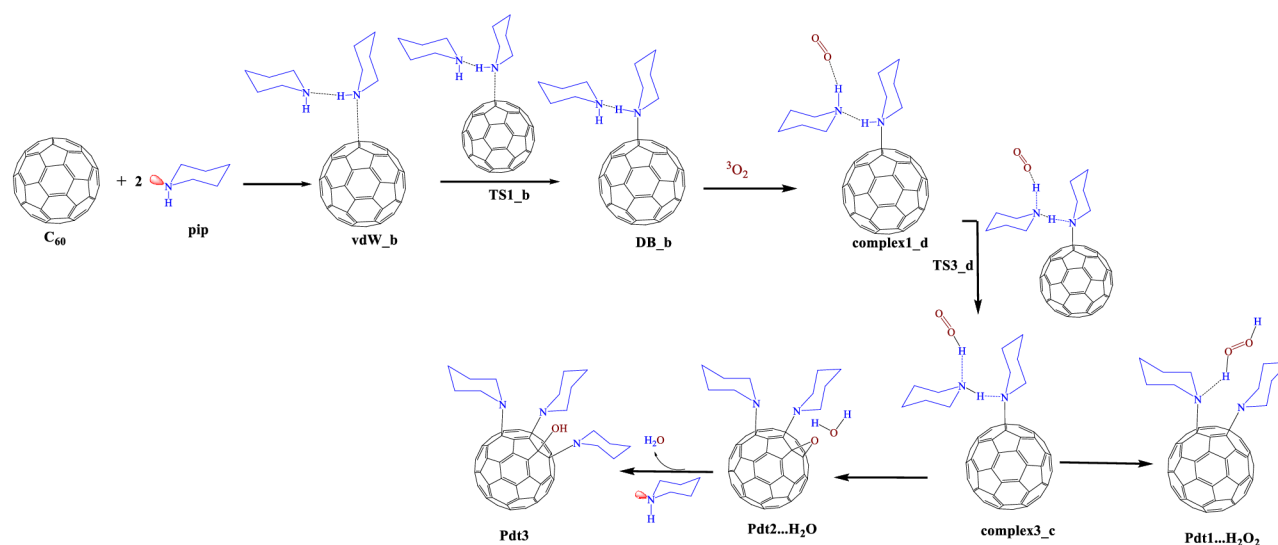
Scheme 4. Schematic Diagram Illustrating the Formation of the Addition Products from C$_{60}$ with Piperidine Dimer in the Presence of O$_2$

Figure 1. Electronic energy diagram for forming the addition product from C$_{60}$ with piperidine in the gas phase (blue color) and pip solvent (red color).

Figure 2. Electronic energy diagram for forming the addition product from C$_{60}$ with piperidine dimer in the gas phase (blue color) and pip solvent (red color).

covalent N−H piperidine bond of about 1.02 Å changes to a noncovalent hydrogen bond of 2.3−2.4 Å. The values of stabilization and activation energies in both the gas and solvent exclude the existence of the complexes with (5,6) binding mode. Pdt$_{(6,6)}$_a corresponds to the most thermodynamically stable structure on the PESs. However, the transition barrier of about 20 kcal/mol calculated for DB_a → Pdt$_{(6,6)}$_a reaction excludes the existence of the latter.

The extension of the system to C$_{60}$−(pip)$_2$ (Scheme 2) leads to significant modifications in the reaction profile (see Figure 2). The vdW complex (vdW_b) forms only in the gas phase. Its stability is larger, about 12 kcal/mol, compared to C$_{60}$−pip (7 kcal/mol). Figure S3 shows the most relevant geometry parameters, i.e., the C−N distance between the piperidine directly bound to C$_{60}$ (*inner* pip) and the hydrogen bond between the *inner* and the second (*outer* pip) molecules. From the vdW_b complex, the system reaches the DB_b complex via the TS1_b transition state with a negligible activation barrier of 0.1 kcal/mol.

The calculations performed in the solvent localized neither vdW_b nor TS1_b structures; instead, the optimization led
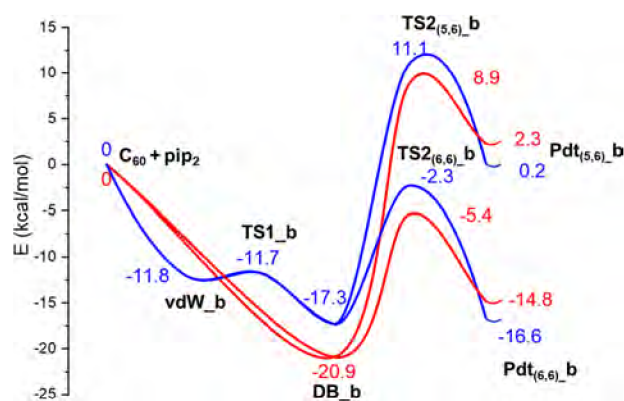
directly to the DB_b complex. This result can be explained by a different charge distribution in pip$_2$ in the gas and solvent phase (Figure S4). The molecular electrostatic potential (MESP) isosurface exhibits a more negative ESP at the N atom in pip$_2$ in the solvent medium (−46.8 and −52.7 kcal/mol in the gas and solvent phase, respectively). The DB_b complex possesses one dative bond between C$_{60}$ and pip dimer, instead of the DB_b′ complex having two direct bonds (Figure S5). The former complex is stabilized by (i) the N → C dative bond with the bond length of about 1.57 Å and (ii) the *inner* pip···*outer* pip hydrogen bond of about 1.75 Å, leading to the overall stabilization energies of 17.3 and 20.9 kcal/mol in the gas phase and solvent, respectively. The latter value is in good agreement with the result (18.0 kcal/mol) obtained with a more accurate SCS-MP2 method. Due to similar energy reasons as in the case of C$_{60}$···pip, only the reaction channel leading to Pdt$_{(6,6)}$_b is discussed next. In this product, the *inner* pip···*outer* pip hydrogen bond breaks, and the hydrogen atom of the former binds to C$_{60}$ and forms a new hydrogen bond, of about 2.2 Å, with the *outer* pip. The Pdt$_{(6,6)}$_b complex stability is 16.6 and 14.8 kcal/mol in the gas

phase and solvent, respectively. The SCS-MP2 stabilization energy in the solvent of 13.0 kcal/mol agrees with the latter DFT-D value. Although this complex stability is only about 2 kcal/mol larger than for $C_{60}\cdots$pip, its formation is much more likely since the activation reaction for the DB_b → $Pdt_{(6,6)}$_b reaction is energetically feasible; i.e., the $TS2_{(6,6)}$_b transition state is stable by 2.3 kcal/mol (the gas phase) and 5.4 kcal/mol (the solvent) with respect to the reactants. However, their relative stabilities indicate that the former is thermodynamically favored. Indeed, the equilibrium between them shifts toward the DB_b complex (K = 0.00003, ΔG is approximated by ΔE), thus disfavoring $Pdt_{(6,6)}$_b formation.

2.1.2. $C_{60}\cdots$pip and $C_{60}\cdots(pip)_2$ in the Presence of O_2. Scheme 3 displays the whole reaction scenario leading to three possible reaction products, Pdt1, Pdt2, and Pdt3, starting with a single pip, referred to in the literature (see refs 29 and 33); Scheme 4 illustrates the modifications caused by the interaction with $(pip)_2$. In the reaction path calculations of both $C_{60}\cdots$pip (see Figure 3 for PES and Figure S6 for the
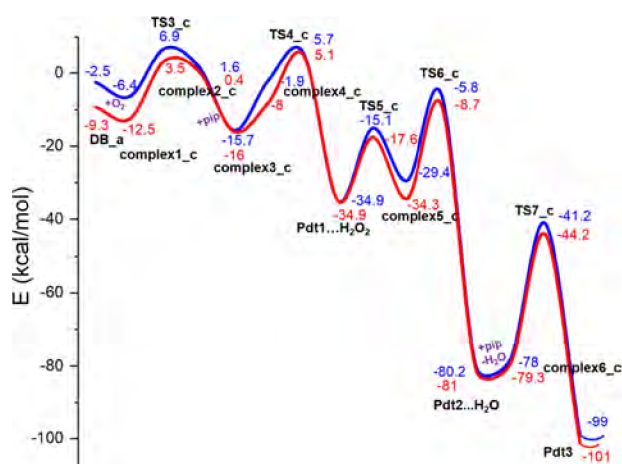

Figure 3. Electronic energy diagram for forming the addition product from C_{60} with pip in the presence of O_2 in the gas phase (blue color) and pip solvent (red color).

structures) and $C_{60}\cdots(pip)_2$ (see Figure 4 for PES and Figure S7 for the structures), the DB complexes (DB_a and DB_b) are considered the starting points for subsequent reactions with O_2. Starting from the $C_{60}\cdots$pip DB_a complex, O_2 binds via an O$\cdots$H−N hydrogen bond to piperidine, forming the complex1_c, stabilized by 6.4 and 12.5 kcal/mol in the gas phase and solvent, respectively. At this point, the hydrogen atom from pip transfers to $^3O_2$ and forms hydroperoxyl radical, which interacts with the nitrogen of piperidine via an N−H hydrogen bond of about 1.6 Å (complex2_c). This reaction proceeds on the triplet potential energy surface. The transition barrier (transition state TS3_c) for this reaction is 6.9 and 3.5 kcal/mol in the gas phase and solvent, respectively, and the complex2_c is slightly unstable, by 1.6 and 0.4 kcal/mol in the gas phase and solvent, respectively. The spin density plots of complex2_c and complex3_c show the distribution of spin in C_{60} and the hydroperoxyl radical (Figure S8). The role of C_{60} in the H transfer is apparent from the energy barriers calculated in the absence of C_{60} and presence of O_2 (Figures S9−S12). The corresponding transition barriers for pip (Figures 3 and S10) and pip dimer (Figures 4 and S12) become smaller in the presence of C_{60}. The binding of $^3O_2$ to
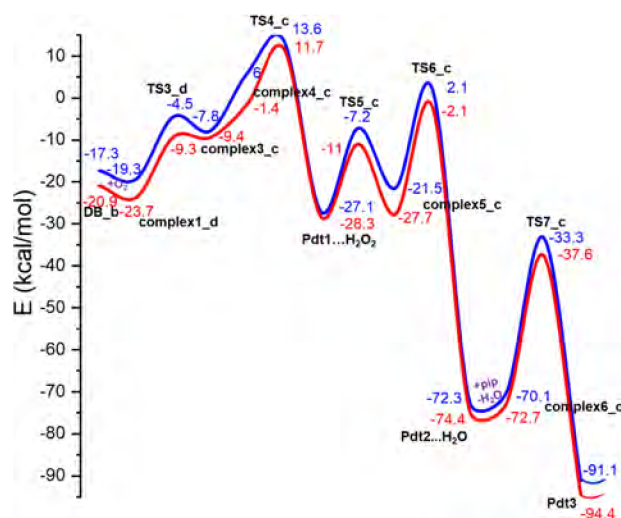

Figure 4. Electronic energy diagram for the formation of the addition product from C_{60} with piperidine dimer in the presence of O_2 in the gas phase (blue color) and pip solvent (red color).

the DB_b complex of $C_{60}\cdots(pip)_2$ provides a different energy profile. The O_2 molecule binds with the same motif as in the previous case to outer piperidine, resulting in the complex1_d with significantly larger stability (19.3 and 23.7 kcal/mol in the gas phase and solvent, respectively) than upon binding of a single pip. Similar to the reaction scheme found for $C_{60}\cdots$pip, the (NH) hydrogen atom transfers to $^3O_2$ and forms complex3_c in which the hydroperoxyl radical binds to the N atom of outer piperidine. An enhanced electrophilicity of the N atom in outer piperidine in the presence of O_2 explains this observation. The calculated local Fukui function value at the N atom of pip_2 is 0.01 and increases to 0.013 in the pip_2-O_2 complex (complex1_f). It assists the (NH) hydrogen transfer from inner to outer piperidine.

This reaction proceeds via the transition state TS3_d. Both structures, complex3_c and TS3_d, are stable, by 7.8 and 4.5 kcal/mol in the gas phase and by about 9.4 and 9.3 kcal/mol in the solvent, respectively, with respect to the isolated substrates.

From complex2_c, the formation of 1,4-diamino-C_{60} (Pdt1) requires additional pip in Scheme 3, while it binds the *outer* pip to C_{60} (complex3_c) in Scheme 4. The additional/outer piperidine molecule reacts with C_{60} through SN2″ pathway to form complex4_c. The reaction path prefers the 1,4-addition over the 1,2-addition of two pip to the hexagon systems, avoiding the steric hindrance in the complex. The hydroperoxyl radical abstracts the hydrogen in complex4_c through a transition state, TS4_c, to form diamionofullerene with hydrogen peroxide (Pdt1$\cdots H_2O_2$). The stabilization of the Pdt1$\cdots H_2O_2$ excludes the possibility of releasing the hydroperoxyl radical over hydrogen peroxide (Figures 3 and 4). The formation of 1,4-diamino-C_{60} epoxide (Pdt2) considers the same modifications. The highly electrophilic fulvene, Pdt1, goes through an epoxidation reaction with hydrogen peroxide. Pdt3 is formed from Pdt2 with additional pip. The direct attack of pip opens the epoxide ring forming a triamino hydroxyl product. In all these cases, the gas phase and the solvent calculation results are very similar, giving largely stabilized adduct products.

2.2. FT-IR Spectra. Figure 5 displays the IR spectra of the mixture of C_{60} with piperidine obtained immediately after the
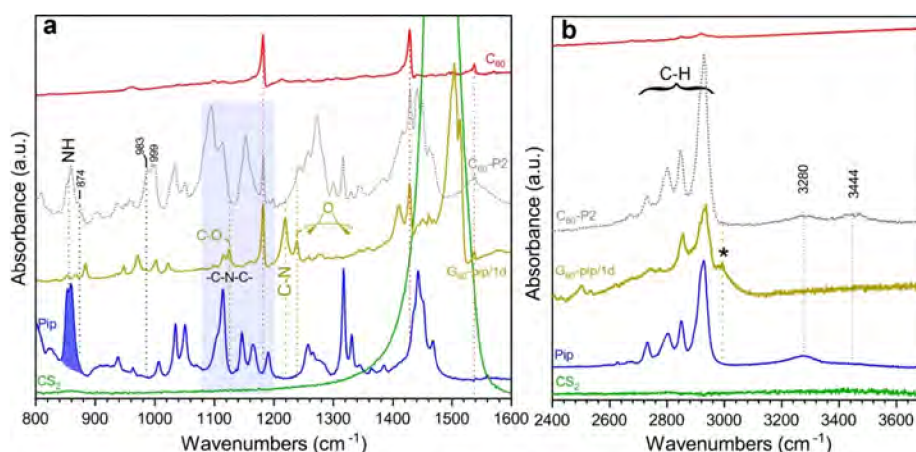
Figure 5. FT-IR spectra of the C$_{60}$−piperidine adduct after mixing in carbon disulfide (CS$_2$) for 1 day and after drying some of the solvent and possibly unbound piperidine molecules (C$_{60}$ pip/1d). Spectra show the regions of (a) the C−N stretching and N−H bending and wagging vibrations and (b) the N−H stretching vibrations. The spectra of pure C$_{60}$, piperidine, CS$_2$, and the coordination complex of C$_{60}$ with piperidine (C$_{60}$-P2, from ref 36) are given for comparison.
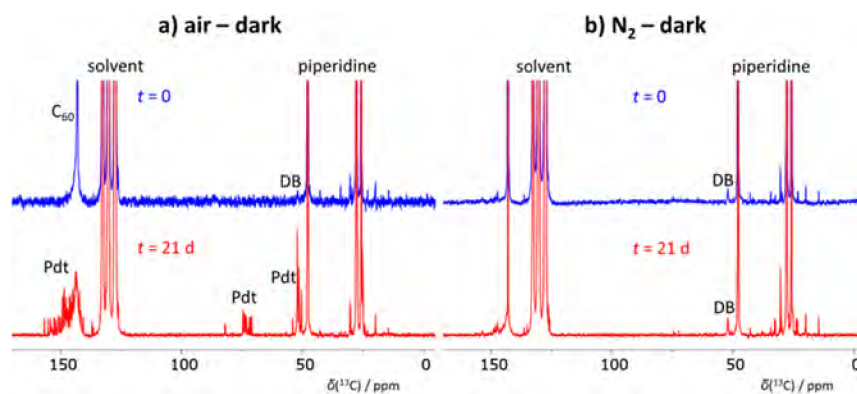

Figure 6. ^{13}C NMR spectra of the 1,2-dichlorobenzene-d_4 solutions of a mixture of C$_{60}$ with piperidine. The samples were kept in the dark and under (a) ambient and (b) nitrogen atmospheres.

reaction starts to avoid a long exposure to air (taken from ref 36, spectrum C$_{60}$-P2 in Figure 5) and with a one-day delay (spectrum C$_{60}$−pip/1d in Figure 5). The latter lacks both the bands previously (ref 36) assigned to bending (Figure 5a) and stretching (Figure 5b) N−H vibrations. The loss of hydrogen from piperidine's N−H group is also visible from the dramatic intensity depletion of the N−H wagging vibration[40] of piperidine at ca. 855 cm^{-1} (Figure 5a). Furthermore, a new band appears slightly below 3000 cm^{-1} (Figure 5b), attributed to the new C−H bond on the fullerene's carbon. The strong covalent C−N between C$_{60}$ and piperidine also emerged with significant intensity (indicated in Figure 5a) at ca. 1220 cm^{-1}. The above-described differences between the C$_{60}$-P2 and C$_{60}$−pip/1d spectra strongly indicate the formation of the addition product. The IR spectra displayed in Figure 5a indicate the existence of Pdt2 and Pdt3 adduct products. In particular, the band at 1125 cm^{-1} (Figure 5a) fits well within the typical C−O bond vibrations of tertiary alcohols, as in Pdt3;[41] the bands in the region of 1230−1280 cm^{-1} correspond to medium-strong C−O stretching vibrations of oxirane groups[42] formed in Pdt2.

2.3. NMR Spectroscopy. *2.3.1. C NMR.* Figures 6 and S13 display the C NMR spectra obtained in the nitrogen and oxygen atmospheres in dark conditions; the spectra in the light conditions are shown in Figure S14. The spectra acquired

shortly after the sample preparation show, apart from the signal of the starting C$_{60}$ at 143 ppm and of the piperidine signals, a low-intense signal at 52 ppm. This signal was previously assigned to the CH$_2$ groups of piperidine in the dative bond with C$_{60}$.[36]

In the nitrogen atmosphere, in both light and dark, the C$_{60}$ signal at 143 ppm persists, and no new signals appear during the time course of the experiment, i.e., 21 days, showing its stability in the oxygen-free environment. On the contrary, the signal at 143 ppm completely disappears within 21 days, and new signals appear in the aromatic 140−155 ppm region in the spectra collected in the ambient atmosphere. Besides, new signals appear in the aliphatic regions at 70−82 ppm and close to 50 ppm. The latter corresponds to the piperidine fragments present in the reaction products. The isolated signal close to 82 ppm corresponds to an sp^3 carbon attached to an OH group, i.e., a product with a structure similar to Pdt3 (Figure S13). The signals in the region of 70−75 ppm correspond to fullerene sp^3 carbon atoms attached to piperidine nitrogen (found in all products of the reaction) and to sp^3 carbon atoms, which are involved in a three-membered oxirane ring (similarly as in Pdt2).

In general, all the chemical shifts' ranges of the newly appeared signals in the experiment performed in the ambient
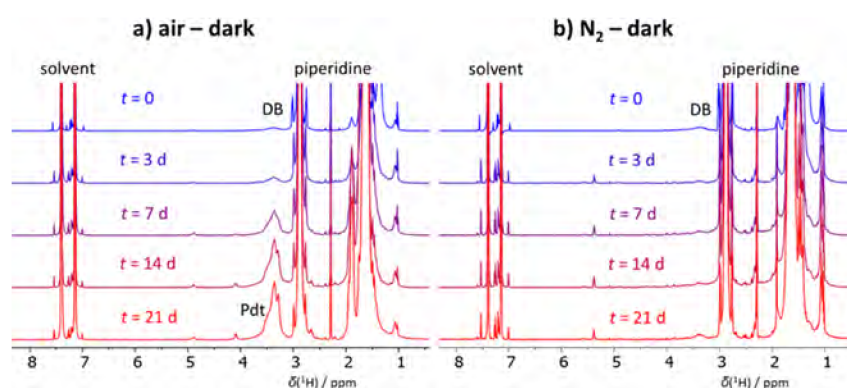
Figure 7. ^{1}H NMR spectra of the 1,2-dichlorobenzene-d_4 solutions of a mixture of C_{60} with piperidine. The samples were kept in the dark and under (a) an ambient atmosphere or (b) a nitrogen atmosphere.

Table 1. Interaction Energies (in kcal/mol) of C_{60} with pip and (pip)$_2$

	vdW	TS1	DB	adduct formation					
				TS2	Pdt				
C_{60}–pip	−5.6	−3.8	−9.3	+20.0	−12.9				
				C1	TS3	C2	Pdt1	Pdt2	Pdt3
C_{60}–pip + O$_2$	−5.6	−3.8	−9.3	−12.5	3.5	0.4	−22.3	−69.3	−101.0
				TS2	Pdt				
C_{60}–(pip)$_2$			−20.9	−5.4	−14.8				
				C1	TS3	C2	Pdt1	Pdt2	Pdt3
C_{60}–(pip)$_2$ + O$_2$			−20.9	−23.7	−9.3	−9.4	−15.7	−62.7	−94.4

atmosphere are close to those observed for piperidine addition to C_{60}.[29]

2.3.2. H NMR. The H NMR spectra (Figure 7) acquired immediately after the sample preparation in nitrogen and ambient atmospheres show a broad low-intense signal at 3.35 ppm. This signal was previously assigned to the CH$_2$ groups of piperidine in the dative bond with C_{60}[36] and proved the DB complex formation at the beginning of the reaction in both atmospheres. After 21 days, this signal changes only slightly in intensity in the nitrogen. Simultaneously, new signals with very low intensity appear in the regions of 3.5 and 5.5 ppm, indicating that some reaction occurs. The new signals are likely to originate from the interference of the 1,2-dichlorobenzene solvent, which might react either with traces of water or with piperidine. The possible product of these reactions is HCl, the presence of which (even traces) shifts the piperidine NH signals to higher chemical shifts.

The spectra of the samples kept in the ambient atmosphere give a more complex character, showing new signals at 3.2−4.2 ppm, which overlap with the original DB signal at 3.35 ppm. These new signals are assigned to the products of the addition reaction with the covalent bonds between C_{60} and piperidine. The NMR spectra of the samples kept in the light conditions are almost identical with those of the samples kept in the dark (see Figure S15).

2.4. Comparison of the Computational and Experimental Results. Table 1 collects the results of the reaction profile calculations given in Figures 1−4. Only the results performed in pip solvent are presented. Since the previous studies on the 5,6 and 6,6 fullerene adducts' relative energies (refs 37−39) and our results predict larger stabilities of the latter in all calculations, only these are used for the discussion. In our previous studies, we have predicted that the DB

complex requires the hydrogen-bonded pip dimer to bind to C_{60}. This has been rationalized by the ΔG gas phase values of $C_{60}\cdots$pip ($\Delta G = 12.9$ kcal/mol and $\Delta E = -2.5$ kcal/mol; see Figure 1 and ref 36) and of $C_{60}\cdots$(pip)$_2$ ($\Delta G = -0.2$ kcal/mol and $\Delta E = -17.3$ kcal/mol; see Figure 2 and ref 36). The current results on the adduct formation support this prediction, giving lower energy barriers to the DB → adduct reaction in all investigated cases. Unlike in calculations performed for reactions in the presence of oxygen, the relative stabilities of DB and adduct Pdt complexes of $C_{60}\cdots$(pip)$_2$, obtained for calculations without O$_2$, predict the former to prevail in the reaction system. The larger stability of DB also follows from the Gibbs free energy calculations performed in the solvent environment, giving the ΔG values of −2.5 and −0.1 kcal/mol for the DB and Pdt, respectively. The calculated ΔG values of −43.2 kcal/mol (Pdt2) and −59.3 kcal/mol (Pdt3) also support the existence of stable adducts referred to in the literature.[29,33]

The results of FT-IR and NMR spectral measurements provide evidence of the dative bond formed at the very beginning of the complexation. Notably, the NMR spectra prove this complex's stability in the oxygen-free environment within the time course of several weeks. This observation agrees with computational predictions on the larger stability and, thus, a higher probability of the DB rather than the adduct complex existence.

Both FT-IR and NMR spectra further show that, with some time delay (1 day according to FT-IR results), the molecular oxygen shifts the reaction toward the addition reaction, previously investigated by several experimental groups (see the Introduction). New IR bands due to the C−H stretching modes slightly below 3000 cm^{-1} demonstrate the adduct formation. Note that the observed vibrational frequencies

nicely agree with the calculated C–H stretching frequencies of 2908 cm^{-1}. The adduct's formation in the air atmosphere is also confirmed by the intensive C–N stretching frequency observed at 1210 cm^{-1}, which is not detected in the DB complex.

Table 2 shows the results of the electronic properties of the $C_{60}\cdots(pip)_2$ complexes considered in the calculations. Notably,

Table 2. Properties of $C_{60}\cdots(pip)_2$ Complexes

	electron affinity[a]	charge transfer[b]	
	gas phase	gas phase	pip solvent
vdW	2.014	−0.160	
DB	1.575	−0.633	−0.683
Pdt(6,6)		−0.253	−0.263
Pdt1	2.121	0.203	0.218
Pdt2		0.661	0.724
Pdt3		0.559	0.550

[a]In eV. [b]Obtained from the NBO analyses.

although $C_{60}^{\bullet-}$ has not been identified in low-polar solvents in the previous studies (see the Introduction), our results of the natural-bond-orbital (NBO) analyses show relatively large electron transfer from pip to C_{60} in the DB complex. The charge transfer in adduct complexes is strikingly different, ranging from small pip → C_{60} electron transfer in Pdt(6,6) to the small transfer in the opposed direction in Pdt1, increasing significantly in Pdt2 and Pdt3, respectively. These differences are reflected in the ESP maps displayed in Figure S16. Importantly, for the redox potential characterizations, also, the values of electron affinities of the DB complex and adducts differ significantly. A comparison of the electron affinity (EA) of the vdW complex and pristine C_{60} (2.169 eV) gives almost an unchanged EA value of Pdt1, while that of DB decreases more significantly. These results indicate an extensive capability of functionalized C_{60} to provide systems with different characteristics by modifying only the surrounding environment.

3. CONCLUSION

The computational and experimental IR and NMR studies of the C_{60} complexes with the secondary amine piperidine have been performed to investigate their character under different reaction conditions. The studies conducted both in the oxygen-free environment and in the presence of O_2 reveal a different nature of the resulting products. The experimental studies prove that the dative bond complex forms at the beginning of the reaction course in all cases and remains stable in the oxygen-free atmosphere. On the basis of the kinetic and thermodynamic criteria obtained from the calculations, both dative bond and adduct formations proceed with pip2 rather than a single pip. The probability of DB and adduct existence differs for oxygen-free and oxygen atmospheres: in the former, the DB complex is more likely, while the calculations in the latter predict, in agreement with the previous and current experiments, the existence of the adduct products. The differences in the calculated electronic properties reflect a considerable versatility of C_{60}, and possibly other fullerenes, to modify their properties even by different conditions upon binding the same functional group. These observations reveal new opportunities for selective and straightforward covalent

functionalization applicable to attractive fields, such as in energy storage (e.g., Li-ion batteries).

■ ASSOCIATED CONTENT

ⓈI Supporting Information

The Supporting Information is available free of charge at https://pubs.acs.org/doi/10.1021/jacs.1c01542.

DFT results, computational details, and IR and NMR spectroscopy (PDF)

■ AUTHOR INFORMATION

Corresponding Authors

Pavel Hobza − *Institute of Organic Chemistry and Biochemistry, Czech Academy of Sciences, 16000 Prague, Czech Republic; IT4Innovations, VŠB-Technical University of Ostrava, 70800 Ostrava-Poruba, Czech Republic;* ⓘ orcid.org/0000-0001-5292-6719; Email: pavel.hobza@uochb.cas.cz

Dana Nachtigallová − *Institute of Organic Chemistry and Biochemistry, Czech Academy of Sciences, 16000 Prague, Czech Republic; IT4Innovations, VŠB-Technical University of Ostrava, 70800 Ostrava-Poruba, Czech Republic;* ⓘ orcid.org/0000-0002-9588-8625; Email: dana.nachtigallova@uochb.cas.cz

Authors

Rabindranath Lo − *Institute of Organic Chemistry and Biochemistry, Czech Academy of Sciences, 16000 Prague, Czech Republic; Regional Centre of Advanced Technologies and Materials, Czech Advanced Technology and Research Institute, Palacký University Olomouc, 77900 Olomouc, Czech Republic;* ⓘ orcid.org/0000-0002-4436-3618

Debashree Manna − *Institute of Organic Chemistry and Biochemistry, Czech Academy of Sciences, 16000 Prague, Czech Republic*

Maximilián Lamanec − *Institute of Organic Chemistry and Biochemistry, Czech Academy of Sciences, 16000 Prague, Czech Republic; Department of Physical Chemistry, Palacký University Olomouc, 77146 Olomouc, Czech Republic; IT4Innovations, VŠB-Technical University of Ostrava, 70800 Ostrava-Poruba, Czech Republic*

Weizhou Wang − *College of Chemistry and Chemical Engineering and Henan Key Laboratory of Function-Oriented Porous Materials, Luoyang Normal University, Luoyang 471934, China;* ⓘ orcid.org/0000-0002-4309-9077

Aristides Bakandritsos − *Regional Centre of Advanced Technologies and Materials, Czech Advanced Technology and Research Institute, Palacký University Olomouc, 77900 Olomouc, Czech Republic; Nanotechnology Centre, Centre of Energy and Environmental Technologies, VŠB-Technical University of Ostrava, 70800 Ostrava-Poruba, Czech Republic;* ⓘ orcid.org/0000-0003-4411-9348

Martin Dračínský − *Institute of Organic Chemistry and Biochemistry, Czech Academy of Sciences, 16000 Prague, Czech Republic*

Radek Zbořil − *Institute of Organic Chemistry and Biochemistry, Czech Academy of Sciences, 16000 Prague, Czech Republic; Regional Centre of Advanced Technologies and Materials, Czech Advanced Technology and Research Institute, Palacký University Olomouc, 77900 Olomouc, Czech Republic; Nanotechnology Centre, Centre of Energy and Environmental Technologies, VŠB-Technical University*

of Ostrava, 70800 Ostrava-Poruba, Czech Republic;
 orcid.org/0000-0002-3147-2196

Complete contact information is available at:
https://pubs.acs.org/10.1021/jacs.1c01542

Author Contributions

‖R.L., D.M., and M.L. contributed equally and are co-first authors.

Notes

The authors declare no competing financial interest.

ACKNOWLEDGMENTS

REFERENCES

(1) Garrido, M.; Gualandi, L.; Di Noja, S.; Filippini, G.; Bosi, S.; Prato, M. Synthesis and Applications of Amino-Functionalized Carbon Nano-materials. *Chem. Commun.* **2020**, *56* (84), 12698−12716.

(2) Maeda-Mamiya, R.; Noiri, E.; Isobe, H.; Nakanishi, W.; Okamoto, K.; Doi, K.; Sugaya, T.; Izumi, T.; Homma, T.; Nakamura, E. In Vivo Gene Delivery by Cationic Tetraamino Fullerene. *Proc. Natl. Acad. Sci. U. S. A.* **2010**, *107* (12), 5339−5344.

(3) Nakamura, E.; Isobe, H. In Vitro and in Vivo Gene Delivery with Tailor-Designed Aminofullerenes. *Chem. Rec.* **2010**, *10* (5), 260−270.

(4) Pantarotto, D.; Bianco, A.; Pellarini, F.; Tossi, A.; Giangaspero, A.; Zelezetsky, I.; Briand, J. P.; Prato, M. Solid-Phase Synthesis of Fullerene-Peptides. *J. Am. Chem. Soc.* **2002**, *124* (42), 12543−12549.

(5) Bosi, S.; Feruglio, L.; Da Ros, T.; Spalluto, G.; Gregoretti, B.; Terdoslavich, M.; Decorti, G.; Passamonti, S.; Moro, S.; Prato, M. Hemolytic Effects of Water-Soluble Fullerene Derivatives. *J. Med. Chem.* **2004**, *47* (27), 6711−6715.

(6) Friedman, S. H.; DeCamp, D. L.; Kenyon, G. L.; Sijbesma, R. P.; Srdanov, G.; Wudl, F. Inhibition of the HIV-1 Protease by Fullerene Derivatives: Model Building Studies and Experimental Verification. *J. Am. Chem. Soc.* **1993**, *115* (15), 6506−6509.

(7) Pastorin, G.; Marchesan, S.; Hoebeke, J.; Da Ros, T.; Ehret-Sabatier, L.; Briand, J. P.; Prato, M.; Bianco, A. Design and Activity of Cationic Fullerene Derivatives as Inhibitors of Acetylcholinesterase. *Org. Biomol. Chem.* **2006**, *4* (13), 2556−2562.

(8) Nakamura, E.; Isobe, H.; Tomita, N.; Sawamura, M.; Jinno, S.; Okayama, H. Functionalized Fullerene as an Artificial Vector for Transfection. *Angew. Chem., Int. Ed.* **2000**, *39* (23), 4254−4257.

(9) Klumpp, C.; Lacerda, L.; Chaloin, O.; Da Ros, T.; Kostarelos, K.; Prato, M.; Bianco, A. Multifunctionalised Cationic Fullerene Adducts for Gene Transfer: Design, Synthesis and DNA Complexation. *Chem. Commun.* **2007**, No. 36, 3762−3764.

(10) Jariwala, D.; Sangwan, V. K.; Lauhon, L. J.; Marks, T. J.; Hersam, M. C. Carbon Nanomaterials for Electronics, Optoelectronics, Photovoltaics, and Sensing. *Chem. Soc. Rev.* **2013**, *42* (7), 2824−2860.

(11) Collavini, S.; Delgado, J. L. Fullerenes: The Stars of Photovoltaics. *Sustainable Energy and Fuels.* **2018**, *2*, 2480−2493.

(12) Fernández, G.; Sánchez, L.; Veldman, D.; Wienk, M. M.; Atienza, C.; Guldi, D. M.; Janssen, R. A. J.; Martín, N. Tetrafullerene Conjugates for All-Organic Photovoltaics. *J. Org. Chem.* **2008**, *73* (8), 3189−3196.

(13) Mateo-Alonso, A.; Ehli, C.; Rahman, G. M. A.; Guldi, D. M.; Fioravanti, G.; Marcaccio, M.; Paolucci, F.; Prato, M. Tuning Electron Transfer through Translational Motion in Molecular Shuttles. *Angew. Chem., Int. Ed.* **2007**, *46* (19), 3521−3525.

(14) Campisciano, V.; Gruttadauria, M.; Giacalone, F. Modified Nanocarbons for Catalysis. *ChemCatChem* **2019**, *11* (1), 90−133.

(15) López-Andarias, J.; Frontera, A.; Matile, S. Anion-π Catalysis on Fullerenes. *J. Am. Chem. Soc.* **2017**, *139* (38), 13296−13299.

(16) Rosso, C.; Emma, M. G.; Martinelli, A.; Lombardo, M.; Quintavalla, A.; Trombini, C.; Syrgiannis, Z.; Prato, M. A Recyclable Chiral 2-(Triphenylmethyl)Pyrrolidine Organocatalyst Anchored to [60]Fullerene. *Adv. Synth. Catal.* **2019**, *361* (12), 2936−2944.

(17) Jiang, Z.; Zhao, Y.; Lu, X.; Xie, J. Fullerenes for Rechargeable Battery Applications: Recent Developments and Future Perspectives. *J. Energy Chem.* **2021**, *55*, 70−79.

(18) Sood, P.; Kim, K. C.; Jang, S. S. Electrochemical and Electronic Properties of Nitrogen Doped Fullerene and Its Derivatives for Lithium-Ion Battery Applications. *J. Energy Chem.* **2018**, *27* (2), 528−534.

(19) Teprovich, J. A.; Weeks, J. A.; Ward, P. A.; Tinkey, S. C.; Huang, C.; Zhou, J.; Zidan, R.; Jena, P. Hydrogenated C_{60} as High-Capacity Stable Anode Materials for Li Ion Batteries. *ACS Appl. Energy Mater.* **2019**, *2* (9), 6453−6460.

(20) Jiang, Z.; Zeng, Z.; Yang, C.; Han, Z.; Hu, W.; Lu, J.; Xie, J. Nitrofullerene, a C_{60}-Based Bifunctional Additive with Smoothing and Protecting Effects for Stable Lithium Metal Anode. *Nano Lett.* **2019**, *19* (12), 8780−8786.

(21) Shan, C.; Yen, H. J.; Wu, K.; Lin, Q.; Zhou, M.; Guo, X.; Wu, D.; Zhang, H.; Wu, G.; Wang, H. L. Functionalized Fullerenes for Highly Efficient Lithium Ion Storage: Structure-Property-Performance Correlation with Energy Implications. *Nano Energy* **2017**, *40*, 327−335.

(22) Hirsch, A.; Li, Q.; Wudl, F. Globe-trotting Hydrogens on the Surface of the Fullerene Compound $C_{60}H_6(N(CH_2CH_2)_2O)_6$. *Angew. Chem., Int. Ed. Engl.* **1991**, *30* (10), 1309−1310.

(23) Wudl, F.; Hirsch, A.; Khemani, K. C.; Suzuki, T.; Allemand, P.-M.; Koch, A.; Eckert, H.; Srdanov, G.; Webb, H. M. Survey of Chemical Reactivity of C_{60}, Electrophile and Dieno−Polarophile Par Excellence. In *Fullerenes*; American Chemical Society, 1992; pp 161−175.

(24) Schick, G.; Kampe, K. D.; Hirsch, A. Reaction of [60]Fullerene with Morpholine and Piperidine: Preferred 1,4-Additions and Fullerene Dimer Formation. *J. Chem. Soc., Chem. Commun.* **1995**, No. 19, 2023−2024.

(25) Hirsch, A. Addition Reactions of Buckminsterfullerene (C60). *Synthesis* **1995**, *1995*, 895−913.

(26) Kampe, K.-D.; Egger, N.; Vogel, M. Diamino and Tetraamino Derivatives of Buckminsterfullerene C_{60}. *Angew. Chem., Int. Ed. Engl.* **1993**, *32* (8), 1174−1176.

(27) Isobe, H.; Ohbayashi, A.; Sawamura, M.; Nakamura, E. A Cage with Fullerene End Caps. *J. Am. Chem. Soc.* **2000**, *122*, 2669−2670.

(28) Isobe, H.; Tomita, N.; Nakamura, E. One-Step Multiple Addition of Amine to [60]Fullerene. Synthesis of Tetra(Amino)-Fullerene Epoxide under Photochemical Aerobic Conditions. *Org. Lett.* **2000**, *2* (23), 3663−3665.

(29) Li, Y.; Gan, L. Selective Addition of Secondary Amines to C_{60}: Formation of Penta- and Hexaamino[60]Fullerenes. *J. Org. Chem.* **2014**, *79* (18), 8912−8916.

(30) Skiebe, A.; Hirsch, A.; Klos, H.; Gotschy, B. [DBU]C_{60}. Spin Pairing in a Fullerene Salt. *Chem. Phys. Lett.* **1994**, *220* (1−2), 138−140.

(31) Klos, H.; Rystau, I.; Schütz, W.; Gotschy, B.; Skiebe, A.; Hirsch, A. Doping of C_{60} with Tertiary Amines: TDAE, DBU, DBN. A Comparative Study. *Chem. Phys. Lett.* **1994**, *224* (3−4), 333−337.

(32) Fujitsuka, M.; Luo, C.; Ito, O. Electron-Transfer Reactions between Fullerenes (C_{60} and C_{70}) and Tetrakis(Dimethylamino)-Ethylene in the Ground and Excited States. *J. Phys. Chem. B* **1999**, *103* (3), 445−449.

(33) Isobe, H.; Tanaka, T.; Nakanishi, W.; Lemière, L.; Nakamura, E. Regioselective Oxygenative Tetraamination of [60]Fullerene. Fullerene-Mediated Reduction of Molecular Oxygen by Amine via Ground State Single Electron Transfer in Dimethyl Sulfoxide. *J. Org. Chem.* **2005**, *70* (12), 4826−4832.

(34) Sun, Y.-P.; Ma, B.; Bunker, C. E. Photoinduced Intramolecular n−π* Electron Transfer in Aminofullerene Derivatives. *J. Phys. Chem. A* **1998**, *102* (39), 7580−7590.

(35) Wang, N. X. Photochemical Addition Reactions of [60]-Fullerene with 1,2-Ethylenediamine and Piperazine. *Tetrahedron* **2002**, *58* (12), 2377−2380.

(36) Lamanec, M.; Lo, R.; Nachtigallová, D.; Bakandritsos, A.; Mohammadi, E.; Dračínský, M.; Zbořil, R.; Hobza, P.; Wang, W. The Existence of a N→C Dative Bond in the C_{60}−Piperidine Complex. *Angew. Chem., Int. Ed.* **2021**, *60*, 1942−1950.

(37) Basiuk, E. V.; Basiuk, V. A.; Shabel'nikov, V. P.; Golovatyi, V. G.; Ocotlán Flores, J.; Saniger, J. M. Reaction of Silica-Supported Fullerene C_{60} with Nonylamine Vapor. *Carbon* **2003**, *41* (12), 2339−2346.

(38) Ramírez-Calera, I. J.; Meza-Laguna, V.; Gromovoy, T. Y.; Chávez-Uribe, M. I.; Basiuk, V. A.; Basiuk, E. V. Solvent-Free Functionalization of Fullerene C_{60} and Pristine Multi-Walled Carbon Nanotubes with Aromatic Amines. *Appl. Surf. Sci.* **2015**, *328*, 45−62.

(39) Thong, N. M.; Vo, Q. V.; Le Huyen, T.; Van Bay, M.; Dung, N. N.; Thu Thao, P. T.; Nam, P. C. Functionalization and Antioxidant Activity of Polyaniline-Fullerene Hybrid Nanomaterials: A Theoretical Investigation. *RSC Adv.* **2020**, *10* (25), 14595−14605.

(40) *The Handbook of Infrared and Raman Characteristic Frequencies of Organic Molecules*; Elsevier Inc., 1991; https://www.sciencedirect.com/book/9780124511606/the-handbook-of-infrared-and-raman-characteristic-frequencies-of-organic-molecules (accessed Jan 14, 2021).

(41) Socrates, G. *Infrared and Raman Characteristic Group Frequencies: Tables and Charts*, 3rd ed.; John Wiley & Sons Ltd.: Chichester, England, 2001; p 94.

(42) Socrates, G. *Infrared and Raman Characteristic Group Frequencies: Tables and Charts*, 3rd ed.; John Wiley & Sons Ltd.: Chichester, England, 2001; p 102.

Hydrogen Bonding with Hydridic Hydrogen−Experimental Low-Temperature IR and Computational Study: Is a Revised Definition of Hydrogen Bonding Appropriate?

Svatopluk Civiš,*,⊥ Maximilián Lamanec,⊥ Vladimír Špirko, Jiří Kubišta, Matej Špeťko, and Pavel Hobza*

ACCESS | 📊 Metrics & More | 📰 Article Recommendations | 🆂ℹ Supporting Information

ABSTRACT: Spectroscopic characteristics of $Me_3Si-H \cdots Y$ complexes (Y = ICF_3, BrCN, and HCN) containing a hydridic hydrogen were determined experimentally by low-temperature IR experiments based on the direct spectral measurement of supersonically expanded intermediates on a cold substrate or by the technique of argon-matrix isolation as well as computationally at harmonic and one-dimensional anharmonic levels. The computations were based on DFT-D, MP2, MP2-F12, and CCSD(T)-F12 levels using various extended AO basis sets. The formation of all complexes related to the redshift of the Si−H stretching frequency upon complex formation was accompanied by an increase in its intensity. Similar results were obtained for another 10 electron acceptors of different types, positive σ-, π-, and p-holes and cations. The formation of $HBe-H \cdots Y$ complexes, studied only computationally and again containing a hydridic hydrogen, was characterized by the blueshift of the Be−H stretching frequency upon complexation accompanied by an increase in its intensity. The spectral shifts and stabilization energies obtained for all presently studied hydridic H-bonded complexes were comparable to those in protonic H-bonded complexes, which has prompted us to propose a modification of the existing IUPAC definition of H-bonding that covers, besides the classical protonic form, the non-classical hydridic and dihydrogen forms.
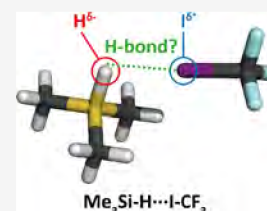
1. INTRODUCTION

Most of the elements in the periodic table have lower electronegativity than hydrogen (2.2), and only a few of them (C, N, O, F, S, Cl, Se, Br, and I) have it higher. Covalent bonds of hydrogen with the more electronegative atom X are characterized by the polarization of the X−H bond and the formation of a partial positive charge on hydrogen (protonic hydrogen). The molecule thus acts as a Lewis acid, and when it interacts with the electron donor Y (Lewis base), a hydrogen bond (H-bond) X−H⋯Y is formed.[1] H-bonds are among the strongest types of non-covalent interactions and are the most common. The specificity of H-bonding is related to its easily detectable spectroscopic manifestation, which originates in different masses of H and X atoms. The formation of the X−H⋯Y H-bond, accompanied by a charge transfer from the Lewis base to the Lewis acid, results in a significant change of the X−H covalent bond. NBO orbital analysis[2] has revealed a charge transfer from the lone pair of Y to the X−H σ^* antibonding orbital. The increase in electron density in the σ^* antibonding orbital weakens the X−H covalent bond and lowers the X−H stretching frequency (redshift).[3] Our theoretical work at the end of the last century[4] showed that the formation of the hydrogen bond could also be accompanied by a blueshift of the X−H stretching frequency. When our predictions were proven experimentally,[5] it was obvious that there was a new type of H-bonding, for which we suggested a new name—blueshifting H-bonding. Extensive discussion in the computational and spectroscopic community led to the proposal of a new definition

covering both types of H-bonding. The new IUPAC definition[6] of the X−H⋯Y hydrogen bond thus includes both the weakening and strengthening of the X−H covalent bond, leading to red- and blueshifts of the X−H stretching frequency. Nevertheless, the characterization of atom X (X is defined as more electronegative than hydrogen) remained the same. As shown above, however, most of the elements in the periodic table are less electronegative (more electropositive). In these complexes, the interaction scheme is the same, namely, X−H⋯Y, but the hydrogen carries a negative charge (hydridic hydrogen) and the molecule acts as a Lewis base, whereas the Y atom carries a positive charge and the molecule acts as a Lewis acid. Both interaction types can be schematically represented as protonic, $X-H^{\delta+} \cdots Y^{\delta-}$, and hydridic, $X-H^{\delta-} \cdots Y^{\delta+}$. It should be emphasized that a very important feature of hydrogen bonding that makes its detection easy, namely, the position of light hydrogen between two much heavier atoms, is retained. This leads to an important question: does the second scheme correspond to H-bonding or is it another interaction type with a different definition and name? Many complexes containing
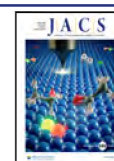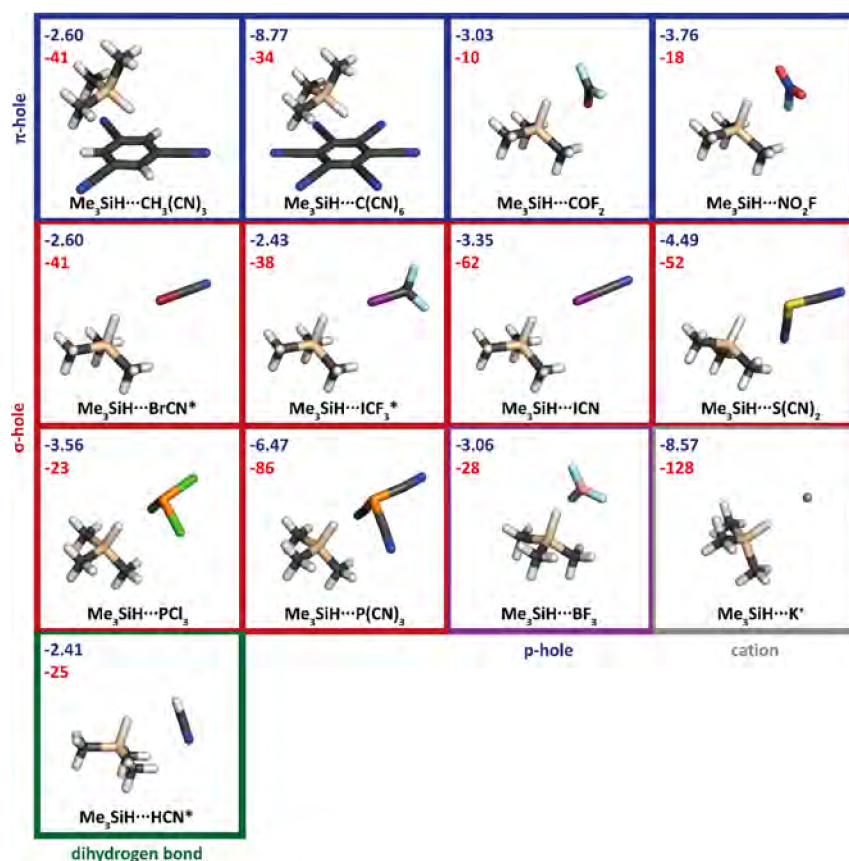
Figure 1. Geometries of the complexes investigated optimized at the MP2/cc-pwCVTZ level (cc-pwCVTZ-PP for Br and I): Si − beige, C − black, H − white, I −violet, F − light blue, Br − burgundy, N − dark blue, P − orange, Cl − green, S − yellow, O − red, K − silver, and B − rose. Dark blue is used for the total interaction energy (in kcal/mol) at the MP2/cc-pwCVTZ level for each complex, and red is used for the shift of the Si−H stretching frequency (in cm^{-1}). The complexes with the experiment are marked with asterisks.

Lewis bases including Si−H, Ge−H, Be−H, Mg−H, Zn−H, Li−H, and Cu−H hydridic bonds and different Lewis acids have been studied computationally in the laboratory of Jabłoński, who has recommended using the name charge-inverted H-bond[7−15] (CIHB). The experimental detection of these non-classical H-bonds is, however, missing; their very existence is thus based on solving the Schrödinger equation only within the rigid rotor−harmonic oscillator−ideal gas approximation. The only exception is one class of CIHB, so-called dihydrogen bonding, where hydridic hydrogen interacts with protonic hydrogen. The structures of several dihydrogen-bonded complexes have been determined by X-ray and neutron diffraction studies; for some of them, theoretical calculations have revealed spectral shifts upon dihydrogen-bond formation.[16] Finally, clusters of phenol and aniline with borane−amines having the B−H⋯H−X dihydrogen bond have been studied in supersonic jets using electronic and vibrational spectroscopy.[17]

Noncovalent interactions have been studied using many different experimental approaches, starting from classical solution-phase studies involving spectroscopic and thermodynamic measurements. More recently, important, complementary information to that obtained in solutions has been provided by studies in the gas phase, particularly the supersonic beam studies of Flygare, Klemperer, and others.[18−21] The binding energy of weakly bound complexes is usually much smaller than room-temperature thermal energy. For this reason, the low temperature of a gas-phase supersonic jet, a rare-gas solid matrix,

or a liquid helium droplet is the typical temperature in which noncovalent complexes are studied in the laboratory.

Besides the direct high-resolution gas-phase techniques, there are also other very powerful low-temperature methods. The possibility of storing spectroscopically detectable concentrations of reaction intermediates in a solid or rare-gas matrix was first recognized by Whittle, Dows, and Pimentel.[22] These matrix materials are often chemically inert and are optically transparent from the far-infrared range well into the vacuum−ultraviolet region. The early experiments demonstrated that at 20 K, which is a temperature conveniently obtained using liquid hydrogen, solid nitrogen and argon are rigid enough to eliminate molecular diffusion and effectively inhibit subsequent chemical reactions. At the cryogenic temperatures required for studying rare-gas solids, molecules reside in their ground electronic and vibrational states. Since diffusion is inhibited, reaction intermediates do not undergo further reaction, and sufficient concentrations of many of them have been obtained for studies of their electronic and infrared spectra.

The aim of the present paper is to study the X′−H⋯Y′ complexes (X′ is more electropositive than hydrogen, X′−H acts as a Lewis base) containing Si−H and Be−H hydridic bonds and various hydridic−hydrogen acceptor Ys (Lewis acids) having a positive σ-, π-, and n-hole or a positive atom (e.g., hydrogen). Spectroscopic characteristics of the Me$_3$Si−H⋯Y′ (Y′ = ICF$_3$, BrCN and HCN) complexes obtained not only at the harmonic but also at the more reliable anharmonic level have been verified by low-temperature IR experiments. Notice that the present
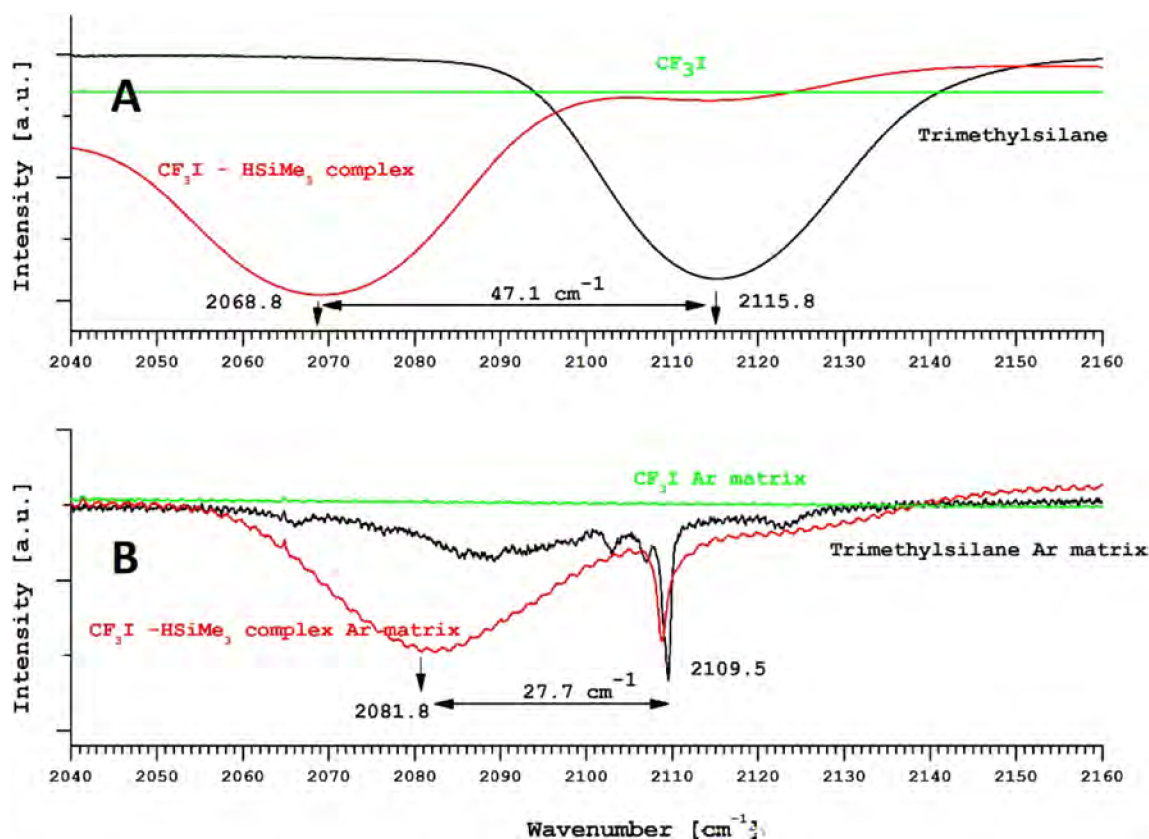
Figure 2. Solid-state and Ar-matrix spectra of the $Me_3Si-H\cdots ICF_3$ complex.

experiments are the first ones to confirm unambiguously the formation of the CIHB. Finally, an attempt has been made to find a new definition of H-bonding that would cover both protonic (red- as well as blueshifting) and hydridic (CIHB) schemes.

2. INSTRUMENTATION AND SPECTRAL MEASUREMENT

In our low-temperature experiments, two different approaches have been applied (for more details, see the SI).

The first of them (A) is the technique of the direct spectral measurement of a supersonically expanded mixture of reaction intermediates on a cold substrate (solid-phase complex, SPC) and the second (B) is the technique of noble-gas matrix isolation (MI).

(A) The procedure of low-temperature experiments has already been described elsewhere.[23,24] The gas mixtures are usually deposited onto a cooled KBr substrate of the cryostat at a temperature of 4−20 K. The relative concentrations of the products have been monitored using the integrated absorption intensities of selected infrared bands. The intermediates forming part of the low-temperature complex have been supersonically expanded into a high vacuum (10^{-6} Torr) on a cold substrate (of 18 K, which is the minimum attainable temperature) inside a Leybold cryostat chamber. The spectra were obtained using a Bruker Vertex spectrometer with KBr optics, a HgCdTe detector, and a KBr beam splitter. The broad spectral region was cut by optical interference filters with transparency in the range of 700−5000 cm^{-1}. The KBr entry window of the spectrometer was used. The unapodized spectral resolution was 0.06 cm^{-1}. Between 30 and 100 scans, depending on the sample,

were used to obtain a reasonable signal-to-noise ratio. The observed wavenumbers were calibrated using CO_2-absorption rotation−vibration lines.

(B) Matrix isolation is a well-known technique frequently used for the measurement of unstable species such as ions, radicals, and low-temperature-existing molecular complexes in a cold matrix of noble gas (Ng). Like in the procedure A, a mixture of reaction intermediates mixed together with argon gas (molar ratio 1:1000) was expanded through a pulse nozzle onto the cold (18 K) KBr substrate, and the spectra were recorded using the Bruker Vertex spectrometer.

3. SYSTEM CONSIDERED

Me_3Si-H and $HBe-H$ systems containing a hydridic hydrogen and different electron acceptors (ICF_3, BrCN, HCN, K^+, $C_6(CN)_6$, $C_6H_3(CN)_3$, BF_3, $P(CN)_3$, PCl_3, $S(CN)_2$, NO_2F, CO_2F, and ICN) forming CIHBs have been considered. Lewis bases contain a positive σ-, π-, and p-hole or a positive hydrogen. The latter complexes are also known as complexes with a dihydrogen bond. All complexes considered are depicted in Figure 1.

In this paper, we use both techniques A and B. It is well known that the method of matrix isolation gives narrow lines, rare-gas atoms isolate the molecules from mutual interaction, and subsequent chemical reactions are effectively inhibited. On the contrary, the A arrangement provides the possibility to study the basic energy characteristic of the molecular complexes, such as thermodynamic stability, on the board temperature scale.
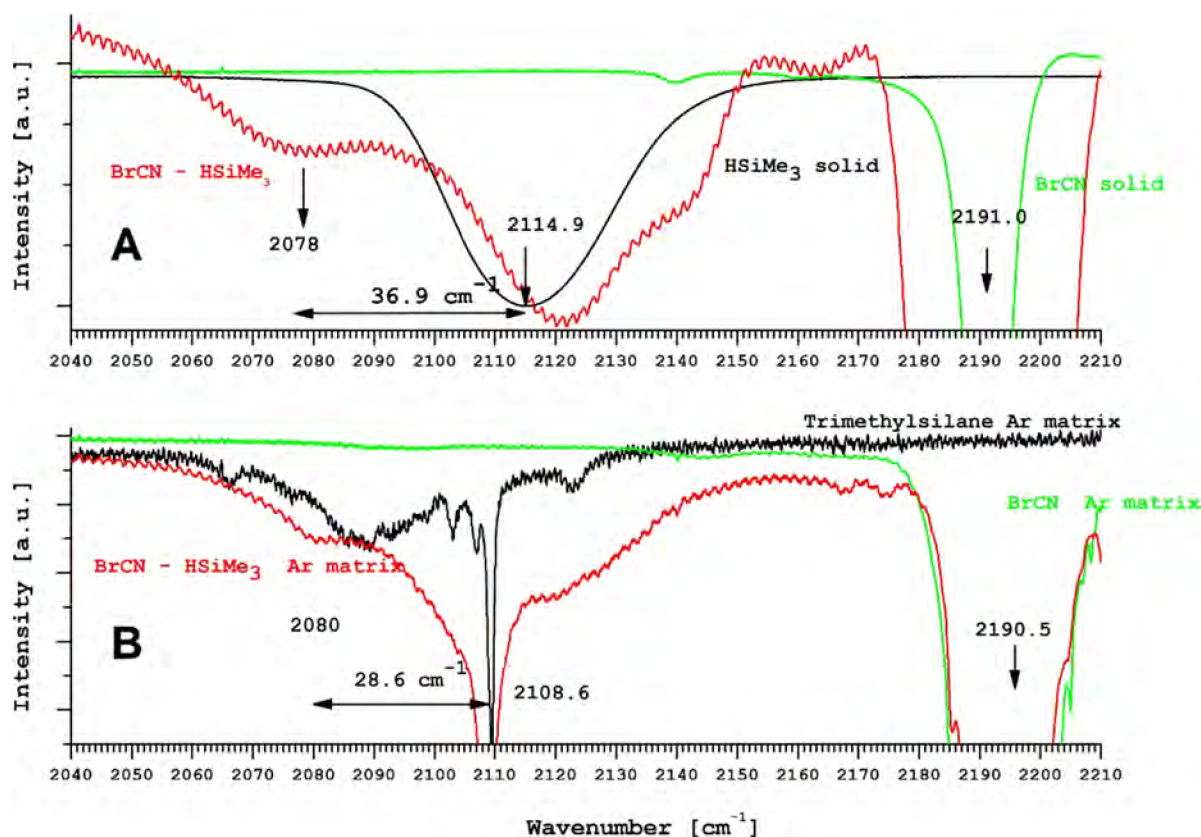
Figure 3. Solid-state and Ar-matrix spectra of the Me$_3$Si−H···BrCN complex.

4. METHODS

4.1. Geometry Optimization and Thermodynamic Properties. Geometries of all subsystems and complexes were optimized at the RI-MP2/cc-pwCVTZ[25] level. For heavy halogens (Br, I), basis sets with pseudopotentials (cc-pwCVTZ-PP[26]) were used. Thermodynamic properties as well as harmonic vibration frequencies, determined using the rigid rotor−harmonic oscillator−ideal gas approximation, were evaluated at the same theoretical level. Geometry optimization and harmonic vibrational analysis on selected complexes (ICF$_3$, BrCn, and HCN complexes with Me$_3$SiH) were also performed using the more reliable explicitly correlated RI-MP2-F12[27] method in cc-pVTZ-F12[28] basis sets (cc-pVTZ-PP-F12 for Br and I). All calculations were performed with MOLPRO 2022.[29,30] The potential energy surfaces for the anharmonic calculations of Si−H frequencies were obtained on the MP2/cc-pVTZ level (cc-pwCVTZ-PP for Br and I) using the Cuby4[31] framework and the TURBOMOLE 7.5[32] program.

4.2. Single-Point Energy Calculations. CCSD(T)-F12[33] energies were determined with cc-pVTZ-F12 (cc-pVTZ-PP-F12 for Br and I) basis sets implemented in the MOLPRO 2022 package on geometries obtained from the MP2−F12 method. All interaction energies were systematically corrected using the Boys and Bernardi counterpoise technique.[34] Energy decomposition analysis was performed using the SAPT2 + 3[35]/aug-cc-pwCVTZ (aug-cc-pwCVTZ-PP for Br and I) method implemented in the PSI4 package.[36]

4.3. NBO Analysis. NBO analysis was performed at the ωB97X-D/cc-pwCVTZ level (cc-pwCVTZ-PP for Br and I) using the NBO^2 program implemented in Gaussian 16.[37]

4.4. One-Dimensional Harmonic and Anharmonic Vibrational Analysis. Like in our previous publications,[38,39] the evaluation of the sought vibrational Si−H stretching frequencies relies on the deep adiabatic separability of the Si−H mode (s) from the rest of the vibrational degrees of freedom of the probed compounds and on the use of a HBJ non-rigid reference configuration of the atomic nuclei that essentially follows the Si−H motion.[40] The vibrational energies can

then be obtained by solving the Schrödinger equation for the following Hamiltonian:

$$H_s = \frac{-1}{2}\mu_{ss}J_s^2 + \frac{1}{2}(J_{ss}\mu_{ss})J_s + V_{\mathrm{pseudo}}(s) + V(s)$$

where $J_s = -i\hbar(d/ds)$, μ_{ss} is the Si−H stretching component of the tensor that is the inverse of the 4 × 4 generalized molecular inertia tensor, μ is the determinant of the matrix $[\mu_{\alpha,\beta}]$ ($\alpha,\beta = x, y, z, s$), with x, y, and z being the Cartesian atomic coordinates in the molecule-fixed axis system, $V_{\mathrm{pseudo}}(s)$ is a mass-dependent kinematic pseudopotential, and $V(s)$ is the Si−H minimum-energy-path stretching potential.

Obviously, mainly for the practical impossibility to account reliably for the aggregation effects of the molecular environments used, the adopted "isolated-molecule" theory may seem inadequate. Nevertheless, if one assumes a purely linear dependence of the atomic coordinates of the probed compounds (deposited on cold substrates or trapped in rare-gas matrices) on the stretching Si−H distortion, the stretching-reduced mass μ_{ss} becomes constant and can thus be used as a single scaling parameter. Interestingly, as illustrated in Figure S1, the assumption of "linearity" seems to hold at least for the minimum-energy-path relaxation effects in isolated molecules (note that the x and y coordinates exhibit even much lower relaxation dependence than their z-counterparts). As shown in Figure S2, the "complete" scaling factors corresponding to the observed spectral shifts $\Delta\nu$ obtained using the argon matrix-isolation technique acquire rather coinciding values, thus explicitly justifying the use of the "linearity" assumption for the rationalization of the Ar-matrix-isolation data. The anharmonic calculation thus appears to be a useful complement to the standard normal coordinate analysis.

5. RESULTS AND DISCUSSION

5.1. Experiment. All complexes were studied in a solid phase on a cold (18 K) KBr substrate and simultaneously in the Ar matrix.
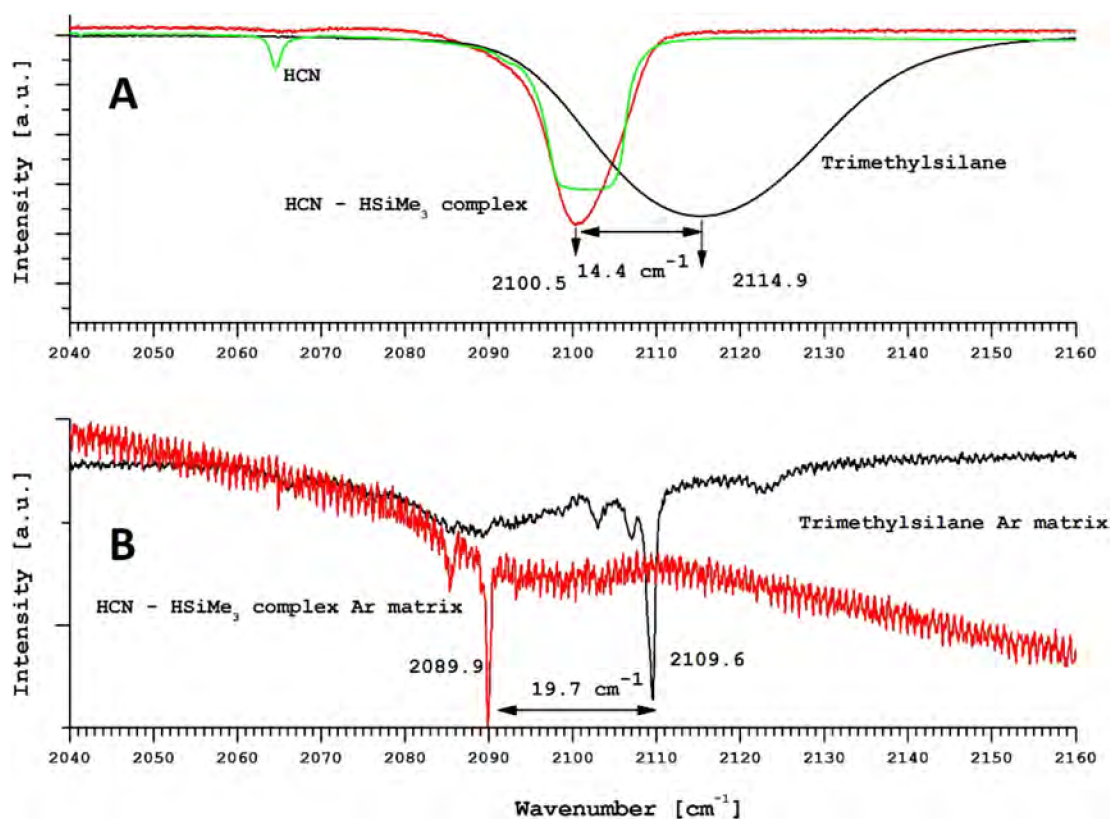
Figure 4. Solid-state and Ar-matrix spectra of the $Me_3Si-H\cdots HCN$ complex.

5.1.1. $Me_3Si-H\cdots ICF_3$ Complex. Panel (A) of Figure 2 depicts the spectrum of trimethylsilane (black) on a cold (18 K) KBr substrate together with the spectrum of the trimethylsilane-CF_3I 1:1 molecular complex (2068.8 cm^{-1}) at 18 K. The obtained redshift of the Si−H bond was estimated to be about 47.1 cm^{-1}. Panel (B) shows the Ar-matrix spectrum of pure trimethylsilane (black) and the spectrum of the $Me_3Si-H\cdots CF_3I$ complex at 18 K (red). The measured Si−H bond shift inside the argon matrix was 27.7 cm^{-1}.

5.1.2. $Me_3Si-H\cdots BrCN$ Complex. Panel (A) in Figure 3 shows the spectrum of trimethylsilane (black) on a cold (18 K) KBr substrate together with the absorption spectrum of BrCN at 18 K (green) and the $Me_3Si-H\cdots BrCN$−silane 1:1 molecular mixture at 18 K. If we accept the formation of the $Me_3Si-H\cdots BrCN$ molecular complex (the broad peak around 2078 cm^{-1}), the obtained redshift of the Si−H bond gives the value of 36.9 cm^{-1} (see Figure 3A). Panel (B) shows the Ar-matrix spectrum of pure trimethylsilane (black) and the spectrum of the Ar−$Me_3Si-H\cdots BrCN$ mixture (2000,1) at 18 K (red) and the argon-matrix spectrum of BrCN (green). From the argon-matrix spectra (Figure 3B), we attributed the broad peak around 2080 cm^{-1} to the molecular $Me_3Si-H\cdots BrCN$ complex, with the resulting redshift of the H-Br bond being 28.6 cm^{-1}.

5.1.3. $Me_3Si-H\cdots HCN$ Complex. Panel (A) in Figure 4 depicts the spectrum of trimethylsilane (black) on a cold (18 K) KBr substrate together with the HCN molecular absorption band at 18 K (green) and the $Me_3Si-H\cdots HCN$ 1:1 molecular complex (2100.5 cm^{-1}) at 18 K. The obtained redshift of the Si−H bond was estimated to be about 14.4 cm^{-1}. Panel (B) shows the Ar-matrix spectrum of pure trimethylsilane (black) and the spectrum of the $Me_3Si-H\cdots HCN$ complex at 18 K. The

measured Si−H bond shift inside the argon matrix was 19.7 cm^{-1}.

5.2. Calculations. *5.2.1. Subsystems.* Electrostatic potentials including the $V_{s,max}$ and $V_{s,min}$ values for the optimized structures of selected Lewis bases and acids (for which experimental measurements have been performed) are visualized in Figure 5. The most basic hydridic hydrogen (i.e.,
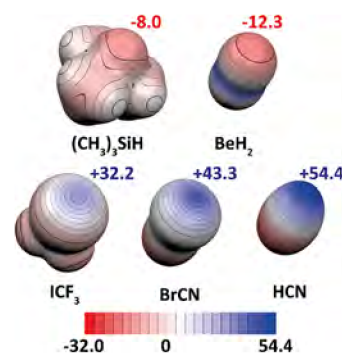

Figure 5. MEP calculated at the ωB97X-D/def2-QZVPP level for the monomers studied. The ESP scale is in kcal/mol. The $V_{s,max}$ on the hydrogen atom from the Me_3SiH molecule is depicted in red. The $V_{s,min}$ in the center of the σ-hole or on top of the hydrogen atom is in blue.

the strongest electron donor) has been found in BeH_2, followed by Me_3Si-H, while the strongest electron acceptor has been detected in HCN.

5.2.2. Complexes. The intramolecular X'−H (X'−H) and intermolecular H...Y' distances for $Me_3Si-H\cdots Y'$ complexes are shown in Table 1, whereas these characteristics for BeH_2 complexes are summarized in Table S1. In comparison with

Table 1. Intermolecular Distances and Changes in Intramolecular Bond Lengths (in Å) of Selected Bonds in Me$_3$SiH···Y′ Complexes (Y′ = ICF$_3$, BrCN, HCN) Calculated at the MP2-F12/cc-pVTZ-F12 Level[b]

	Δr(Si−H)	Δr(Si−C)	Δr(I−C)	H···I/vdW[a]
ICF$_3$	0.007	−0.003/−0.001/−0.001	0.002	2.874/−0.573
	Δr(Si−H)	Δr(Si−C)	Δr(Br−C)	H···Br/vdW[a]
BrCN	0.008	−0.003/−0.002/−0.002	0.005	2.705/−0.585
	Δr(Si−H)	Δr(Si−C)	Δr(H−C)	H···H/vdW[a]
HCN	0.005	−0.003/−0.003/0	0	2.729/+0.320

[a]The difference between the intermolecular distance and the sum of the vdW radii. [b]All values are in Å.

the sum of the vdW radii,[41] the intermolecular distances in complexes with ICF$_3$ and BrCN are significantly shorter (by 0.573 and 0.585 Å); in the complex with HCN, it is longer. Table 1 further shows that all intramolecular Si−H distances are systematically elongated upon complex formation. Notice that the elongation of the Si−H bond is smaller than that of the X−H bonds in the X−H···Y H-bonded systems. As expected, the Si−C bonds are contracted, but the respective changes are smaller. Finally, upon complex formation, the I−C and Br−C intramolecular distances are elongated, whereas the H−C distance is not changed. Qualitatively similar results have also been obtained for HBeH···Y′ complexes.

5.2.3. Energies. Table 2 contains calculated energy characteristics for Me$_3$Si−H···Y′ complexes, specifically MP2, MP2−F12,

Table 2. Energy Characteristics of the Me$_3$SiH···Y′ Complexes (Y′ = ICF$_3$, BrCN, HCN)[a]

Y′	$\Delta E^{MP2}/\Delta E^{MP2-F12}/\Delta E^{CCSD(T)-F12}$	ΔG^{MP2}(18 K)/$\Delta G^{MP2-F12}$(18 K)
ICF$_3$	−2.43/−3.27/−2.70	−1.85/−2.42
BrCN	−2.60/−3.02/−2.76	−2.07/−2.77
HCN	−2.41/−2.59/−2.24	−1.79/−1.97

[a]The total interaction energy calculated at the MP2/cc-pwCVTZ level (ΔE^{MP2}) and at the MP2-F12/cc-pVTZ-F12 level ($\Delta E^{MP2-F12}$), intrinsic interaction energy with counterpoise correction at the CCSD(T)-F12/cc-pVTZ-F12 level on the MP2-F12/cc-pVTZ-F12 geometries ($\Delta E^{CCSD(T)-F12}$) and Gibbs free energy at MP2/cc-pwCVTZ (ΔG^{MP2}) and MP2-F12/cc-pVTZ-F12 ($\Delta G^{MP2-F12}$) levels. All values are in kcal/mol.

and CCSD(T)-F12 interaction energies and binding free energies at 18 K based on the MP2 and MP2−F12 characteristics. Corresponding results obtained for BeH$_2$ complexes are collected in Table S2.

The MP2 stabilization energies of all CIHB complexes are comparable, whereas the more reliable MP2−F12 and mainly CCSD(T)−F12 energies of the first two complexes are similar and are higher than that of the third (dihydrogen-bonded) one. Further, all MP2−F12 and CCSD(T)−F12 stabilization energies lie between 2.6 and 3.3 kcal/mol and between 2.2 and 2.8 kcal/mol, respectively, and are thus well comparable to those of classical H-bonded complexes. These findings contradict the results from the previous subchapter (Subsystems), showing that the strongest electron acceptor is HCN, followed by BrCN and ICF$_3$. Therefore, the complex with HCN was expected to be the strongest. The fact that the opposite is true, i.e., this complex is the weakest, is caused by dispersion energy. The SAPT2 + 3[35] dispersion and total interaction energies for

the complexes of Me$_3$Si−H with CF$_3$I, BrCN, and HCN amount to −4.35, −3.79, and −3.05 kcal/mol and − 3.34, −3.20, −2.50 kcal/mol, respectively. Clearly, the smallest dispersion energy for the last complex is responsible for its smallest stabilization energy. Notice that the SAPT2 + 3 interaction energies for all three complexes agree surprisingly well with the MP2−F12 ones. The negative binding free energies calculated for all the complexes indicate their formation at 18 K. The MP2 and CCSD(T) interaction energies of BeH$_2$ complexes are systematically smaller, with the largest values found for the HBeH··· BrCN complex. The binding free energies of all complexes are smaller than those of Me$_3$Si−H, but they are still negative, which ensures their formation at 18 K.

Table 3 shows the difference in the orbital occupancies (of monomers and complexes) of occupied and unoccupied Si−H

Table 3. Orbital−Occupation Difference between Monomers and in Me$_3$SiH···Y′ Complexes Using NBO Analysis Calculated at the ωB97X-D/aug-cc-pwCVTZ Level on MP2-F12/cc-pVTZ-F12 Geometries

Y′	σ/σ* Si−H	σ/σ* I−C	ΣLP I
ICF$_3$	−0.010/0.004	−0.003/0.005	−0.005
Y′	σ/σ* Si−H	σ/σ* Br−C	ΣLP Br
BrCN	−0.010/0.004	−0.001/0.009	−0.002
Y′	σ/σ* Si−H	σ/σ* H−C	LP N
HCN	−0.001/0.002	−0.001/0	−0.001

σ-orbitals (the corresponding values for the BeH$_2$ complexes are included in Table S3). Changes in orbital occupancies are related to changes in bond lengths; the biggest changes have been found for the Si−H bond. A decrease in the occupancy of the Si−H σ-orbitals and its increase in the case of the σ*-orbitals, found for all three complexes, lead to a weakening of the Si−H bond, which is manifested by the elongation of the Si−H bond (cf. Table 1). Very similar results were obtained for the I−C, Br−C, and H−C bonds in the ICF3, BrCN, and HCN electron acceptors, respectively. In these cases, the elongation of the respective bonds was smaller and, in the case of HCN even, equal to zero.

Other occupancy changes and the respective bond-length changes are less pronounced and are not discussed below.

5.2.4. Vibration Frequencies. Table 4 presents the experimental and calculated shifts of Si−H stretching frequencies upon complex formation. First, both experimental techniques predict larger shifts for the first two complexes; the same trend appears in all calculated shifts. Second, the calculated MP2−F12 harmonic shifts are systematically larger than the

Table 4. IR Shift ($\Delta \nu$ in cm^{-1}) and Change of Intensity (ΔI in km/mol) of the Si−H Band upon the Formation of Me$_3$SiH··· Y′ Complexes

Y′	$\Delta \nu$[a]	ΔI[b]
ICF$_3$	−47/−28//−31(−52)/−38(−49[c])	+136
BrCN	−37/−29//−36(−55)/−41(−50)	+138
HCN	−14/−20//−20(−35)/−25(−29)	+37

[a]Experimental − cold substrate/experimental − Ar-matrix//calculated anharmonic scaled (calculated anharmonic unscaled)/calculated harmonic at the MP2/cc-pwCVTZ level (calculated harmonic at the MP2-F12/cc-pVTZ-F12 level). [b]Calculated harmonic at the MP2/cc-pwCVTZ level. [c]Geometry minimum with one negative frequency.
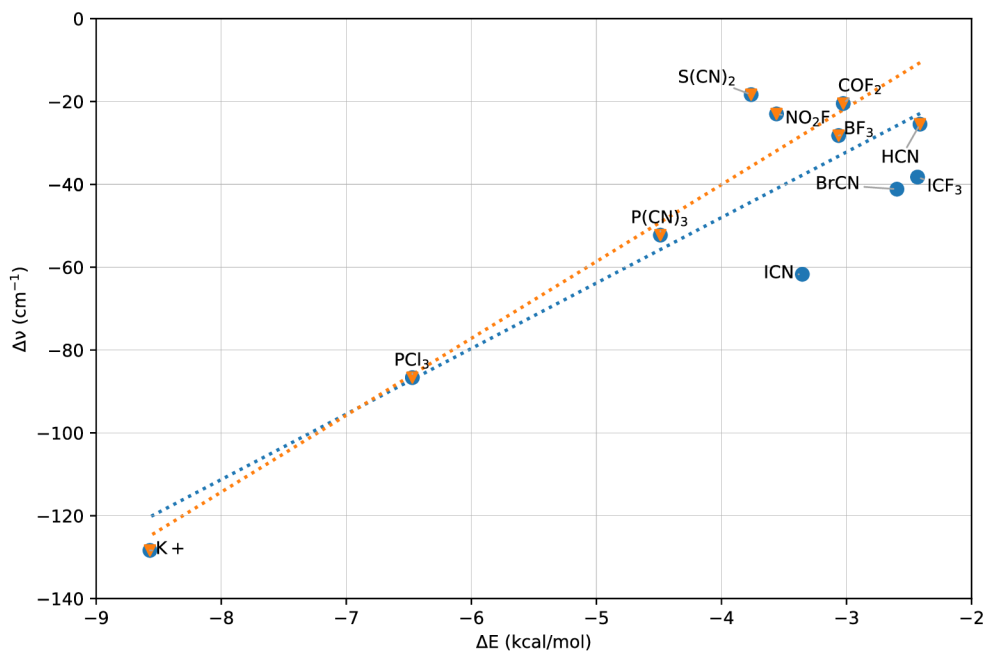
Figure 6. Correlation between the total interaction energy (ΔE) and the shift of the Si−H stretching frequency ($\Delta \nu$) for selected complexes of Me_3SiH with various electron acceptors. All values are calculated at the MP2/cc-pwCVTZ level. The blue correlation includes all electron acceptors; in the orange one, the electron acceptors exhibiting σ-holes (ICN, BrCN, and ICF_3) have been omitted.

MP2 harmonic ones and are similar to the anharmonic unscaled ones. Finally, the agreement between the experimental and calculated frequencies is very good, which supports the reliability and suitability of all calculated techniques. In summary, the agreement between the experimental and calculated frequency shifts is satisfactory and all Si−H frequencies are redshifted upon complex formation. As expected, the magnitude of the redshifts correlates with the complex stability. Finally, the intensities of the Si−H stretch in all three complexes have increased upon complex formation. Notice here that the experimental technique adopted has not made it possible to detect intensity changes.

In the case of Be−H, the lower-energy symmetric stretching vibrations are forbidden; thus, only the antisymmetric vibrations, which are higher in energy, are discussed. As observed for the above-discussed Si−H frequencies, the intensities of the Be−H stretching frequencies (see Table S4 for the calculated harmonic Be−H stretching frequencies and their intensities) upon complexes formation also significantly increase. Frequency shifts, on the other hand, provide a different picture, with a blueshift in HBeH···BrCN, redshift in HBeH···HCN, and only negligible shift in HBeH···ICF_3.

5.2.5. Characterization and Classification of the Complexes Studied. The classification of Me_3Si−H···Y′ (Y′ = ICF_3, BrCN, HCN) complexes, studied both experimentally and computationally, is not unique. The first two complexes can be viewed either as CIHB or as halogen-bonded (XB) ones. Their classification is not easy because both forms are involved—the stabilization of the complex comes from Si−H···Y′ CIHB as well as from the $H^{\delta-} \rightarrow I$ (Br) σ-hole halogen bond. The dominant role of the former contribution is supported by the following evidence:

(i) The CIHB is accompanied by a charge transfer (CT) from Y′ to Me_3Si−H, whereas the CT accompanying the XB is reversed, i.e., from Me_3Si−H to Y′. Because of the

partial compensation of both contributions, the total CT between the subsystems should be small, which is fully supported by the calculated value (0.007 and 0.003 electrons transferred from Me3SiH to BrCN and ICF_3, respectively). This is further verified by the NBO E2 charge-transfer energies (Me_3Si−H $\rightarrow$ Y′ and Y′ $\rightarrow$ Me_3Si−H), which are almost equal for both complexes. Table 3 shows that electron density in these two complexes is transferred predominantly to the σ- and σ^* Si−H orbitals, which leads to the weakening and elongation of this bond, accompanied by a redshift of the Si−H stretching frequency. In the reverse case, the electron density in the X−C σ- and σ^* orbitals of ICF_3 and BrCN also decreases and increases, resulting again in the weakening and elongation of the bond accompanied by a redshift of the respective stretching frequencies. The redshifts of X−C stretching frequencies are smaller than that in that in the previous case (Si−H) due to the presence of two heavy atoms (I,C and Br,C). Shifts of the Si−H bond stretching vibration frequencies are thus the most visible presentation of the complex formation.

(ii) The strength of the XB in Me_3Si−H···Y′ (Y′ = ICF_3, BrCN) complexes can only be estimated indirectly. The stabilization energy of the XB complexes with identical electron acceptors and a different electron donor, namely, H_3N···BrCN and H_3N···ICF_3, where stabilization comes exclusively from the halogen bond, is considerably higher (6.0 and 5.4 kcal/mol, respectively) than that of parent complexes with Me_3Si−H (cf. Table 2). This finding corroborates the fact that XB in Me_3Si−H···Y′ (Y′ = ICF_3, BrCN) complexes is only weak.

(iii) The most conclusive evidence comes from the correlation between the stabilization energy and shift of the Si−H stretching frequency upon Me_3Si−H···Y′ complex formation. Thirteen different electron acceptors have been considered here: first, those having pronounced σ- (ICF_3,

BrCN, ICN, $P(CN)_3$, PCl_3, $S(CN)_2$,) and π- ($CH_3(CN)_3$, $C(CN)_6$, COF_2, NO_2F) holes, allowing the formation of the XB; next, an electron acceptor with a p-hole (BF_3); and, finally, electron acceptors with a positive charge (K^+, HCN). The respective structures, stabilization energies, and shifts of the Si−H stretching frequencies are shown in Figure 1. The formation of CIHB is systematically manifested by the redshift of the Si−H stretching frequency. As expected, this shift is proportional to the stabilization energy of the complex (cf. Figure 6). The figure depicts two correlation lines: the blue one shows correlation for all electron acceptors, while in the case of the orange one, the electron acceptors exhibiting σ-holes (ICF3, BrCN, and ICN) have been omitted. Evidently, both correlations are very similar, which indicates that the nature of stabilization in the last three complexes is not significantly different from those complexes where XB character is absent.

Finally, the third complex for which experimental results exist, $Me_3Si−H...HCN$, can be characterized as the CIHB or the dihydrogen one. In this case, the classification is easier because we can directly compare shifts of Si−H and C−H vibration stretching frequencies in both H-bonds as both possess hydrogen. Upon complex formation, the computed Si−H stretching frequency is redshifted (by 25 cm^{-1}), whereas the C−H stretching frequency is blueshifted. The blueshift is, however, considerably smaller (7 cm^{-1}). This means that the CIHB character of the complex is dominant over the dihydrogen-bonded one, which is further supported by correlation between the stabilization energy and vibration shifts, discussed in previous the paragraph ($Me_3Si−H\cdots HCN$ is very close to the ideal correlation line).

We can thus conclude that in all three complexes studied experimentally as well as computationally, the CIHB form is dominant over the XB and dihydrogen forms. This is reflected in the moderate redshift of Si−H stretching frequency, which is the largest among the stretching frequencies. These shifts are well comparable to redshifts in complexes with protonic H-bonds.

6. CONCLUSIONS AND REVISED DEFINITION OF H-BONDING

The complexation of $Me_3Si−H$ and $HBe−H$ molecules (containing a hydridic hydrogen) with different electron acceptors is accompanied by red- and blueshifts of the Si−H and Be−H stretching frequencies, which are comparable with those in protonic H-bonded complexes. Both the red- or blueshifts were accompanied by an increase in intensity (the experiment did not make it possible to detect the intensity changes during complex formation), comparable to intensity changes of protonic H-bonded complexes.

An important question arises as to what to call these interactions with hydridic−hydrogen participation. Jabłoński, who studied these interactions intensely, introduced a new name for them, namely, charge-inverted H-bonding. In our opinion, this name does not capture the nature of the interaction, and "hydridic H-bonding" seems more appropriate. The wide use of this term is, however, connected with another problem. If we characterize the type of hydrogen bond by the charge on the participating hydrogen, we should consistently use "protonic H-bond" instead of "H-bond". The undesirable inflation of new names in this case can easily be avoided by changing the current IUPAC definition of hydrogen bonding. The current IUPAC

definition requires "X (from X−H) to be more electronegative than H." We prefer this avenue because the relevant change in the definition (mainly concerning the relative electronegativities of X and H) is only marginal and, besides hydridic and protonic H-bonding, it will also cover the dihydrogen bond. Below, we present the very first draft of this modification including a part of the original IUPAC definition, with the proposed corrections in italics and with the part of the definition to be removed underscored. The revised version covers three different interaction schemes where hydrogen plays a dominant role: $X−H^{\delta+}\cdots Y^{\delta-}$ (protonic H-bond), $X'−H^{\delta-}\cdots Y'^{\delta+}$ (hydridic H-bond), and $X'−H^{\delta-}\cdots H'^{\delta+}−Z$ (dihydrogen bond). We realize that any change of existing definition is difficult and cannot be rushed and requires an extended, broad, and in-depth discussion within the scientific community. Despite that, the benefit is obvious: the simplification and clarification of the nomenclature of one of the most important type of non-covalent interactions.

Our proposed definition of the hydrogen bond is as follows: The hydrogen bond is an attractive interaction between a hydrogen atom from a molecule or a molecular fragment X−H in which X is more or less electronegative than H and an atom or a group of atoms in the same or a different molecule in which there is evidence of bond formation. A typical hydrogen bond may be depicted as X−H⋯Y−Z, where the three dots denote the bond.

Depending on the electronegativity of X, the hydrogen carries a positive charge (protonic hydrogen) and thus acts as the hydrogen-bond donor (Lewis acid) or a negative charge (hydridic hydrogen) and thus acts as the hydrogen-bond acceptor (Lewis base). The atom Y in the molecule in the former case may be an electron-rich region such as, but not limited to, a lone electron pair of Y or a π-bonded pair of Y-Z, while in the second case, it may be an electron-deficient region such as σ-, n-, or π-hole or a positively-charged atom including hydrogen or an ion or a fragment of a molecule. X−H represents the hydrogen bond donor. The accep-tor may be an atom or an anion Y, or a fragment or a mole-cule Y−Z, where Y is bonded to Z. In some cases, X and Y are the same. In more specific cases, X and Y are the same and X−H and Y−H distances are the same as well leading to symmetric hydrogen bonds. In any event, the acceptor is an electron rich region such as, but not lim-ited to, a lone pair of Y or π-bonded pair of Y−Z.

The other parts of the original IUPAC definition remain unchanged.

■ ASSOCIATED CONTENT

Ⓢ Supporting Information

The Supporting Information is available free of charge at https://pubs.acs.org/doi/10.1021/jacs.3c00802.

   BeH_2 complexes, figures, and MP2-optimized geometries (PDF)

■ AUTHOR INFORMATION

Corresponding Authors

Svatopluk Civiš − *Institute of Organic Chemistry and Biochemistry, Czech Academy of Sciences, 160 00 Prague, Czech Republic; J. Heyrovský Institute of Physical Chemistry, Czech Academy of Sciences, 18200 Prague 8, Czech Republic;* ⓞ orcid.org/0000-0001-6215-0256; Email: svatopluk.civis@jh-inst.cas.cz

Pavel Hobza − *Institute of Organic Chemistry and Biochemistry, Czech Academy of Sciences, 160 00 Prague, Czech Republic;*

IT4Innovations, VŠB − Technical University of Ostrava, 708 00 Ostrava-Poruba, Czech Republic; ● orcid.org/0000-0001-5292-6719; Email: pavel.hobza@uochb.cas.cz

Authors

Maximilián Lamanec − *Institute of Organic Chemistry and Biochemistry, Czech Academy of Sciences, 160 00 Prague, Czech Republic; IT4Innovations, VŠB − Technical University of Ostrava, 708 00 Ostrava-Poruba, Czech Republic; Department of Physical Chemistry, Palacký University Olomouc, 771 46 Olomouc, Czech Republic;* ● orcid.org/0000-0002-7304-2207

Vladimír Špirko − *Institute of Organic Chemistry and Biochemistry, Czech Academy of Sciences, 160 00 Prague, Czech Republic*

Jiří Kubišta − *J. Heyrovský Institute of Physical Chemistry, Czech Academy of Sciences, 18200 Prague 8, Czech Republic*

Matej Špeťko − *IT4Innovations, VŠB − Technical University of Ostrava, 708 00 Ostrava-Poruba, Czech Republic;* ● orcid.org/0000-0002-5486-0503

Complete contact information is available at:
https://pubs.acs.org/10.1021/jacs.3c00802

Author Contributions

⊥S.C. and M.L. contributed equally to this work as co-first authors.

Notes

The authors declare no competing financial interest.

■ REFERENCES

(1) Kollman, P. A.; Allen, L. C. The Theory of Hydrogen Bond. *Chem. Rev.* **1972**, *72*, 283−303.

(2) Reed, A. E.; Weinhold, F.; Curtiss, L. A.; Pochatko, D. J. Natural Bond Orbital Analysis of Molecular Interactions: Theoretical Studies of Binary Complexes of HF, H_2O, NH_3, N_2, O_2, F_2, CO, and CO_2 with HF, H_2O, and NH_3. *J. Chem. Phys.* **1998**, *84*, 5687.

(3) Grabowski, S. J. What Is the Covalency of Hydrogen Bonding? *Chem. Rev.* **2011**, *111*, 2597−2625.

(4) Hobza, P.; Havlas, Z. Blue-Shifting Hydrogen Bonds. *Chem. Rev.* **2000**, *100*, 4253−4264.

(5) Hobza, P.; Špirko, V.; Havlas, Z.; Buchhold, K.; Reimann, B.; Barth, H. D.; Brutschy, B. Anti-Hydrogen Bond between Chloroform and Fluorobenzene. *Chem. Phys. Lett.* **1999**, *299*, 180−186.

(6) Arunan, E.; et al. Defining the Hydrogen Bond: An Account (IUPAC Technical Report). *Pure Appl. Chem.* **2011**, *83*, 1619−1636.

(7) Jabłoński, M. Binding of X−H to the Lone-Pair Vacancy: Charge-Inverted Hydrogen Bond. *Chem. Phys. Lett.* **2009**, *477*, 374−376.

(8) Jabłoński. Full vs. Constrain Geometry Optimization in the Open-Closed Method in Estimating the Energy of Intramolecular Charge-Inverted Hydrogen Bonds. *Chem. Phys.* **2010**, *376*, 76−83.

(9) Jabłoński, M. Intramolecular Charge-Inverted Hydrogen Bond. *J. Mol. Struct. THEOCHEM* **2010**, *948*, 21−24.

(10) Jabłoński, M.; Sokalski, W. A. Physical Nature of Interactions in Charge-Inverted Hydrogen Bonds. *Chem. Phys. Lett.* **2012**, *552*, 156−161.

(11) Jabłoński, M. Theoretical Insight into the Nature of the Intermolecular Charge-Inverted Hydrogen Bond. *Comput. Theor. Chem.* **2012**, *998*, 39−45.

(12) Jabłoński. Charge-Inverted Hydrogen Bond vs. Other Interactions Possessing a Hydridic Hydrogen Atom. *Chem. Phys.* **2014**, *433*, 76−84.

(13) Jabłoński, M. Comparative Study of Geometric and QTAIM-Based Differences between X-H⋯Y Intramolecular Charge-Inverted Hydrogen Bonds, M1⋯(H−X) Agostic Bonds and M2⋯(H2-XH) σ Interactions (X = Si, Ge). *Comput. Theor. Chem.* **2016**, *1096*, 54−65.

(14) Jabłoński, M. Strength of Si-H⋯B Charge-Inverted Hydrogen Bonds in 1-Silacyclopent-2-Enes and 1-Silacyclohex-2-Enes. *Struct. Chem.* **2017**, *28*, 1697−1706.

(15) Jabłoński, M. Ten Years of Charge-Inverted Hydrogen Bonds. *Struct. Chem.* **2020**, *31*, 61−80.

(16) Crabtree, R. H.; Siegbahn, P. E. M.; Eisenstein, O.; Rheingold, A. L.; Koetzle, T. F. A New Intermolecular Interaction: Unconventional Hydrogen Bonds with Element-Hydride Bonds as Proton Acceptor. *Acc. Chem. Res.* **1996**, *29*, 348−354.

(17) Guillot, B. A Reappraisal of What We Have Learnt during Three Decades of Computer Simulations on Water. *J. Mol. Liq.* **2002**, *101*, 219−260.

(18) Shea, J. A.; Flygare, W. H. The Rotational Spectrum and Molecular Structure of the Ethylene−HF Complex. *J. Chem. Phys.* **1998**, *76*, 4857.

(19) Novick, S. E.; Davies, P. B.; Dyke, T. R.; Klemperer, W. Polarity of van Der Waals Molecules. *J. Am. Chem. Soc.* **1973**, *95*, 8547−8550.

(20) Bondybey, V. E.; Smith, A. M.; Agreiter, J. New Developments in Matrix Isolation Spectroscopy. *Chem. Rev.* **1996**, *96*, 2113−2134.

(21) Potapov, A. Weakly Bound Molecular Complexes in the Laboratory and in the Interstellar Medium: A Lost Interest? *Mol. Astrophys.* **2017**, *6*, 16−21.

(22) Whittle, E.; Dows, D. A.; Pimentel, G. C. Matrix Isolation Method for the Experimental Study of Unstable Species. *J Chem Phys* **1954**, *22*, 1943.

(23) Jacox, M. E. The Spectroscopy of Molecular Reaction Intermediates Trapped in the Solid Rare Gases. *Chem. Soc. Rev.* **2002**, *31*, 108−115.

(24) Klemperer, W.; Vaida, V. Molecular Complexes in Close and Far Away. *Proc. Natl. Acad. Sci. U. S. A.* **2006**, *103*, 10584−10588.

(25) Peterson, K. A.; Dunning, T. H. Accurate Correlation Consistent Basis Sets for Molecular Core−Valence Correlation Effects: The Second Row Atoms Al−Ar, and the First Row Atoms B−Ne Revisited. *J. Chem. Phys.* **2002**, *117*, 10548.

(26) Peterson, K. A.; Yousaf, K. E. Molecular Core-Valence Correlation Effects Involving the Post-d Elements Ga−Rn: Benchmarks and New Pseudopotential-Based Correlation Consistent Basis Sets. *J Chem Phys* **2010**, *133*, No. 174116.

(27) Werner, H. J.; Adler, T. B.; Manby, F. R. General Orbital Invariant MP2-F12 Theory. *J Chem Phys* **2007**, *126*, No. 164102.

(28) Peterson, K. A.; Adler, T. B.; Werner, H. J. Systematically Convergent Basis Sets for Explicitly Correlated Wavefunctions: The Atoms H, He, B−Ne, and Al−Ar. *J Chem Phys* **2008**, *128*, No. 084102.

(29) Werner, H. J.; Knowles, P. J.; Knizia, G.; Manby, F. R.; Schütz, M. Molpro: A General-Purpose Quantum Chemistry Program Package. *Wiley Interdiscip Rev Comput Mol Sci* **2012**, *2*, 242−253.

(30) Werner, H. J.; Knowles, P. J.; Manby, F. R.; Black, J. A.; Doll, K.; Heßelmann, A.; Kats, D.; Köhn, A.; Korona, T.; Kreplin, D. A.; Ma, Q.; Miller, T. F.; Mitrushchenkov, A.; Peterson, K. A.; Polyak, I.; Rauhut, G.; Sibaev, M. The Molpro Quantum Chemistry Package. *J. Chem. Phys.* **2020**, *152*, No. 144107.

(31) Řezáč, J. Cuby: An Integrative Framework for Computational Chemistry. *J. Comput. Chem.* **2016**, *37*, 1230−1237.

(32) *TURBOMOLE V7.5 2020, a development of University of Karlsruhe and Forschungszentrum Karlsruhe GmbH, 1989−2007,*

TURBOMOLE GmbH, since 2007; available from http://www.turbomole.com.

(33) Adler, T. B.; Knizia, G.; Werner, H. J. A Simple and Efficient CCSD(T)-F12 Approximation. *J. Chem. Phys.* **2007**, *127*, No. 221106.

(34) Boys, S. F.; Bernardi, F. The Calculation of Small Molecular Interactions by the Differences of Separate Total Energies. Some Procedures with Reduced Errors. *Mol. Phys.* **1970**, *19*, 553−566.

(35) Jeziorski, B.; Moszynski, R.; Szalewicz, K. Perturbation Theory Approach to Intermolecular Potential Energy Surfaces of van Der Waals Complexes. *Chem. Rev.* **1994**, *94*, 1887−1930.

(36) Parrish, R. M.; Burns, L. A.; Smith, D. G. A.; Simmonett, A. C.; DePrince, A. E.; Hohenstein, E. G.; Bozkaya, U.; Sokolov, A. Y.; di Remigio, R.; Richard, R. M.; Gonthier, J. F.; James, A. M.; McAlexander, H. R.; Kumar, A.; Saitow, M.; Wang, X.; Pritchard, B. P.; Verma, P.; Schaefer, H. F.; Patkowski, K.; King, R. A.; Valeev, E. F.; Evangelista, F. A.; Turney, J. M.; Crawford, T. D.; Sherrill, C. D. Psi4 1.1: An Open-Source Electronic Structure Program Emphasizing Automation, Advanced Libraries, and Interoperability. *J. Chem. Theory Comput.* **2017**, *13*, 3185−3197.

(37) Frisch, M. J.; Trucks, G. W.; Schlegel, H. B.; Scuseria, G. E.; Robb, M. A.; Cheeseman, J. R.; Scalmani, G.; Barone, V.; Petersson, G. A.; Nakatsuji, H.; Li, X.; Caricato, M.; Marenich, A. V.; Bloino, J.; Janesko, B. G.; Gomperts, R.; Mennucci, B.; Hratchian, H. P.; Ortiz, J. V.; Izmaylov, A. F.; Sonnenberg, J. L.; Williams; Ding, F.; Lipparini, F.; Egidi, F.; Goings, J.; Peng, B.; Petrone, A.; Henderson, T.; Ranasinghe, D.; Zakrzewski, V. G.; Gao, J.; Rega, N.; Zheng, G.; Liang, W.; Hada, M.; Ehara, M.; Toyota, K.; Fukuda, R.; Hasegawa, J.; Ishida, M.; Nakajima, T.; Honda, Y.; Kitao, O.; Nakai, H.; Vreven, T.; Throssell, K.; Montgomery, Jr., J. A.; Peralta, J. E.; Ogliaro, F.; Bearpark, M. J.; Heyd, J. J.; Brothers, E. N.; Kudin, K. N.; Staroverov, V. N.; Keith, T. A.; Kobayashi, R.; Normand, J.; Raghavachari, K.; Rendell, A. P.; Burant, J. C.; Iyengar, S. S.; Tomasi, J.; Cossi, M.; Millam, J. M.; Klene, M.; Adamo, C.; Cammi, R.; Ochterski, J. W.; Martin, R. L.; Morokuma, K.; Farkas, O.; Foresman, J. B.; Fox, D. J. *G16_C01. 2016, p Gaussian 16*, Revision C.01, Gaussian, Inc., Wallin.

(38) Mallada, B.; Gallardo, A.; Lamanec, M.; de la Torre, B.; Špirko, V.; Hobza, P.; Jelinek, P. Real-Space Imaging of Anisotropic Charge of σ-Hole by Means of Kelvin Probe Force Microscopy. *Science* **2021**, *374*, 863−867.

(39) Lo, R.; Manna, D.; Lamanec, M.; Dračínský, M.; Bouř, P.; Wu, T.; Bastien, G.; Kaleta, J.; Miriyala, V. M.; Špirko, V.; Mašínová, A.; Nachtigallová, D.; Hobza, P. The Stability of Covalent Dative Bond Significantly Increases with Increasing Solvent Polarity. *Nat. Commun.* **2022**, *13*, 1−7.

(40) Hougen, J. T.; Bunker, P. R.; Johns, J. W. C. The Vibration-Rotation Problem in Triatomic Molecules Allowing for a Large-Amplitude Bending Vibration. *J. Mol. Spectrosc.* **1970**, *34*, 136−172.

(41) Van Der Batsanov, S. S. Waals Radii of Elements. *Inorg. Mater.* **2001**, *37*, 871−885.

📖 Recommended by ACS

SPECTROSCOPY

Real-space imaging of anisotropic charge of σ-hole by means of Kelvin probe force microscopy

B. Mallada[1,2,3]†, A. Gallardo[2,4]†, M. Lamanec[3,5]†, B. de la Torre[1,2], V. Špirko[5,6], P. Hobza[5,7]*, P. Jelínek[1,2]*

An anisotropic charge distribution on individual atoms, such as σ-holes, may strongly affect the material and structural properties of systems. However, the spatial resolution of such anisotropic charge distributions on an atom represents a long-standing experimental challenge. In particular, the existence of the σ-hole on halogen atoms has been demonstrated only indirectly through the determination of the crystal structures of organic molecules containing halogens or with theoretical calculations, consequently calling for its direct experimental visualization. We show that Kelvin probe force microscopy with a properly functionalized probe can image the anisotropic charge of the σ-hole and the quadrupolar charge of a carbon monoxide molecule. This opens a new way to characterize biological and chemical systems in which anisotropic atomic charges play a decisive role.

The observation of molecular structures with the unusual atomic arrangement of possessing two adjacent halogens or a pair of halogen atoms and electron donor motifs (oxygen, nitrogen, sulfur, …), found in different crystals in the second half of the 20th century (1–4), represented a long-standing puzzle in supramolecular chemistry. Both halogens and electron donors are electronegative elements that carry a negative charge. Thus, close contacts of these atoms should theoretically cause highly repulsive electrostatic interaction. Counterintuitively, such atoms are frequently found to form intermolecular bonds, called latter halogen bonds, that stabilize the molecular crystal structure. An elegant solution offered by Auffinger *et al.* (5), Clark *et al.* (6), and Politzer *et al.* (7, 8) showed that the formation of a covalent bond between certain halogen atoms (chlorine, bromine, and iodine) and a more electronegative atom (such as carbon) gives rise to a so-called σ-hole that has an anisotropic charge distribution on the halogen atom. Thus, a physical observable corresponding electrostatic potential around the halogen atom is not uniform (as considered within all empirical force fields) but exhibits an electropositive distal to covalently bound carbon crown surrounded by an electronegative belt (Fig. 1A).

Consequently, halogen bonding is attributed to attractive electrostatic interaction between a halogen's electropositive σ-hole and an electronegative belt of the other halogen or an electronegative atom with negative charge. The International Union of Pure and Applied Chemistry (IUPAC) definition of a halogen bond (9) states that a halogen bond "occurs when there is evidence of a net attractive interaction between an electrophilic region associated with a halogen atom in a molecular entity and a nucleophilic region in another, or the same, molecular entity." Stability of the σ-hole bonding is comparable with that of hydrogen-bonded complexes, and attraction in both types of noncovalent complexes was originally assigned to electrostatic interaction. Although this scenario is basically true for H-bonded complexes, in the case of halogen-bonded systems, the importance of dispersion interaction (10) was highlighted. The importance of the dispersion interaction is not surprising because close contact takes place between two heavy atoms with high polarizability in halogen-bonded complexes.

The concept of halogen bonding was later generalized to a σ-hole bonding concept. In particular, the halogen (group 17), chalcogen (group 16), pnicogen (group 15), tetrel (group 14), and aerogen bonding (group 18) were established according to the name of the electronegative atom bearing the positive σ-hole. The existence of a σ-hole in atoms of the mentioned groups of elements has a common origin in the unequal occupation of valence orbitals.

The σ-hole bonding plays a key role in supramolecular chemistry (11), including the engineering of molecular crystals or in biological macromolecular systems (5). Despite its relevance and intensive research devoted to σ-hole bonding, the existence of the σ-hole itself was confirmed only indirectly with quantum calculations (5–8) or crystal structures of complexes containing σ-hole donors and electron acceptors (11–15). However, a direct visualization of this entity allowing for the resolution of its peculiar shape has thus far been missing.

The cause of the σ-hole is the anisotropic distribution of the atomic charge on a halogen atom. The imaging of anisotropic atomic charge represents an unfulfilled challenge for experimental techniques, including scanning probe microscopy (SPM), electron microscopy, and diffraction methods. Thus, we sought a technique in which the imaging mechanism relies on the electrostatic force to facilitate the visualization of the anisotropic charge distribution on a halogen atom with a sub-ångstrom spatial resolution. We show that real-space visualization of the σ-hole can be achieved through Kelvin probe force microscopy (KPFM) under ultrahigh vacuum (UHV) conditions (16, 17) with unprecedented spatial resolution.

KPFM belongs to a family of SPM techniques that routinely provide real-space atomic resolution of surfaces. In the KPFM technique, the variation of the frequency shift Δf of an oscillating probe on applied bias voltage V with the quadratic form $\Delta f \sim V^2$ is recorded (18). The vertex of the Kelvin parabola $\Delta f(V)$ determines the difference between work functions of tip and sample, also called the contact potential difference V_{CPD}. Moreover, the spatial variation of the contact potential difference V_{CPD} across the surface allows the mapping of local variation of surface dipole on the sample (V_{LCPD}) (17). Recent developments of the KPFM technique operating in UHV conditions made it possible to reach true atomic resolution on surfaces (19, 20) to image intramolecular charge distribution (21), to control single-electron charge states (22), to resolve bond polarity (23), or to discriminate charge (24).

The atomic contrast in KPFM images originates from a microscopic electrostatic force between static (ρ_0) and polarized charge densities ($\delta\rho$) located on frontier atoms from the tip apex and sample when an external bias is applied (17). There are two dominant components of this force: the interaction between the polarized charge on the apex $\delta\rho_t$, which is linearly proportional to the applied bias voltage (V), and the static charge on sample ρ_s^0. The second term consists of the electrostatic interaction between the polarized charge on the sample $\delta\rho_s$ and the static charge on tip ρ_t^0. Consequently, these two components cause local variation of the contact potential difference V_{LCPD} (a detailed description of the mechanism is provided in the supplementary materials), thus providing atomic-scale contrast.

Results

Consequently, KPFM appears to be the tool of choice for imaging anisotropic charge distribution within a single atom, such as the

[1]Regional Centre of Advanced Technologies and Materials, Czech Advanced Technology and Research Institute (CATRIN), Palacký University Olomouc, 78371 Olomouc, Czech Republic. [2]Institute of Physics, Academy of Sciences of the Czech Republic, Prague, Czech Republic. [3]Department of Physical Chemistry, Palacký University Olomouc, tr. 17. listopadu 12, 771 46 Olomouc, Czech Republic. [4]Department of Condensed Matter Physics, Faculty of Mathematics and Physics, Charles University, V Holešovičkách 2, 180 00 Prague, Czech Republic. [5]Institute of Organic Chemistry and Biochemistry, Czech Academy of Sciences, Flemingovo Náměstí 542/2, 16000 Prague, Czech Republic. [6]Department of Chemical Physics and Optics, Faculty of Mathematics and Physics, Charles University in Prague, Ke Karlovu 3, 12116 Prague, Czech Republic. [7]IT4Innovations, VŠB-Technical University of Ostrava, 17. listopadu 2172/15, 70800 Ostrava-Poruba, Czech Republic.
*Corresponding author. Email: pavel.hobza@uochb.cas.cz (P.H.); jelinekp@fzu.cz (P.J.)
†These authors contributed equally to this work.

Fig. 1. Schematic view of the KPFM measurements to image a σ-hole. (**A** and **B**) Models of 4BrPhM and 4FPhM molecules, including corresponding electrostatic potential map on outermost Br/F atom. They reveal the presence of the σ-hole on a Br atom, and there is an isotropic negative charge on the F atom. (**C**) Schematic view of the acquisition method of the KPFM measurement with a functionalized Xe-tip on a 2D grid. (**D**) Corresponding $\Delta f(V)$ parabolas acquired in the central part (blue) of the 2D grid and on the periphery (red). Vertical dashed lines indicate the value of V_{LCPD} for the given $\Delta f(V)$ parabola, which forms the 2D KPFM image. (**E**) 3D representation of the KPFM images (V_{LCPD} maps) acquired with an Xe-tip over bromide and fluoride atoms of 4BrPhM and 4FPhM molecules. Blue indicates low values of V_{LCPD}, and red indicates high values of V_{LCPD}.
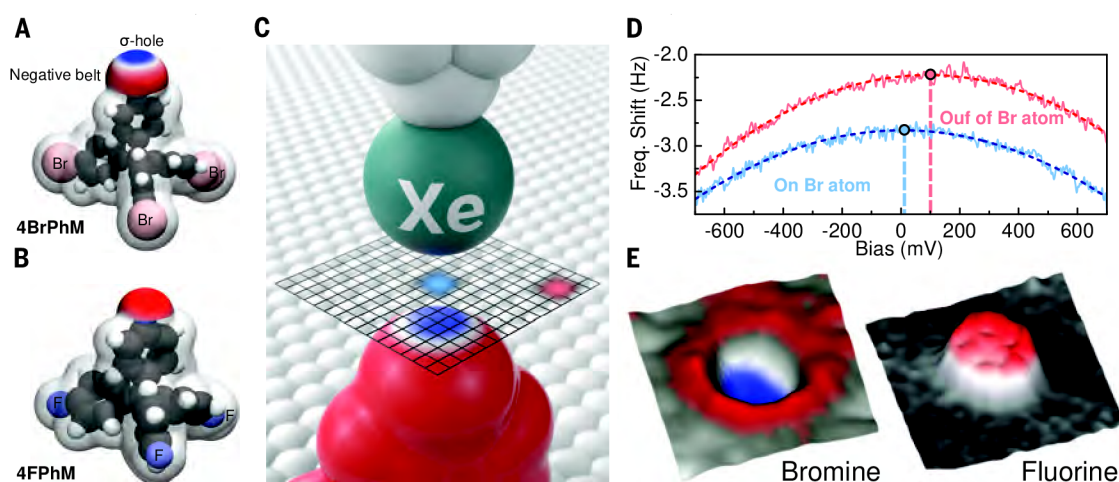
σ-hole. To test this hypothesis, we deliberately chose tetrakis(4-bromophenyl) methane (4BrPhM) and tetrakis(4-fluorophenyl) methane (4FPhM) compounds (Fig. 1, A and B). The skeleton arrangement of these compounds facilitates a tripodal configuration once deposited onto a surface with a single bromine-fluor atom oriented outward from the surface (fig. S1). This arrangement facilitated direct inspection of the σ-hole on a halogen atom by the front-most atom of a scanning probe, (Fig. 1C). Deposition of the molecules in low coverage (less than 1 monolayer) on the Ag(111) surface held at room temperature under UHV conditions led to the formation of well-ordered, self-assembled molecular arrangements in a rectangular formation (Fig. 2, A and B). Bromine atoms of the 4BrPhM molecule have a substantial positive σ-hole (Fig. 1A), and fluorine atoms possess an isotropic negative charge (Fig. 1B). This enabled us to perform comparative measurements on similar systems with and without the presence of the σ-hole.

Shown in Fig. 2, C and D, is a substantial contrast between two-dimensional (2D) constant-height KPFM maps acquired over Br and F front-most atoms of the molecular compounds with an Xe-decorated tip. In the case of the 4FPhM molecule, we observed a monotonous elliptical increase of the V_{LCPD} signal over the fluorine atom. In comparison, the KPFM image over the 4BrPhM molecule featured a notable ring-like shape. The 2D KPFM maps were recorded in the attractive tip-sample interaction regime near the minimum of the Δf-z curve (fig. S2) to avoid undesired topographic cross-talk (fig. S3 and supplementary text) or the effect of lateral bending of the functionalized probe due to repulsive forces (25) that could cause image distortions. Evolution of the contrast of the KPFM image of the σ-hole
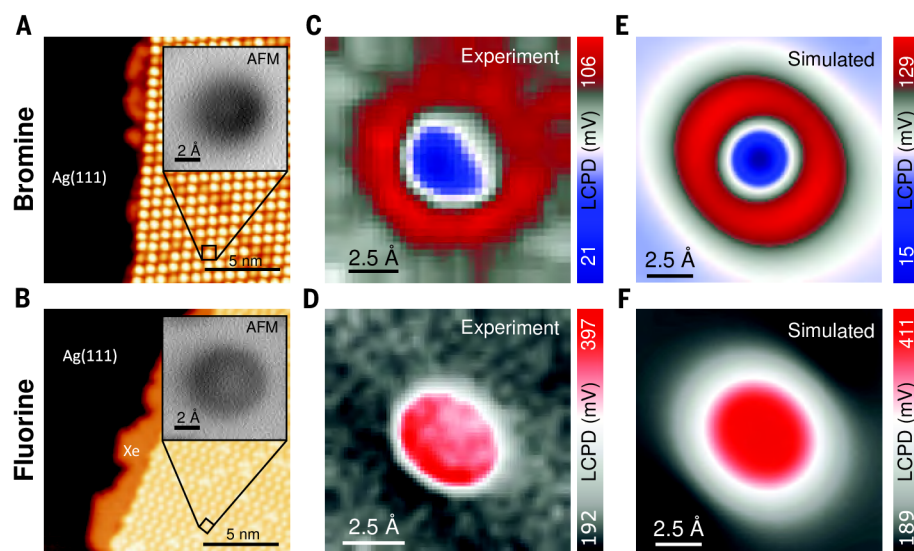
on the front-most Br atom with the tip-sample distance is shown in fig. S4.

Discussion

To confirm the origin of the anisotropic contrast observed experimentally on the Br atom, we carried out KPFM simulations using static ρ_0 and polarized $\delta\rho$ charges of Br and F-terminated molecules and Xe-tip models obtained from density functional theory (DFT) calculations (fig. S5). Simulated KPFM images that are perfectly matched to the experimental

maps are shown in Fig. 2, E and F. Our theoretical model allowed us to decompose the two leading contributions: the electrostatic interaction of the polarized charge on tip $\delta\rho_t$ with the static charge on the molecule and the counterpart term of the electrostatic interaction between the polarized charge on molecule $\delta\rho_s$ with the ρ_t^0 static charge of the tip (fig. S5). We found that the anisotropic contrast obtained on the Br-terminated molecule can be rationalized from a variation of the microscopic electrostatic interaction between

Fig. 2. KPFM imaging of 4BrPhM and 4FPhM molecules with an Xe-tip. (**A** and **B**) STM images of a molecular self-assembled submonolayer of 4BrPhM and 4FPhM molecules on an Ag(111) surface. (Insets) AFM images acquired on a single molecule with a Xe tip at the minima of the frequency shift. (**C** and **D**) Experimental KPFM images obtained with a functionalized Xe tip over bromide and fluoride atoms of single 4BrPhM and 4FPhM molecules. (**E** and **F**) Calculated KPFM images with a functionalized Xe tip of single 4BrPhM and 4FPhM molecules. Blue indicates low values of V_{LCPD} and red indicates high values of V_{LCPD}.

atomic-scale charges of tip and sample. On the periphery of the Br atom, the positive shift of V_{CPD} is given by the electrostatic interaction of the spherical polarized charge, $\delta\rho_t$ of the Xe-tip apex, with the belt of negative charge surrounding the positive σ-hole. By contrast, in the central part, the electrostatic interaction with the positive crown of the σ-hole turned the V_{LCPD} value with respect to that on the peripheral region. In the case of the 4FPhM molecule, both terms provided a trivial contrast with a positive shift of the V_{LCPD} over the atom. The term corresponding to the static charge ρ_s^0 on the molecule revealed an elliptical shape originating from neighbor positively charged hydrogen atoms in the underlying phenyl group of the 4FPhM molecule. Therefore, the shape of the feature presented in the KPFM image provided additional information about the internal arrangement of the molecule on the surface.

We deliberately used a single Xe atom to functionalize the tip apex instead of the more commonly used carbon monoxide (CO). As discussed above, the Xe tip allowed us to optimize the imaging conditions of the σ-hole because static charge density ρ_0 on the apex of the CO-tip had a strong quadrupolar character (Fig. 3A), and the charge on the Xe tip was highly spherical (fig. S5). This choice eliminated spurious spatial variation of the V_{LCPD} signal, which did not belong directly to the σ-hole. In particular, a component of the microscopic electrostatic interaction between static charge ρ_t^0 of the tip and polarized charge on sample $\delta\rho_s$ needs to be abolished. In the case of the Xe-tip, the spatial variation of the local V_{CPD} was dominated by the component that includes the interaction of a spherically polarized charge on the Xe atom $\delta\rho_t$ with the anisotropic electrostatic field of the σ-hole. This enabled a direct mapping of the spatial charge distribution of the σ-hole by means of the KPFM technique.

Thus, it is instructive to look at the KPFM images acquired with the CO tip on the 4FPhM molecule as well. Despite the frontier fluorine atom of the 4FPhM molecule having an isotropic charge distribution, the experimental KPFM image (Fig. 3B) features a nontrivial ringlike shape with lower values of the V_{LCPD} signal on the center of the fluorine atom. Our KPFM simulation using a CO-tip (Fig. 3C) coincided qualitatively with the experimental counterpart. From a detailed analysis of the electrostatic components (fig. S6), we found that the contrast arose from the interaction of the spherical polarized charge $\delta\rho_s$ on a fluorine atom with the static quadrupole charge on a CO tip, composed of a negative crown of density on an oxygen atom surrounded by a positive charge belt (Fig. 3A). Thus, the KPFM features resolved on the 4FPhM molecule re-

flected the quadrupolar charge distribution of the CO tip. Thus, from the spatial variation of the V_{LCPD} signal, we could determine the sign of the quadrupole of the CO molecule on the tip. The shift of V_{LCPD} toward lower values in the central part of the KPFM image was caused by the negative charge crown of the quadrupole charge localized at oxygen (Fig. 3A). The enhanced V_{LCPD} value on the periphery reflects the positively charged belt of the quadrupole charge of the CO molecule. This reverse shift of V_{LCPD} with respect to the previous case of the σ-hole was caused by our inspection of the anisotropic charge on the tip instead of the sample. A detailed explanation of the origin and sign of V_{LCPD} shift is available in the supplementary materials.

Alternatively, some works reported subatomic features in noncontact atomic force microscopy (nc-AFM) (26) images with CO functionalized tips (27). However, the origin of such contrast and their interpretation of the physical meaning are under debate (28, 29). Additionally, nc-AFM has demonstrated unprecedented chemical resolution of single molecules (30) or their charge distribution (31). Thus, we were intrigued by the possibility of imaging the σ-hole by means of nc-AFM with functionalized tips (27).

A series of high-resolution nc-AFM images acquired at a wide range of tip-sample distances are shown in fig. S7 with a CO tip and Xe tip, respectively. At the onset of the atomic contrast in nc-AFM mode, the tip-sample interaction was dominated by an attractive dispersion. The resulting AFM contrast for both 4FPhM and 4BrPhM molecules had a similar spherical character that lacks any subatomic feature. Also, in close tip-sample distances, the AFM contrast remained similar for both molecular compounds, featuring a bright spot in the center caused by the Pauli repulsion. Thus, we found that the AFM images did not

reveal any signature of the σ-hole in the whole range of tip-sample distances covering both an attractive and repulsive interaction regime.

To understand in detail this experimental observation, we performed theoretical analysis of the nc-AFM images with a CO tip using the probe particle SPM model (25). Shown in figs. S8 and S9 are lateral cross sections of different force components of the interaction energy acting between the CO tip and the outermost F and Br atoms of the 4FPhM and 4BrPhM molecules, respectively. The calculated AFM images showed similar atomic contrast, ruling out the possibility to image the σ-hole with a CO tip. From the analysis, we inferred that the AFM contrast was dominated by dispersive and Pauli interaction, both of which have a highly spherical character. On the other hand, the electrostatic interaction possesses an anisotropic character caused by the presence of both a σ-hole on the Br atom and a quadrupolar charge distribution on the apex of the CO-tip (Fig. 3A). Nevertheless, the magnitude of the electrostatic interaction was about one order smaller than the competing dispersion and Pauli interactions, which made the σ-hole hard to image in the AFM technique. From this analysis, we could conclude that the resolution of anisotropic atomic charges requires a technique such as KPFM, whose contrast mechanism is mastered by the electrostatic interaction that maps the charge distribution on the forefront atoms.

Next, we investigated the influence of the σ-hole on the noncovalent intermolecular interaction energies. The nc-AFM technique provided the distinctive possibility to explore interaction energies between individual atoms and molecules placed on the tip apex and sample by means of site-specific force spectroscopies (32–35). Apart from a quantitative evaluation of the interaction energies between well-defined entities, the nc-AFM
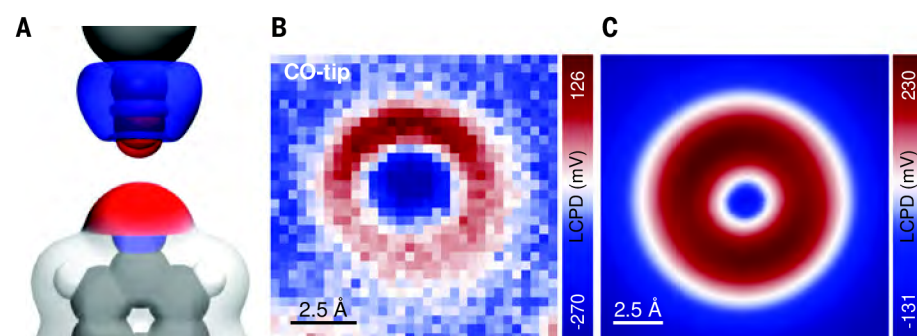

Fig. 3. KPFM imaging of a 4FPhM molecule with a CO tip. (**A**) Schematic view of a CO tip above a 4FPhM molecule with a superimposed calculated differential charge density of the CO tip, revealing (top) a quadrupole charge of a CO-tip model and (bottom) calculated electrostatic potential of 4FPhM molecule showing an isotropic negative charge on the frontier fluorine atom in 4FPhM. (**B**) Experimental KPFM image acquired over the frontier fluorine atom with a CO tip. (**C**) Simulated KPFM image of a 4FPhM molecule with a CO tip. Blue indicates low values of V_{LCPD}, and red indicates high values of V_{LCPD}.
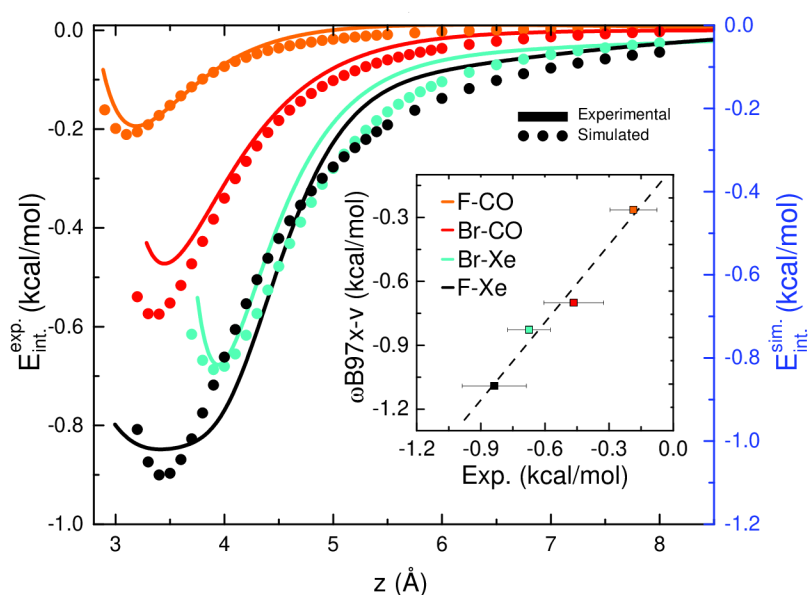
Fig. 4. Comparison of experimental and theoretical interaction energies of four complexes. Experimental (solid curves) and calculated (dots, obtained with DFT/ωB97X-V) energy curves versus tip-sample distance between 4FPhM and 4BrPhM molecules and Xe and CO tips. (Inset) The correlation between experimental and theoretical values [coefficient of determination (R^2) = 0.98] of the energy minima for all complexes. Bars indicate an estimated experimental error of the energy minima calculated as the difference between a polynomial fit and the experimental energy (fig. S12).

technique also gave an invaluable opportunity to benchmark the accuracy of different theoretical methods to describe these weak noncovalent interactions (*34–36*).

Tip functionalization offered an opportunity to explore distinct scenarios of the interaction mechanisms with molecular complexes. The Xe tip has a positive net charge and large polarizability, but the CO tip possesses a quadrupolar charge (O and C carry negative and positive net charge, respectively) and a relatively small polarizability. Their interaction energies are shown in Fig. 4, with the 4FPhM and 4BrPhM molecules as a function of the tip-sample distance. Small values of the maximum energies of 0.2 to 0.83 kcal/mol revealed a noncovalent bonding mechanism. In general, the complexes with an Xe-tip are more stable than the complexes with a CO tip, which may be rationalized by a larger dispersion interaction caused by an Xe tip. We observed that the Xe-4BrPhM complex was less stable than the Xe-4FPhM complex (by 0.67 and 0.83 kcal/mol, respectively) despite the larger polarizability of Br that determines the magnitude of the polarization interaction. This effect was caused by the presence of the repulsive electrostatic interaction between the positive σ-hole on a Br atom and the positively charged Xe tip, which partially cancelled the attractive dispersive interaction in the Xe-4BrPhM complex. On the other hand, the dispersive and electrostatic forces are both attractive in the case of the Xe-4FPhM complex, resulting

in a larger total interaction energy. This observation not only supported the presence of the positive σ-hole on the Br atom, it also explained the origin of a peculiar intermolecular orientation of halogen-bonded molecular systems (*12–15*).

Recently, a vigorous effort has been devoted to the development of computational methods based on DFT with dispersion correction that are able to reliably describe intermolecular interactions in noncovalent complexes (*37*). But their transferability is still limited owing to adopted approximations, and thus, careful benchmarking is desired. From this perspective, the above-described complexes represent interesting noncovalent systems for benchmarks with a complex interplay between the dispersion and the electrostatic interaction. The maximum interaction energies measured were below 1 kcal/mol, which used to be considered as the limit of chemical accuracy, further strengthening the benchmark.

Accurate interaction energies for different types of noncovalent complexes could be obtained from a nonempirical coupled-cluster method covering triple-excitations [CCSD(T)]. Unfortunately, its large computational demands made it impossible to apply this method to a system of the size of the molecules we investigated in the present work.

To circumvent this problem, we performed the CCSD(T) calculations on smaller reference model systems consisting of F- and Br-benzene, exhibiting similar characteristics as

4BrPhM and 4FPhM molecules (supplementary materials). We compared the calculated CCSD(T) interaction energies to interaction energies obtained with several popular DFT functionals (table S3). We found that the range-separated ωB97X-V functional (*38*) that implicitly covers dispersion energy provided good agreement with the benchmarked dataset (table S3). Because this functional was also shown to provide the best results among other popular DFT functionals for various types of systems with noncovalent interactions (*38*), we selected this functional for further use.

To check its transferability to our larger molecular systems, we calculated the interaction energies between 4FPhM and 4BrPhM molecules and Xe- and CO-tip models. Excellent agreement between the ωB97X-V interaction energies and the experimental data results is shown in Fig. 4. The calculated energy minima for all complexes fit the measured values perfectly within the experimental error (Fig. 4, inset). The PBE0 functional (*39*) with the D3 correction (*40*) reproduced the CCSD(T) results on small-model systems as well (table S3 and fig. S10). However, its transferability on the large systems was no longer as good as the range-separated ωB97X-V functional (fig. S11).

The ωB97X-V functional describes well the interaction trend for all considered systems (Fig. 4, inset), with the caveat that it systematically slightly overestimates the interaction energy by ~0.1 kcal/mol. The perfect agreement between theoretical and experimental values could not be expected because calculations were limited to free-standing 4FPhM and 4BrPhM molecules interacting with Xe- and CO-tip model, and in the experiment, 4FPhM and 4BrPhM molecules were adsorbed at Ag(111) surface. The results confirmed good transferability of the ωB97X-V functional toward larger systems. Moreover, the good agreement between calculated and experimental datasets obtained for all four complexes also gave confidence in the multiscale benchmark technique that uses small-model complexes with the Xe-tip model. Therefore, this approach makes it possible to accurately describe systems whose size does not allow for the direct application of the accurate coupled-cluster technique (or a similar technique), or when other direct experimental measurements are currently not feasible.

Conclusions

We report the possibility of achieving the spatial resolution of anisotropic atomic charge with the KPFM technique, which not only provided direct evidence of the existence of σ-holes but is expected to substantially extend the possibility to characterize charge distribution in complex molecular systems and on surfaces. We anticipate that this technique could

be further extended to provide invaluable information about the local inhomogeneous polarizability of individual atoms on surfaces or within molecules with unprecedented spatial resolution in chemical and biologically relevant systems.

REFERENCES AND NOTES

1. N. Ramasubbu, R. Parthasarathy, P. Murray-Rust, *J. Am. Chem. Soc.* **108**, 4308–4314 (1986).
2. O. Hassel, J. Hvoslef, E. H. Vihovde, N. A. Sörensen, *Acta Chem. Scand.* **8**, 873–873 (1954).
3. O. Hassel *et al.*, *Acta Chem. Scand.* **13**, 275–280 (1959).
4. O. Hassel *et al.*, *Acta Chem. Scand.* **12**, 1146–1146 (1958).
5. P. Auffinger, F. A. Hays, E. Westhof, P. S. Ho, *Proc. Natl. Acad. Sci. U.S.A.* **101**, 16789–16794 (2004).
6. T. Clark, M. Hennemann, J. S. Murray, P. Politzer, *J. Mol. Model.* **13**, 291–296 (2007).
7. T. Brinck, J. S. Murray, P. Politzer, *Int. J. Quantum Chem.* **44** (S19), 57–64 (1992).
8. P. Politzer, P. Lane, M. C. Concha, Y. Ma, J. S. Murray, *J. Mol. Model.* **13**, 305–311 (2007).
9. G. R. Desiraju *et al.*, *Pure Appl. Chem.* **85**, 1711–1713 (2013).
10. K. E. Riley, P. Hobza, *Phys. Chem. Chem. Phys.* **15**, 17742–17751 (2013).
11. L. C. Gilday *et al.*, *Chem. Rev.* **115**, 7118–7195 (2015).
12. Z. Han *et al.*, *Science* **358**, 206–210 (2017).
13. J. Tschakert *et al.*, *Nat. Commun.* **11**, 5630 (2020).
14. S. Kawai *et al.*, *ACS Nano* **9**, 2574–2583 (2015).
15. H. Huang *et al.*, *ACS Nano* **10**, 3198–3205 (2016).
16. M. Nonnenmacher, M. P. O'Boyle, H. K. Wickramasinghe, *Appl. Phys. Lett.* **58**, 2921–2923 (1991).
17. T. Glatzel, S. Sadewasser, Eds., *Kelvin Probe Force Microscopy* (Springer, 2018), vol. 65.
18. W. Melitz, J. Shen, A. C. Kummel, S. Lee, *Surf. Sci. Rep.* **66**, 1–27 (2011).
19. L. Nony, A. S. Foster, F. Bocquet, C. Loppacher, *Phys. Rev. Lett.* **103**, 036802 (2009).
20. S. Sadewasser *et al.*, *Phys. Rev. Lett.* **103**, 266103 (2009).
21. F. Mohn, L. Gross, N. Moll, G. Meyer, *Nat. Nanotechnol.* **7**, 227–231 (2012).
22. L. Gross *et al.*, *Science* **324**, 1428–1431 (2009).
23. F. Albrecht *et al.*, *Phys. Rev. Lett.* **115**, 076101 (2015).
24. B. Mallada *et al.*, *ACS Sustain. Chem. Eng.* **8**, 3437–3444 (2020).
25. P. Hapala *et al.*, *Phys. Rev. B Condens. Matter Mater. Phys.* **90**, 085421 (2014).
26. T. R. Albrecht, P. Grütter, D. Horne, D. Rugar, *J. Appl. Phys.* **69**, 668–673 (1991).
27. P. Jelínek, *J. Phys. Condens. Matter* **29**, 343002 (2017).
28. F. Huber *et al.*, *Science* **366**, 235–238 (2019).
29. M. Emmrich *et al.*, *Science* **348**, 308–311 (2015).
30. L. Gross, F. Mohn, N. Moll, P. Liljeroth, G. Meyer, *Science* **325**, 1110–1114 (2009).
31. P. Hapala *et al.*, *Nat. Commun.* **7**, 11560 (2016).
32. M. A. Lantz *et al.*, *Science* **291**, 2580–2583 (2001).
33. Y. Sugimoto *et al.*, *Nature* **446**, 64–67 (2007).
34. S. Kawai *et al.*, *Nat. Commun.* **7**, 11559 (2016).
35. Z. Sun, M. P. Boneschanscher, I. Swart, D. Vanmaekelbergh, P. Liljeroth, *Phys. Rev. Lett.* **106**, 046104 (2011).
36. C. Wagner *et al.*, *Nat. Commun.* **5**, 5568 (2014).
37. S. Grimme, A. Hansen, J. G. Brandenburg, C. Bannwarth, *Chem. Rev.* **116**, 5105–5154 (2016).
38. N. Mardirossian, M. Head-Gordon, *Phys. Chem. Chem. Phys.* **16**, 9904–9924 (2014).
39. C. Adamo, V. Barone, *J. Chem. Phys.* **110**, 6158–6170 (1999).
40. S. Grimme, J. Antony, S. Ehrlich, H. Krieg, *J. Chem. Phys.* **132**, 154104 (2010).
41. B. Mallada *et al.*, Data for "Real-space imaging of anisotropic charge of σ-hole by means of Kelvin probe force microscopy". *Zenodo* (2020); doi:10.5281/zenodo.5172233.

Visualization of π-hole in molecules by means of Kelvin probe force microscopy

B. Mallada [1,2,3,6], M. Ondráček [1,6], M. Lamanec [3,4,5,6], A. Gallardo[1], A. Jiménez-Martín[1,2], B. de la Torre [1,2] ✉, P. Hobza [4,5] ✉ & P. Jelínek [1,2] ✉

Submolecular charge distribution significantly affects the physical-chemical properties of molecules and their mutual interaction. One example is the presence of a π-electron-deficient cavity in halogen-substituted polyaromatic hydrocarbon compounds, the so-called π-holes, the existence of which was predicted theoretically, but the direct experimental observation is still missing. Here we present the resolution of the π-hole on a single molecule using the Kelvin probe force microscopy, which supports the theoretical prediction of its existence. In addition, experimental measurements supported by theoretical calculations show the importance of π-holes in the process of adsorption of molecules on solid-state surfaces. This study expands our understanding of the π-hole systems and, at the same time, opens up possibilities for studying the influence of submolecular charge distribution on the chemical properties of molecules and their mutual interaction.

Non-covalent interactions are crucial in many chemical and biological processes, such as supramolecular assembling, ion recognition, and protein stability. The nature of non-covalent intermolecular bonds is determined, among others, by dispersion and electrostatic forces. While the dispersion force is always attractive and directionless, the electrostatic component can be attractive or repulsive and is highly directional. The nature of the electrostatic interaction is intimately linked to the internal charge distribution within the molecule. Therefore, precise knowledge of the charge distribution in molecules is a fundamental requirement for comprehending non-covalent interactions[1].

For instance, in the most prevalent category of molecular species, polycyclic aromatic hydrocarbons (PAHs), the larger electronegativity of carbon compared to the peripheral hydrogen results in an accumulation of electron density in the delocalized/conjugated π-bonds on the carbon skeleton. This electron-rich delocalized/conjugated π-bond system, which is evenly distributed above and below the molecular plane, generates a negative quadrupole moment for the PAH

molecules, see Fig. 1. However, substituting peripheral hydrogens with other substituents that are more electronegative than carbon, such as fluorine or chlorine, reverses the electron population of the π-bond system to make it electron-deficient[2], see Fig. 1. Consequently, the quadrupole moment of such a molecule becomes positive[3]. The presence of a π-electron-deficient cavity in the central part of the molecule is called a π-hole[4,5].

The π-hole concept can be vividly illustrated by comparing the electron distribution of benzene, C_6H_6, and hexafluorobenzene, C_6F_6. In benzene, electrons are localized within the aromatic carbon skeleton, as depicted in the electrostatic potential map shown in Fig. 1. Conversely, in hexafluorobenzene, the higher electronegativity of fluorine results in electron withdrawal from carbon atoms towards halogens, leading to a depletion of electron density in the central π-system on the carbon atoms. The origin of the distinct localization of the electron density in both systems is closely associated with the different characteristics of occupied molecular orbitals. Namely, in the case of C_6F_6, the occupied orbitals are delocalized over both carbon

[1]Institute of Physics, Academy of Sciences of the Czech Republic, Prague, Czech Republic. [2]Regional Centre of Advanced Technologies and Materials, Czech Advanced Technology and Research Institute (CATRIN), Palacký University Olomouc, 78371 Olomouc, Czech Republic. [3]Department of Physical Chemistry, Palacký University Olomouc, Tr. 17. listopadu 12, 771 46 Olomouc, Czech Republic. [4]Institute of Organic Chemistry and Biochemistry, Czech Academy of Sciences, Flemingovo Náměstí 542/2, 16000 Prague, Czech Republic. [5]IT4Innovations, VŠB – Technical University of Ostrava, 17. Listopadu 2172/15, 708 00 Ostrava-Poruba, Czech Republic. [6]These authors contributed equally: B. Mallada, M. Ondráček, M. Lamanec. ✉e-mail: bruno.de@upol.cz; pavel.hobza@uochb.cas.cz; jelinekp@fzu.cz
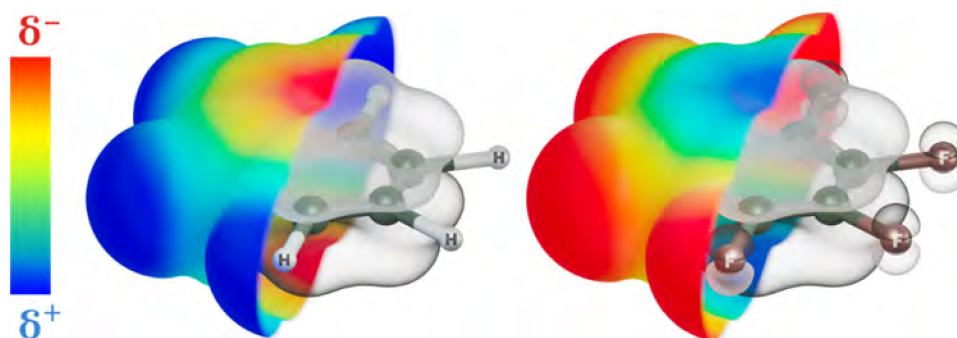
Fig. 1 | Schematic description of the concept of π-hole. The spatial distribution of the highest occupied molecular orbitals (HOMO) (grey-shaded volumes) of benzene (C_6H_6) on the left and hexafluorobenzene (C_6F_6) on the right overlapped with the electrostatic potential map (coloured surface from red (negative charge) to blue (positive charge)).

and fluorine atoms. In contrast, in the case of C_6H_6 molecule, they are predominantly localized on carbon atoms only, as seen in the grey surfaces in Fig. 1.

As discussed above, the presence of a positively charged π-hole significantly affects non-covalent intermolecular interactions. For example, intermolecular stacking interactions[6], which play an essential role in the stabilization of the helical structure of DNA bases, can be strongly affected by the presence of a π-hole. The decisive role of the electrostatic interaction on the stacked structure can be well documented for the simplest stacked aromatic systems, dimers of benzene C_6H_6 and/or hexafluorobenzene, C_6F_6. In the case of homodimers, their stabilization is entirely caused by dispersion interaction, as the electrostatic quadrupole-quadrupole interaction is repulsive. However, in the case of heterodimers, the situation changes due to the attractive electrostatic quadrupole-quadrupole interaction, which allows a close approach of the aromatic rings resulting in significant dispersion interaction and, consequently, resulting in substantial stabilization of the heterodimers[3].

It is evident that the presence of π-hole may strongly affect the physicochemical properties of molecular systems. So far, the concept of π-hole has been developed exclusively on a theoretical basis using quantum calculations. Experimentally, the existence of π-hole has only been proven indirectly based on measured data, the interpretation of which can only explain the presence of π-hole[7] However, a direct experimental observation that would clearly prove the existence of the π-hole has been lacking so far.

Of all the experimental techniques, scanning probe microscopy (SPM) emerges as the most appropriate tool for the direct visualization of π-holes in molecular systems. In recent years, the development of SPM with a functionalized probe[8,9] has enabled the unprecedented spatial resolution not only of the chemical[8] and spin[10] structure of molecules on the surfaces but also of the anisotropic atomic charge on individual atoms, the so-called σ-hole[11]. In this article, we will show that the Kelvin probe force microscopy (KPFM) method, which enabled us to resolve the σ-hole for the first time, is an ideal imaging tool for the real space observation of the π-hole system as well.

Results and discussion
Experimental results
Here, we experimentally visualize the π-hole in 9,10-Dichloroocta-fluoroanthracene $C_{14}F_8Cl_2$ (FCl-An) molecule and, at the same time, its absence in anthracene $C_{14}H_{10}$ (An). As discussed above, the presence of different substituents rules the charge transfer between π-orbitals of the carbon skeleton and the substituents. Supplementary Fig. 1 displays selected occupied orbitals of An and FCl-An, whose comparison reveals their different shapes. Similarly, as in the case of C_6H_6 and C_6F_6, the molecular orbitals in An are localized only at the carbon skeleton, while these in FCl-An are also extended at all halogen

substituents. In the latter case, this gives rise to the presence of π-hole localized on the carbon skeleton. The presence of π-hole could also be seen in electron density difference maps[12], see Supplementary Fig. 2.

Here we investigated heterogeneous molecular self-assemblies consisting of FCl-An and An molecules. Figure 2a displays the molecular self-assembly grown by simultaneous sublimation of the two compounds on an atomically clean Au (111) surface kept at room temperature in an ultrahigh vacuum. Scanning probe microscopy images, acquired at a base temperature of 4.8 K, reveal large-scale ordered molecular islands composed of both molecular species alternating in a periodic fashion (Fig. 2a, b).

To determine the detailed arrangement of the molecular species in the assembly, we use noncontact atomic force microscopy (nc-AFM) with a functionalized carbon monoxide (CO) tip. The high-resolution nc-AFM images acquired at a constant height mode in Fig. 2b clearly distinguish two different molecular species. To gain insight into the self-assembly structure, we carried out total energy density functional theory (DFT) calculations as well as AFM imaging of the supramolecular structure on the Au (111) surface. The perfect agreement between experimental and theoretical nc-AFM images allowed us to unambiguously resolve the chemical structure of both An and FCl-An molecules, as well as their arrangement. The supramolecular assembly comprises a rhombic periodic structure with one An and two FCl-An molecules in the unit cell, as shown in Fig. 2b,c. The arrangement is dictated by attractive intermolecular electrostatic interactions between negatively charged fluorine atoms, σ-hole on chlorine, and positively charged hydrogen atoms (Fig. 2d). This scenario is supported by the fact that the mere deposition of An on the surface does not result in the formation of self-organized molecular structures, as shown in Supplementary Fig. 3.

Notably, the high-resolution AFM images show, apart from the difference in the apparent size of the molecular species, a relatively similar contrast of the carbon skeleton for both types of molecules. In addition, AFM images show that FCl-An molecules are systematically imaged brighter than An molecules due to a topographic effect, as we will discuss below. Thus, the AFM images apparently do not provide any direct experimental evidence of π-hole.

Therefore, we employed Kelvin Probe Force Microscopy, which records the spatial variation of the local contact potential difference (LCPD) across the surface[13]. At short tip-sample distances, the magnitude of the LCPD is affected by a short-range electrostatic interaction between the tip apex and surfaces, enabling us to map the charge distribution (See Fig. 3a, d) with atomic resolution[11,14]. The KPFM technique was employed to investigate the charge distribution at the atomic and molecular levels. This technique is useful for the detection of single electron charge states of individual atoms[15] and molecule[16], mapping charge distribution within molecules[17], resolving molecular dipolar moments[18], and visualizing the anisotropic charge
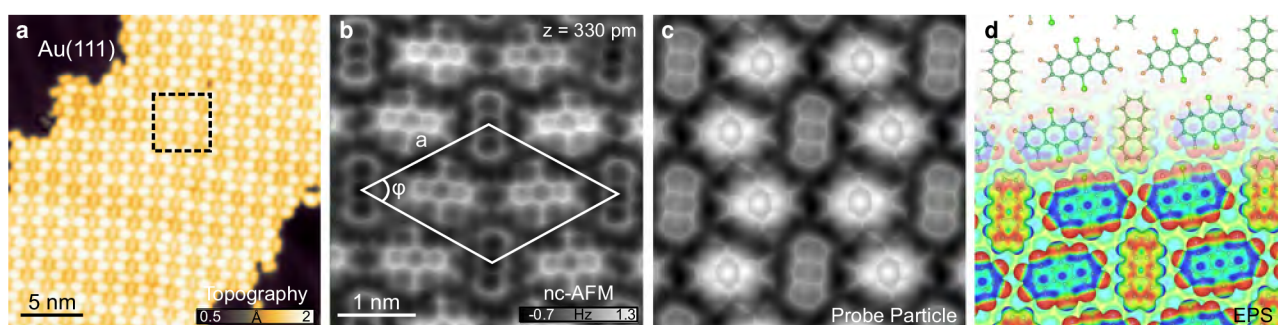
Fig. 2 | Overview and description of the system. a STM (V_{Bias} = 500 mV, I_{tunnel} = 10 pA) topography overview of the ordered self-assembly structure of An and FCl-An molecules on Au(111). **b** Constant height nc-AFM with CO-tip of the unit cell of the self-assembly (white solid line, a = 1.85 ± 0.02 nm, φ = 122 ± 0.6°). **c** Probe Particle simulated nc-AFM image. **d** Model of the self-assembly of An and FCl-An (top) and the electrostatic potential map of the optimized supramolecular structure (bottom). Source data are provided as a Source Data file.
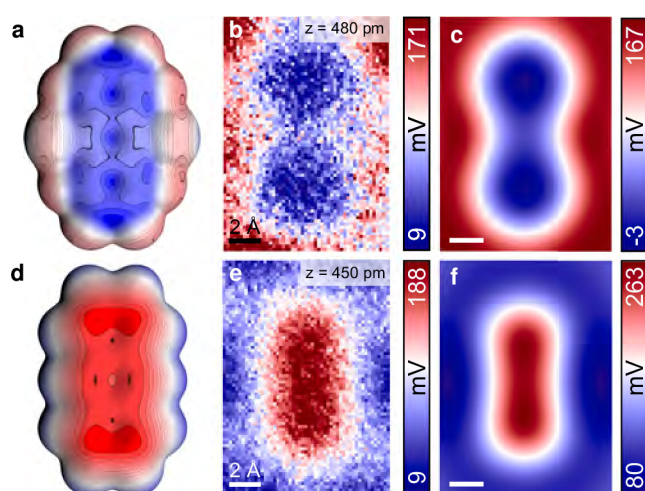

Fig. 3 | Simulated and experimental charge distributions of FCl-An and An. a, d Electrostatic potential maps of free-standing FCl-An and An molecules. **b, e** Experimental LCPD maps of FCl-An and An acquired with the same CO-tip in constant height mode. **c, f** Probe Particle simulated LCPD maps of FCl-An and An. Source data are provided as a Source Data file.

distributions in single atoms[11]. In previous work, it was demonstrated that the sensitivity of the KPFM method could be substantially enhanced[11,17,19,20] using functionalized probes. Moreover, it was demonstrated that the KPFM technique could capture contrast inversion for fluorinated and hydrogenated benzene rings within the same molecules[21]. These results indicate the possibility of resolving π-hole by the KPFM technique.

Figures 3b and 3e depict constant height KPFM maps conducted with the same CO-terminated tip of individual An and FCl-An molecules, respectively. These maps reveal a striking difference in the LCPD contrast between the two molecular species. Specifically, the LCPD signal over An/FCl-An molecule is shifted to a higher/lower value, indicating a decrease/increase in the local work function. The anthracene molecule possesses a uniform positive LCPD signal, representing a negative charge distribution. At the same time, the fluorinated counterpart exhibits a bow-tie shape of negative LCPD, indicating a positive charge distribution. Large KPFM images (Supplementary Fig. 4) of molecules adsorbed at various sites demonstrate the same trend, suggesting that the observed effects are not attributable to spatial variations in the LCPD of the substrate.

In terms of KPFM measurements, it is important to note that the obtained contrast is highly dependent on the tip-sample distance, as illustrated in Supplementary Fig. 5. Specifically when the tip-sample

distance is far, the KPFM images do not exhibit intramolecular features. As the tip-sample distance decreases, submolecular contrast becomes increasingly pronounced. Nonetheless, tip relaxations can noticeably influence the KPFM signal at shorter tip-sample distances and generate measurement artifacts. In contrast to nc-AFM imaging, where tip-relaxations improve the submolecular resolution, in KPFM measurement, such relaxations cause a noticeable deviation in the LCPD signal from its parabolic shape[22]. Therefore, we opt for a tip-sample height close to the Δf minima on both molecules, which ensures the absence of tip relaxation and enhances the contrast. This choice is further supported by the absence of submolecular resolution in Δf^* images (Δf^* corresponds to the Δf(V) maximum, that is, Δf at compensated LCPD, see Methods) for either An or FCl-An, as shown in Supplementary Fig. 5 and 6.

To rationalize the experimental KPFM images, we performed KPFM simulations using the optimized supramolecular structures obtained from DFT calculations using PP-AFM code[11,23]. The simulated KPFM images shown in Fig. 3c,f match very well with the experimental evidence. In particular, they also reproduce submolecular variation of the LCPD signal with the characteristic bow-tie pattern presented in the central part of FCl-An molecule. This internal variation of the LCPD signal also nicely matches the distribution of the electrostatic potential calculated for a free-standing FCl-An molecule, shown in Fig. 3a. This effect is associated with the heterogeneous charge distribution of the π-hole due to the different electronegativity of fluorine and chlorine modulating the charge transfer from the π-system locally.

It should be noted that KPFM measurements on the atomic scale are only qualitative and themselves cannot say anything about the sign of the charge on the substrate. To prove that the observed variation of LCPD contrast in the central part of the FCl-An molecule corresponds to the presence of the positive charge associated with π-hole, we take advantage of the presence of a positively charged σ-hole on Cl, see Fig. 2d. The σ-hole can be partially visualized when the probe is sufficiently close to the substrate, see Supplementary Fig. 7. Importantly, both the central region of the molecule and σ-hole show very similar LCPD vales ~110 mV. This direct comparison enables us to confirm the presence of a positively charged region associated with π-hole. Optionally, the presence of a positive charge in the central part of the FCl-An molecule is also indirectly supported by the good agreement between the range of LCPD values in the experimental and simulated patterns shown in Fig. 3b, c.

The influence of π-hole in the adsorption height

We already mentioned that the presence of a π-hole can substantially change the stacking interaction. Thus, we analysed how the presence of π-hole affects the adsorption of the molecules on a metallic substrate. A series of constant height AFM images, shown in Supplementary Fig. 8, reveal that submolecular contrast first emerges on FCl-An
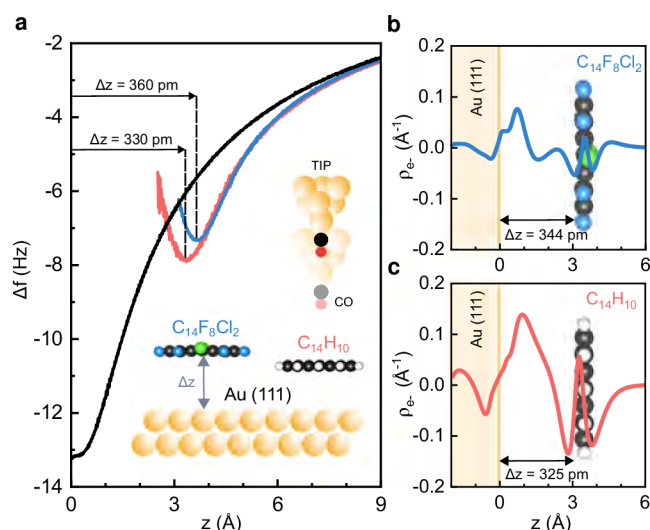
Fig. 4 | Charge transfer and π-hole effect on the adsorption height.
a Experimental adsorption heights estimated with Δf-z spectroscopies in the middle hexagon of the molecules (inset) FCl-An (blue line) and An (red line) respect to Au(111) substrate (black-line), see Supplementary Fig. 9. **b, c** Calculated induced electron density of FCl-An (top, blue line) on Au(111) and An (bottom, red line) as a function of the distance between the surface and the molecule. Source data are provided as a Source Data file.

molecules independently of their adsorption site. This observation suggests different adsorption heights of the FCl-An and An molecules on the Au(111) surface. To analyse in more detail the different adsorption heights of the molecules, we carried out specific-site force-distance spectroscopy. Figure 4a displays Δf-z spectroscopy acquired with the same CO-tip above the central benzene unit of both An and FCl-An molecules. The difference between the minima of two Δf-z curves of 30 pm can be directly related to the difference in the adsorption height of the molecule[24]. Moreover, we also acquired Δf-z spectroscopy over the bare Au(111) surface, which enables us to determine the relative height of the molecules above the Au(111) surface, to be 330 and 360 pm for An and FCl-An, respectively. These values match reasonably well with the adsorption height obtained from the total energy DFT calculations of molecular assembly on Au(111) surface (325 and 344 pm, respectively).

One may argue that the greater adsorption height of FCl-An molecule is caused by the presence of chlorine atoms in FCl-An. A larger atomic radius of chlorine atoms (1.75 Å (Cl) and 1.47 Å (F)) may enhance Pauli repulsion pushing the molecule out of the Au(111) surface. However, the total energy DFT simulation of the fully fluorinated molecule provides a remarkably similar adsorption height of 343 pm over the Au(111) surface, see Supplementary Table 1 Thus, the presence of chlorine atoms does not influence the adsorption height. Next, we looked at the character of bonding interaction between the molecules and metallic substrate. According to DFT calculations, both molecules are physiosorbed with negligible hybridization of molecular orbitals (see Supplementary Figs. 10 and S11), and the interaction is dominated by dispersion interaction, see Supplementary Table 2. Figure 4b, c represents the calculated induced electron density between An and FCl-An molecules and the Au (111) surfaces. We observe that there is more significant induced electron density in the interface between An molecule and metallic substrate compared to FCl-An/Au(111) interface. The induced charge density is a consequence of attractive electrostatic interaction between the molecule and the surface. In the case of An molecule, the HOMO orbital is found close to the Fermi level of metal, which facilitates the charge induction upon the adsorption (Supplementary Fig. 10). However, in the case of the FCl-An molecule, the presence of π-hole increases the ionization potential and consequently

suppresses the charge density induction at the molecule/metal interface.

To get more detailed insight into the adsorption energy, we perform the symmetry-adapted perturbation treatment (SAPT0), which provides the interaction energy decomposition scheme[25]. The SAPT0 analysis was performed on a cluster model, which gives very similar results to the slab model. It is also worth noting that DFT and SAPT0 calculations give very similar results of adsorption energies of molecules on Au(111), see Supplementary Table 2. Supplementary Table 3 presents the SAPT0 energy decomposition for all three molecules. It is evident that in all cases, the attractive interaction dominates the dispersion energy compared to the electrostatic and induction terms. Importantly, the induction energy describing stabilization energy due to electrostatic interaction between permanent charge multipoles and the induced charge is larger for An than for FCl-An molecule. This trend fully agrees with the above-mentioned findings on the relative magnitude of induced electron densities in An and FCl-An predicted by the DFT slab calculation, see Fig. 4b,c.

Here, we presented the experimental imaging of π-hole in molecular systems by its real space imaging on a single molecule by means of Kelvin probe force microscopy. We showed that the presence of π-hole also influences the electrostatic interaction between the molecule and a metallic surface and, consequently, the adsorption height of the molecule. Namely, the π-hole increases the ionization potential of the molecule, which inhibits the induction of the charge density at the molecule/metal interface. This results in weakened induced electrostatic interactions and, consequently, in larger adsorption height of the molecule. This study shows the potential of scanning microscopy for studying the internal charge distribution in molecules, which fundamentally affects their physical and chemical properties.

Methods
Experimental methods
The experiments were conducted at a temperature of 4.2 K using a commercial STM/nc-AFM microscope (Createc GmbH). Pt/Ir tips, sharpened by focused ion beam (FIB), were utilized and were further cleaned and shaped by gentle indentation (-1 nm) in the bare metallic substrate. STM topography was acquired in constant current mode with the bias voltage applied to the sample. In nc-AFM imaging, a qPlus sensor (resonant frequency ≈ 30 kHz; stiffness ≈ 1800 N/m) was operated in frequency modulation mode with an oscillation amplitude of 200 pm. Both nc-AFM and KPFM images were captured in constant height mode. The Au(111) substrate was prepared by repeated cycles of Ar+ sputtering (1 keV) and subsequent annealing at ~800 K. The STM/nc-AFM/KPFM images were processed using WSxM software[26].

Molecular deposition
9,10-Dichlorooctafluoroanthracene (FCl-An) and anthracene (An) molecules were sublimated with two Knudsen cells simultaneously in UHV conditions at RT on the sample of Au (111) for 15 s.

KPFM characterization and analysis
LCPD maps were obtained by fitting a parabolic expression to frequency shift vs bias spectroscopies ($\Delta f(V, x, y)$) collected at all the points of a 64 × 80 pixels rectangular grid of size 3 nm × 5 nm. The data was collected at constant height using the same CO functionalized tip for both anthracene and chlorinated molecules. Each data point was acquired in approximately 3 s, with each parabola containing 600 points. Following the acquisition, we fitted the data with a parabolic expression of the form $\Delta f(V) = a \times (V - LCPD)^2 + \Delta f^*$. The LCPD value, which corresponds to the bias at which the parabola has a maximum, and the Δf^* parameter, which is the maximum frequency shift value, were extracted from the fitted parabolas and plotted separately in the (x, y) grids to generate maps. The data did not exhibit any significant distortion or deviation from expected parabolic behaviour within the

bias range of (−150, 400) mV for either molecule or tip. The acquisition height was chosen to be in the attractive regime to maximize the electrostatic contribution for both molecules.

Theoretical methods

The optimized geometries of free-standing molecules, individual molecules adsorbed on the Au(111) surface, and the supramolecular assembly, both free standing and on-surface, were calculated using DFT-based methods implemented in the FHI-AIMS (Fritz Haber Institute Ab-Initio Materials Simulation) code[27]. Local atom-centred basis sets consisted of the "light" default basis sets (the version from 2010) for individual species as distributed with FHI-AIMS. The PBE[28] version of the GGA was employed for the exchange-correlation function. The surface Brillouin zone was represented by only one k-point (Γ). This lightweight setup – "light" basis, PBE functional, no k-grid – was needed to cope with the relatively large supercells in calculations that involved the Au(111) surface. For individual free-standing molecules, calculations with the hybrid PBE0[29,30] functional and the "tight" basis have also been carried out without substantial changes in either the geometry or charge distribution. The Au(111) slab consisted of 4 atomic layers. The size of the surface supercell intended to represent isolated molecules on the surface corresponded to the 6 × 6-unit cell of the unreconstructed Au(111) surface. In the case of the supramolecular structure, we first optimized the size of the supercell without the Au surface. Then, we constructed a √39 × √39 surface cell of Au(111) and deformed it somewhat (stretched by 1.20 % in one main crystallographic direction, compressed by 1.06% in the other, and reduced the angle between the two directions from 60° to 56.3°) so as to exactly match 2 optimal unit cells of the supramolecular structure. During geometry optimization, the free-standing molecules were forced to remain planar while for molecules on the surface, all atoms in the system except the bottom layer Au atoms were allowed to relax. Van der Waals correction of interatomic forces based on the Tkatchenko-Scheffler method with Hirshfeld partitioning[31] was applied to the molecular structures on the surface, excluding direct Au-Au interaction. The geometries were considered fully optimized when all forces except those corresponding to a constraint were under 2 meV/Å.

The AFM and KPFM images have been simulated using the Probe Particle (PP) model[23] adapted to a CO-terminated tip. The elastic deflection of the CO molecule has been modelled using the lateral (along the surface) spring constant of 0.25 N/m. DFT-calculated electron densities of the sample surface have been used in the PP model to evaluate the Pauli repulsion[32]. Furthermore, DFT-calculated maps of electrostatic potential and electrical polarizability (derived from the difference of electron densities in the external field of 0.1 eV/Å and without the external field, respectively) have been employed to generate the simulated KPFM maps[11] while assuming the d_{z^2}-like charge quadrupole of −0.2 e/Å^2 for the CO tip termination. The long-range contribution of the LCPD signal was adopted from the experimental $\Delta f(V)$ taken in the far tip-sample distance.

The molecular orbitals, as well as the electrostatic potential maps of isolated An and FCl-An were calculated for MP2/cc-pVTZ[33] optimized geometries. The cluster calculations used for SAPT0 analysis consisted of a single molecule An and FCl-An and surface represented by one layer made of 38 gold atoms with (111) orientation. Both studied molecules were optimized on the gold layer using PBE0[29] functional with Grimme's D3[34] dispersion correction using the Becke-Johnoson damping[35] and def2-TZVPP[36] basis set. The molecule was fully relaxed while the atoms of the gold layer were fixed. All these calculations were carried out by ORCA quantum chemistry program package[37]. SAPT0 calculations were made on the cluster models by PSI4[38] program in cc-pVDZ (cc-pwCVDZ-PP[39] for Au) basis set.

Data availability

Source data are provided with this paper. The data supporting this study's findings are also available from the authors on request and in the repository https://doi.org/10.6084/m9.figshare.23660622. Source data are provided with this paper.

References

1. Müller-Dethlefs, K. & Hobza, P. Noncovalent interactions: a challenge for experiment and theory. *Chem. Rev.* **100**, 143–168 (2000).
2. Murray, J. S., Shields, Z. P. I., Seybold, P. G. & Politzer, P. Intuitive and counterintuitive noncovalent interactions of aromatic π regions with the hydrogen and the nitrogen of HCN. *J. Comput. Sci.* **10**, 209–216 (2015).
3. Pluháčková, K., Jurečka, P. & Hobza, P. Stabilisation energy of C_6H_6 ···C_6X_6 (X = F, Cl, Br, I, CN) complexes: complete basis set limit calculations at MP2 and CCSD(T) levels. *Phys. Chem. Chem. Phys.* **9**, 755–760 (2007).
4. Murray, J. S., Lane, P., Clark, T., Riley, K. E. & Politzer, P. σ-Holes, π-holes and electrostatically-driven interactions. *J. Mol. Model* **18**, 541–548 (2012).
5. Politzer, P., Murray, J. S. & Clark, T. The π-hole revisited. *Phys. Chem. Chem. Phys.* **23**, 16458–16468 (2021).
6. Řezáč, J. & Hobza, P. Benchmark calculations of interaction energies in noncovalent complexes and their applications. *Chem. Rev.* **116**, 5038–5071 (2016).
7. Wang, H., Wang, W. & Jin, W. J. σ-hole bond vs π-hole bond: a comparison based on halogen bond. *Chem. Rev.* **116**, 5072–5104 (2016).
8. Gross, L., Mohn, F., Moll, N., Liljeroth, P. & Meyer, G. The chemical structure of a molecule resolved by atomic force microscopy. *Science (1979)* **325**, 1110–1114 (2009).
9. Jelínek, P. High resolution SPM imaging of organic molecules with functionalized tips. *J. Phys. Condens. Matter* **29**, 343002 (2017).
10. Wäckerlin, C. et al. Role of the magnetic anisotropy in atomic-spin sensing of 1D molecular chains. *ACS Nano* **16**, 16402–16413 (2022).
11. Mallada, B. et al. Real-space imaging of anisotropic charge of σ-hole by means of Kelvin probe force microscopy. *Science (1979)* **374**, 863–867 (2021).
12. Wheeler, S. E. & Houk, K. N. Through-space effects of substituents dominate molecular electrostatic potentials of substituted arenes. *J. Chem. Theory Comput.* **5**, 2301–2312 (2009).
13. Sadewasser, S. & Glatzel, T. In Kelvin Probe Force Microscopy: from Single Charge Detection to Device Characterization (Springer International Publishing, Cham, 2018).
14. Sadewasser, S. et al. New insights on atomic-resolution frequency-modulation kelvin-probe force-microscopy imaging of semiconductors. *Phys Rev. Lett.* **103**, 266103 (2009).
15. Gross, L. et al. Measuring the charge state of an adatom with non-contact atomic force microscopy. *Science (1979)* **324**, 1428–1431 (2009).
16. Berger, J. et al. Quantum dissipation driven by electron transfer within a single molecule investigated with atomic force microscopy. *Nat. Commun.* **11**, 1337 (2020).
17. Mohn, F., Gross, L., Moll, N. & Meyer, G. Imaging the charge distribution within a single molecule. *Nat. Nanotechnol.* **7**, 227–231 (2012).
18. Klein, B. P. et al. Molecular topology and the surface chemical bond: alternant versus nonalternant aromatic systems as functional structural elements. *Phys. Rev. X* **9**, 011030 (2019).
19. Mallada, B. et al. Atomic-scale charge distribution mapping of single substitutional p-and n-Type dopants in graphene. *ACS Sustain Chem Eng* **8**, 3437–3444 (2020).
20. Mohn, F., Schuler, B., Gross, L. & Meyer, G. Different tips for high-resolution atomic force microscopy and scanning tunneling

microscopy of single molecules. *Appl. Phys. Lett.* **102**, 073109 (2013).

21. Moll, N. et al. Image distortions of a partially fluorinated hydrocarbon molecule in atomic force microscopy with carbon monoxide terminated tips. *Nano Lett.* **14**, 6127–6131 (2014).

22. Albrecht, F. et al. Probing charges on the atomic scale by means of atomic force microscopy. *Phys. Rev. Lett.* **115**, 076101 (2015).

23. Hapala, P. et al. Mechanism of high-resolution STM/AFM imaging with functionalized tips. *Phys. Rev. B Condens Matter Mater Phys.* **90**, 085421 (2014).

24. Schuler, B. et al. Adsorption geometry determination of single molecules by atomic force microscopy. *Phys. Rev. Lett.* **111**, 106103 (2013).

25. Gonthier, J. F. & Sherrill, C. D. Density-fitted open-shell symmetry-adapted perturbation theory and application to π-stacking in benzene dimer cation and ionized DNA base pair steps. *J. Chem. Phys.* **145**, 134106 (2016).

26. Horcas, I. et al. WSXM: a software for scanning probe microscopy and a tool for nanotechnology. *Rev. Sci. Instrum.* **78**, 013705 (2007).

27. Blum, V. et al. Ab initio molecular simulations with numeric atom-centered orbitals. *Comput. Phys. Commun.* **180**, 2175–2196 (2009).

28. Perdew, J. P., Burke, K. & Ernzerhof, M. Generalized gradient approximation made simple. *Phys. Rev. Lett.* **77**, 3865–3868 (1996).

29. Adamo, C. & Barone, V. Toward reliable density functional methods without adjustable parameters: the PBE0 model. *J. Chem. Phys.* **110**, 6158 (1999).

30. Ren, X. et al. Resolution-of-identity approach to Hartree–Fock, hybrid density functionals, RPA, MP2 and *GW* with numeric atom-centered orbital basis functions. *New. J. Phys.* **14**, 053020 (2012).

31. Tkatchenko, A. & Scheffler, M. Accurate molecular van der Waals interactions from ground-state electron density and free-atom reference data. *Phys. Rev. Lett.* **102**, 073005 (2009).

32. Krejčí, O., Hapala, P., Ondráček, M. & Jelínek, P. Principles and simulations of high-resolution STM imaging with a flexible tip apex. *Phys. Rev. B* **95**, 045407 (2017).

33. Dunning, T. H. Gaussian basis sets for use in correlated molecular calculations. I. The atoms boron through neon and hydrogen. *J. Chem. Phys.* **90**, 1007–1023 (1989).

34. Grimme, S., Antony, J., Ehrlich, S. & Krieg, H. A consistent and accurate ab initio parametrization of density functional dispersion correction (DFT-D) for the 94 elements H-Pu. *J. Chem. Phys.* **132**, 154104 (2010).

35. Grimme, S., Ehrlich, S. & Goerigk, L. Effect of the damping function in dispersion corrected density functional theory. *J. Comput. Chem.* **32**, 1456–1465 (2011).

36. Weigend, F. & Ahlrichs, R. Balanced basis sets of split valence, triple zeta valence and quadruple zeta valence quality for H to Rn: design and assessment of accuracy. *Phys. Chem. Chem. Phys.* **7**, 3297 (2005).

37. Neese, F., Wennmohs, F., Becker, U. & Riplinger, C. The ORCA quantum chemistry program package. *J. Chem. Phys.* **152**, 224108 (2020).

38. Smith, D. G. A. et al. PSI4 1.4: open-source software for high-throughput quantum chemistry. *J. Chem. Phys.* **152**, 184108 (2020).

39. Peterson, K. A. & Puzzarini, C. Systematically convergent basis sets for transition metals. II. Pseudopotential-based correlation consistent basis sets for the group 11 (Cu, Ag, Au) and 12 (Zn, Cd, Hg) elements. *Theor. Chem. Acc.* **114**, 283–296 (2005).

Author contributions

Conceptualization: P.J., P.H. Methodology: B.M., B.T., P.J. Theoretical calculations: M.O., A.G., M.L., P.J., P.H. Experimental: B.M., A.J-M., B.T. Funding acquisition: P.H., P.J., B.T. Supervision: B.T., P.H., P.J. Writing – original draft: B.M., B.T., P.H., P.J.

Competing interests

The authors declare no competing interests.

Additional information

Supplementary information The online version contains supplementary material available at https://doi.org/10.1038/s41467-023-40593-3.

Correspondence and requests for materials should be addressed to B. de la Torre, P. Hobza or P. Jelínek.

Peer review information *Nature Communications* thanks Leo Gross and the other, anonymous, reviewer(s) for their contribution to the peer review of this work. A peer review file is available.

Reprints and permissions information is available at http://www.nature.com/reprints

From Theory to Experiment:

A Computational Chemistry Perspective

on Covalent Dative Bond

and Non-covalent Interactions

Mgr. Maximilián Lamanec

Supervisor: prof. Ing. Pavel Hobza, DrSc.

Co-supervisor: RNDr. Dana Nachtigallová, PhD.

Faculty of Science | Palacký University

Olomouc

2024

Abstract

This thesis explores advanced computational chemistry methods to investigate chemical bonding and molecular interactions. It uses computational approaches like DFT, MP2, CCSD(T), alongside other methods of computational chemistry, to analyze electronic structures and various properties of molecular systems. The study further examines covalent dative bonds in p-group elements, elucidating their formation, unexpected behavior upon solvation, and significant role in addition reactions of secondary amines with fullerenes. Subsequently, it focuses on the behavior of molecules with hydridic hydrogen, highlighting their unique interactions when hydrogen acts as an electron donor and interacts with electrophiles. Finally, the thesis combines advanced computational chemistry methods with atomic force microscopy and for the first time demonstrates the anisotropic charge distribution on the surface of a covalently bonded halogen (σ-hole) and in the center of an aromatic ring with electronwithdrawing substituents (π-hole), showing excellent correlation between computational models and experimental observations.

Keywords: dative covalent bond, non-covalent interactions, hydridic hydrogen, σ-hole, π-hole, QM calculations

Abstrakt

Táto dizertačná práca používa pokročilé metódy výpočtovej chémie na skúmanie chemických väzieb a molekulových interakcií. Pomocou výpočtových metód ako DFT, MP2, CCSD(T) a ďalších metód výpočtovej chémie, analyzuje elektronové štruktúry a rôzne vlastnosti molekulových systémov. Dizertačná práca odhaľuje tvorbu datívnej väzby v prvkoch p-skupiny, jej neočakávané správanie pri solvatácii a významnú úlohu v adičných reakciách sekundárnych amínov s fulerénmi. Následne sa zameriava na molekuly obsahujúce hydridický vodík, zdôrazňujúc ich jedinečné interakcie, keď vodík pôsobí ako donor elektrónov a interaguje s elektrofilmi. Nakoniec práca spája pokročilé metódy výpočtovej chémie s mikroskopiou atomárnych síl a po prvýkrát ukazuje nerovnomerné rozloženie náboja na povrchu kovalentne viazaného halogénu (σ-dieru) a v strede aromatického kruhu s elektrofilnými substituentmi (π-dieru), ukazujúc vynikajúcu koreláciu medzi výpočtovými modelmi a experimentálnymi pozorovaniami.

Kľúčové slová: datívna väzba. nekovalentné interakcie, hydridický vodík, σ-diera, π-diera, kvantovomechanické výpočty

Contents

List of Author's Publications

Articles published in years 2019-2024

1   M. LAMANEC[*], R. LO[*], D. NACHTIGALLOVÁ, A. BAKANDRITSOS, E. MO-
    HAMMADI, M. DRAČÍNSKÝ, R. ZBOŘIL, P. HOBZA and W. WANG:
    'The Existence of a N→C Dative Bond in the C_{60}–Piperidine Complex',
    Angewandte Chemie International Edition **60**, 1942–1950 (2021).

2   R. LO[*], M. LAMANEC[*], W. WANG, D. MANNA, A. BAKANDRITSOS, M. DRA-
    ČÍNSKÝ, R. ZBOŘIL, D. NACHTIGALLOVÁ and P. HOBZA:
    'Structure-directed formation of the dative/covalent bonds in complexes
    with C_{70}⋯piperidine',
    Physical Chemistry Chemical Physics **23**, 4365–4375 (2021).

3   R. LO[*], D. MANNA[*], M. LAMANEC[*], W. WANG, A. BAKANDRITSOS, M. DRA-
    ČÍNSKÝ, R. ZBOŘIL, D. NACHTIGALLOVÁ and P. HOBZA:
    'Addition Reaction between Piperidine and C_{60} to Form 1,4-Disubsti-

tuted C_{60} Proceeds through van der Waals and Dative Bond Complexes: Theoretical and Experimental Study',
Journal of the American Chemical Society **143**, 10930–10939 (2021).

4   B. Mallada[*], A. Gallardo[*], M. Lamanec[*], B. de la Torre, V. Špirko, P. Hobza and P. Jelínek:
    'Visualization of σ-hole in molecules by means of Kelvin probe force microscopy',
    Science **374**, 863–867 (2021).

5   R. Lo, D. Manna, M. Lamanec, M. Dračínský, P. Bouř, T. Wu, G. Bastien, J. Kaleta, V. M. Miriyala, V. Špirko, A. Mašínová, D. Nachtigallová and P. Hobza:
    'The stability of covalent dative bond significantly increases with increasing solvent polarity',
    Nature Communications **13**, 2107 (2022).

6   R. Lo, A. Mašínová, M. Lamanec, D. Nachtigallová and P. Hobza:
    'The unusual stability of H-bonded complexes in solvent caused by greater solvation energy of complex compared to those of isolated fragments',
    Journal of Computational Chemistry **44**, 329–333 (2022).

7   S. Civiš[*], M. Lamanec[*], V. Špirko, J. Kubišta, M. Špeťko and P. Hobza:
    'Hydrogen Bonding with Hydridic Hydrogen–Experimental Low-Temperature IR and Computational Study: Is a Revised Definition of Hydrogen Bonding Appropriate?',
    Journal of the American Chemical Society **145**, 8550–8559 (2023).

8   B. Mallada[*], M. Ondráček[*], M. Lamanec[*], A. Gallardo, A. Jiménez-Martín, B. de la Torre, P. Hobza and P. Jelínek:
    'Visualization of π-hole in molecules by means of Kelvin probe force microscopy',
    Nature Communications **14**, 4954 (2023).

Chapter 1

Introduction

Significant advances in computer technology have powered the remarkable rise of computational chemistry in recent years. This field has become indispensable across various domains of chemistry, including drug discovery, materials science, and catalysis, providing insights that are often infeasible through experimental methods alone. By allowing the exploration of molecular interactions, reaction mechanisms, and potential energy surfaces *in silico*, computational chemistry not only accelerates the research and development cycle but also offers a deeper understanding of fundamental chemical principles. Strategies for solving the Schrödinger equation range in precision, providing insights into the subtleties of chemical bonding.

The spectrum extends from the foundational Hartree-Fock (HF) method to the computationally intensive Full Configuration Interaction (FCI), which encompasses all electron correlations. Positioned between these is the Coupled Cluster (CC) approach, which is often heralded as the 'gold standard' of quantum chemistry in its form with variational treatment of single and double excitations and perturbative triples (CCSD(T)). Alternatively, to these wavefunction-based methods, Density Functional Theory (DFT) offers a different perspective by treating the Schrödinger equation as a functional of electron density. Through a multitude of functionals, DFT can address a wide array of both general and specific chemical problems.

This thesis focuses on chemical bonding from a computational chemistry perspective. Dative covalent bond, hydridic hydrogen bond and interactions with anisotropic charge distribution on the surface of molecule σ-hole and π-hole.

1.1   Dative Bond

A dative covalent bond, also known as a donor-acceptor bond, represents a unique bonding interaction in which two atoms share an electron pair, with both electrons originating from the same atom. In this configuration, the electron donor—the atom providing the electron pair—is typically a Lewis base, while the electron acceptor is a Lewis acid[1]. This mode of bonding is dis-

tinct from a covalent bond, where each atom contributes one electron to the shared pair. Upon dissociation, a dative bond cleaves heterolytically, allowing the donor atom to retain the electron pair[2,3]. The corresponding wavefunction foe dative covalent bond can be written as:

$$\Psi_{\text{dative}}(D^+ - A^-) = a\Psi_{\text{covalent}}(D - A) + b\Psi_{\text{ionic}}(D^+, A^-) \quad (1.1)$$

Here, the covalent and ionic structures are distinct for the donor (D)–acceptor (A) complex, and the coefficients a and b depend on the ability of D to donate an electron (ionization potential) and A to accept the electron (electron affinity)[4].

1.2 Hydrogen Bond a Charge Inverted Hydrogen Bond

The hydrogen bond, which is widely recognized as one of the strongest and most prevalent noncovalent interactions, plays a crucial role in numerous chemical processes. It is characterized by the formation of an X-H···Y-Z bond, where X represents a more electronegative atom than hydrogen (H), and Y can be an atom, anion, fragment of a molecule, or a π-electron system. X-H is a proton donor and Y-Z is a proton acceptor[5].

The presence of a hydrogen bond can be easily detected through various spectroscopic techniques. This detection is

facilitated by the fact that the atom X is always heavier than hydrogen. When a hydrogen bond is formed, there is a transfer of electron from the electron donor Y to the σ^* antibonding orbital of the X-H bond[6–8].

The charge-inverted hydrogen bond (CIHB) is a distinctive non-covalent interaction wherein a hydrogen atom is linked to a less electronegative atom, conferring upon it a partial negative charge. This peculiar arrangement permits the hydrogen to form bonds with electrophiles[9]. Notably, CIHBs exhibit bond elongation and vibrational red-shifting, characteristic of standard hydrogen bonds but arising from a reverse charge transfer direction, specifically $\sigma_{XH} \rightarrow p_y$, as opposed to the conventional $\sigma_{XH} \leftarrow p_y$. Furthermore, dimers such as $H_3X-H \cdots YH_3$ display non-linear structures and interaction energies that are consistent with moderately strong hydrogen bonds, despite their charge-inverted nature[10].

1.3 σ-hole and π-hole bonding

The halogens were conventionally considered as uniformly negative. Research leaders mainly by Peter Politzer showed, that covalently bonded halogens can exhibits a positively char-ged region atop the halogen atom, diametrically opposed to the covalent bond[11–15]. The presence of a positively charged region on covalently bonded halogens can be rationalized through the

example of the bromobenzene molecule. Bromine's valence shell electron configuration is $4s^2\ 3d^{10}\ 4p_x^2 4p_y^2 4p_z^1$. Hybridization of the halogen atoms has negligible influence since the s-orbital is energetically much lower than the p-orbitals[16]. The p_x and p_y orbitals are both doubly occupied, forming a negatively charged belt around the bromine atom. On the other hand, one electron from the p_z orbital participates in a covalent bond, resulting in a positive "cap" located opposite to the covalent bond.

The π-hole refers to a region of positive electrostatic potential that emerges above and below the plane of a π-system, like an aromatic ring or a conjugated system. This arises from an asymmetric distribution of electronic charge, especially pronounced in molecules with electronegative substituents. The π-hole is characterized by a relative electron deficiency due to electron withdrawal from the π-system. In hexafluorobenzene, electrons are also distributed around the fluorine atoms, leading to the formation of a positive 'hole' in the center of the conjugated system.

The π-hole refers to a region of positive electrostatic potential that emerges above and below the plane of a π-system, like an aromatic ring or a conjugated system. This arises from an asymmetric distribution of electronic charge, especially pronounced in molecules with electronegative substituents. The π-hole is characterized by a relative electron deficiency due to electron withdrawal from the π-system. In hexafluorobenzene,

electrons are also distributed around the fluorine atoms, leading to the formation of a positive 'hole' in the center of the conjugated system[17,18].

1.4 Computational Modeling Non-Covalent Interactions

The analysis of non-covalent interactions requires more sophisticated computational methods than those typically necessary for covalent bonds due to their subtler energy scales. Particularly for hydrogen-bonded systems where dispersion forces are significant, a nuanced approach to correlation energy is essential. Advanced quantum mechanical techniques that accurately quantify energy contributions on 1 kcal/mol are thus vital[19]. Interaction Energy (ΔE) is a fundamental metric for assessing the magnitude of these bonds, disassembling a complex (AB) into its individual components (A and B)[20]. There are two principal metrics for evaluating ΔE: Total interaction energy (ΔE^T), which includes deformation energy, defined as follows:

$$\Delta E^T(AB) = E(AB) - E(A_{opt}) - E(B_{opt}) \qquad (1.2)$$

In this equation, $E(AB)$ denotes the total energy of the complex, while $E(A_{opt})$ and $E(B_{opt})$ indicate the energies of the

independently optimized fragments. The Intrinsic interaction energy, conversely, is determined by:

$$\Delta E^I(AB) = E(AB) - E(A) - E(B) \qquad (1.3)$$

where $E(AB)$ represents the total energy of the complex, with $E(A)$ and $E(B)$ reflecting the energies of the separate fragments in complex geometry.

In computational chemistry, the finite basis set introduces an error known as the basis set superposition error (BSSE), which stems from the imbalanced treatment of fragments versus the entire complex. In dimer calculations, each monomer utilizes basis set functions from both monomers, but in monomer calculations, the counterpart's basis set functions are absent. This leads to an artificially stabilized complex compared to its dissociated state. The counterpoise correction (CP) technique, introduced by Boys and Bernardi[21], corrects for this discrepancy:

$$\Delta E^I_{CP}(AB) = E(AB) - E(A^{AB}) - E(B^{AB}) \qquad (1.4)$$

In this correction, $E(A^{AB})$ and $E(B^{AB})$ refer to the energies of the fragments calculated within the basis set of the complex, addressing the BSSE to yield more reliable interaction energies.

1.4.1   Vibrational Analysis

In computational chemistry, the Rigid Rotor Harmonic Oscillator (RRHO) model is a QM approximation used to describe the rotational and vibrational motions of molecules. In this model, the 'rigid rotor' component assumes that the molecule rotates without any deformation, akin to a rigid body, while the 'harmonic oscillator' portion posits that the atoms within the molecule vibrate about their equilibrium positions in a harmonic fashion, where the forces restoring the atoms to their original positions are proportional to their displacements. This harmonic potential leads to quantized energy levels that are equidistant, a characteristic of an ideal harmonic oscillator. The calculation of vibrational frequencies within this model involves determining the force constants from the molecular geometry, which are then used to solve the Schrödinger equation for vibrational motion. This yields energy levels and corresponding vibrational frequencies that are integral to understanding molecular spectroscopy. However, the RRHO model simplifies the potential energy surface to a quadratic form, which only approximates the true behavior of molecular vibrations at low energies or small displacements from equilibrium positions[22].

Specifically, the RRHO model's depiction of X-H vibrations often proves inadequate due to inherent anharmonic behavior. These bonds exhibit pronounced anharmonicity as the energy

levels increase, deviating significantly from the idealized equidistant spacing. Such anharmonicity arises because the potential energy well of the X-H bond is not perfectly parabolic, becoming steeper as the atoms move closer and shallower at longer distances. This leads to a breakdown in the RRHO approximation for high-energy vibrational states or when atoms experience large displacements from equilibrium. As a result, more sophisticated models that incorporate anharmonic corrections are required to accurately predict the vibrational spectra of molecules, particularly for the description of high-energy vibrational modes and overtones[23].

The **Introduction** provides an overview of computational chemistry, underscoring its extensive applications across various research domains. It emphasizes the significance of basic research within this field and introduces the specific research area addressed in the thesis. Additionally, it offers a brief preview of each chapter, outlining their core focus and contributions to the overarching theme of the dissertation.

Chapter 2 offers an overview of various types of chemical bonds, ranging from the strongest covalent bond through the covalent dative bond to various non-covalent interactions like hydrogen bond, charge-inverted hydrogen bond, and bonds associated with σ-holes and π-holes. The chapter aims to provide a clear understanding of these bonds' roles and significance in molecular structures and interactions.

Chapter 3 offers an overview of computational chemistry

methods, introducing the Schrödinger equation and the Born-Oppenheimer approximation. It details the Hartree-Fock (HF) method, laying the foundation for advanced post-Hartree-Fock techniques like Møller-Plesset perturbation theory and the Coupled Cluster method. It briefly introduces Density Functional Theory and various types of functionals used. Additionally, the chapter outlines essential tools for analyzing non-covalent interactions, including interaction energy and vibrational analysis via the Rigid Rotor Harmonic Oscillator approximation, providing a comprehensive guide to the theoretical framework underlying computational chemistry.

In **Chapter 4**, a novel type of dative bond involving a nitrogen donor and a carbon acceptor is explored. This chapter presents the formation of N→C dative bonds between piperidine and fullerenes, highlighting carbon's unique role as an electron pair acceptor. It examines various bonding types between single piperidine and C_{60}, noting that the dative bond complex is least stable initially but becomes the most stable upon adding a second piperidine due to cascade charge transfer. The chapter also discusses the unusual strengthening of dative bonds upon solvation, contrasting with other bonds, and concludes by considering the dative bond complex in piperidine's addition reaction to C_{60} fullerene as an intermediate.

Chapter 5 challenges conventional hydrogen bonding concept by introducing hydridic hydrogen bonds, where hydrogen is attached to less electronegative elements, gaining a negative

partial charge. Unlike traditional hydrogen bonds, hydridic hydrogen acts as an electron donor, enabling interactions with electrophiles. This chapter investigates Me_3SiH interactions with the σ-holes of ICF_3 and $BrCN$.

Chapter 6 summarizes coordination of compoutational chemistry and Kelvin Probe Force Microscopy to visualize anisotropic charge distributions directly, bringing theoretical predictions to direct observation. Through the visualization of σ-holes and π-holes, this chapter effectively demonstrates the alignment of computational predictions with experimental findings, highlighting the symbiotic relationship between theoretical insights and empirical validation.

Conclusion compiles all the key findings of this thesis, encapsulating the novel insights and contributions to the field of chemistry. It provides a concise recapitulation of the research outcomes and discusses potential directions for future investigations based on the results presented.

Chapter 2

Conclusion

This thesis presents my research between 2019 and 2024, summarizing findings from publications 24, 25, 26, 27, 28, 29, and 30.

In **Chapter 4**, we introduced a novel type of dative bond wherein nitrogen acts as the donor and carbon as the acceptor. Due to their distinctive geometry, fullerenes can function as electron pair acceptors, thus forming dative bonds. We demonstrated that piperidine can interact with C_{60} to form various structures stabilized by van der Waals forces, tetrel bond, and dative bond. In a 1:1 ratio, the dative bond product exhibits lesser stability. However, the introduction of a second piperidine molecule significantly stabilizes the dative bond complex

due to a cascade of charge transfers from the outer piperidine through the dative bonded piperidine to the C_{60} fullerene. This theoretical prediction was corroborated by IR spectroscopy.

While C_{60}, with its I_h symmetry, has equivalent carbon atoms, the transition to the larger C_{70}, which exhibits D_{5h} symmetry, introduces diverse structural motifs. Designated as sites A, B, and C in descending order of curvature, the analysis reveals the most stable dative bond occurs between the piperidine dimer and carbon at site A, with decreasing stability at sites B and C. A comparison of the curvatures of C_{60}, C_{70}, and analogous motifs from other molecules with the respective interaction energies for piperidine dative bonded to these sites indicates that significant curvature is essential for the formation of a dative bond with the carbon framework.

Typically, both covalent and non-covalent interactions exhibit bond weakening upon solvation. However, dative bonds display a distinctive behavior where their strength increases with solvent polarity. Our computational studies predicted stabilization in various complexes featuring N→B, N→C, P→B, and P→C dative bonds. Particularly, the dative bond complex Me_3N-BH_3 was studied in more detail, revealing a decrease in the N-B distance and an increase of stabilization energy across solvents of varying polarities (ε=1.0, 2.0, 2.3, 4.8, 9.9, and 78.0). These computational predictions were validated experimentally using Raman spectroscopy to analyze the Me_3N-BH_3 complex in cyclohexane, benzene, chloroform, and water. The B-

N stretching frequency exhibited a consistent blue shift in line with our theoretical predictions.

Hydrogen bonded to an element less electronegative than itself exhibits behavior distinct from that in a conventional hydrogen bond, acting as a nucleophile. This unique interaction has led to various terminologies such as charge-inverted hydrogen bond or agostic bond. Our research, detailed in **Chapter 5**, demonstrates that hydridic hydrogen bonds exhibit similarities with conventional hydrogen bonds in terms of interaction energies and shifts in the X-H stretching frequency. Specifically, complexes of Me_3SiH with ICF_3 and BrCN were found to exhibit interaction energies and shifts in the X-H stretching frequency analogous to those observed in conventional hydrogen bonds. Infrared spectroscopy in an argon matrix confirmed the formation of complexes involving hydridic hydrogen. Given these findings, the term "hydridic hydrogen bond" was suggested, proposing that conventional hydrogen bonds might be better termed as "protonic hydrogen bonds." To resolve this nomenclature ambiguity, we proposed a revised definition of hydrogen bonds in ref. 27 covering both types of interactions.

Chapter 6 summarizes visualization of σ- and π-hole. Advances in microscopy of atomic forces and the specific functionalization of a silver tip with a xenon atom and a CO molecule have enabled subatomic resolution, crucial for visualizing σ-hole and, subsequently, π-holes. An advantage of the

nc-AFM technique is its ability to measure interaction energy directly. For a simplified model, we calculated the potential energy curve and benchmarked various DFT functionals. The ωB97X-V functional demonstrated the best correlation with the CCSD(T) reference, enabling us to accurately reproduce the interaction energy minima for four systems. The separation between these minima was less than 1 kcal/mol, aligning with the threshold for chemical accuracy. Notably, two distinct minima were observed in the nc-AFM analysis for the 4FPhM system using a xenon-functionalized silver tip, identified as contact Xe-F and Xe-H interactions, attributed to tilting of 4FPhM molecule on the surface. This exemplifies how computational chemistry not only corroborates experimental results but also provides insights when experimental data are ambiguous.

In conclusion, the research shared in this thesis makes a notable impact on the field of computational chemistry, especially concerning molecular interactions and chemical bonding. The author's work, recognized in esteemed scientific publications, underscores the relevance and caliber of the research undertaken. The proposed future directions offer a clear guide for forthcoming studies, promising continued progress and innovative discoveries in understanding and applying computational chemistry methods to explore molecular systems and interactions.

References

Articles and Books

1 G. Frenking, K. Wichmann, N. Fröhlich, C. Loschen, M. Lein, J. Frunzke and V. M. Rayón:
'Towards a rigorously defined quantum chemical analysis of the chemical bond in donor–acceptor complexes',
Coordination Chemistry Reviews **238-239**, Theoretical and Computational Chemistry, 55–82 (2003).

2 A. Nandi and S. Kozuch:
'History and Future of Dative Bonds',
Chemistry – A European Journal **26**, 759–772 (2020).

3 B. A. Smith and K. D. Vogiatzis:
'σ-Donation and π-Backdonation Effects in Dative Bonds of Main-Group Elements',
The Journal of Physical Chemistry A **125**, 7956–7966 (2021).

4   J. A. Plumley and J. D. Evanseck:
    'Covalent and Ionic Nature of the Dative Bond and Account of Accurate
    Ammonia Borane Binding Enthalpies',
    The Journal of Physical Chemistry A **111**, 13472–13483 (2007).

5   E. Arunan, G. R. Desiraju, R. A. Klein, J. Sadlej, S. Scheiner, I. Al-
    korta, D. C. Clary, R. H. Crabtree, J. J. Dannenberg, P. Hobza, H. G.
    Kjaergaard, A. C. Legon, B. Mennucci and D. J. Nesbitt:
    'Definition of the hydrogen bond (IUPAC Recommendations 2011)',
    83, 1637–1641 (2011).

6   G. Pimentel and A. McClellan:
    The Hydrogen Bond,
    (W. H. Freeman & Co. Ltd., 1960).

7   G. R. Desiraju, P. S. Ho, L. Kloo, A. C. Legon, R. Marquardt, P.
    Metrangolo, P. Politzer, G. Resnati and K. Rissanen:
    'Definition of the halogen bond (IUPAC Recommendations 2013)',
    Pure and Applied Chemistry **85**, 1711–1713 (2013).

8   A. E. Reed, F. Weinhold, L. A. Curtiss and D. J. Pochatko:
    'Natural bond orbital analysis of molecular interactions: Theoretical
    studies of binary complexes of HF, H_2O, NH_3, N_2, O_2, F_2, CO, and CO_2
    with HF, H_2O, and NH_3',
    The Journal of Chemical Physics **84**, 5687–5705 (1986).

9   M. Jabłoński:
    'Binding of X–H to the lone-pair vacancy: Charge-inverted hydrogen
    bond',
    Chemical Physics Letters **477**, 374–376 (2009).

10 M. Jabłoński:
    'Ten years of charge-inverted hydrogen bonds',
    Structural Chemistry **31**, 61–80 (2020).

11   T. Brinck, J. S. Murray and P. Politzer:
     'Surface electrostatic potentials of halogenated methanes as indicators
     of directional intermolecular interactions',
     International Journal of Quantum Chemistry **44**, 57–64 (1992).

12   P. Metrangolo, H. Neukirch, T. Pilati and G. Resnati:
     'Halogen Bonding Based Recognition Processes: A World Parallel to
     Hydrogen Bonding',
     Accounts of Chemical Research **38**, 386–395 (2005).

13   P. Politzer, P. Lane, M. C. Concha, Y. Ma and J. S. Murray:
     'An overview of halogen bonding',
     Journal of Molecular Modeling **13**, 305–311 (2007).

14   P. Metrangolo and G. Resnati:
     Halogen Bonding,
     (Springer Berlin, 2007).

15   P. Metrangolo, F. Meyer, T. Pilati, G. Resnati and G. Terraneo:
     'Halogen Bonding in Supramolecular Chemistry',
     Angewandte Chemie International Edition **47**, 6114–6127 (2008).

16   M. H. Kolář and P. Hobza:
     'Computer Modeling of Halogen Bonds and Other σ-Hole Interactions',
     Chemical Reviews **116**, 5155–5187 (2016).

17   H. Wang, W. Wang and W. J. Jin:
     'σ-Hole Bond vs π-Hole Bond: A Comparison Based on Halogen Bond',
     Chemical Reviews **116**, 5072–5104 (2016).

18   J. S. Murray, P. Lane, T. Clark, K. E. Riley and P. Politzer:
     'σ-holes, π-holes and electrostatically-driven interactions',
     Journal of Molecular Modeling **18**, 541–548 (2012).

19 P. Hobza:
'Calculations on noncovalent interactions and databases of benchmark interaction energies',
Accounts of Chemical Research **45**, 663–672 (2012).

20 P. Hobza and R. Zahradník:
Weak Intermolecular Interactions in Chemistry and Biology,
(Academia, 1980).

21 S. Boys and F. Bernardi:
'The calculation of small molecular interactions by the differences of separate total energies. Some procedures with reduced errors',
Molecular Physics **19**, 553–566 (1970).

22 C. H. Allen and C. P. Cross:
Molecular Vib-rotors: The Theory and Interpretation of High Resolution Infra-red Spectra,
(Wiley, 1963).

23 D. Papoušek and M. R. Aliev:
Molecular vibrational/rotational spectra,
(Academia, 1982).

24 M. Lamanec, R. Lo, D. Nachtigallová, A. Bakandritsos, E. Mohammadi, M. Dračínský, R. Zbořil, P. Hobza and W. Wang:
'The Existence of a N→C Dative Bond in the C_{60}–Piperidine Complex',
Angewandte Chemie International Edition **60**, 1942–1950 (2021).

25 R. Lo, M. Lamanec, W. Wang, D. Manna, A. Bakandritsos, M. Dračínský, R. Zbořil, D. Nachtigallová and P. Hobza:
'Structure-directed formation of the dative/covalent bonds in complexes with $C_{70}\cdots$piperidine',
Physical Chemistry Chemical Physics **23**, 4365–4375 (2021).

26   R. Lo, D. Manna, M. Lamanec, W. Wang, A. Bakandritsos, M. Dračín-
      ský, R. Zbořil, D. Nachtigallová and P. Hobza:
      'Addition Reaction between Piperidine and C_{60} to Form 1,4-Disubstitu-
      ted C_{60} Proceeds through van der Waals and Dative Bond Complexes:
      Theoretical and Experimental Study',
      Journal of the American Chemical Society **143**, 10930–10939 (2021).

27   S. Civiš, M. Lamanec, V. Špirko, J. Kubišta, M. Špeťko and P. Hobza:
      'Hydrogen Bonding with Hydridic Hydrogen–Experimental Low-Tem-
      perature IR and Computational Study: Is a Revised Definition of Hydro-
      gen Bonding Appropriate?',
      Journal of the American Chemical Society **145**, 8550–8559 (2023).

28   R. Lo, D. Manna, M. Lamanec, M. Dračínský, P. Bouř, T. Wu, G. Bas-
      tien, J. Kaleta, V. M. Miriyala, V. Špirko, A. Mašínová, D. Nachti-
      gallová and P. Hobza:
      'The stability of covalent dative bond significantly increases with in-
      creasing solvent polarity',
      Nature Communications 2022 13:1 **13**, 1–7 (2022).

29   B. Mallada, A. Gallardo, M. Lamanec, B. de la Torre, V. Špirko, P.
      Hobza and P. Jelinek:
      'Real-space imaging of anisotropic charge of σ-hole by means of Kelvin
      probe force microscopy',
      Science **374**, 863–867 (2021).

30   B. Mallada, M. Ondráček, M. Lamanec, A. Gallardo, A. Jiménez-
      Martín, B. de la Torre, P. Hobza and P. Jelínek:
      'Visualization of π-hole in molecules by means of Kelvin probe force
      microscopy',
      Nature Communications **14**, 4954 (2023).